

EVOLVING STARBURST MODEL OF FIR/SUB-MM/MM LINE EMISSION
AND ITS APPLICATIONS TO M82 AND NEARBY LUMINOUS INFRARED
GALAXIES

by

Lihong Yao

A thesis submitted in conformity with the requirements
for the degree of Doctor of Philosophy
Graduate Department of Astronomy and Astrophysics
University of Toronto

Copyright © 2009 by Lihong Yao

Abstract

Evolving Starburst Model of FIR/sub-mm/mm Line Emission and Its Applications to
M82 and Nearby Luminous Infrared Galaxies

Lihong Yao

Doctor of Philosophy

Graduate Department of Astronomy and Astrophysics

University of Toronto

2009

This thesis presents a starburst model for far-infrared/sub-millimeter/millimeter (FIR/sub-mm/mm) line emission of molecular and atomic gas in an evolving starburst region, which is treated as an ensemble of non-interacting hot bubbles which drive spherical shells of swept-up gas into a surrounding uniform gas medium. These bubbles and shells are driven by winds and supernovae within massive star clusters formed during an instantaneous starburst. The underlying stellar radiation from the evolving clusters affects the properties and structure of photodissociation regions (PDRs) in the shells, and hence the spectral energy distributions (SEDs) of the molecular and atomic line emission from these swept-up shells and the associated parent giant molecular clouds (GMCs) contains a signature of the stage evolution of the starburst.

The physical and chemical properties of the shells and their structure are computed using a simple well known similarity solution for the shell expansion, a stellar population synthesis code, and a time-dependent PDR chemistry model. The SEDs for several molecular and atomic lines (^{12}CO and its isotope ^{13}CO , HCN, HCO^+ , C, O, and C^+) are computed using a non-local thermodynamic equilibrium (non-LTE) line radiative transfer model.

By comparing our models with the available observed data of nearby infrared bright galaxies, especially M 82, we constrain the models and in the case of M 82, provide

estimates for the age of the recent starburst activity. We also derive the total H_2 gas mass in the measured regions of the central 1 kpc starburst disk of M 82. In addition, we apply the model to represent various stages of starburst evolution in a well known sample of nearby luminous infrared galaxies (LIRGs). In this way, we interpret the relationship between the degree of molecular excitation and ratio of FIR to CO luminosity to possibly reflect different stages of the evolution of star-forming activity within their nuclear regions.

We conclude with an assessment of the strengths and weaknesses of this approach to dating starbursts, and suggest future work for improving the model.

Acknowledgements

First and foremost, I would like to thank my thesis advisor, Professor Ernie Seaquist, for his guidance and support throughout the course of this work. Especially, I thank Ernie for his patient and understanding, because much of our discussions on this thesis work were carried out through long distant, sometimes very frustrating email and telephone communications for the last five years.

I thank Dr. Howard Yee, Dr. Bill Clarke, my Ph.D. committee members Dr. Bob Abraham, Dr. Barth Netterfield, Department of Astronomy and Astrophysics, and School of Graduate Studies at the University of Toronto, for allowing me to complete this thesis work off-campus. I also thank all of the departmental staff for their kind help with my computer related issue, yearly registration, travel expense claim, and library references.

I am grateful to the Canadian Institute for Theoretical Astrophysics at the University of Toronto for their generosity in allowing me to use their computing facility to run the PDR and Radiative Transfer simulations. I am also grateful of the use of PPARC funded Miracle Computing Facility, located at UCL, to test the Radiative Transfer code. This research was supported by a research grant from the Natural Sciences and Engineering Research Council of Canada to Professor Ernie Seaquist, and a Reinhardt Graduated Student Travel Fellowship from the Department of Astronomy and Astrophysics at the University of Toronto.

Since July 2003 I have been living in United States, I became a off-campus student, so I can share the custody of my young child in the US, while battling the most ridiculous, expensive, heart-aching custody of my daughter lunched by my ex, which has caused me face starving and nearly homeless multiple times. The working conditions throughout a long-period of this thesis project is very poor for me. When I had to work as a full-time employee in industry from time to time to pay my quarter million US dollars legal bill, I worked at home while my daughter was taking naps or asleep. I worked before meetings

with my attorney, composed ideas while I was driving, eating, or sleeping. I risked my full-time job, sneaked behind my industrial boss to work on my thesis at work. I devoted my heart, my soul, and my hard work to the completion of this project, despite many times I was forced to quit, I had chosen never giving it up.

However, without the kind help from my thesis advisor Professor Seaquist, several organizations, and many kind people, the completion of this thesis would be impossible. I would like to thank the Space Telescope and Science Institute (STScI), Department of Physics and Astronomy at Johns Hopkins University (JHU), and National Radio Astronomy Observatory (NRAO) in the United States for kindly hosting me as their pre-doc visiting student, allowing me to have an office to stay, and to attend their scientific seminars. My sincere thanks to my collaborators Dr. Tom Bell at Caltech, Dr. Serena Viti and Dr. Jeremy Yates at University College London (UCL). I also thank Dr. Claus Leitherer, other staff members at STScI, Dr. Ron Allen, and other professors at JHU, and Dr. Dana Balser at NRAO for their encouragement. I thank Mr. Fred Schwab, Mr. Chris Clark, Mr. Wolfgang Baudler, and Ms. Patricia Smiley at NRAO for their kind help on providing computing resources.

Finally, my deep gratitude goes out to my beautiful daughters Aoife and Madison, every one in my family, my dear friends Ron, Ji-Hong., C.C., Evan, Joyce, M.T., X.S., and many others, for your constant love, always believing in me, always supporting and praying for me through all the years. Without all of you, many times I would be starved, homeless, losing the precious custody time with my daughter Aoife, and it would be impossible to complete this thesis. Thank you all from the bottom of my heart. I know within my life time I can not pay back your kindness, but you make this planet a forever better place to live.

Contents

1	Introduction	1
1.1	The Role of Starbursts	2
1.2	Molecular Gas and Clouds	4
1.3	Photodissociation Regions and Modeling	8
1.4	Previous Work and A New Starburst Model	10
1.5	Thesis Outline	16
2	Physics of The Models	17
2.1	Application of the Bubble Similarity Model	18
2.1.1	Winds Phase	19
2.1.2	Post-SN Phase	20
2.2	Physical Conditions of The Swept-up Gas	22
2.3	The Cooling Lines as PDR Diagnostics	25
2.4	Chemical Evolution of Star-forming Regions	27
2.5	Non-LTE Line Radiative Transfer	30
2.6	Evolving Starburst Models	31
3	Simulation Methodology	33
3.1	Model Outline	34
3.2	Initial Parameters	36
3.2.1	Winds Phase	36

3.2.2	Post-SN Phase	39
3.3	Shell Structure and UCL_PDR Code	41
3.4	SMMOL Code	50
3.5	Starburst99	52
3.6	Summary of Model Parameters and Variables	54
4	Model Results	58
4.1	Kinematics of The Swept-up Gas	58
4.2	Thermal Properties and Chemistry of the PDRs	65
4.2.1	Density and Temperature	68
4.2.2	Chemical Evolution	82
4.3	FIR/sub-mm/mm Line Emission in Individual Shells and GMCs	101
4.3.1	Molecular Line Profiles	101
4.3.2	Integrated Line Flux of An Expanding Shell	105
4.4	FIR/sub-mm/mm Line Emission in A Shell/GMC Ensemble	109
4.4.1	^{12}CO and Its Isotope ^{13}CO	109
4.4.2	HCN and HCO^+	119
4.4.3	Atomic C, O, and C^+	128
5	Understanding of Molecular Gas and Starburst Ages in M 82	136
5.1	The Supershell Surrounding SNR 41.9 + 58	136
5.2	FIR/Sub-mm/mm Line Emission in The Central Region	139
5.2.1	Observational Data	141
5.2.2	Model Fit to the Line Spectral Energy Distribution	148
5.2.3	Molecular and Atomic Line Ratio Diagrams	158
5.3	Discussion and Summary	164
5.3.1	An Expanding Supershell Associated with SNR 41.9+58	164
5.3.2	Central Starburst Region	165

5.3.3	Limitations of Our Model and Their Impacts	170
6	Applications to Luminous Infrared Galaxies Beyond M 82	177
6.1	Degree of CO Excitation and Star Formation Properties	178
6.2	The CO-to-H ₂ Conversion Factor X	186
7	Summary and Future Directions	191
7.1	Summary	191
7.2	Future Directions	197
	Appendix	199
	A List of Acronyms	199
	B List of Math Symbols	202
	Bibliography	208

List of Tables

2.1	Transition properties of the main PDR emission lines.	26
2.2	Summary of assumptions used in our evolving starburst model.	32
3.1	Initial conditions of GMCs and SCs in a modeling starburst system. . .	40
3.2	Observed column density of various ISM components in the center of M82.	41
3.3	Standard input parameters for the time-dependent UCL_PDR model. . .	47
3.4	Standard gas-phase elemental abundances used in UCL_PDR code (relative to total hydrogen nuclei).	48
3.5	Standard dust grain properties adopted in the UCL_PDR code.	49
3.6	Model parameters and variables	55
4.1	Modeling kinematics of expanding shells.	61
4.1	Modeling kinematics of expanding shells.	62
4.1	Modeling kinematics of expanding shells.	63
4.2	Integrated CO line flux for a model M7 GMC and shell.	106
4.2	Integrated CO line flux for a model M7 GMC and shell.	107
4.3	Fraction of emission from a M7 GMC to total integrated CO line flux. . .	108
4.4	Integrated ^{12}CO line flux for a model shell ensemble.	112
4.4	Integrated ^{12}CO line flux for a model shell ensemble.	113
4.5	Percentage fraction of integrated ^{12}CO line emission from different shells predicted by our ESbM models.	114

4.5	Percentage fraction of integrated ^{12}CO line emission from different shells predicted by our ESbM models.	115
4.6	Integrated ^{13}CO line flux predicted by our ESbM models.	117
4.6	Integrated ^{13}CO line flux predicted by our ESbM models.	118
4.7	Integrated HCN line flux predicted by our ESbM models.	122
4.7	Integrated HCN line flux predicted by our ESbM models.	123
4.8	Integrated HCO^+ line flux predicted by our ESbM models.	124
4.8	Integrated HCO^+ line flux predicted by our ESbM models.	125
4.9	Percentage fraction of integrated HCN line emission from different shells predicted by our ESbM models.	126
4.10	Percentage fraction of integrated HCO^+ line emission from different shells predicted by our ESbM models.	127
4.11	Integrated C line flux predicted by our ESbM models.	133
4.12	Integrated O line flux predicted by our ESbM models.	134
4.13	Integrated $\text{C}^+(1-0)$ line flux predicted by our ESbM models.	135
5.1	Characteristics of the expanding supershell in M 82.	138
5.2	Observations of molecular ^{12}CO in the center 1 kpc of M 82.	144
5.3	Observations of molecular HCN, and HCO^+ in the center $22''$ of M 82.	145
5.4	Observations of molecular ^{12}CO and ^{13}CO in the center $22''$ of M 82.	146
5.5	Observations of atomic O and C^+ in the center $80''$ of M 82.	147
5.6	The chi-squared fitting results to the observed ^{12}CO line SED.	150
5.7	The chi-squared fitting results to the observed HCN and HCO^+ line SEDs ($22''$).	155

List of Figures

1.1	A multiwavelength view of nearby starburst galaxy M 82	5
1.2	Images of the Tarantula Nebula and the Hodge 301 SC in the LMC . . .	9
2.1	A schematic structure of an evolving GMC centrally illuminated by a young SC	18
3.1	Structural components associated with a single SC within our model . . .	53
3.2	A flow diagram of key computational modules used in our model	56
3.3	A flow diagram of input parameters and methods used in our PDR simu- lations	57
4.1	Total swept-up molecular gas mass as a function of time	64
4.2	Mechanical wind power as a function of time	66
4.3	FUV radiation field strength G_0 as a function of time	67
4.5	Shell density and thickness as a function of time	69
4.5	(continued)	70
4.6	Gas and dust temperatures as a function of A_V for an ensemble of shells	73
4.6	(continued)	74
4.6	(continued)	75
4.6	(continued)	76
4.6	(continued)	77
4.6	(continued)	78

4.6 (continued)	79
4.6 (continued)	80
4.7 Gas and dust temperatures inside an M7 cloud as a function of A_V	81
4.8 Chemical abundances of H, H ₂ , H ⁺ , e ⁻ , C, C ⁺ , O, and CO as a function of A_V for an ensemble of shells	83
4.8 (continued)	84
4.8 (continued)	85
4.8 (continued)	86
4.8 (continued)	87
4.8 (continued)	88
4.8 (continued)	89
4.8 (continued)	90
4.9 Chemical abundances of HCN and HCO ⁺ as a function of A_V for an ensemble of expanding shells	91
4.9 (continued)	92
4.9 (continued)	93
4.9 (continued)	94
4.9 (continued)	95
4.9 (continued)	96
4.9 (continued)	97
4.9 (continued)	98
4.10 Chemical abundances of H, H ₂ , H ⁺ , e ⁻ , C, C ⁺ , O, and CO as a function of A_V for an M7 cloud	99
4.11 Chemical abundances of HCN and HCO ⁺ as a function of A_V for an M7 cloud	100
4.12 Model line profiles of ¹² CO and ¹³ CO for an M7 shell at age 5 Myr	103
4.13 Model line profiles of ¹² CO and ¹³ CO for an M7 shell at age 20 Myr	104

4.14	Model ^{12}CO line SEDs	111
4.15	Model ^{13}CO line SEDs	116
4.16	Model HCN line SEDs	120
4.17	Model HCO^+ line SEDs	121
4.18	Model neutral atomic carbon line flux as a function of time	130
4.19	Model atomic oxygen line flux as a function of time	131
4.20	Model $\text{C}^+(1-0)$ line flux as a function of time	132
5.1	Model line ratios of ^{12}CO as a function of rotational quantum number J	140
5.2	A contour plot of χ^2 values as a function of mass coefficient and burst age	151
5.3	A χ^2 fit to the ^{12}CO line SED for the central 1 kpc disk region of M 82	152
5.4	A χ^2 fit to the HCN line SED for the central $22''$ region of M 82	156
5.5	A χ^2 fit to the HCO^+ line SED for the central $22''$ region of M 82	157
5.6	^{12}CO line intensity ratios as a function of rotational quantum number J for a sequence of burst ages	159
5.7	Ratio-ratio diagrams of molecular ^{12}CO and ^{13}CO line intensities	161
5.8	Ratio-ratio diagram of atomic fine structure line fluxes	163
6.1	Line intensity ratio r_{31} versus $L_{FIR}/M(\text{H}_2)$ ratio	182
6.2	Histograms of our model $L_{SC}/M(\text{H}_2)$ ratio and observed $L_{FIR}/M(\text{H}_2)$ ratio in SLUGS galaxies	185
6.3	Histograms of our model r_{31} ratio and observed r_{31} ratio in SLUGS galaxies	185
6.4	Model CO-to- H_2 conversion factor X as a function of time	188

Chapter 1

Introduction

Knowledge of the physical properties and evolution of the gas and dust content in the interstellar medium (ISM) of starburst galaxies is essential for understanding the cause and temporal evolution of star-forming activity. In particular, studies of such galaxies in the nearby universe are essential as a step in understanding the role of the starburst phenomenon in the cosmic evolution of galaxies. To constrain theories of how the ISM evolves, one needs to investigate both individual galaxies and large statistical samples of data at multiple wavelengths. Especially, with the available data for the dust component, studying the gas in the co-space ISM becomes more interesting and important.

Starburst galaxies have impressive reservoirs of molecular gas in their centers to fuel the massive star formation. Observations of far-infrared/sub-millimeter/millimeter line emission from external starburst objects can certainly provide us with detailed information on the connection between the gas properties and the active star formation. The main drawback is that these extragalactic sources are further away, and hence higher resolutions and sensitivities are required to map individual starbursts in these galaxies. In this study, we construct a set of starburst models for FIR/sub-mm/mm line emission of molecular gas in evolving starburst regions. By comparing with the available observed data on nearby starburst galaxies, we can constrain the models and provide

better interpretations for the observations.

The main goals of this work are (1) to show that it is possible to model the FIR/sub-mm/mm line emission of molecular and atomic gas by following the evolution of a starburst region, as in certain infrared (IR) models; (2) to relate the observed molecular line properties of a starburst galaxy to its age, and hence to constrain the global star formation history; (3) to understand the formation mechanism of the molecular rings in M 82; (4) to interpret certain observed correlations between parameters of the ISM and star formation properties observed among starburst galaxies as also consequences of starburst evolution; (5) and finally, to provide useful information for the interpretation of future high resolution maps of molecular gas on small and large scales in starburst galaxies, in order to provide a deeper understanding of the structure, dynamics, and evolution of the neutral ISM and its relationship with active star formation.

In this chapter, first we present a brief introduction of the role of starbursts throughout the cosmic scale and their properties. Then we describe properties of molecular gas and clouds, and what molecules and atoms can be used to probe the gas conditions of different ISM components. We discuss why studies of the time-dependent PDR chemistry affected in particular by the strong ultra-violet (UV) fields is particularly important in star-forming regions. We present previous work of studying neutral ISM in starburst galaxies, and how our new evolutionary starburst model can contribute to the field. Finally, we present the outline of this thesis work.

1.1 The Role of Starbursts

A starburst is a phenomenon occurring when the star formation rate (SFR) cannot be sustained for the lifetime of the galaxy. It is now clear that active star formation or starburst activity is common throughout the universe (e.g. Heckman et al., 1998; Adelberger & Steidel, 2000). Bursts of massive star formation can dramatically alter

the structure and evolution of their host galaxies by injecting large amounts of energy and mass into the ISM via strong stellar winds and repeated supernova explosions. The evolution of the superbubbles and supershells that have sizes ranging from several tens to hundreds of parsecs plays an important role in determining the amount and distribution of warm gas in the ISM.

Several decades ago, studies of far-infrared emission from the central regions of galaxies revealed that large infrared luminosities are associated with a large star formation rate and star formation efficiency (SFE; Rieke & Low, 1975; Harwit & Pacini, 1975). Since then, starbursts have been found in many different galactic environments whose FIR luminosities L_{FIR} are between 10^{10} and $10^{14} L_{\odot}$. The SFR associated with the nuclei of luminous infrared galaxies can be a few orders of magnitude higher than in the entire Milky Way galaxy (Kennicutt, 1983). Recent studies of the integrated ultra-violet, optical, and infrared emission from field galaxies have suggested that the universal star formation rate may have peaked at redshift of $z \sim 1.5$ (Madau et al., 1998).

In the nearby universe, Messier 82 (M 82¹) is the closest (~ 3.25 Mpc) and brightest ($L_{IR} = 3 \times 10^{10} L_{\odot}$), and hence most well studied prototypical starburst galaxy. M 82 has a sufficient amount of gas to sustain star formation for a few hundreds of million years (Rieke et al., 1980; Wills et al., 1999; Walter et al., 2002). Its nuclear starburst, located in the central 1 kpc, has been the subject of continuum and line observations made in virtually all wavelengths from X-rays to the radio domain, as shown in Fig. 1.1. The high supernova rate has created a biconical outflow of hot gas also observed in the cold gas and dust. The strong UV fields have created an extreme physical environment in the molecular gas reservoir of M 82 (Stutzki et al., 1997; Mao et al., 2000; Weiss et al., 2001). At distances beyond M 82, the starburst in combination with active galactic nuclei (AGN) becomes the dominant power source of the bright IR luminosity. There are two types of IR bright galaxies: the luminous infrared galaxy has an IR luminosity L_{IR}

¹<http://www.maa.clell.de/Messier/E/m082.html>

$\sim 10^{11} - 10^{12} L_{\odot}$ and the ultra luminous infrared galaxy (ULIRG) has an IR luminosity $L_{IR} \geq 10^{12} L_{\odot}$. The ULIRGs are found to be vastly more numerous at high redshift ($z > 1$) (e.g. Lonsdale et al., 2006, and references therein). Understanding the characteristics of these starburst galaxies and their relationship with the ISM, as well as being able to parametrize the global history of star formation, are crucial in understanding the physics and evolution of starburst galaxies, the contribution of high redshift luminous IR galaxies to the cosmic infrared background, and the role of starbursts as diagnostics of the formation of massive galaxies and large-scale structures.

Despite extensive studies in the past two decades, a detailed and quantitative understanding of the starburst phenomenon is still lacking. Crucial issues that remain open include the evolution and feedback effects of starburst activity, its triggering and quenching mechanisms, and the mass distribution of the stars formed in starbursts. Progress has been hindered by the scarcity of spatially resolved data. Furthermore, high resolution optical and ultraviolet studies are often hampered by severe dust obscuration. But nevertheless it was suggested that the first generations of stars may be due to the formation of super star clusters (Meurer et al., 1995) in the cores of giant molecular clouds (Carlstrom & Kronberg, 1991). The current star formation might be due to the presence of tides, shocks due to cloud-cloud collisions, winds and supernova ejecta from newly born massive stars compressing gas into shells (Dopita et al., 1985), and strong non-axisymmetric gravitational forces due to either a bar in the center (Wills et al., 2000) or galaxy interactions/mergers (Sanders et al., 1988).

1.2 Molecular Gas and Clouds

Most of the molecular gas in the ISM is in the form of molecular hydrogen (H_2). The H_2 molecule is symmetric, causing electric dipole transitions to be forbidden, and its energy levels are also widely spaced. Therefore, little or no radiation is detectable from H_2 in

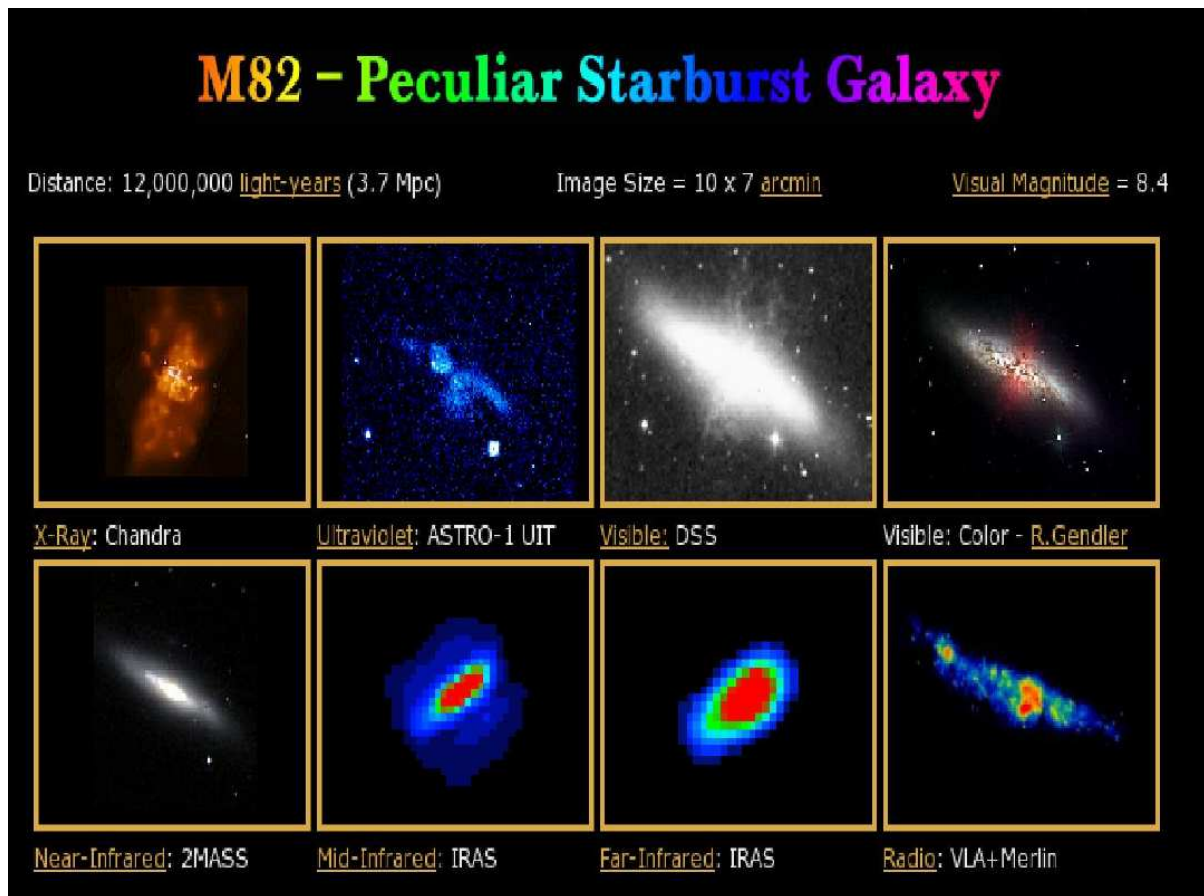


Figure 1.1 A multiwavelength view of nearby prototypical starburst galaxy M 82 (see <http://www.maa.clell.de/Messier/E/m082.html>).

normal cool ISM environments. The most suitable tracer of the molecular gas is carbon monoxide (^{12}CO or simply CO), the second most abundant molecule after H_2 , which has a dipole moment and is easily excited, hence has bright lines. Molecular CO has a small dipole moment (0.1 debye) and a moderate rotational constant ($B_0 = 57.6 \text{ GHz}$), so the CO lines at low rotational quantum number (J) are easily excited at relatively low densities ($n \geq 10^2 \text{ cm}^{-3}$) and temperatures ($T_{kin} \geq 5 \text{ K}$), which are found in essentially every molecular gas cloud. Consequently, CO emission in general does not discriminate between the dense gas in the immediate vicinity of star formation and more diffuse molecular gas. It is therefore widely used as a transitional tracer for diffuse gas and the total molecular gas content in a galaxy. This is valid for molecular clouds in the Galaxy and also for external galaxies. But it is not considered a good tracer of dense or opaque and highly excited gas that is directly involved in the burst of star formation. In spite of the high opacity, the ^{12}CO brightness temperature, line intensity, and line ratios are often used to give an estimate of the gas temperature, density, and mass. The CO -to- H_2 conversion factor X derived from the $^{12}\text{CO}(1-0)$ line intensity is now known to vary from galaxy to galaxy, and from the nucleus to the disk of a galaxy. This controversial factor is believed to be 4 - 10 times lower for LIRGs (Yao et al., 2003) and ULIRGs (Solomon et al., 1997) than the standard X -factor derived for our galaxy (Strong et al., 1988). The total amount of molecular gas is therefore significantly overestimated in the central regions of starburst galaxies, if the standard value for the X -factor is applied. The less abundant CO isotope ^{13}CO has a much lower optical depth than ^{12}CO . The line ratios between optically thin transitions in this molecule are more sensitive probes of the gas conditions.

Molecules such as HCN and HCO^+ are the most frequently observed molecules after CO . These molecules trace high-density gas better than CO , because their critical densities are significantly higher than that of CO . The critical density is the density at which the downward collisional transition rate equals the spontaneous emission rate. Since the

critical density is proportional to the square of the dipole moment and to the cube of the transition frequency, dense gas is best traced by high-dipole moment species and high-frequency transitions. Furthermore, the high-frequency transitions have larger excitation energies, so they also trace the warm gas associated with star-forming activities. With the recent development of sub-mm telescopes and receivers, it is now possible to observe the faint higher frequency transitions of these species in external galaxies. The HCN traces molecular gas at densities $> 3.0 \times 10^4/\tau \text{ cm}^{-3}$, where $\tau \geq 1.0$ is the optical depth of the HCN(1-0) line, compared to densities of $\sim 500 \text{ cm}^{-3}$ traced by CO. Hence, these molecules are better indicators of active star formation than CO, but they are poor in tracing the total molecular gas content of a galaxy. Critical densities for HCN (1-0) and (3-2) are $2.4 \times 10^5 \text{ cm}^{-3}$ and $8.5 \times 10^6 \text{ cm}^{-3}$, respectively. They are $4.2 \times 10^5 \text{ cm}^{-3}$ and $1.4 \times 10^7 \text{ cm}^{-3}$ for HCO⁺(1-0) and (3-2), respectively.

Multiwavelength based evidence indicates that the properties of molecular gas in the central starburst regions differ from that of quiescent star forming disks. The spectacular energies injected in the gas reservoirs of starbursts coming as strong radiation fields (UV, X-rays), cosmic rays, powerful winds and jets can dramatically alter the ISM structures surrounding them. Therefore, the main excitation mechanisms for molecular gas in a starburst galaxy are the combination of collisional processes in dense gas and strong UV radiation field stemming from photoelectric heating, far-UV pumping of H₂, strong mechanical energy produced by wind and supernova (SN) explosions, enhanced cosmic rays and X-rays, as well as shock and turbulent heating. But the atomic fine structure transitions (e.g. [C I], [O I], and [C II]) are forbidden lines, hence these lines are populated by collisions only. Both gas and dust temperatures are expected to be high during the earlier phases of starburst evolution. Being able to diagnose the physical and the complex chemical evolution of molecular and atomic gas and its links to other ISM components is of prime importance. Typical tracers used in studying different gas components in starburst galaxies are molecular ¹²CO and its isotope ¹³CO, HCN, HCO⁺, and atomic

C, C⁺, and O.

Molecular clouds, as the name implies, consist of mainly molecular gas. Observational studies have shown that the giant molecular clouds in the Milky Way have a distinct mass spectrum M_{GMC}^α , with $\alpha = -1.5 \pm 0.1$ (Sanders et al., 1985; Solomon et al., 1987) for cloud masses ranging between 10^2 and $10^7 M_\odot$. The giant molecular clouds ($M_{GMC} \geq 10^4 M_\odot$), especially their dense cores, are known to be associated with active formation of massive stars which often grouped in a form known as a super star cluster (SSC), for example, the Hodge 301 star cluster in the Tarantula Nebula in Large Magellanic Cloud (Grebel & Chu, 2000), as shown in Fig. 1.2. The distribution of core masses of a GMC determines the resulting distribution of stellar masses inside a star cluster (the initial mass function or IMF). The cloud mass distribution in starburst galaxy M 82 is found to follow a similar index to the galactic one (Keto et al., 2005). It was suggested that the mass scale of the molecular clouds determines the mass scale of the clusters (Keto et al., 2005). Therefore, we would expect much of the luminosity of the starburst to arise from the GMCs with a fairly narrow range of masses. It is also known that low-mass clouds, like the nearby Taurus and Ophiuchus clouds, tend to form predominantly low-mass stars.

1.3 Photodissociation Regions and Modeling

Photon dominated regions or photodissociation regions (i.e. PDRs) play an important role in modern astrophysics as they are responsible for many emission characteristics of the ISM. These regions dominate the IR and sub-mm spectra of star-forming regions and galaxies as a whole. Theoretical models addressing the structure of PDRs have been available for more than two decades and have evolved into advanced computer codes accounting for a growing number of physical effects with increasing accuracy. The model setups vary greatly among different model codes. This includes the assumed model ge-

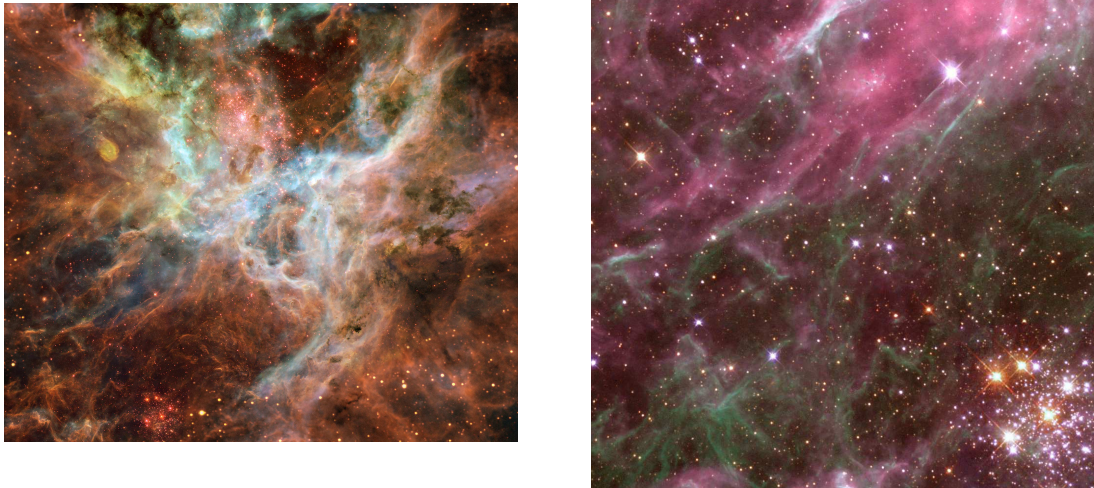


Figure 1.2 Color images of the Tarantula Nebula and the Hodge 301 star cluster in the Large Magellanic Cloud taken by *Hubble Space Telescope* (HST). Credit: *National Aeronautics and Space Administration/European Space Agency* (NASA/ESA).

ometry, physical and chemical structure, the choice of free parameters, and other details. As a result, significant variations in the physical and chemical PDR structure predicted by the various PDR codes can occur. This diversity can in principle prevent a unique interpretation of observed data in terms of parameters of the observed clouds. Detailed benchmarking of various PDR codes of their sensitivities and pitfalls has been presented by Röllig et al. (2007) and references therein. Accuracies of different aspects used in different codes, for example plane-parallel versus spherical geometry, steady-state versus time-dependent chemistry, different chemical reaction rates and networks, treatment of dust and PAHs, gas heating and cooling, range of input parameters, numerical treatment, and gridding, are studied in detail by this article.

In this study, we focus on studies of PDRs in massive star-forming regions. In such regions, we expect that for solar metallicity the formation timescale for H_2 on grains, $\tau_{\text{H}_2} \sim \frac{10^3 \text{ Myr}}{n(\text{H}_2) \text{ cm}^{-3}}$, which dominates the chemical timescale, is of the same order as that for the significant change in the far-ultra violet (FUV) flux and the density $n(\text{H}_2)$. Hence, the abundance of H_2 does not reach steady-state until late in the starburst evolution. Theoretical studies of time-dependent PDRs have been presented in the past (e.g. Sttörzer et al., 1997; Hollenbach & Tielens, 1997; Bell, 2006). Most recently, Bell et al. (2006) indicated that time-dependence in low-metallicity environments is important, since the reduced H_2 formation rate means that the chemistry does not reach steady state for cloud ages below 100 Myr. For starburst galaxies with solar metallicity, the H_2 formation timescale may vary from 10^5 to 10^7 yr for molecular gas with density of $10^2 - 10^4 \text{ cm}^{-3}$.

1.4 Previous Work and A New Starburst Model

The neutral ISM in a galaxy responds rapidly to the presence of young, massive stars. In less than 1 Myr, an O star will modify its surroundings through photoionization and

photodiassociation of the cloud, and mechanical displacement of gas by its stellar wind. By 2 - 3 Myr the first type II supernovae explode, and shell formation is under way. Within a few tens of Myr a supershell can form size comparable to the vertical pressure scale height of a galaxy's disk. Over a comparable time span, the supernova remnants accelerate new cosmic rays, thereby renewing this pervasive component of galaxies. The fast response of the ISM to young stars means that these two components are tightly linked. Some of the effects of these processes are obvious, as in the presence of H II regions, supernova remnants, and supershells. Conversely, radial gradients in the metal content of the ISM are observed on kpc scales across the disks of spirals. This variation is thought to relate to the star formation history, with many cycles of star formation having occurred in the inner parts of disks and few in the outer regions.

The number of multiwavelength observations of starburst galaxies throughout the cosmic-scale has increased dramatically due to the significant improvement in the sensitivity and resolution of telescopes. These observations provide an essential basis for starburst modeling, and such modeling provides systematic predictions of the properties of the ISM in idealized models of starburst galaxies for comparison with these observations. For example, M 82, which is classified as an irregular starburst galaxy (*I0*), with an inclination of 81° , possesses current starburst activity which was likely triggered by tidal interaction with its companion M 81 beginning about 10^8 yr ago. The infrared luminosity of M 82 arises mostly from the central ~ 600 pc region, which has a stellar bar structure and currently has a high supernova rate of $\sim 0.05 - 0.1 \text{ yr}^{-1}$ (Muxlow et al., 1994). M 82 has a complex system of clumps and filaments which extend up to ~ 2 kpc along the minor axis discovered by Lynds & Sandage (1963). The formation mechanism of this complex system and the evolutionary scheme in M 82 remain under debate (e.g. Visvanathan, 1974; Carlstrom & Kronberg, 1991; Shen & Lo, 1996; Wills et al., 2000; Yao et al., 2006). It is therefore not an easy task to present a conclusive picture of molecular gas in a starburst galaxy, because the gas kinematics, thermal and chemical structures

are strongly influenced by the central starbursts (the UV field is about 10^4 times greater than the ISM in our Galaxy). In 1978 Beck et al. presented in some detail the motion of gas in and out of the plane, and concluded that the energy sources responsible for material expanding rapidly out of the plane are very luminous stars or supernovae. In 1984 Olofsson & Rydbeck showed that molecular gas and ionized gas in M 82 have essentially the same kinematics. Hence, the CO emission must represent the true motion of the gas and it can not be due to scattering. In 1991 Carlstrom & Kronberg suggested that the molecular rings in M 82 is a product of material swept-up by the nuclear starburst activity. But a number of authors interpreted the rings as a product of Linblad resonance instabilities associated with the gravitational effects of the bar (e.g. Shen & Lo, 1996; Wills et al., 2000). Most recently, Yao et al. (2006) conducted an ideal case study of an expanding shell model in M 82, and suggested that the circumnuclear rings seen in a nearly edge-on barred galaxy may possibly be a consequence of the evolution of swept-up gas caused by the starbursts occurred in the center ~ 100 Myr ago.

Can the molecular rings in M 82 be a product of swept-up gas due to massive star formation in its center?

The age estimates of the starburst in M 82, the principal target galaxy discussed in this study, has been presented by many authors. Yun et al. (1993) compared the disk HI with optical maps, and found a large amount of gas being channeled into the core of the galaxy over the last 200 Myr due to the tidal encounter with its large spiral neighbor galaxy M 81. Ages derived from SSCs in optical images are ~ 50 Myr (de Grijs et al., 2001), $\sim 30 - 100$ Myr (Rieke et al., 1993; Barker et al., 2008), $\sim 4 - 6$, and $10 - 30$ Myr (Förster-Schreiber et al., 2003; Smith et al., 2006). The corresponding estimates of the average star formation rate over the 200 Myr period is roughly about $10 M_{\odot} \text{ yr}^{-1}$. One particular study of interest to this thesis involves using a radiative transfer method to compute the mid- and far-IR emission in dust media within M 82 (e.g. Efstathiou et

al., 2000; Galliano et al., 2003; Siebenmorgen & Krügel, 2007). Their approach was to approximate the starburst by a group of identical stars surrounded by optically thick swept-up shells. With these models they could account for the hot dust component and found that it dominates the mid-IR emission (Siebenmorgen & Krügel, 2007), and the observed *Infrared Astronomical Satellite* (IRAS) distributions, as well as two starbursts in M 82 peaking at 10 and 30 Myr. Colbert et al. (1999) compared a steady-state PDR model with atomic data (C, O, C+, N+), and suggested the burst age for M 82 is 3 - 5 Myr. It is clear that the estimation of M 82 starburst age has a large uncertainty.

Can the molecular sub-mm and mm lines provide an alternative tool for estimating the starburst ages?

Large surveys of molecular line emission in nearby LIRGs/ULIRs have provided new and useful data in recent years, e.g. *SCUBA Local Universe Galaxy Survey* (SLUGS) CO survey by Yao et al. (2003), the HCN survey by Gao & Solomon (2004a,b). Interesting and yet puzzling relations between molecular gas luminosity and dust FIR luminosity, gas excitation and star formation parameters have been interpreted in terms of localized starburst phenomena. More luminous FIR galaxies tend to have warmer and denser gas, with higher star formation efficiency, and the excitation of the molecular gas appears correlated with star formation efficiency. Another question is then:

What is the reason for such correlations?

Many authors have modeled the molecular line emission in nearby starburst galaxies (e.g. Wild et al., 1992; Mao et al., 2000; Seaquist & Frayer, 2000; Yao et al., 2003, and references therein). The modeling methods include the *Large Velocity Gradient* (LVG) method (Goldreich & Kwan, 1974), the steady-state PDR model (Tielens & Hollenbach, 1985), and inhomogeneous radiative transfer models taking into account non-local thermodynamic equilibrium (Wild et al., 1992). All of these previous models have successfully

determined (1) the origin of the FIR/sub-mm/mm line emission; (2) the relations between the degree of molecular excitation measured by different line ratios and the concentration and distribution of different gas components, as well as the efficiency of star-forming activity; (3) estimates of the CO-to-H₂ conversion factor X that is 4-10 times lower than the conventional X -factor derived for our Galaxy; and (4) that the physical states of the ISM (such as gas density, FUV flux, and gas kinetic temperature) are enhanced in starburst regions. However, none of these models was able to physically link the observed properties of molecular gas to the stellar properties or to the age of starburst.

Motivated by the abundant evidence of giant bubbles and shells found in Milky Way, 30 Doradus in the Large Magellanic Cloud (LMC), and nearby starburst galaxies, the success of using the dusty starburst model to constrain the star formation history of observed IRAS starburst galaxies by following an ensemble of GMCs (Efstathiou et al., 2000), and the available multiple transitions in several molecular tracers, we construct a series of starburst models, called *Evolving Starburst Model* (ESbM) for a molecular line emission study. In this study, we treat a starburst galaxy as an ensemble of evolving GMCs centrally illuminated by a compact star cluster (SC), in which the GMCs in the ensemble follow a power-law mass spectrum. We take advantage of an existing non-local thermal equilibrium radiative transfer code to model molecular line spectral energy distributions (as a function of rotational quantum number) for each individual evolving shell/GMC. The global line spectral energy distribution at each simulated age is then the sum of the line SEDs produced by each of these shells/GMCs at that time step. A time-dependent PDR model is also used; in this approach we can follow the chemical evolution in great detail. Our time-dependent PDR model also takes into account the dynamical evolution of molecular gas that captures the changes in gas density and temperature, so we can obtain a full range of physical conditions of molecular gas encountered in a starburst region. We compute the line SEDs and in particular various line ratios for several molecules and atoms (¹²CO and its isotope ¹³CO, HCN, HCO⁺, C, O, and

C⁺), whose line intensities depend not only on the shell temperature and density, but also the chemical abundances that vary with the shell evolution. We can then derive the total gas mass and burst age(s) in the measured region, and interpret the previous gas-SF correlations, in particular, the degree of molecular excitation and star formation efficiency (Yao et al., 2003), in terms of a new dimensional parameter (burst age). The traditional LVG model may be able to produce the observed CO data precisely for a proposed scenario, but it is clearly impossible to follow the evolution of a starburst and predict more complex gas excitation scenarios.

In this study, we do not model the hydrogen 21 cm line emission, because there are no multiple transitions, and the (optically thin) HI line intensity depends only on the column density, no matter how warm or dense the gas is. In other words, gas temperature and density which change drastically in a starburst region play no role in the level population in the HI 21 cm line radiative transfer. Therefore, for our purposes HI 21 cm line is not a good probe to the extreme gas environment such as in a starburst galaxy.

In addition to the dependencies on temperature, density and chemical abundance, the integrated line flux density depends on the total gas mass in the measured region, cloud mass range, and mass spectrum power index, while the line ratio between any two spectral lines depends usually only on the ratio of minimum and maximum cloud masses and the mass spectrum power index. Therefore, we can use the spectral energy distribution of molecular lines to constraint the predicted total gas mass and burst age. The ratio of two integrated line flux densities can be used to derive estimates of the physical conditions. The physical conditions recovered from the analysis of line ratios refer of course to the average conditions for all clouds within the beam.

Through this study, we hope to provide some answers to those intriguing questions mentioned above, and to lay a foundation for future starburst modeling for neutral gas media.

1.5 Thesis Outline

In Chapter 2 *Physics of The Models* we discuss the model assumptions and theoretical background for each of the physics elements that are contained in our ESbM models. We explain why each of these individual elements are important in evaluating the physical and chemical properties of molecular gas in a starburst galaxy, and the shortcomings that are associated with our model assumptions. In Chapter 3 *Simulation Methodology* we present the detailed modeling procedure in order to predict the FIR/sub-mm/mm line emission. We discuss the methods of application and limitations of each of the computational codes used in this study. A summary of all model parameters and adopted values is also presented in this chapter. In Chapter 4 *Model Results* we present modeling results for the kinematics, shell density and temperature structures, chemical evolution, and FIR/sub-mm/mm line properties of various molecules and atoms for individual expanding shells surrounding a massive star cluster produced from an ensemble of GMCs. In Chapter 5 *Understanding of Molecular Gas and Starburst Ages in M 82* we present an application of the model to derive the age of the starburst and molecular gas swept up by the shells in M 82, and to provide new insights into the nature and physical state of the ISM in its starburst region. We also discuss applications to the supershell surrounding supernova remnant (SNR) 41.9 + 58. In Chapter 6, we present *Applications to Luminous Infrared Galaxies Beyond M 82* using our FIR/sub-mm/mm starburst model. We discuss the relationships between the excitation of CO molecule and SF properties of LIRG galaxies, and derive the behavior of the model CO-to-H₂ conversion factor X in a starburst galaxy. Chapter 7 presents the *Summary and Future Directions* of this work.

Chapter 2

Physics of The Models

Our starburst models incorporate a standard similarity model for the bubble/shell structure around a young star cluster, which has been described in many publications (e.g. Castor, McCray, & Weaver, 1975; Weaver et al., 1977; McCray & Kafatos, 1987; Franco et al., 1990; Koo & McKee, 1992; Yao et al., 2006), a time-dependent stellar population synthesis model (Leitherer et al., 1999), a fully time-dependent chemistry model for the PDRs (Bell et al., 2005), and a non-LTE radiative transfer model for molecular lines (Rawlings & Yates, 2001). Our model results are used for comparing with the FIR/sub-mm/mm line emission observations of starburst galaxies. Few previous models for neutral gas media, if any, have all these physical elements included at the same time.

The basic assumptions for the models are (1) star formation occurs within the dense optically thick spherical cloud (e.g. Gao et al., 2001), and star formation takes place instantaneously, with the star cluster treated as a point source (see Fig. 2.1); (2) absorption of the starlight from the central cluster is produced by dust associated with the gas, assuming a constant gas-to-dust ratio; and (3) the gas responding to star formation in a starburst galaxy is treated as an ensemble of GMCs with different initial masses, each of which responds to massive star formation at its center. More modeling assumptions are summarized later in this chapter.

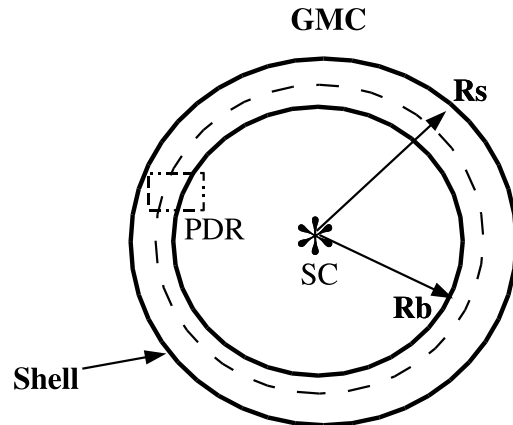


Figure 2.1 A schematic showing the structure of an evolving GMC centrally illuminated by a compact young star cluster. R_{sh} is the radius of the shell, and R_b is the radius of the bubble. The PDR lies between the thin, dense swept-up shell and the bubble interior.

In this chapter, we describe the bubble similarity expansion model, physical conditions of the swept-up gas, and chemical evolution of massive star-forming regions, as well as the non-LTE radiative transfer theory for molecular and atomic line emission.

2.1 Application of the Bubble Similarity Model

We divide the evolutionary scheme of the expanding shell/GMC ensemble into two phases referred to as *Winds* and *post-SN*. The *Winds* phase begins with the formation of a star cluster and an H II region inside the GMC owing to ionizing stellar radiation. This is followed by the formation of a rapidly expanding hot bubble produced by strong stellar

winds. This phase ends when the bubble breaks out of its parent GMC. In this phase, the parent GMC is assumed to be stationary, and acts as a dense uniform ambient ISM to the expanding shell formed by gas swept up by the bubble. The *post-SN* phase starts when the most massive star in the ensemble reaches its main-sequence lifetime, and explodes into a supernova. The shell expansion in this phase is first driven by repeated supernova explosions, then changes from pressure-driven (*adiabatic*) to zero pressure (*non-adiabatic*) as the hot bubble cools. In the *post-SN* phase, the shell expands into a less dense uniform ambient ISM. A steady-state mechanical power and energy for each phase is assumed, in order to satisfy the requirements of the similarity model. The two phases are discussed in more detail below.

2.1.1 Winds Phase

The evolution of a giant molecular cloud is determined by the H II expansion in the very early stage, when a bubble surrounded by a thin dense shell structure is created. The radius (pc) and velocity (km s^{-1}) of the H II expansion due to ionization can be written as (Spitzer, 1978; Franco et al., 1990),

$$R_{HII}(t) = R_S \left(1 + \frac{7 c_i t}{4 R_S} \right)^{\frac{4}{7}}, \quad (2.1)$$

$$V_{HII}(t) = c_i \left(1 + \frac{7 c_i t}{4 R_S} \right)^{-\frac{3}{7}} \quad (2.2)$$

where $c_i \simeq 11.5 \text{ km s}^{-1}$ is the sound speed in the ionized gas with an equilibrium temperature of $\sim 10^4 \text{ K}$, and R_S is the initial Strömngren radius in pc given by the following (Franco et al., 1990; Efstathiou et al., 2000, and references therein),

$$R_S = 4.9 \left(\frac{F_*}{5 \times 10^{52} \text{ s}^{-1}} \right)^{\frac{1}{3}} \left(\frac{n_c}{2 \times 10^3 \text{ cm}^{-3}} \right)^{-\frac{2}{3}}, \quad (2.3)$$

$$F_* = 5 \times 10^{52} \left(\frac{\eta}{0.25} \right) \left(\frac{M_{GMC}}{10^7 M_\odot} \right) \text{ s}^{-1} \quad (2.4)$$

where F_* is the number of Lyman continuum photons, n_c is the core density of the GMC, η is the star formation efficiency, and M_{GMC} is the GMC mass. Almost as soon as the initial Strömgen sphere is formed, the strong winds start to impart large amounts of mechanical energy resulting in a shock which forms a hot bubble. The pressure within this bubble leads to an expansion which sweeps up the surrounding gas into a shell. About 96% of the total wind energy is generated by stars with masses $> 30 M_\odot$ (McCray & Kafatos, 1987). Since the size of the hot bubble is much larger than the thickness of the swept-up shell, the radius and velocity of the shell in the *Winds* phase can be approximated as (McCray & Kafatos, 1987),

$$R_w(t) = 269.0 \left(\frac{L_{38}}{2n_0} \right)^{\frac{1}{5}} (t_7)^{\frac{3}{5}}, \quad (2.5)$$

$$V_w(t) = 16.1 \left(\frac{L_{38}}{2n_0} \right)^{\frac{1}{5}} (t_7)^{-\frac{2}{5}} \quad (2.6)$$

where $L_{38} = L_w / (10^{38} \text{ ergs s}^{-1})$, $L_w = \int_{m_1}^{m_2} C_w C_m m_*^{\gamma-2.35} dm_*$ is the wind mechanical luminosity, $t_7 = t / (10^7 \text{ yr})$, n_0 is the uniform GMC H_2 density in cm^{-3} , $C_w = 1.0 \times 10^{29}$, $C_m = 429.0$, $\gamma = 3.7$ (derived from Abbott 1982), m_1 and m_2 are the lower and upper limits of stellar mass in a cluster.

2.1.2 Post-SN Phase

After the most massive star in the SCs terminates its lifetime, the ejecta from the ongoing and steady supernova activity form a continuous wind which adiabatically drives the further expansion of the swept-up shell. The radius (pc) and velocity (km s^{-1}) of the shell in the *post-SN* phase can be parametrized as (McCray & Kafatos, 1987),

$$R_{SN}(t) = 97.0 \left(\frac{N_* E_{51}}{2n_{ism}} \right)^{\frac{1}{5}} (t_7)^{\frac{3}{5}}, \quad (2.7)$$

$$V_{SN}(t) = 5.7 \left(\frac{N_* E_{51}}{2n_{ism}} \right)^{\frac{1}{5}} (t_7)^{-\frac{2}{5}} \quad (2.8)$$

where N_* is defined as the number of stars with masses $\geq 8 M_\odot$ in the cluster, $E_{51} = E_{SN}/(10^{51} \text{ ergs s}^{-1})$, E_{SN} is the energy produced by each supernova explosion, and n_{ism} is the uniform ambient ISM H_2 density. The mean mechanical power produced by supernova explosions from N_* stars in the cluster is $\sim 6.3 \times 10^{35} N_* E_{51} \text{ ergs s}^{-1}$ (McCray & Kafatos, 1987). When the energy produced by stellar winds or supernova explosions is much greater than the radiative losses, the bubble is adiabatic. This *adiabatic* phase persists until the radiative cooling becomes important for the hot bubble at t_c (years), where,

$$t_c = 4 \times 10^6 \text{ yr } \mathcal{Z}^{-1.5} (N_* E_{51})^{\frac{3}{10}} (2n_{ism})^{-\frac{7}{10}} \quad (2.9)$$

where \mathcal{Z} is the metallicity with respect to solar. After time t_c , the expansion of the bubble pressure drops to zero and the solution is subsequently governed by the constant momentum *snow-plow* solution, namely (McCray & Kafatos, 1987),

$$R_{SP}(t) = R_c \left(\frac{t}{t_c} \right)^{\frac{1}{4}}, \quad (2.10)$$

$$V_{SP}(t) = \frac{R_c}{4t_c} \left(\frac{t}{t_c} \right)^{-\frac{3}{4}} \quad (2.11)$$

where R_c is the radius of the bubble at cooling time t_c . In a physically real system, the shell expansion ends when its expansion velocity is close to the thermal sound speed of the uniform ambient ISM, i.e. $c_{ism} = (P_{external}/\rho_{ism})^{\frac{1}{2}}$, where $P_{external}$ is the external or ambient gas pressure (including components, for example, thermal, turbulent, magnetic, and cosmic rays), and ρ_{ism} is the ambient ISM volume density. Then the shell stalls and ultimately disperses, possibly assisted by *Rayleigh-Taylor* (R-T) and gravitational instabilities. However, the effect of external pressure is not part of the similarity model, and accordingly we neglect the pressure of the ISM so the shell slows down but expands indefinitely.

It must also be borne in mind that the similarity solutions for the different phases

represented by Equations (2.5) - (2.6) and (2.7) - (2.8) must be treated as two distinct regimes. In particular, the mass in the shell is not conserved across the boundary between the *Winds* and *post-SN* phases. This discontinuity and that associated with the boundary between *adiabatic* and *snow-plow* phases produce velocity jumps which are artifacts of this treatment, but they are essentially inconsequential to the final results.

2.2 Physical Conditions of The Swept-up Gas

For the shell surrounding each cluster the inside face, exposed to the far-ultraviolet from the cluster, forms a PDR zone where gas is ionized and photo-dissociated. Physical conditions within photodissociation regions are very different from those within the cold gas components in the ISM. The gas in PDRs is thermally coupled to the FUV ($6 < h\nu < 13.6$ eV) field, and the penetration of the FUV photons affects the survival and abundances of several important molecular species, for example, H_2 and CO . The structure of the PDRs is determined primarily from the absorption and scattering of FUV photons into their interiors. Dust grains provide the major source of continuum opacity in interstellar clouds and attenuate the incident radiation field by selectively absorbing and scattering light at visible and UV wavelengths. In our model, the spherical swept-up shells are treated as a series of identical thin one-dimensional plane-parallel PDR slabs (see Figure 3, a schematic diagram of a PDR region in Hollenbach & Tielens (1997)). This is the common assumption made by the majority of PDR models. The surface of the PDR is then the point at which the FUV radiation first comes into contact with the inner edge of the shell (i.e. facing the cluster) and is perpendicular to the path of the incoming light. Hence, the mean FUV radiation intensity inside the shell and/or the cloud in the radial direction is given by (Bell, 2006).

$$G(t, A_V) = G_0(t)e^{-\xi_\lambda k_G A_V} \quad (2.12)$$

where G_0 is the FUV radiation intensity in the units of Habing field at visual extinction $A_V = 0$ measured from the inner surface of the shell, ξ_λ is the ratio of the extinction at wavelength λ to that in the visual ($\lambda_V \sim 5550 \text{ \AA}$), and $k_G = \sqrt{3(1-\omega)(1-\omega g)}$ (Bell, 2006), where ω is the albedo of the dust grains and g is the scattering phase function (i.e., the mean cosine of the scattering angle).

Studies have shown that changes in the shell temperature, density, and accumulation of molecular gas due to dust absorption in H II regions are relatively small (e.g. Hosokawa & Inutsuka, 2005). The temperature and density of neutral gas in the PDRs are a few orders of magnitude higher due to the strong FUV radiation and shock compression.

Absorption by interstellar dust grains provides an important heating source for neutral gas in the PDRs. The mechanism by which this energy transfer takes place is the photoelectric ejection of electrons from small dust grains and polycyclic aromatic hydrocarbons (PAHs). FUV photons absorbed by a dust grain produce mobile electrons. These electrons can diffuse through the dust grain, and reach the surface of the grain. If the electrons are sufficiently energetic, they can overcome the work function of the grain (W) and any Coulomb potential (ϕ_c) due to a positive grain charge, so that they can be ejected into the gas with excess kinetic energy, which is then converted to thermal energy of the gas via inelastic collisions. Hence, unless the gas-grain coupling is very effective, the gas temperature is generally higher than the dust temperature, which is determined by the absorption and emission of radiation. Another dominant PDR heating source is the FUV pumping of H_2 molecules, which occurs via the absorption of Lyman and Werner band photons ($912 \text{ \AA} \leq \lambda \leq 1100 \text{ \AA}$). This FUV pumping is followed by spontaneous UV fluorescence to the ground electronic state, with 10-15% of molecules left in the vibrational continuum and dissociating, and 85-90% of molecules left in vibrationally excited bound states (Bell, 2006). For higher density PDRs, the excited molecules are returned to a thermalized ro-vibrational state through collisional de-excitation, rather than radiative decay. This process heats the gas and provides an efficient coupling to

the FUV photons when molecular H₂ self-shielding outweighs dust extinction, for example, in the case when $G_0/n \lesssim 0.04 \text{ cm}^3$ (Draine & Bertoldi, 1996), where n is the total number density of atomic and molecular hydrogen, i.e. $n = n_H + 2n(\text{H}_2) \text{ cm}^{-3}$, where n_H and $n(\text{H}_2)$ are the number densities of atomic hydrogen and molecular hydrogen in units of cm^{-3} , respectively. The critical density n_{cr} is the characteristic density at which the collisional de-excitation rate competes with the radiative transition rate. The main collisional partner for H₂ is the atomic hydrogen, and the typical value of n_{cr} is $\sim 10^4 - 10^5 \text{ cm}^{-3}$ depending on the gas temperature (Martin & Mandy, 1995). Above the critical density, vibrationally excited molecules lose their internal energy through collisions, and that energy is carried away by the hydrogen atoms and is then transferred to the thermal energy of the gas. This heating mechanism is most efficient in the atomic [HI] zone (nearest the PDR surface), where the FUV pumping rate is highest and molecular H₂ is undergoing frequent collisional de-excitation with the abundant atomic H. Other PDR heating sources include formation and photodestruction of H₂ near the surface of the PDR when the FUV flux is high, or through the energy released by photoionization of neutral carbon atoms. The contribution from the latter mechanism is generally small and drops rapidly at the C⁺/C/CO transition layer. Additional heating sources of the gas are collisions with warmer grains, the decay of turbulence within the shell and pumping of neutral oxygen to excited states by absorption of FIR emission from warm dust, and cosmic-ray ionization and excitation. Contributions to the total heating rate from these additional heating processes is usually small as well at smaller depths ($A_V \lesssim 6 \text{ mag}$), but can become important at large depths. At the very inner edge of the PDRs, the temperature can become so high (several thousand K) that photoevaporation becomes effective.

The gas in the PDRs cools by radiating away its thermal energy at mid- and far-infrared, submillimeter, and millimeter wavelengths. The primary cooling is via the FIR fine structure lines ([C II] 158 μm , [O I] 63 μm and 146 μm , [C I] 609 μm and 370

μm), mid-IR line ([Si II] $35 \mu\text{m}$), and near-IR H_2 ro-vibrational lines, as well as molecular rotational lines (primarily CO, but also of OH and H_2O). Table 2.1 lists several of the most important cooling transitions arising in PDRs, their wavelengths, upper energy levels E_{upper} and critical densities n_{cr} (Bell, 2006). In particular, the [C II] $158 \mu\text{m}$ line is the dominant cooling in the warm neutral ISM ($30 < T_{gas} < 10^4$ K). Along with the [O I] fine structure lines and the FIR continuum emission, it can be used to constrain the density n and incident FUV flux G_0 in the neutral gas (e.g. Kaufman et al., 1999). However, [C II] line emission occurs in both ionized and neutral gas, and the individual contribution from each component must be determined before the line can be used as a diagnostic of the conditions in the PDRs. After [C II], the [O I] $63 \mu\text{m}$ transition is the main coolant in PDRs. High FUV flux and density can lead to excess gas temperature (> 5000 K) at the surface of the PDR. At this high temperature, significant cooling can occur in Ly- α lines, [O I] 6300 \AA , the [Fe II] $1.26 \mu\text{m}$ and $1.64 \mu\text{m}$. Collisions between the hot gas and cooler dust grains at higher density provide more efficient cooling of the gas, while the impact on the dust temperature is negligible (Tielens & Hollenbach, 1985). The dust itself cools efficiently through continuum emission in the far-infrared. The overall structure of a PDR is the result of a very complex interplay between radiative transfer, energy balance, and chemical reactions.

2.3 The Cooling Lines as PDR Diagnostics

The line intensity ratio [O I] $145 \mu\text{m}$ /[O I] $63 \mu\text{m}$ is sensitive to gas temperatures less than 300 K, because the excitation energy of the $145 \mu\text{m}$ line is ~ 100 K higher than that of the $63 \mu\text{m}$ line (see Table 2.1). Since the FUV radiation strength governs the heating of the gas, this line ratio is a useful diagnostic tool of G_0 . Since both [O I] $145 \mu\text{m}$ and $63 \mu\text{m}$ transitions have similar critical densities, their line ratio is relatively insensitive to density, although it does show a gradual decrease for $n > 10^5 \text{ cm}^{-3}$ (Kaufman et al.,

Table 2.1. Transition properties of the main PDR emission lines.

Species	Transition	Wavelength μm	E_{upper}/k K	Critical Density n_{cr} (cm^{-3})
[C I]	$^3P_1 \rightarrow ^3P_0$	609.1	24	5×10^2 [H]
[C I]	$^3P_2 \rightarrow ^3P_1$	369.9	63	3×10^3 [H]
[O I]	$^3P_2 \rightarrow ^3P_1$	145.5	326	6×10^4 [H]
[O I]	$^3P_1 \rightarrow ^3P_0$	63.2	228	4×10^5 [H]
[C II]	$^2P_{3/2} \rightarrow ^2P_{1/2}$	157.7	92	3×10^3 [H]
CO	$J = 1 \rightarrow 0$	2600.8	6	3×10^3 [H ₂]
CO	$J = 2 \rightarrow 1$	1300.4	17	1×10^4 [H ₂]
CO	$J = 3 \rightarrow 2$	867.0	33	5×10^4 [H ₂]
CO	$J = 6 \rightarrow 5$	433.6	116	4×10^5 [H ₂]

1999). The $[\text{O I}] 145 \mu\text{m}/[\text{O I}] 63 \mu\text{m}$ can also be used as an indicator of optical depth in the $63 \mu\text{m}$ line, because the $63 \mu\text{m}$ line is often found to be optically thick (i.e. the line optical depth is greater than unity) in PDRs, while the $145 \mu\text{m}$ line is by contrast optically thin under almost all conditions (Stacey et al., 1993).

Another line intensity ratio $[\text{O I}] 63 \mu\text{m}/[\text{C II}] 158 \mu\text{m}$ is found to be most sensitive to G_0 due to a correlation with the FIR continuum color, since the FIR color depends on the dust temperature and therefore on G_0 alone (e.g. Kaufman et al., 1999; Bell, 2006, and references therein). This line ratio is also found to be sensitive to G_0/n , but the relation breaks down in the outer regions of the PDR, because $[\text{C I}]$ and CO line emission become more effective at cooling the gas than the $[\text{O I}]$ and $[\text{C II}]$ lines (Bakes & Tielens, 1994).

2.4 Chemical Evolution of Star-forming Regions

In a plane-parallel PDR slab, the attenuation of the FUV flux with distance into the PDR gives rise to a characteristic depth-dependent chemical structure. For example, the surface layer contains atomic H, C, C^+ and O. The transition from atomic to molecular hydrogen occurs at the center H/H_2 layer, while C^+ is converted into C and then CO at greater depth. Further inward, the H_2 molecule provides effective self-shielding from the FUV radiation field. The CO layer also shows a degree of self-shielding, and therefore extends deeper into the shell. The sizes and locations of the chemical zones depend on the key parameters of the PDR, i.e. density and FUV flux, on the gas-phase elemental abundances, and on the cosmic-ray particle flux.

Molecular H_2 plays a crucial role in PDR chemistry. The mechanisms that govern the formation of H_2 on dust grains are now fairly well understood at low temperature (e.g. dark cloud), but the H_2 formation rate at higher grain temperature found in the PDRs remains rather uncertain. Given this uncertainty, a simple approximation for the

H_2 formation rate of $R_f \sim 10^{-17} \text{ cm}^{-3} \text{ s}^{-1}$ at a temperature of 100 K is often assumed (Jura, 1974). The mechanisms of H_2 photodissociation in PDRs are described in detail in Hollenbach & Tielens (1999).

Molecular CO is also important in PDR chemistry. The CO photodissociation occurs through discrete absorption into predissociating bound excited electronic states, followed by transition to a repulsive electronic state and dissociation. This line absorption process implies that CO is also affected by self-shielding. Overlap with atomic hydrogen and molecular H_2 lines plays a significant role, due to the large optical depths in the H_2 lines. The CO photodissociation rate as a function of depth is crucial in the $\text{C}^+/\text{C}/\text{CO}$ transition layer. Since this rate rapidly declines once molecular H_2 is abundant, the depth of the $\text{C}^+/\text{C}/\text{CO}$ transition layer is linked to that of the H/H_2 transition layer, at which time H_2 self-shielding is more important than dust attenuation. Detailed calculations of radiative transfer in the CO absorption lines taking into account the full effects of self-shielding and line overlap have been presented in detail by van Dishoeck & Black (1988). Despite the self-shielding effect, the photoionization of carbon maintains high abundances to considerable depths within the PDR. The C^+/C transition layer is balanced by photoionization and radiative recombination reactions. The recombination becomes dominant as the FUV radiation diminishes. This occurs at the $\text{C}^+/\text{C}/\text{CO}$ transition layer, where the neutral carbon abundance peaks. As the depth increases, neutral carbon becomes locked into the stable molecular CO by burning of small neutral radicals (i.e. CH and CH_2).

On a larger scale, ranging from cold molecular cloud cores prior to star formation (phase one) to the cloud core collapse (phase two), and finally to the formation of PDRs created by newly formed stars (phase three), the chemical abundances of molecular gas are expected to change significantly. Since these molecular species are particularly sensitive to different routes of formation, they may be useful in distinguishing between a variety of environments and histories of the ISM. Details of the chemical evolution of these three

phases are discussed in the review by van Dishoeck & Blake (1998).

2.5 Non-LTE Line Radiative Transfer

Molecular and FIR atomic lines are excellent probes of the physical and chemical conditions in GMCs, shells, and PDRs in star forming regions. The interpretation of such lines requires the use of line radiative transfer methods which can calculate accurately the non-LTE level populations and the line spectra simultaneously.

The basic equations for the radiative transfer problems are given by the following (Rybicki & Lightman, 1979),

$$\frac{dI_\nu}{ds} = j_\nu - \alpha_\nu I_\nu \quad (2.13)$$

$$\frac{dI_\nu}{d\tau_\nu} = S_\nu - I_\nu \quad (2.14)$$

$$I_\nu(\tau) = \int_0^\tau S_\nu(\tau') e^{-\tau'} d\tau' \quad (2.15)$$

where I_ν is the radiative intensity along the path of photons ds at frequency ν , j_ν and α_ν are the emission and absorption coefficients, τ_ν is the optical depth between the point where I_ν is evaluated and spatial infinity long the line of sight, $S_\nu = j_\nu/\alpha_\nu$ is the source function, i.e. the emissivity of the medium per unit optical depth, and $d\tau_\nu = \alpha_\nu ds$. For the radiative transfer of molecular lines, the j_ν and α_ν coefficients are determined by the transition rates between the various rotational/vibrational levels and the population of these levels. Both the emission and absorption coefficients and hence the source function depend on the level populations, which in turn depend on the radiative intensity. Thus the intensity and level populations are coupled. The latter is obtained by integrating the source function along all possible straight lines through the medium. A coupled set of equations for the molecular line radiative transfer problems has been presented by van Zadelhoff et al. (2002).

Different methods and codes have been developed in the past for solving the line radiative transfer problem. Since the radiation field is coupled to the level populations, a method that can iteratively solve the coupled equations is needed in order to obtain

the true level populations and in turn the mean radiative line intensity without requiring excessive computing time. The use of various techniques to validate different methods with many independent line radiative transfer codes has been described in detail by van Zadelhoff et al. (2002). In this study, we adopt *Accelerated Lambda Iteration* (ALI) method which uses the direct inversion of a simplified subset of the equations, and iterations to solve the problem. It represents a modification of the more general *Lambda Iteration* (LI) method.

2.6 Evolving Starburst Models

Abundant evidence has been found for giant bubbles and shells, observed at multiple wavelengths, in the Milky Way and other spiral and irregular galaxies in the Local Group. These bubbles and shells have sizes ranging from several tens of parsecs (e.g. Pedlar et al., 2003) to more than one kiloparsec (de Grijs et al., 2001), and kinetic energies ranging from $\sim 10^{50}$ ergs to more than 10^{54} ergs. These shells generally appear in the form of partial arcs, or fragments, or cloud-like clumps due to the combined effects of strong winds and supernova explosions, shell-shell and shell-cloud interactions; only a few are visible as full circular arcs. It is likely that such shell features are located in all nearby spiral and irregular starburst galaxies and will be found when high resolution maps are available using more advanced instruments such as the *Atacama Large Millimeter Array* (ALMA).

In this study we present an ensemble of ideal three-dimensional, spherical expanding shells, in order to model the line emission of neutral ISM in massive star-forming regions in a starburst galaxy like M 82. A summary of the model assumptions are listed in Table 2.2. Our instantaneous starburst model does not address issues related to more complicated geometry in order to understand how these shells are distributed in a galaxy, how they interact, or how the gas becomes available for fueling the massive star formation

Table 2.2. Summary of assumptions used in our evolving starburst model.

Name	Description
Assumptions:	<ul style="list-style-type: none"> - spherical geometry, non-magnetized (GMCs and shells) - uniform density of molecular gas inside each stationary GMC - uniform ambient molecular gas density surrounding each shell with zero gas pressure - instantaneous star formation with no stars forming inside the shells - absence of external starlight entering the shells or GMCs - absence of dust inside the H II regions - no interactions between shells - representation of gas in a starburst galaxy by an ensemble of GMCs or shells centrally illuminated by a star cluster - representation of shell kinematic behavior by a simple similarity solution

in our model GMCs. Our non-LTE line radiative transfer method simply sums the line emission from the model shells and parent GMCs in the ensemble for the *Winds* phase, and just the model shells for the *post-SN* phase. In reality, the actual ISM components are cloud-like clumps, partial arcs, fragments, and a few visible full circular arcs. Hence, our model is an idealistic approximation for a starburst galaxy; it may be considered the first step toward simulating the response of the gas environment in an evolving starburst region for the purpose of examining the effects of this evolution. An outline of our models and quantitative values of the physical and chemical properties of GMCs and shells will be presented in Chapter 3.

Chapter 3

Simulation Methodology

In previous chapters we have discussed the goals of this thesis, the properties of giant molecular clouds and wind driven expanding shells that are to be employed in constructing a family of models for an evolving starburst. Here we present the numerical simulation methodology used to predict the FIR/sub-mm/mm line emission properties in massive star-forming regions. In particular, computations for individual shells and the ensemble of shells obtained by these methods can be used to relate the model results to the observed data. This will then allow us to examine (1) whether the molecular line data from starburst galaxies can be modeled to adequately represent the state of the gas as it responds to a massive star-forming event, as opposed to the gas in the pre-starburst state; and (2) whether currently available sub-mm molecular line and atomic line emission data reflect the age of the starburst by modeling the consequences of the effects on the gas of the evolution of the stars and expanding shells.

A brief description of the model outline, model parameters and variables, computational methods, as well as a summary of the model are given in the following sections. Detailed descriptions of each of the related methods can be found in the references given.

3.1 Model Outline

Our basic model comprises a series of non-overlapping (i.e. non-interacting) spherical shells expanding into a uniform gas medium. These shells are all driven by winds from star clusters formed during an instantaneous starburst. The interior hot bubble is produced by stellar wind from an underlying super star cluster, whose properties are selected as discussed later. The thrust of our model simulation is to compute the molecular line emission from the swept-up shells and the associated parent GMCs. Since the underlying stellar radiation from the clusters has a pronounced effect on the properties of PDR regions of the shells, and since these properties are therefore also affected by the radius of the shell and evolutionary stage of the cluster, the SED of the molecular line emission from these shells contains a *signature* of the stage of evolution of the starburst. This variation with time, predicted by our model, offers a way of dating the starburst, at least in principle.

The set of our starburst models is divided into two phases, namely the *Winds* and *post-SN* phases as defined in Chapter 2. In the *Winds* phase, the shells propagate into their parent clouds, which are substantially more dense than the surrounding ISM in which they are embedded. In the *post-SN* phase, the shell breaks out of the parent cloud and expands into the uniform lower density ISM which pervades the entire galaxy. The same bubble/shell dynamical theory by McCray & Kafatos (1987) described in Chapter 2 is used to describe the shell behavior in both phases. Since the simple similarity relations do not apply to a nonuniform ambient medium, we do not follow the shell expansion across the transition from cloud to the surrounding ISM. Instead the two phases are treated independently according to the equations for the McCray & Kafatos theory also described in Chapter 2. Thus, although the behavior in the *post-SN* phase is regarded as a continuation of the shell evolution from the parent cloud into the ISM, continuity at the transition is only maintained in the mechanical luminosity of the wind (L_w) and the stellar luminosity (L_*) evolution of the central star clusters. There is accordingly a

discontinuity in the radius (R_s), velocity (V_s), and consequently the temperature (T_s), density (n_s), thickness (d_s), and the mass of each expanding shell across the boundary between the two phases. These quantities asymptotically approach those of a continuous model when the mass of the ISM swept up in the *post-SN* phase becomes greater than the mass of the parent GMC in the *Winds* phase. The *Winds* phase thus comprises younger and denser shells than in the *post-SN* phase. In this way, it is possible to model data with starbursts occupying a large range of potential ages and molecular gas excitation conditions, which is an essential goal of this study.

In each phase, the shell structure is computed with time as the independent variable. The final output dependent variables are the line fluxes (and profiles) for several molecules and atoms each at a number of observed transitions, computed by a non-LTE line radiative transfer code applied to each shell and its parent cloud. The integrated line flux for each shell (and GMC) is the sum over the emission from the entire emitting region. The total line flux for the shell ensemble is then the sum of the integrated line fluxes of all shells (and GMCs). Intermediate variables which determine these fluxes include the radius and velocity of each shell, its chemical structure, shell temperature and density structure, which are computed using a *Shell Dynamics* model code and a time-dependent PDR model code. These codes are described in detail later in § 3.3 - § 3.5.

Our two-phase starburst model described above must also be characterized by a number of fixed parameters with adopted plausible values. These include, for example, the initial giant molecular cloud parameters (mass M_{GMC} , initial H₂ density n_0 , and core H₂ density n_c), the star formation efficiency (η), the star cluster related parameters (IMF, individual star mass m_*), the initial chemical composition of the parent clouds, and the density of the ambient ISM. These parameters, along with others, and their numerical values, are discussed in detail in the subsequent sections, in association with the discussion of the PDR and radiative transfer codes. A brief summary of all variables and

parameters as well as methods are presented in Table 3.6, Figs. 3.2 and 3.3 at the end of this Chapter.

Finally, a chi-square (χ^2) method will be used for fitting the model line spectral energy distribution to a set of molecular line data in order to estimate the starburst age(s) and total H_2 mass in the observed nuclear disk of M 82. Detailed definition and implementation of the χ^2 method will be described in Chapter 5. As an extension of this work, comparisons of the line intensity ratio-ratio diagrams between our modeling results and observed data of M 82 and LIRGs data may help us understand better the relationships between molecular gas properties and star formation history in active star-forming regions.

3.2 Initial Parameters

3.2.1 Winds Phase

In 2005 Keto et al. observed $^{12}\text{CO}(2-1)$ emission in the center of M 82 with a linear resolution of 17 pc at the source. They resolved ~ 300 molecular clouds with masses ranging from $\sim 2 \times 10^3$ to $2 \times 10^6 M_\odot$. The mass spectrum of these GMCs scales as $dN/dM_{\text{GMC}} \propto M_{\text{GMC}}^{-1.5 \pm 0.1}$, similar to the Galactic one (Sanders et al., 1985; Solomon et al., 1987). Keto et al. also found that the mass spectrum of star clusters in M 82 follow the same power-law distribution, suggesting that individual molecular clouds are transformed in the starburst into individual star clusters in their dense cores. Combing this result with other studies (e.g. Weiss et al., 2005), we assume the GMC mass distribution responsible for the stellar outburst in our model has a power-law index of 1.5, and the mass ranges between 3.16×10^3 and $10^7 M_\odot$. About 70% of molecular gas mass in a model starburst will then be contained in the clouds with masses $> 10^6 M_\odot$. It is also expected that much of the FIR luminosity due to star formation would arise from these massive clouds. To reduce the computation time, a discrete and arbitrary number of giant molecular clouds

distributed similar to that discussed in Keto et al. (2005) is assumed. The masses for these discrete GMCs are 3.16×10^3 , 10^4 , 3.16×10^4 , 10^5 , 3.16×10^5 , 10^6 , 3.16×10^6 , and $10^7 M_\odot$, and are hereafter denoted as 3M3, M4, 3M4, M5, 3M5, M6, 3M6, and M7. The total number of clouds is about ~ 400 , and the total H_2 mass in this GMC ensemble is $\sim 1.69 \times 10^7 M_\odot$ with a total star clusters mass of $4.2 \times 10^6 M_\odot$. This selection is intended to provide a template cloud/cluster mass for scaling the model to fit the data for M 82. The best fitting molecular H_2 gas mass and the initial star cluster mass will be determined from a χ^2 fitting method, as described later in Chapter 5.

The average gas densities of GMCs in our Galaxy and starburst galaxies are in the range a few 10 to a few times 10^2 cm^{-3} (Dame et al., 1986; Jog & Solomon, 1992; Wilson et al., 2008), but their cores, where most of the stars form, have densities three or more orders of magnitude higher. Higher gas densities are expected in more actively star-forming galaxies in accordance with the Schmidt law (Kennicutt, 1998). Therefore, we adopt a value of 300 cm^{-3} for the uniform initial H_2 gas density (i.e. n_0) for the M7 cloud based on the densities for the most massive clouds in the study of molecular cloud properties in the active spiral M 51 by Scoville & Wilson (2004). The core densities of the GMCs are three or more orders of magnitude higher than the average gas density of the GMCs. Higher densities are deduced in more actively star-forming galaxies in accordance with the Schmidt law (Kennicutt, 1998). Since this study is proposed to be a complementary study to the dusty starburst models developed by Efstathiou et al. (2000), we adopt the same core density namely $n_c = 2 \times 10^3 \text{ cm}^{-3}$. The radius of this $10^7 M_\odot$ cloud is 47 pc derived from the mass of the cloud and the assumed density with the assumed effective molecular weight $\mu = 2.36$ (e.g. Elmegreen et al., 1979; McCray & Kafatos, 1987).

We know that star formation takes place primarily in the dense cores of GMCs, but the details of the physical processes involved are not yet well understood. The efficiency of star formation (or the gas consumption rate) ranges from about 1% in late-type spirals

to 60% or more in active star-forming galaxies (Kennicutt, 1998). In this study we adopt a moderate star formation efficiency $\eta = 25\%$ for our model starburst galaxies. Given the lack of knowledge about n_c , whether any dust remains in the initial H II region, and whether, according to our assumption, all star formation in a given GMC occurs instantaneously, Equation (2.3) provides only a rough estimate (i.e. an upper limit) of the Strömngren radius R_S value.

We assume that the relationship between cloud mass and radius is the same as that derived from a CO survey for 273 giant molecular clouds in the Galactic inner disk by Solomon et al. (1987). From the measured relationship between the cloud size and the velocity line width, and the application of the virial theorem, they derived a power-law cloud density and mass relation, in which the mean gas density of the cloud is inversely proportional to the cloud size. Hence, the cloud mass is proportional to the square of the cloud radius (i.e. the mass surface density is a constant). From the studies of independent methods of determining the H₂ mass, Solomon et al. (1987) also demonstrated that these giant molecular clouds are bound principally by self-gravity and not by external pressure exerted by a hot phase of the ISM. Since we assume the mass distribution of GMCs in a starburst galaxy is similar to that in our Galaxy, we adopted the power-law relations of mass, radius, and density for our model GMCs as those defined in Solomon et al. (1987). This mass - radius relation has also been studied for GMCs in other galaxies, for example M 51 by Bastian et al. (2005), and has been found to be similar in form. Hence, the density and the radius for a model GMC having mass less than $10^7 M_\odot$ can be written in the following forms,

$$n_0 = 300 \text{ cm}^{-3} \times \left(\frac{R_{GMC}}{47 \text{ pc}} \right)^{-1}, \quad (3.1)$$

$$R_{GMC} = 47 \text{ pc} \times \left(\frac{M_{GMC}}{10^7 M_\odot} \right)^{\frac{1}{2}} \quad (3.2)$$

where R_{GMC} is the radius of the GMC with mass M_{GMC} that is less than $10^7 M_\odot$.

Table 3.1 summarizes the number distribution of the GMCs and their initial physical properties. For GMC mass less than $3.16 \times 10^3 M_{\odot}$, the predicted number of very massive stars ($> 30 M_{\odot}$) in the star cluster is below 1.0. In addition the supernova wind will not be steady as assumed in our model, because of the relatively small numbers of contributing stars.

3.2.2 Post-SN Phase

As discussed in Chapter 2, all shells are propelled into a less dense ambient ISM during the *post-SN* phase. The intercloud medium of the central 1 kpc region of the Galaxy has been studied by Jog & Solomon (1992), who find it to be mostly molecular with density between 30 and 100 cm^{-3} . Bally et al. (1988) also obtained an average molecular gas density of 50 cm^{-3} for the region within a radius of 500 pc of the center of our Galaxy. In this study, we assume a uniform ambient ISM with similar density surrounding the GMCs for our model.

To investigate whether this medium should be considered as atomic or molecular, and to get an estimate of its mean density, we compare the observational constraints for various ambient ISM constituents (H_2 , HI, and H II) for the central 1 kpc region of M 82. Table 3.2 shows that gas with a column density of about 10^{23} cm^{-2} is required by observations, and that the dominant state of the ISM is molecular. Hence, from this observed H_2 column density, and an adopted diameter of 1 kpc for the starburst region, we can derive the number H_2 density of about 30 cm^{-3} , and we adopt this figure for modeling the central 1 kpc region in M 82.

In reality, intercloud gas in M 82 is unlikely to be uniformly distributed, as assumed in our model. Recent studies (e.g. Glover & Mac Low, 2007, and references therein) show that a smoothly distributed turbulent medium consisting of atomic gas would quickly (within a few 10^6 yr) develop density fluctuations, becoming a highly non-uniform medium of molecular H_2 , with density enhancements up to a factor of 100 or more times

Table 3.1. Initial conditions of GMCs and SCs in a modeling starburst system.

GMC (N_{norm}) ^a	$\log_{10}M_{GMC}$ ^b	n_0 ^c	n_c ^d	R_{GMC} ^e	$\log_{10}M_{SC}$ ^f	N_* ^g		$\log_{10}L_{SC}^*$ ^h	$\log_{10}L_{SC}^{mech}$ ⁱ	
	(M_\odot)	(cm^{-3})	(cm^{-3})	(pc)	(M_\odot)	Total	$M_* \geq 8 M_\odot$	$M_* \geq 30 M_\odot$	(L_\odot)	(L_\odot)
M7 (1.0)	7.0	300	2000	46.8	6.4	7.1E6	2.2E4	5.0E3	42.8	40.1
3M6 (1.77)	6.5	534	3558	26.3	5.9	2.2E6	7.0E3	1.6E3	42.3	39.6
M6 (3.1)	6.0	949	6325	14.8	5.3	7.1E5	2.2E3	5.0E2	41.8	39.1
3M5 (5.6)	5.5	1688	11251	8.3	4.9	2.2E5	7.0E2	1.6E2	41.3	38.6
M5 (10.0)	5.0	3000	20000	4.7	4.4	7.1E4	2.2E2	50.0	40.8	38.1
3M4 (17.7)	4.5	5337	35578	2.6	3.9	2.2E4	70.0	15.0	40.3	37.6
M4 (31.6)	4.0	9487	63246	1.5	3.4	7.1E3	22.0	5.0	39.9	37.2
3M3 (56.2)	3.5	16876	112509	0.8	2.9	2.2E3	7.0	1.0	39.4	36.7
Ensemble (127)	7.27	6.63	1.57E7	4.9E4	1.1E4	43.1	...

Note. — All data listed in the above table are for single SC, except for the Ensemble.

^aGMC type (number of GMC in an ensemble).

^bGMC mass.

^cAverage gas density of a GMC.

^dGMC core density.

^eGMC radius.

^fStar cluster mass.

^gStar number for different stellar mass ranges.

^hStellar bolometric luminosity.

ⁱMechanical luminosity (Stellar wind + SN).

Table 3.2. Observed column density of various ISM components in the center of M82.

Type	Column Density (cm^{-2})	Reference
H ₂	6.1×10^{22}	Wild et al. (1992)
	a few $\times 10^{23}$	Mao et al. (2000)
HI	2.6×10^{22}	Weliachew et al. (1984)
H II	9.0×10^{22}	Carlstrom & Kronberg (1991)

the mean density. For simplicity, we ignore these density fluctuations, and regard this medium as represented by its mean density, treating it as uniform for the purpose of computing the material swept-up by the expanding shells.

3.3 Shell Structure and UCL_PDR Code

The chemistry and thermal balance are solved self-consistently within the shell using a time- and depth-dependent PDR model (i.e. *UCL_PDR* code). This yields the abundance of each species included in the chemical network and their associated column densities, the gas and dust temperatures, all of which are functions of depth z and time t . The *UCL_PDR* includes 128 species involved in a network of over 1700 reactions (Bell, 2006, and references therein). What this means is that the *UCL_PDR* code treats the chemistry time-dependently, so that the abundances change over time and the chemistry is non-equilibrium in this sense. Freeze-out of atoms and molecules onto grains is neglected. The reaction rates are taken from the UMIST chemical database (Le Teuff et al., 2000). Microturbulence (Doppler velocity 1.5 km s^{-1}) is used in the chemical reaction rate calculation (Hollenbach & Tielens, 1999). The H₂ formation rate per unit volume, averaged over the grain size distribution, in units of $\text{cm}^{-3} \text{ s}^{-1}$ is given as (Bell, 2006),

$$R_f \sim 3 \times 10^{-18} \text{ cm}^{-3} \text{ s}^{-1} S(T, T_{dust}) \eta(T_{dust}) T^{\frac{1}{2}} n n(H) \quad (3.3)$$

where $S(T, T_{dust})$ is the probability that a hydrogen atom with temperature T , colliding with a dust grain of temperature T_{dust} , will stick to the grain surface, $\eta(T_{dust})$ is the probability that a trapped grain will traverse the grain surface, find another H atom and recombine, the H_2 molecule subsequently evaporating from the grain surface, n_H is the number density of atomic hydrogen in cm^{-3} , n is the total number density of hydrogen nuclei, and solar metallicity is assumed. In this study, $R_f = 3 \times 10^{-18} \text{ cm}^{-3} \text{ s}^{-1}$ is adopted (Bell, 2006). The gas in the PDR is assumed to be initially in atomic form, with all metals possessing ionization potentials below 13.6 eV in singly ionized form.

The *UCL_PDR* code assumes a plane-parallel geometry and models the shell as a semi-infinite plane-parallel slab of homogeneous density at a given time step. The term semi-infinite is used here to mean that the FUV radiation enters from only one side of the slab. For our model, there is only one uni-directional flux of FUV photons incident upon the inner surface of the shell and no photons are incident upon the shell-cloud interface. The code iterates through all depth steps for a given time step before advancing to the next time step. An adaptive grid of depth steps is used in the model, such that the variation in the H_2 self-shielding function (Draine & Bertoldi, 1996) is small between depth points ($< 10\%$). This ensures that changes in chemical abundances are fully resolved. At each depth step, the code calculates the attenuation of the FUV field before beginning an iterative cycle to determine the gas temperature at which the total heating and cooling rates are equal (to within some error tolerance), i.e. the condition of thermal balance is satisfied. The implicit assumption made in this approach is that the gas is always in thermal equilibrium. Heating by collisional de-excitation of FUV-pumped H_2 , photodissociation of H_2 molecules, cosmic-ray, carbon photoionization, H_2 formation, gas-grain collisions, and turbulence are included in the calculation of thermal balance in the *UCL_PDR* code. Heating due to shocks is not included. Gas cooling is mainly

through emission from collisionally excited atoms and molecules and by interactions with the cooler dust grains. Detailed heating and cooling rates and related parameters can be obtained in literature (e.g. Bell, 2006, and references therein).

For each iteration, the chemistry is first calculated, based on the gas temperature and attenuated FUV flux, after which the heating and cooling rates are computed, using the revised chemical abundances. Once the thermal balance criteria have been met, the chemical and physical properties calculated at the appropriate temperature are stored to file and the code advances to the next depth or time step. During the iteration cycle, thermal balance is considered to have been reached if the difference in the total heating and cooling rates is $< 0.5\%$ or if the change in gas temperature between iterations is < 0.1 K. In contrast, the dust temperature is calculated using the analytical expression of Hollenbach et al. (1991) and is a function of the incident FUV flux and the visual extinction at the current depth.

In our models, the swept-up shell itself is supported by thermal gas pressure and non-thermal pressure due to micro-turbulence. The gas temperature decreases toward the outer surface of the shell, and the total gas density is assumed uniform. Therefore the pressure is lower at the outer surface. Such non-constant pressure shell structure is not physically realistic, but it is an approximation driven by the fact that the PDR code can not handle a non-constant density. The shell density n_s refers to the total number density of molecular hydrogen (i.e. $n(\text{H}_2)$ cm^{-3}). This shell density is derived at each time step from balancing the pressure at the outer surface of the shell with the ram pressure as follows,

$$n_s(t) = \frac{n_a v_s^2(t)}{kT_{gas}(t)/(\mu m_H) + \delta v_D^2} \quad (3.4)$$

where n_a is the ambient number density of molecular hydrogen, i.e. the density of material colliding with the expanding shell, $v_s(t)$ is the expansion velocity, k is the Boltzmann constant, $T_{gas}(t)$ is the gas temperature at the outer surface of the shell, μ

is the mean molecular weight, $\mu = 2.36$, m_H is the mass of the hydrogen atom, and δv_D is the micro-turbulent velocity inside the shell as viewed along the line of sight (i.e. the Doppler velocity). The effect of the static pressure in the external ISM is not taken into account in the above pressure balance equation, which is consistent also with our neglect of the static pressure of the ambient medium on the expansion of the shell. The thickness of the shell d_s at each time step is in turn calculated using the continuity equation (or mass conservation law),

$$d_s(t) = \frac{n_a r_s(t)}{3n_s(t)} \quad (3.5)$$

Because the quantity n_s in Equation (3.4) involves the knowledge of T_{gas} , and these two parameters are interdependent in the PDR code, they must be solved together by iterative means, subject to the constraint imposed by this equation. Hence, we have modified the original *UCL-PDR* code to carry out the procedure of pressure balance. First, a set of initial guessed parameters (T_{gas} , n_s , d_s) is used for the very first iteration of simulations. The initial T_{gas} is derived using a black-body radiation, $T_{gas} = \left[\frac{L}{4\pi R_{GMC}^2 \sigma} \right]^{\frac{1}{4}}$, where L is the radiative luminosity, R_{GMC} is the cloud radius, and σ is the Stephan-Boltzmann constant. The T_{gas} values for the subsequent iterations are computed by comparing the shell pressure at its outer edge and the ambient gas pressure until the difference is less than 10%. For each T_{gas} value, the n_s and d_s values are calculated using Equations (3.4) and (3.5), and the new set of parameters (T_{gas} , n_s , d_s) become the input of next iteration to the *UCL-PDR* code. Numerically, shell density and thickness values are computed using the *Shell Dynamics* code developed by myself. The theory has been discussed in § 2.1 of Chapter 2.

The time-dependent stellar luminosity and FUV field strength are calculated using the stellar population synthesis code *Starburst99* (see § 3.5). A Salpeter IMF is assumed, i.e. $dN/dm_* \propto m_*^{-2.35}$ (IMF; Salpeter, 1955), and the stellar mass is in the range 0.1 - 120 M_\odot . The phase-dependent wind mechanical power for a given cluster is estimated

by averaging the time-dependent values in each of the two phases of the shell evolution.

Table 3.3 summarizes the standard input parameters in the *UCL-PDR* code that describe the physical properties of the model shell. They are the total number density of hydrogen nuclei n (cm^{-3}); the flux of FUV photons incident upon the inner surface of the shell and cloud, G_0 (Habing field); the rate of H_2 ionization by cosmic-ray, ζ (s^{-1}); the metallicity, $\mathcal{Z} / \mathcal{Z}_\odot$; the microturbulent Doppler velocity, δv_D (km s^{-1}); and the gas-phase elemental abundances relative to total hydrogen nuclei, $X(i) = n(i) / n$, where $n(i)$ is the number density of species i (cm^{-3}). The minimum value of the chemical abundance for the selected species used in the non-LTE line radiative transfer problems is $\frac{n(i)}{n} = 1.0 \times 10^{-12}$ (i.e. the $X(i)$ is then set to zero). The cosmic-ray ionization rate is enhanced by a factor of 1.5 at later time ($t > 10$ Myr) to artificially include the soft X-rays heating effect on the gas of the shell. The value for ζ adopted in the PDR code is the standard one for the Milky Way fixed in the code, which is two orders of magnitude lower than that measured in M 82. In Chapter 5, we discuss the possible impact of a higher ζ value on the conclusions, specifically regarding the applications to M 82. The code reads these values from a separate input parameter file upon execution, allowing different parameter files to be used in succession to construct a grid of models. One of the main features of the *UCL-PDR* code is its ability to treat the conditions within the shell time-dependently. As such, it is capable of handling time-varying physical parameters and can accept input files listing the various free parameters as a function of time.

The initial abundance of H_2 is set to $n(\text{H}_2)/n_H = 0.5$ (Hartquist et al., 2003). At the first time step ($t = 0$ yr) all depth steps take as their initial abundances those produced by a single-point dense dark-cloud model in the *Winds* phase (private communication with Dr. Serena Viti at UCL). The input parameters for the dark-cloud modeling are $n_H = 4 \times 10^5 \text{ cm}^{-3}$, $T_{GMC} = 10$ K, $G_0 = 1$ Habing field, and the standard gas-phase atomic abundances relative to H nuclei listed in Table 3.4 (Bell, 2006, and references therein). The dark-cloud assumption of chemistry is the same for all depth steps; it is a reasonable

guess for the initial gas conditions in a GMC before star formation occurs. Our starburst model time step begins at $t = 1.0 \times 10^4$ yr, adopted as the time when the massive star formation occurs in the center of the GMC. For this time step and the subsequent time steps, the input abundances are re-set to the output abundances of the previous time step generated by the *UCL-PDR* code. As mentioned earlier, the chemistry at first iteration is calculated from gas temperature and attenuated FUV flux, and then revised iteratively until the balance criteria of heating and cooling is reached for each depth step at each time step. The final results are therefore not significantly dependent on our initial dark cloud chemistry input at $t = 0$ yr. The metallicity dependence appears in several key processes in the *UCL-PDR* code, and accordingly we adopt solar abundances for the metals, i.e. unit metallicity. The dust-to-gas mass ratio is adopted as 1/100.

The chemical timescale is generally governed by the H_2 formation rate, density, and FUV field strength, and possibly molecular fraction of hydrogen (Hollenbach & Tielens, 1997). Hence, for typical molecular cloud conditions, the chemical timescale is short and is more sensitive to the input parameters during the first 10^5 yr, since the input parameters vary on a timescale of the same order. More generally, a steady-state PDR model does not handle the changes of input parameters with time, since it assumes an equilibrium chemistry, i.e. the chemical timescale is much shorter than the timescale for the variation of physical conditions. A steady-state PDR code includes only equilibrium reaction rates which ensure that the abundances do not change with time (T. Bell, 2008 private communications). During a starburst event, the physical conditions of gas surrounding a starburst are expected to change drastically in a very short timescale. Hence, the use of a full time-dependent PDR code in which temperature, density, and chemistry of gas change with time is necessary, particularly in modeling the shell evolution in a starburst galaxy. Detailed comparisons of a steady-state PDR model with time-dependent *UCL-PDR* code for various cloud conditions ($n = 10^2 - 10^{5.5} \text{ cm}^{-3}$, FUV field 17 - 1.7×10^5 Habing field, $Z = 0.01 - 1 Z_\odot$) were discussed by Bell (2006) and

Table 3.3. Standard input parameters for the time-dependent UCL_PDR model.

Parameter (Units)	Symbol	Value
Starburst age (yr)	t	$0 \leq t < 10^8$
Incident FUV flux (Habing field)	G_0	$10 < G_0 \leq 10^8$
Turbulent (microturbulence) velocity (km s ⁻¹)	δv_D	1.5
PDR surface density ($A_V = 0$ mag)	n	$10^3 \leq n < 10^7$
Initial gas-phase abundances relative to H ^a		
PAH abundance	x_{PAH}	4.0×10^{-7}
Dust visual absorption cross section (cm ⁻²)	σ_v	3.1×10^{-10}
H ₂ formation rate on dust at $A_V = 0$ (cm ³ s ⁻¹)	η_{H_2}	3.0×10^{-18}
Cosmic-ray ionization rate (s ⁻¹)	ζ	1.3×10^{-17}

^aThe initial gas-phase abundances for all depths at the first time step ($t = 0$ yr) are produced by a single-point dense dark-cloud model (see text for details).

benchmark results presented on the web site at <http://www.astro.uni-koeln.de/site/pdr-comparison/intro1.htm>. The additional computational expense necessary to model the changing chemistry is repaid by the ability to consider phenomena that evolve on short time scales. For example, low metallicity environments can be far from chemical equilibrium until 1 Gyr (for $Z = 0.01 Z_\odot$), due to the inhibited H₂ formation as a result of depletion of the grain surface area available for catalysis, and this has implications for the timescales required to reach chemical equilibrium.

When calculating the attenuation of the FUV field $G(t, A_V)$, the distance into the shell, then its ambient gas, is expressed in terms of the visual extinction A_V ($\lambda_V \sim 5550 \text{ \AA}$) and is related to the shell depth through Equation (2.12). Since no light leaks from

Table 3.4 Standard gas-phase elemental abundances used in *UCL_PDR* code (relative to total hydrogen nuclei).

He 7.5×10^{-2}	C 1.4×10^{-4}	N 6.5×10^{-5}
O 4.4×10^{-4}	Na 8.8×10^{-7}	Mg 5.1×10^{-6}
Si 8.2×10^{-7}	S 1.4×10^{-6}	Cl 1.1×10^{-7}
Ca 5.7×10^{-10}	Fe 3.6×10^{-7}	

one cloud and sheds on to another cloud, the scale size of the FUV penetration depends solely on the shell or ambient ISM density. Standard values of dust properties are used in the model (see Table 3.5; Bell 2006), though the *UCL_PDR* code allows the various dust properties to be specified as free parameters which can vary with shell depth and time. Hence, assuming a value of $\xi_\lambda = 2.4$ at 1000 \AA and the $k_G = 0.575$ (ξ_λ and k_G are defined in Equation 2.12), the FUV radiation is attenuated by a factor $e^{-1.38A_V}$ at 1000 \AA for each A_V .

The chemistry within the parent GMC outside the shell is also handled by the same PDR analysis, using the different (lower) density in this region. The incident FUV strength for the cloud region is the attenuated radiation field emerging from the outer boundary of the shell, and the FUV strength inside the cloud is computed in the same way as for the shell, with the computation of A_V taking account of the lower density of the dust.

Finally, an issue that is worth bearing in mind is how the *UCL_PDR* code handles thermal equilibrium across the shells. This code assumes that all species are in thermal equilibrium and the chemical reaction rates are then based on the gas temperature (at each depth and time step). There are, however, certain reactions which proceed much faster if the reactant species are in vibrationally excited states. The most important example of this is vibrationally excited H_2 (often labeled H_2^*). The *UCL_PDR* code does

Table 3.5. Standard dust grain properties adopted in the UCL_PDR code.

Parameter	Symbol	Value
Radius (cm)	r_g	10^{-5}
Mass density (g cm ⁻³)	ρ_g	2
Mass (g)	m_g	18×10^{-15}
Number density ^a ($\mathcal{Z}n$ cm ⁻³)	n_g	2×10^{-12}
Cross-section (cm ²)	σ_g	3×10^{-10}
Albedo	ω	0.7
Mean scattering angle	g	0.9

^aThe \mathcal{Z} is the metallicity with respect to the solar, and n is the total number density of atomic and molecular hydrogen.

not account for these reactions, since determining the different ro-vibrational states of H_2 (or other molecules) would slow down the code considerably and there are still fairly significant uncertainties in these calculations. Detailed information on this issue can be found at section II.B.2 (Non-Maxwellian chemistry) of Hollenbach & Tielens (1999).

3.4 SMMOL Code

Before we can calculate the line emission of various molecules and atoms in the shell and its parent cloud using the non-LTE radiative transfer code *SMMOL*, the physical and chemical structures of the shell and its parent GMC need to be computed with time using *Shell Dynamics* and *PDR* codes. Several modules were developed in order to separate and extract gas and dust temperatures and fractional abundances for molecular and atomic species calculated by the *UCL_PDR* code. These extracted gas and dust temperatures and abundances, along with the shell density, thickness, radius, and expansion velocity computed by the *Shell Dynamics* code, are re-gridded for a spherical geometry and used as input parameters for the *SMMOL* code.

The line radiative transfer code *SMMOL* was developed by Dr. Jeremy Yates at UCL (Rawlings & Yates, 2001). This code has already been used to model the molecular line emission of a variety of astronomical objects, for examples, gas inflow and outflow (Rawlings & Yates, 2001), and the PDR and shocked gas in the Orion KL cluster (Lerate et al., 2006). The model has been successfully benchmarked with similar models (van Zadelhoff et al., 2002).

The *SMMOL* code implements the ALI method discussed in § 2.5 of Chapter 2, and it solves the multi-level non-LTE radiative transfer problem in both molecular lines and the dust continuum. It includes an empirical dust extinction model (see Table 1 in Mathis 1990). The dust temperature is an input parameter generated by the time-dependent PDR code as described in the previous section. As the first step, the code calculates the

total radiation field and level populations assuming LTE and the interstellar radiation field (plus the cosmic background radiation 2.73 K) as input continuum using data (e.g. specific intensity averaged over all directions at a given frequency I_ν , average flux S_ν , brightness temperature in the Rayleigh-Jeans limit corresponding to I_ν , and radiation brightness temperature) from Mathis et al. (1983) and Black (1994). Next, the code re-calculates the total radiation field, and checks for the convergence criterion, i.e. $(n_i - n_{(i-1)}) / n_i = 10^{-3}$, where n_i and n_{i-1} are the population densities for the i and $i - 1$ levels. The space is discretized into 100 grid points, and at each grid point along the radial direction the code generates the level populations and the line source functions. The emergent intensity distributions may then be convolved with the telescope beam, so that the model can directly predict the line profiles for a given source as observed with a given telescope. In our models, we assume the entire region containing all of the shells is unresolved.

The radiative transfer analysis requires molecular data in the form of energy levels, statistical weights and transition frequencies as well as the spontaneous emission probabilities (Einstein A coefficients) and the collisional rate coefficients. In our study, the Einstein A and collisional rate coefficients for the molecular and atomic lines are taken from the Leiden Atomic and Molecular Database (Schöier et al., 2005). The lowest ten energy levels are incorporated for molecular species (CO, HCN, HCO⁺, CN, HNC), three levels for atomic [C I] and [O I], and two levels for atomic [C II]. Multiple collisional partners (H, e⁻, H⁺, p-H₂, o-H₂, He) are taken into account in the statistical equilibrium equation calculation. The collisional excitation of molecular lines involves two partners, i.e. p-H₂ and o-H₂, but the excitation of [C I] fine structure lines is affected by collisions with all six particles, five (without He) for [O I] lines, and four (without He and H⁺) for [C II] lines. Since these forbidden lines have very low radiative transition probabilities, the upper states are populated primarily by collisions, and they are usually optically thin.

The input parameters to the *SMMOL* model are (1) molecular data including molecular mass, energy levels, transition frequencies, radiative rates and collisional rates; and (2) physical data describing the object to model. This includes the physical distance of the current grid point to the center of the shell, gas density, number densities of the six collisional partners (H, e^- , H^+ , p- H_2 , o- H_2 , He), the fractional abundance of molecules or atoms, the gas (kinetic) and dust (thermal) temperatures, shell expansion velocity, and the microturbulent velocity. A schematic diagram of the model components (PDR or shell and its parent GMC) is shown in Fig. 3.1. In this study, we treat the PDR and shell as one gas component. The line intensity/flux for the shell and GMC components are calculated using the same method. For the *Winds* phase, the integrated line intensity/flux at each time step is the sum of line emission in the shell and its parent cloud. For the *post-SN* phase, the integrated line intensity/flux is the emission from the shell only. Due to the incomplete knowledge of the structure and physical state of the ambient ISM in a starburst galaxy, we do not include the molecular or atomic line emission from this component in our model. In Chapter 5, we discuss the possible impact of this exclusion on the conclusions, specifically regarding the applications to M 82.

3.5 Starburst99

To account for the evolution of star clusters in the center of our model GMCs, a web based software and data package called *Starburst99* is used in this study. This package is designed to model spectrophotometric and related properties of star-forming galaxies. It was developed at Space Telescope Science Institute lead by Claus Leitherer. A description of the code and its physical basis is in Leitherer et al. (1999) and Vazquez & Leitherer (2005).

We use the same input star cluster parameters and assumptions for *Starburst99* as those used in the *Shell Dynamics* calculations. A suggested time step is chosen as 0.1

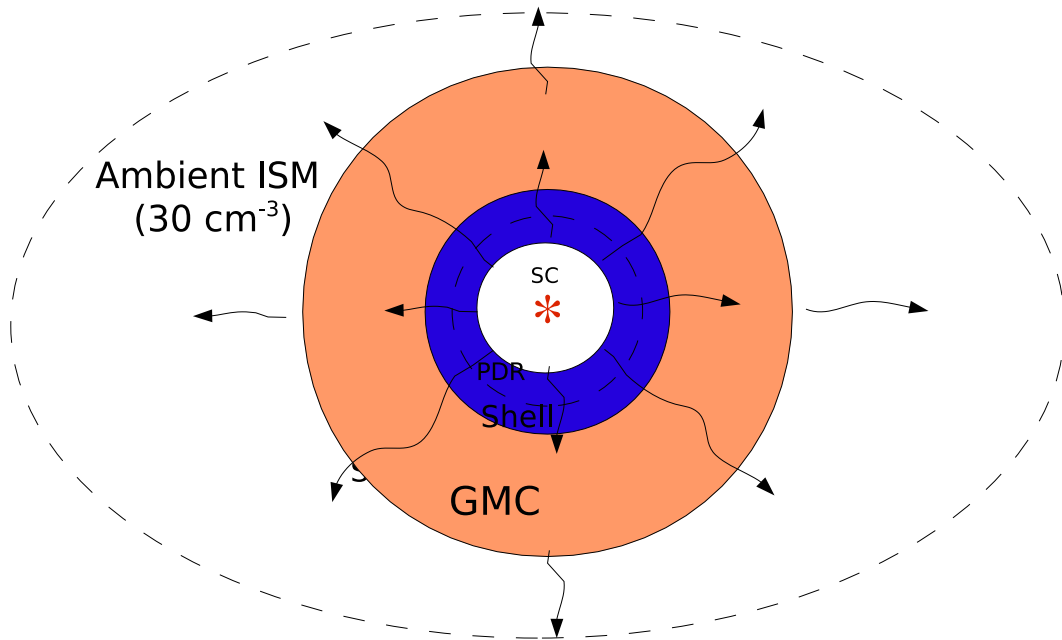


Figure 3.1 This diagram illustrates the structural components associated with a single star cluster within our model. The white region is the hot cluster wind, the blue region is the shell of material swept up from the giant molecular cloud, represented by the orange region. The region exterior to the GMC is the ambient interstellar medium (ISM) with a fixed H_2 density of 30 cm^{-3} .

Myr. A smaller time step than 0.1 Myr would be very expensive in computing time and output data storage, but on the other hand, for a time step larger than 0.1 Myr, short evolutionary phases can be missed. We use Padova Evolutionary Tracks, corresponding to a selection of the 1992 - 1994 Padova tracks with thermally pulsing asymptotic giant branch (AGB) stars added (Fagotto et al., 1994). Our *Shell Dynamics* code takes the FUV flux from the *Starburst99* simulation output and sums the flux for wavelengths between 912 Å and 2055 Å in the stellar population spectrum to obtain a total FUV flux for each time step. The *Shell Dynamics* code then calculates the FUV field strength G_0 incident on the inner surface of the shell (i.e. $A_V = 0$) by dividing the total FUV flux by the surface area of $4\pi R_s^2(t)$ of the expanding shell/GMC. We also use this code to compute the average stellar luminosity and mechanical power (stellar wind or supernova explosion) for each phase, which is needed for our shell dynamic calculations.

3.6 Summary of Model Parameters and Variables

Table 3.6 summarizes the parameters and variables used in our simulations. Fig. 3.2 illustrates several key computational modules, i.e. *Shell Dynamics*, *Starburst99*, *UCL_PDR*, *SMMOL*, which comprises our evolving starburst model. Other modules included in the *Shell Dynamics* package are for calculating the GMC mass function, and converting the CO luminosity to H₂ mass. The physical data describing the object to model and molecular data are used as input parameters for the *SMMOL* code to compute total line intensity or flux for various molecular and atomic species. Fig. 3.3 illustrates a detailed flow diagram of the input parameters involved in the time-dependent *UCL_PDR* simulations.

Table 3.6. Model parameters and variables

Models	Description
Independent Variable:	time or starburst age t
Dependent Variables:	shell radius R_s , expansion velocity V_s , number density n_s , and thickness d_s gas (kinetic) temperature T_{gas} , dust (thermal) temperature T_{dust} chemical abundances of different molecules and atoms in the shell number densities of collisional partners H, e^- , H^+ , p- H_2 , o- H_2 , and He
Fixed Parameters:	GMC mass M_{GMC} : $3.16 \times 10^3 - 10^7 M_\odot$ stellar mass m_* : 0.1 - 120 M_\odot SFE $\eta = 0.25$ for <i>Winds</i> , $\eta = 1.0$ for <i>post-SN</i> metallicity $Z = 1.0 Z_\odot$ gas-to-dust ratio = 100 ambient ISM density of each shell n_{ism} (parent GMC at <i>Winds</i> , 30 cm^{-3} at <i>post-SN</i>) microturbulent velocity $\delta v_D = 1.5 \text{ km s}^{-1}$
Fitting Parameters:	total gas mass of the ensemble M_{total} , burst age t
Outputs:	line profiles for each transition in each molecules and atoms integrated line intensity or flux

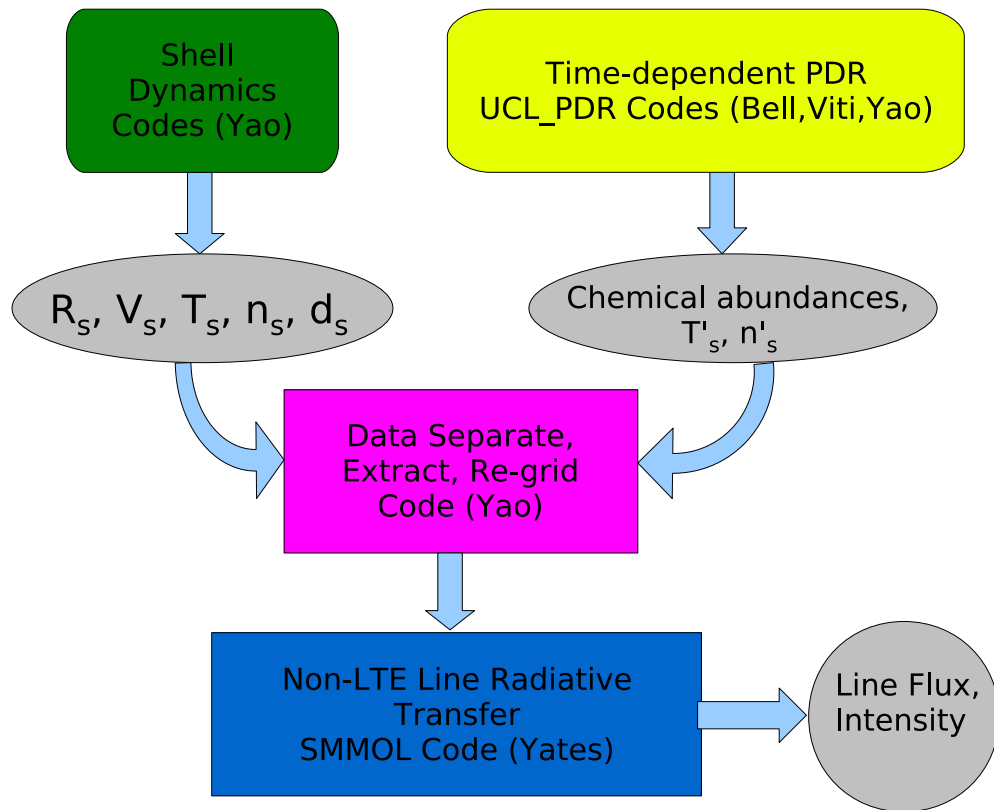


Figure 3.2 A flow diagram of key computational modules used in our modeling.

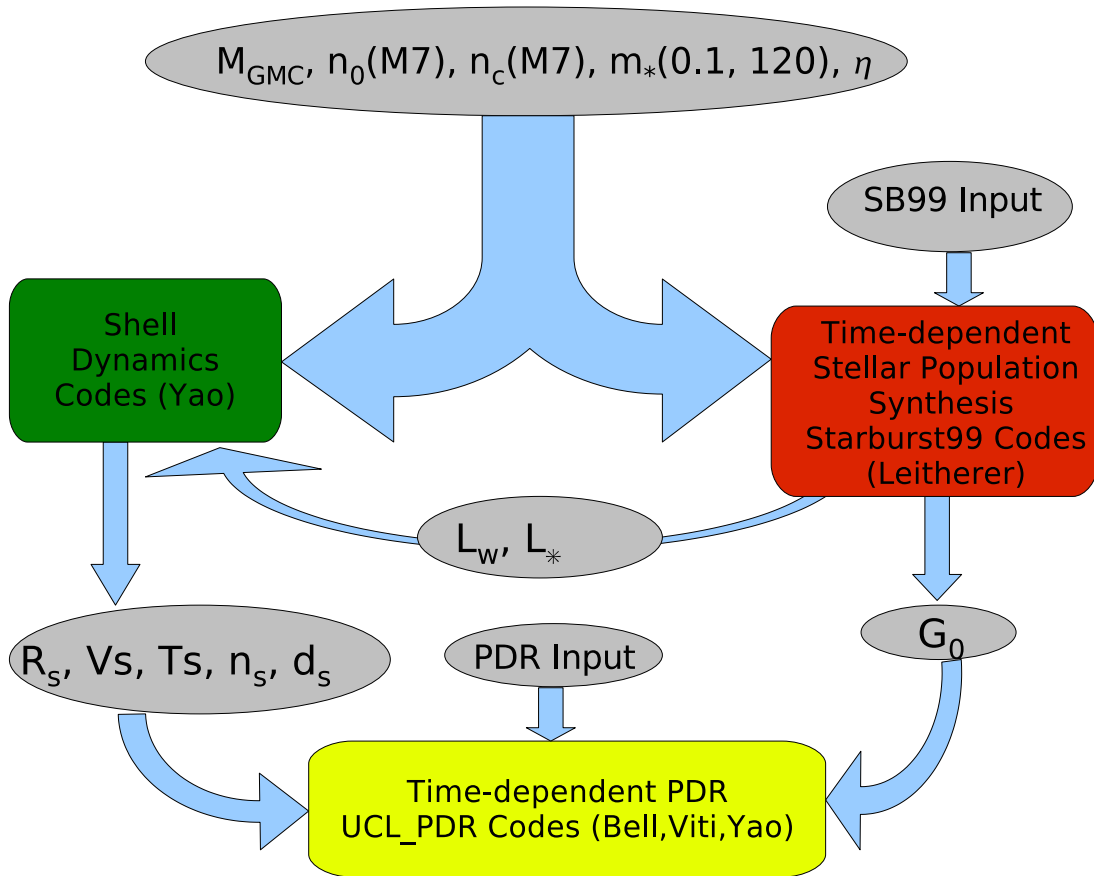


Figure 3.3 A flow diagram of the input parameters and methods involved in our time-dependent UCL_PDR simulations.

Chapter 4

Model Results

In this chapter, we present the results of simulations for individual expanding shells centrally illuminated by massive star clusters produced from an ensemble of GMCs described in the previous chapter. These shells are modeled in a similar way for both *Winds* and *post-SN* phases as described in previous chapters. A family of these evolving shells form the basis of our starburst models in accordance with our description in Chapter 3. Applications of the shell ensemble to M 82 and more distant starburst galaxies will be presented in subsequent chapters.

The two modeling phases are indicated by *Winds* and *post-SN* labels in tables and plots throughout the remainder of this thesis.

4.1 Kinematics of The Swept-up Gas

The strong stellar winds and supernova explosions from hundreds to thousands of the massive stars fuel the hot bubbles over a timescale > 10 Myr. The kinetic energy in the supersonic wind is thermalized by a stand-off shock, and the high pressure downstream drives a strong shock into the ambient ISM. The swept-up gas condenses into a narrow shell as a result of radiative cooling. The wind mechanical luminosity E_{mech} comes mainly from Wolf-Rayet (WR) stars, with some contribution from O stars. All other

stars produce a negligible effect since wind power of cool stars is lower by two orders of magnitude.

Table 4.1 summarizes coarse-grid simulations of shell radius, expansion velocity, mass of swept-up gas, shell kinetic energy, and the mechanical energy contributed by stellar winds and supernova explosions in each star cluster as the starburst evolves. A fine-grid version of these simulations is available through the online materials¹. During the *Winds* phase, the sizes of the initial Strömgren spheres in our model ensemble increase slowly with time. The Strömgren radius ranges from 0.02 to 4.9 pc with the number of Lyman continuum photons between 1.5×10^{49} and $5 \times 10^{52} \text{ s}^{-1}$ generated from the central star clusters derived from Equation (2.3) and (2.4). The wind bubble catches up with the ionization front of the compressed shell in a time less than 10^5 yr. The strong stellar winds cause the bubbles to expand quickly into their parent clouds and to sweep up more gas into the shells. When the most massive star in the most massive star cluster (i.e. $120 M_{\odot}$ star in the M7 cloud) terminates as a supernova at ~ 0.8 Myr (Mac Low & McCray, 1988), this marks the beginning of *post-SN* phase. At this time, the largest thin shell (M7) caused by the stellar winds is expanding at a speed of $\sim 50 \text{ km s}^{-1}$, and all the shells have swept up the material in their parent clouds. The *Winds* phase ends earlier (< 0.8 Myr) for shells smaller than that for the M7 cloud. After 0.8 Myr, the shells begin to expand into a less dense uniform ambient ISM (i.e. 30 cm^{-3}). The mechanical energy produced by the first supernova and the subsequent ones re-energizes the shell formed in the *Winds* phase.

The hot bubbles begin to cool at ~ 0.7 Myr for the 3M3 shell and ~ 7.5 Myr for the M7 shell. At this time, the radius and velocity of the M7 shell are about 270 pc and 24 km s^{-1} , respectively. After this time, the superbubbles start to lose their internal pressure, and the shell expansion velocity decreases rapidly. When the shell velocity approaches the sound speed of the ambient ISM, the shells should stall and become thicker and less

¹<http://www.astro.utoronto.ca/~yao/phdthesis/OnlineMaterials>

dense. The latter effect is not included in our model, since the external pressure of the ISM is ignored. It is clear that the lifetime of the progenitor GMCs may be short, but the birth of massive star clusters and their impact on the surrounding ISM is profound.

In addition, we calculate the total amount of swept-up gas M_{model} following the evolution of the shells, as shown in Fig. 4.1. The discontinuity seen at 1 Myr is caused by the phase change (*Winds* to *post-SN*), in which the parent GMC mass contained in the shell is no longer taken into account after the shell sweeps up all material in its parent GMC. This mass will be used as a template or reference value to be scaled to the total H₂ gas mass in a measured region of M 82 using a χ^2 analysis for our model line SEDs, under the assumption that the line flux in the measured region is proportional to the total molecular gas mass (see Chapter 5 for details).

Table 4.1. Modeling kinematics of expanding shells.

GMC (N_{GMC}) ^a	t ^b (Myr)	R_{sh} ^c (pc)	V_{sh} ^d (km s ⁻¹)	$M(\text{H}_2)$ ^e (M_{\odot})	$\log_{10} E_{kin}$ ^f (ergs)	$\log_{10} E_{mech}$ ^g (ergs)
M7 (1.0)	Winds					
	0	4.9	11.5	7.5E6	48.9	51.6
	0.01	5.0	11.3	7.5E6	49.0	51.6
	0.1	14.6	87.2	7.5E6	52.1	52.7
	0.3	28.2	56.2	7.5E6	52.6	53.1
	post-SN					
	1	64.4	53.7	1.5E6	52.6	53.6
	3	149.8	34.6	1.9E7	53.1	54.2
	10	300.5	13.7	1.5E8	53.5	54.9
	30	422.8	10.6	4.3E8	53.7	55.2
	100	678.5	8.5	1.8E9	54.1	55.3
	3M6 (1.7)	Winds				
0		2.3	11.5	2.4E6	48.2	51.1
0.01		2.9	173.9	2.4E6	50.6	51.1
0.1		11.6	69.2	2.4E6	51.6	52.2
0.3		22.4	44.6	2.4E6	52.1	52.6
post-SN						
1		57.2	42.7	1.1E6	52.7	53.1
3		125.0	27.5	1.1E7	52.6	53.7
10		214.7	10.7	5.6E7	52.8	54.4
30		298.1	8.1	1.5E8	53.1	54.8
100		462.1	6.7	5.6E8	53.3	54.8
M6 (3.1)		Winds				
	0	1.06	11.5	7.5E5	47.4	50.6
	0.01	2.31	138.2	7.5E5	50.1	50.6
	0.1	9.19	55.0	7.5E5	51.1	51.7
	0.2	19.32	56.2	7.5E5	51.3	52.1
	post-SN					
	1	49.1	33.9	6.7E5	51.9	52.6
	3	102.9	21.8	6.2E6	52.1	53.2
	10	153.1	8.3	2.0E7	52.2	53.9
	30	209.6	6.3	5.2E7	52.3	54.2
	100	315.0	5.4	1.8E8	52.7	54.3

Table 4.1—Continued

GMC (N_{GMC}) ^a	t ^b (Myr)	R_{sh} ^c (pc)	V_{sh} ^d (km s ⁻¹)	$M(\text{H}_2)$ ^e (M_{\odot})	$\log_{10} E_{kin}$ ^f (ergs)	$\log_{10} E_{mech}$ ^g (ergs)
3M5 (5.6)			Winds			
	0	0.49	11.5	2.4E5	46.7	50.1
	0.01	1.83	109.7	2.4E5	49.1	50.1
	0.1	7.30	43.7	2.4E5	49.6	51.2
	post-SN					
	1	41.0	26.9	3.9E5	50.6	52.1
	3	79.9	10.3	2.9E6	50.8	52.7
	10	108.8	6.5	7.3E6	51.5	53.4
	30	147.2	5.1	1.8E7	51.7	53.8
	100	215.5	4.4	5.6E7	52.0	53.8
M5 (10.0)			Winds			
	0	0.23	11.5	7.5E4	45.9	49.6
	0.01	1.46	87.2	7.5E4	49.1	49.6
	post-SN					
	1	33.8	21.4	2.2E5	50.9	51.6
	3	56.7	8.0	1.0E6	50.8	52.2
	10	77.1	5.2	2.6E6	50.8	52.9
	30	103.5	4.2	6.3E6	51.0	53.2
	100	148.2	3.7	1.9E7	51.4	53.3
3M4 (17.7)			Winds			
	0	0.11	11.5	2.4E4	45.2	49.1
	0.01	1.16	69.2	2.4E4	48.6	49.1
	post-SN					
	1	27.4	17.0	1.2E5	50.5	51.1
	3	40.2	6.2	3.7E5	50.1	51.7
	10	54.5	4.2	9.1E5	50.2	52.5
	30	72.7	3.5	2.2E6	50.4	52.8
	100	102.4	3.1	6.0E6	50.8	52.8
M4 (31.6)			Winds			
	0	0.05	11.5	7.5E3	44.4	48.7
	0.01	0.92	55.0	7.5E3	48.1	48.7
	post-SN					
	1	21.6	7.9	5.8E4	49.5	50.7

Table 4.1—Continued

GMC (N_{GMC}) ^a	t ^b (Myr)	R_{sh} ^c (pc)	V_{sh} ^d (km s ⁻¹)	$M(\text{H}_2)$ ^e (M_{\odot})	$\log_{10} E_{kin}$ ^f (ergs)	$\log_{10} E_{mech}$ ^g (ergs)
	3	28.5	4.8	1.3E5	49.5	51.3
	10	38.6	3.4	3.3E5	49.6	52.0
	30	51.2	2.9	7.7E5	49.8	52.3
	100	71.2	2.7	2.1E6	50.2	52.4
3M3 (56.2)			Winds			
	0	0.02	11.5	2.4E3	43.7	48.2
	0.01	0.73	43.7	2.4E3	47.6	48.2
			post-SN			
	1	14.6	6.0	1.7E4	48.7	50.2
	3	19.2	3.9	4.0E4	48.7	50.8
	10	26.0	3.0	9.9E4	48.8	51.5
	30	34.4	2.6	2.3E5	49.1	51.8
	100	47.3	2.5	6.0E5	49.4	51.9
Shell Ensemble			Winds			
	0	1.69E7
	0.01	1.69E7
	0.1	1.69E7
	0.3	1.73E7
			post-SN			
	1	1.49E7
	3	9.72E7
	10	4.11E8
	30	1.09E9
	100	4.0E9

^aGMC name (number of GMCs or shells in the ensemble).

^bAge.

^cShell radius.

^dShell expansion velocity.

^eMolecular H₂ mass (shell + GMC for *Winds* phase, shell only for *post-SN* phase).

^fShell kinetic energy.

^gMechanical energy for each SC in the ensemble.

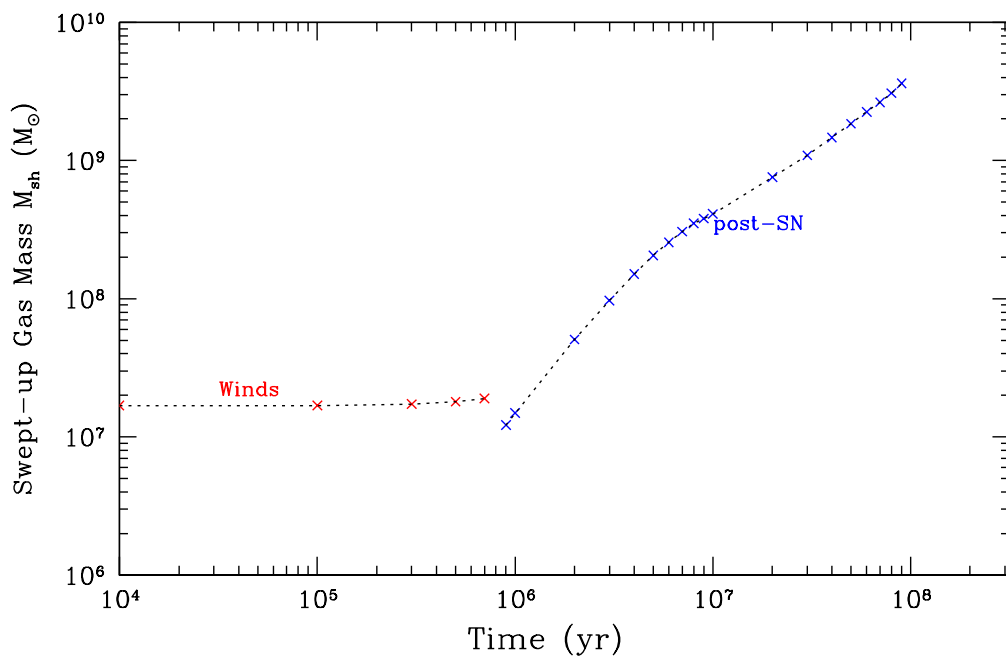


Figure 4.1 Plot of the total molecular gas mass swept-up by the shells ensemble as a function of time.

4.2 Thermal Properties and Chemistry of the PDRs

Over the 100 Myr of shell evolution the total mechanical wind power of individual shells, calculated using *Starburst99* code, varies from 10^{37} - 10^{40} erg s⁻¹, as shown in Fig. 4.2. In this study, the mechanical power profile is used only for obtaining average values over each phase in order to compute the shell dynamics. The kinetic energy of the shells is between 10^{43} ergs and 10^{54} ergs, depending on cluster mass. Fig. 4.3 shows the FUV radiation strength G_0 ($\propto R_s^{-2}$), also calculated using *Starburst99*, incident on the inner surface of the shells ($A_V = 0$) as a function of time. The G_0 value is in units of the Habing field (1.6×10^{-3} ergs cm⁻² s⁻¹) throughout this study. This value decreases from about 10^6 - 10^8 (depending on cluster mass) at the onset of massive star formation (i.e. $t = 0$ yr) to between 10^2 and 10^5 respectively at 5 Myr when most of the massive stars ($M_* > 30 M_\odot$) reach the end of their lifetime. At $t = 100$ Myr, the G_0 values drop by 4 - 5 orders of magnitude.

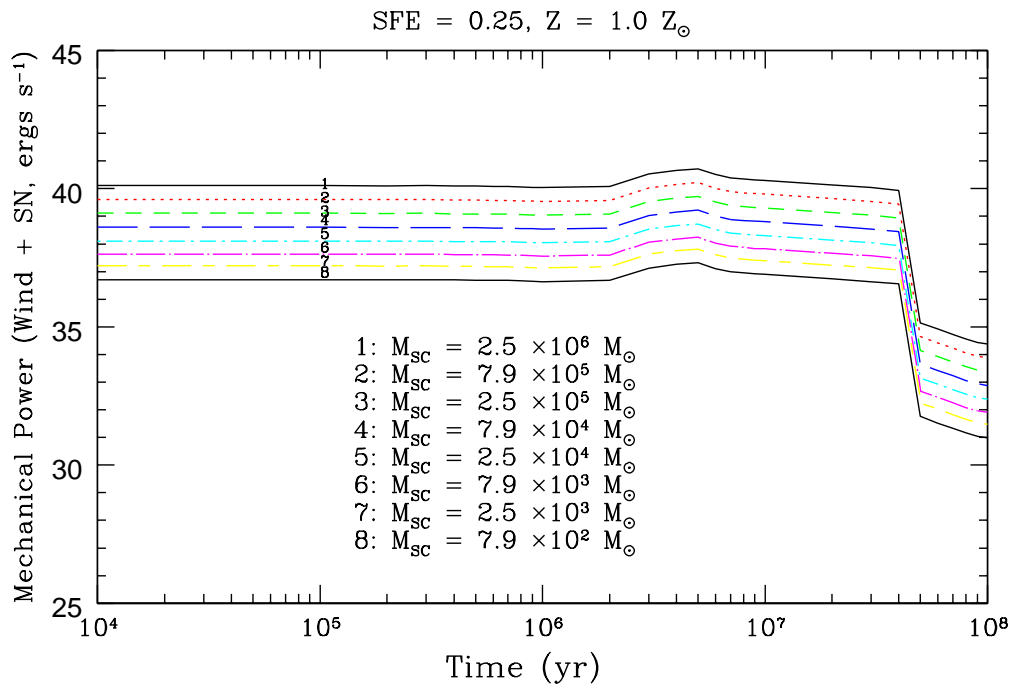


Figure 4.2 Plot of stellar wind plus SN mechanical power as a function of time generated by each star cluster.

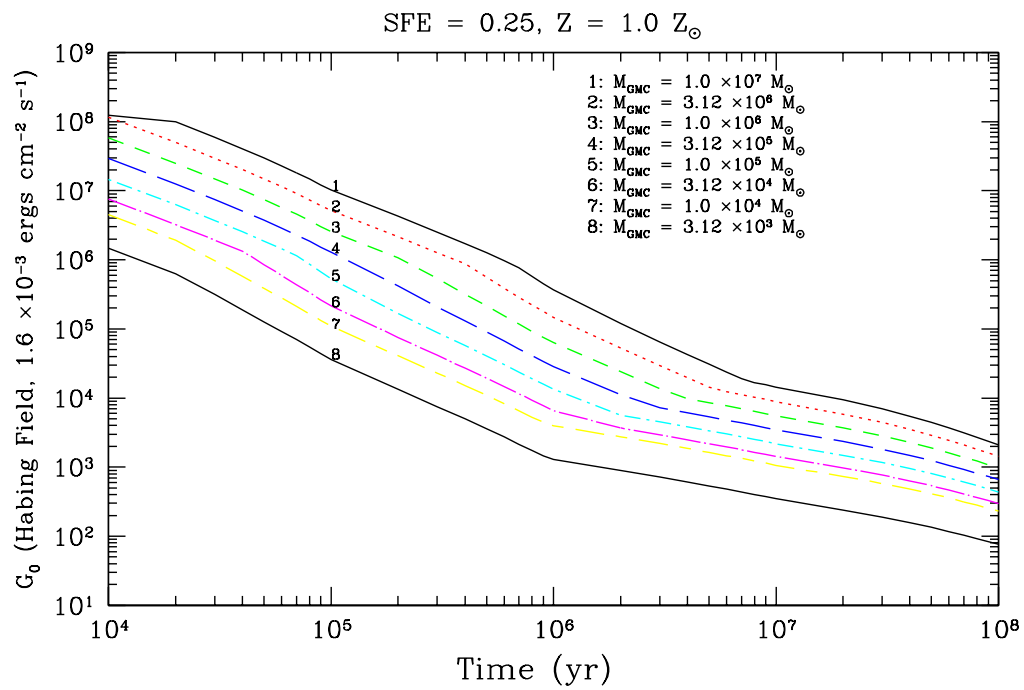


Figure 4.3 Plot of the FUV radiation field strength G_0 incident on the inner surface of each shell ($A_V = 0$) in the ensemble as a function of time.

4.2.1 Density and Temperature

The shell density, thickness, and temperature are calculated for both *Winds* and *post-SN* phases, as shown in Fig. 4.5. The density value varies from 10^2 to 10^6 cm^{-3} and the thickness is between 10^{-3} and ~ 10 pc over a 100 Myr period, depending on cluster mass. The *plateaus* seen at the beginning of the *Winds* phase are due to small changes in the expansion velocity and shell temperature. Before the shell sweeps up all of the material in its parent cloud ($t < 0.8$ Myr), the shell density declines with increasing shell radius and decreasing shell velocity, and the shell thickness increases with time. The dense phase of the shells ($10^4 - 10^6$ cm^{-3}) is very short lived (between $10^4 - 10^6$ yr). After the first supernova occurs (i.e. *post-SN* phase), the bubble continues expanding adiabatically into a lower density ambient ISM until a time t_c (indicated in the plots), when this hot interior begins to cool and the shell enters the *snow-plow* phase while conserving its total momentum. The shell velocity then decreases rapidly with a corresponding decrease in shell density, to about three orders of magnitude lower than that at the *adiabatic* phase. Such large variation in the shell density is due to the range of dynamical pressure produced by the range in the shell expansion speed. The shell thickness increases from 0.1 pc at the beginning of the *post-SN* phase to 10 pc at 100 Myr. Similarly, the thickness covers a large range because in the early phases, the shells are highly compressed and contain very little mass, so they are thin compared to later phases where these conditions are reversed.

In the plots, the first big jump occurs when the wind shock front catches up with the ionization front, and the expansion changes from H II to wind driven. For smaller GMCs, this transition takes place in less than 10^3 yr. The discontinuity (or gap) between *Winds* and *post-SN* phases is due to the model change from *Winds* to *post-SN* phase where the parent GMC mass contained in the shell is not taken into account in the *post-SN* phase. A smaller jump is also seen when radiative cooling inside the bubble becomes dominant, the shell switches from the *adiabatic* to the zero pressure *snow-plow* phase.

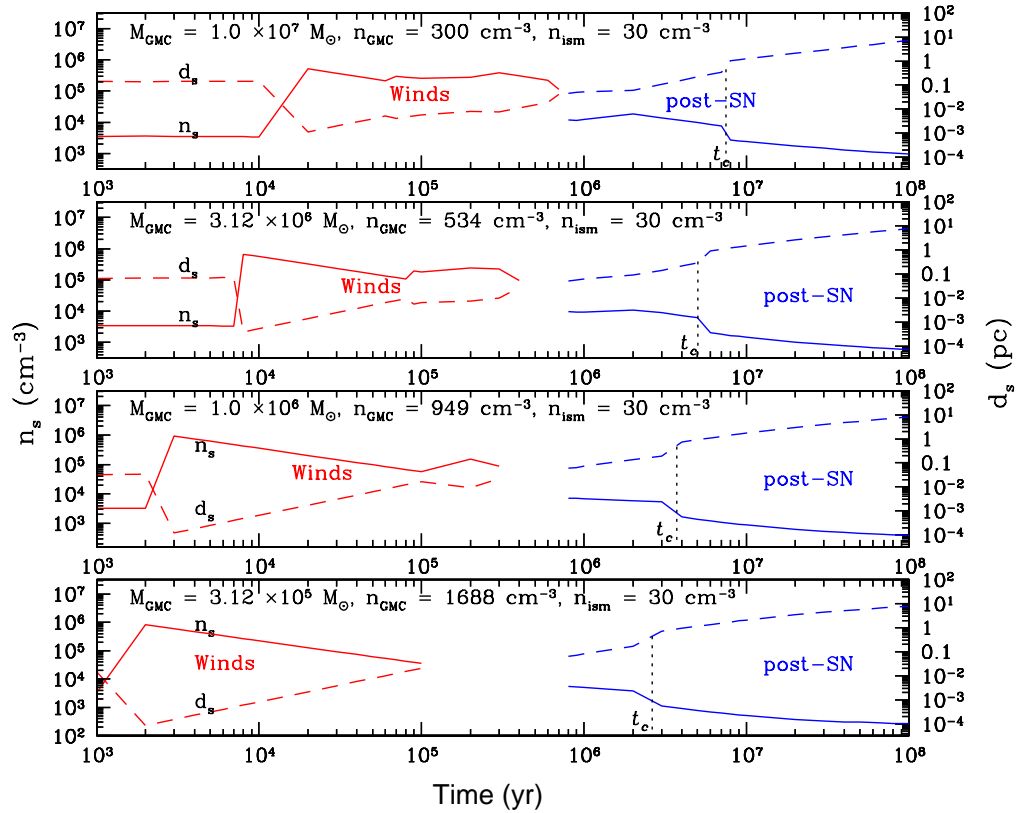


Figure 4.5 Plot of the shell density (n_s , solid line) and thickness (d_s , dashed line) as a function of time. The *Winds* phase is indicated by red curves, while the *post-SN* phase is indicated by blue curves. The radiative cooling of the hot interior occurs at t_c indicated by the dotted lines.

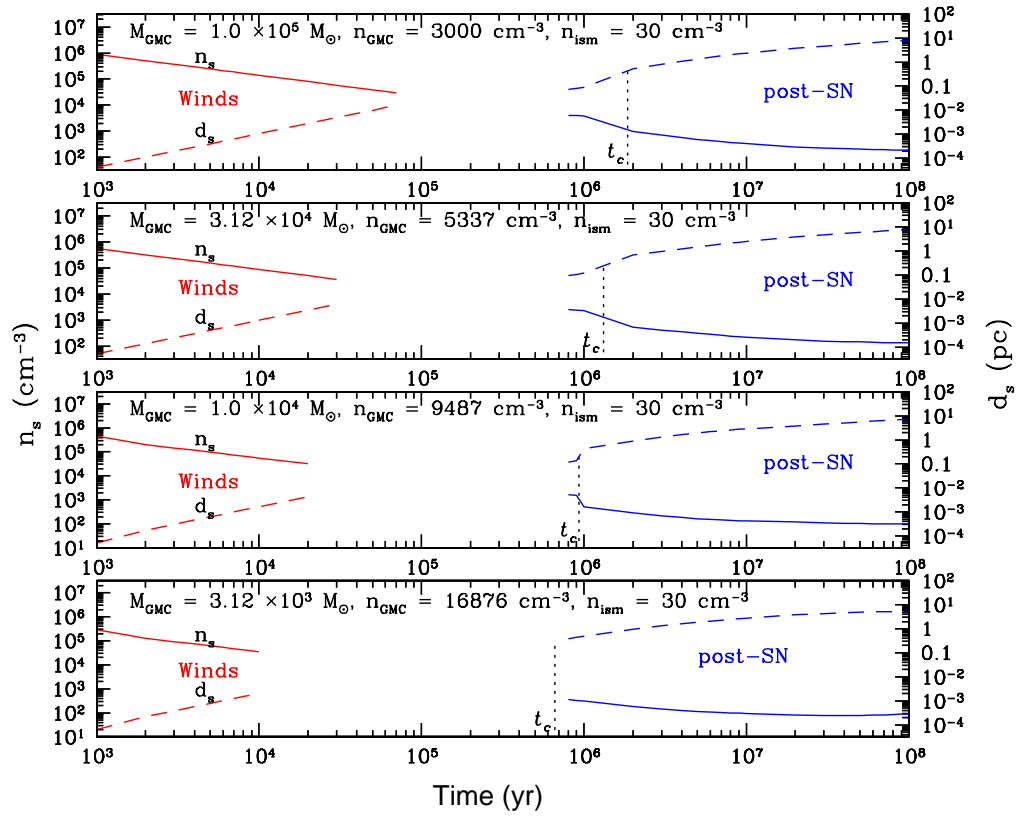


Figure 4.5 (continued)

Fig. 4.6 shows the gas and dust temperatures as a function of the visual extinction A_V for different starburst ages. The A_V is set to be 0 at the inner surface of the shell (i.e. boundary between the hot bubble and the shell), and increases toward the outer edge of the shell (i.e. boundary between the shell and its parent cloud or the ambient ISM). During the *Winds* phase, the cloud A_V progresses from the outer edge of the shell to the outer edge of the GMC (i.e. boundary between the GMC and its ambient ISM). The gas temperature has a negative gradient from the inner edges of the shells to the outer edges, because the FUV flux is attenuated owing to dust extinction resulting in decreasing photoelectric heating across the shells. The FUV field strength $G(t, A_V)$ at different A_V (or depth in the shell) is a factor of $e^{-1.38A_V}$ less than the flux at the surface of the PDR (or G_0). For example, at 1 Myr the FUV field strength at $A_V = 2$ (layer of $C^+/C/CO$ transition) is attenuated to $\sim 6\%$ of the value at the surface ($G_0 \sim 10^3 - 10^6$) for the shells in the ensemble. The gas temperature is in the range 10 - 1000 K across the shells. It is about 1 - 2 orders of magnitude higher than the dust temperature at the surface of the PDRs. Fig. 4.7 shows an example of the temperature structure for an M7 cloud before the shell sweeps up all of its materials. The parent cloud is also heated by FUV radiation from the central star cluster. The minimum A_V for the GMC corresponds to the extinction due to the shell at the shell-cloud interface, and the maximum A_V is the extinction at the outer edge of the cloud. The gas temperature changes from 1000 K to about 10 K across the clouds. The increasing T_{gas} toward the outer edge of the cloud at age beyond 0.3 Myr is due to heating by warm dust (i.e. collision between cool gas and warm dust grains).

Although the physical properties of each giant molecular cloud and the star cluster born in its center vary greatly with cluster and cloud mass, the model profiles for the shell density, thickness and temperature are similar. This implies that different initial cloud conditions in a starburst environment may yield similar gas properties through the entire evolution. However, for individual shells, the physical properties of gas inside

the shells change drastically with time. These gas properties that contain the imprint of different evolutionary phases, also determine the molecular line radiative transfer, and hence the spectral energy distribution of line fluxes. It allows us in principle to date the burst age by modeling the line spectrum energy distribution for various molecular tracers and comparing them with the observations of a starburst galaxy.

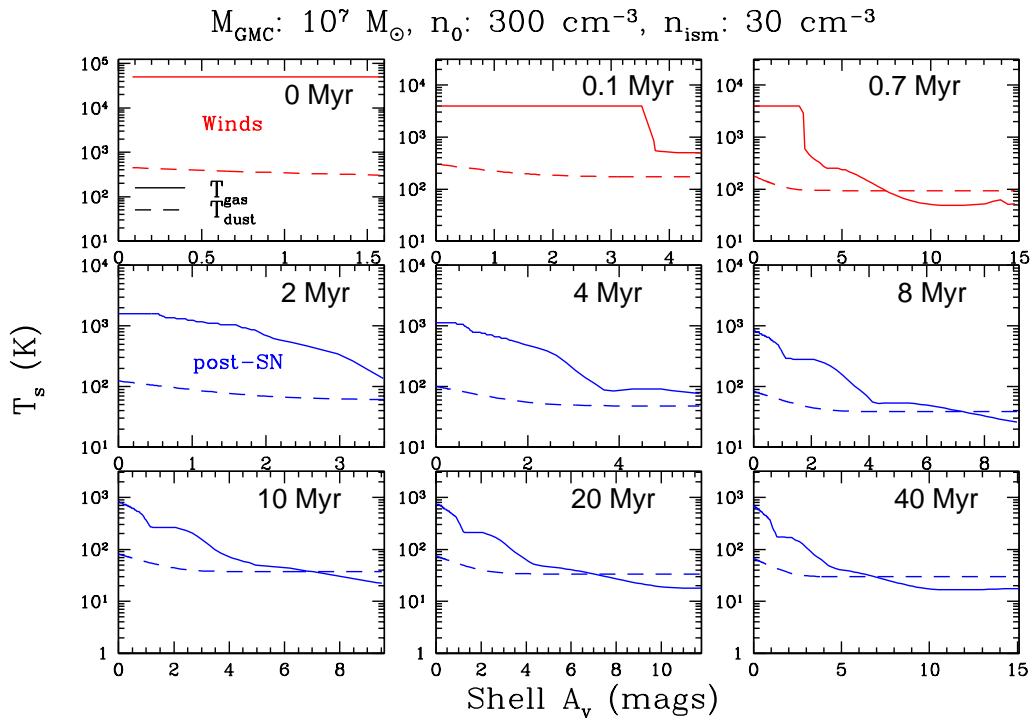


Figure 4.6 Plots of the time-dependent gas and dust temperatures as a function of visual extinction A_V for an ensemble of expanding shells. Solid lines represent gas temperature, and dashed lines indicate dust temperature. The *Winds* phase model is indicated by red curves, and the *post-SN* phase model is indicated by blue curves.

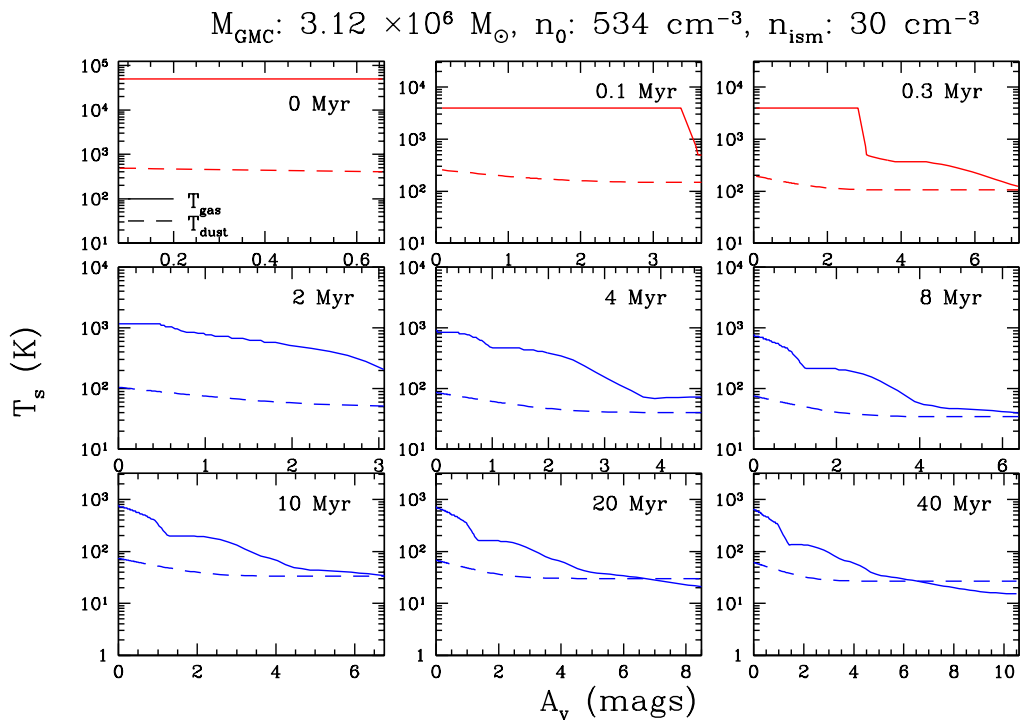


Figure 4.6 (continued)

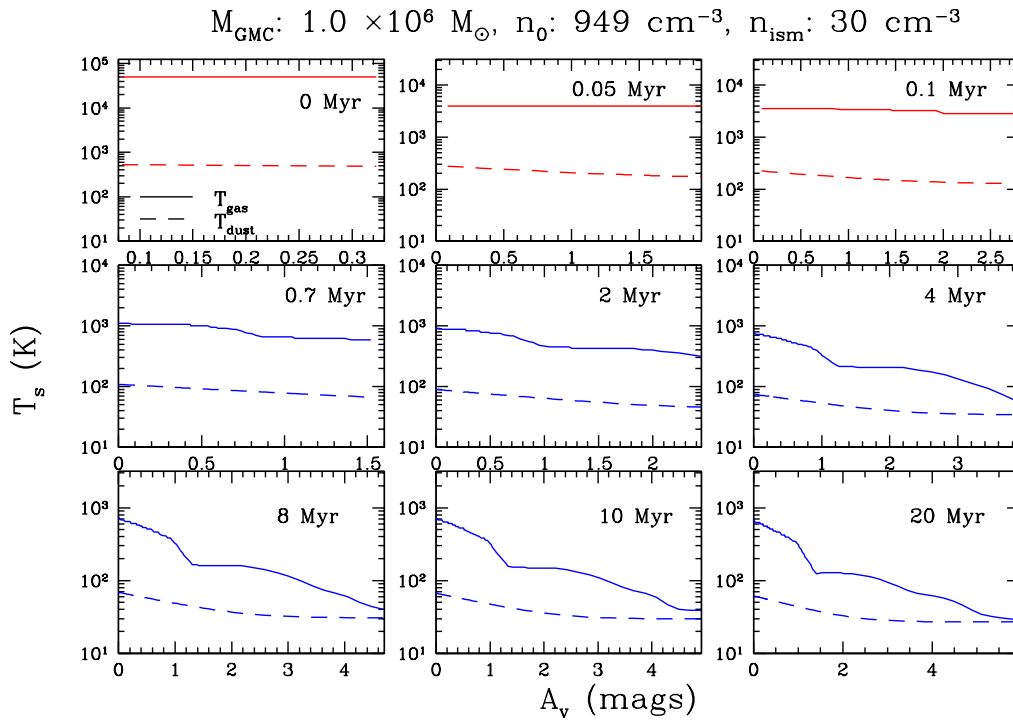


Figure 4.6 (continued)

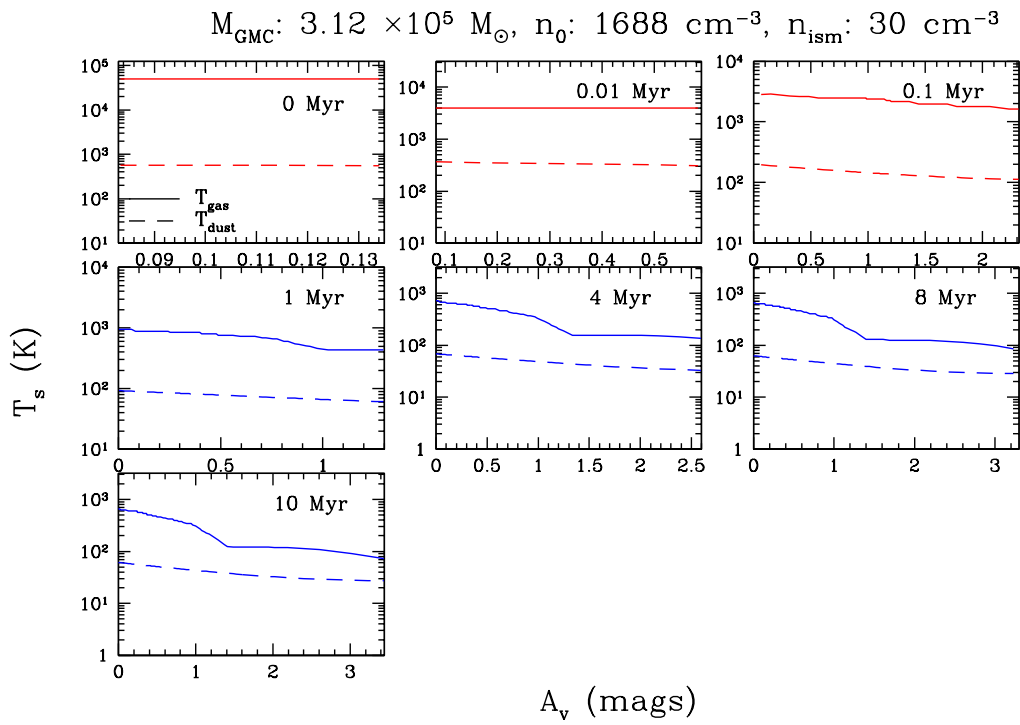


Figure 4.6 (continued)

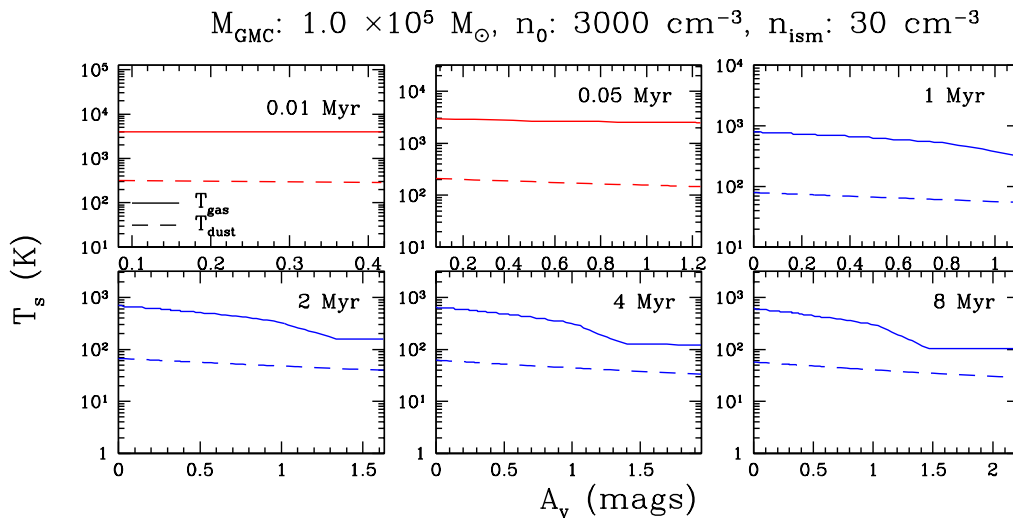


Figure 4.6 (continued)

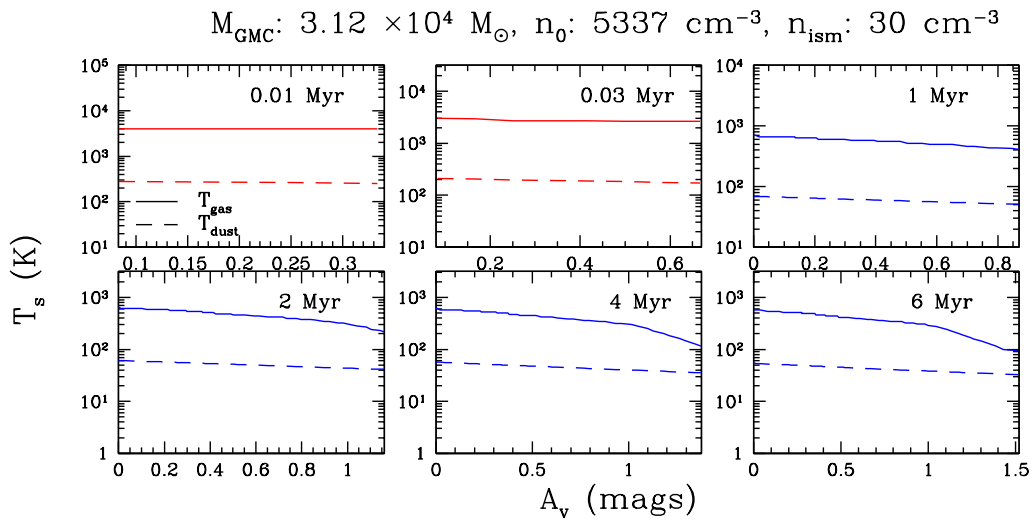


Figure 4.6 (continued)

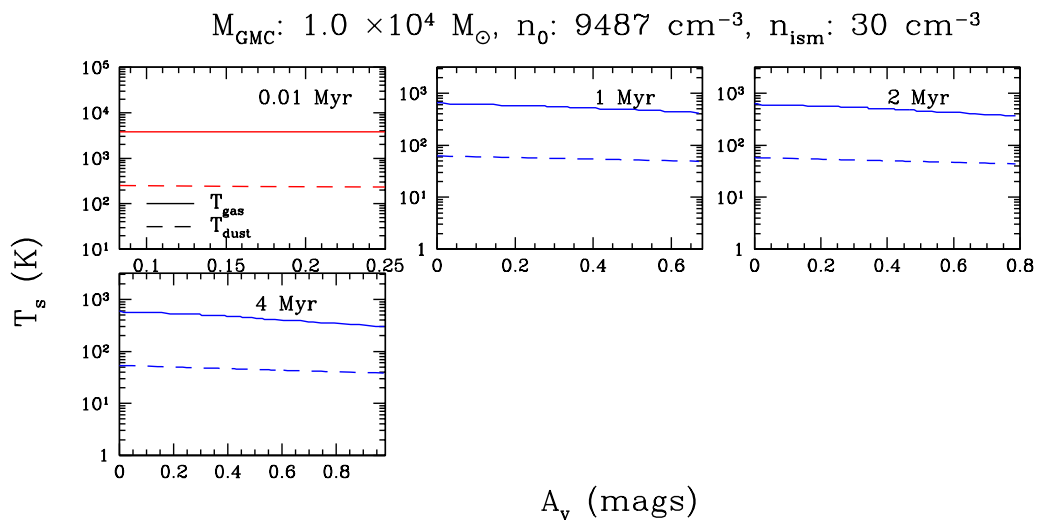


Figure 4.6 (continued)

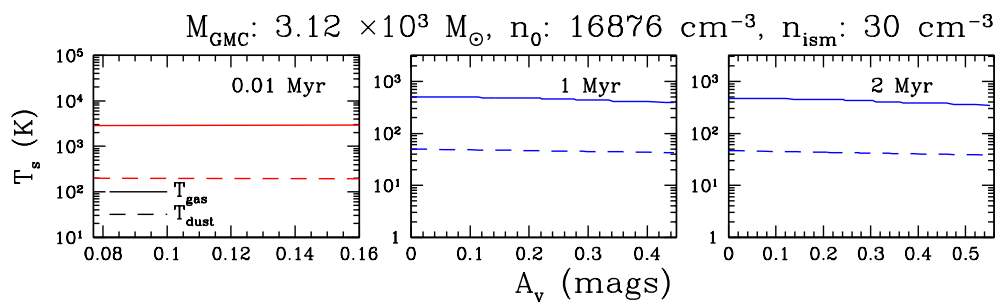


Figure 4.6 (continued)

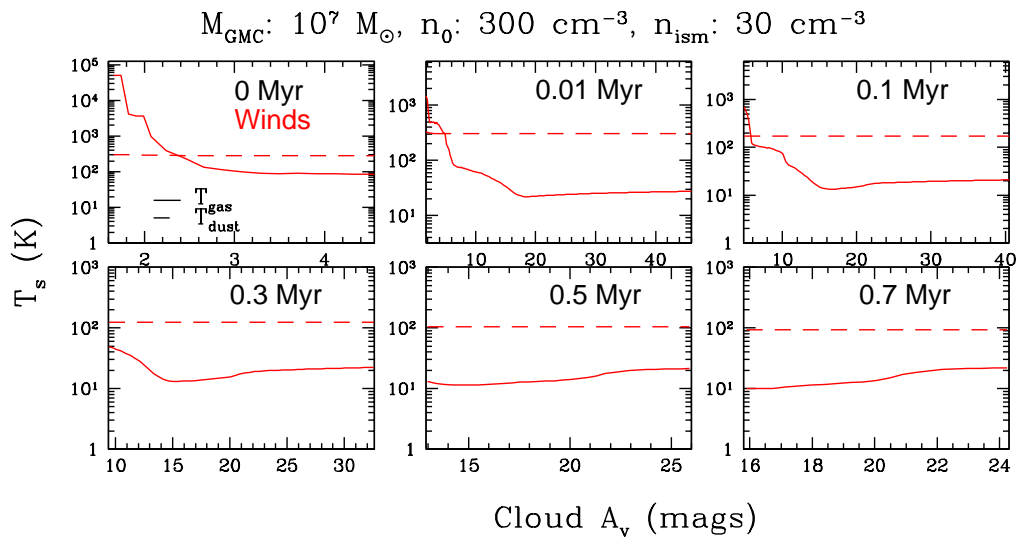


Figure 4.7 Plot of the time-dependent gas and dust temperatures in the parent GMC (M7 cloud) as a function of visual extinction A_V . Solid lines represent gas temperature, and dashed lines indicate dust temperature.

4.2.2 Chemical Evolution

The chemical structure inside the shell is stratified. The FUV photons are gradually absorbed and lead to relatively sharp transitions. In Fig. 4.8, the transitions of atomic species (H^+/H , C^+/C , O) to molecular gas (H_2 and CO) are shown. The H_2 abundance becomes much more enhanced at $A_V > 1$, and the formation of CO occurs at $A_V = 3 - 4$. Fig. 4.9 shows the abundance evolution for two dense molecular gas tracers (HCN and HCO^+) used in our models. At the surfaces of the shells, the dominant coolant is the [O I] $63 \mu\text{m}$ fine-structure line. Deeper into the shells and the clouds the cooling by [C II] $158 \mu\text{m}$, [C I] $610 \mu\text{m}$, and CO becomes dominant (not shown). The abundance of dense gas tracers (e.g. HCN , HCO^+) is very sensitive to the temperature, with the abundance increasing from 10^{-30} to 10^{-6} when T_{gas} decreases from a few $\times 10^3$ K to ~ 50 K (see M7 case in Fig. 4.8). The chemical structure inside the shells changes significantly for the first few million years. This further justifies the use of a time-dependent PDR model for our shell evolutionary models. Figs. 4.10 and 4.11 show the chemical evolution inside an M7 cloud, before the shell sweeps up all of its material. Predictions of chemical evolution of other molecular species, for examples, HNC , CS , CN , and H_2CO for our shell ensemble are available through online materials².

²<http://www.astro.utoronto.ca/~yao/phdthesis/OnlineMaterials>

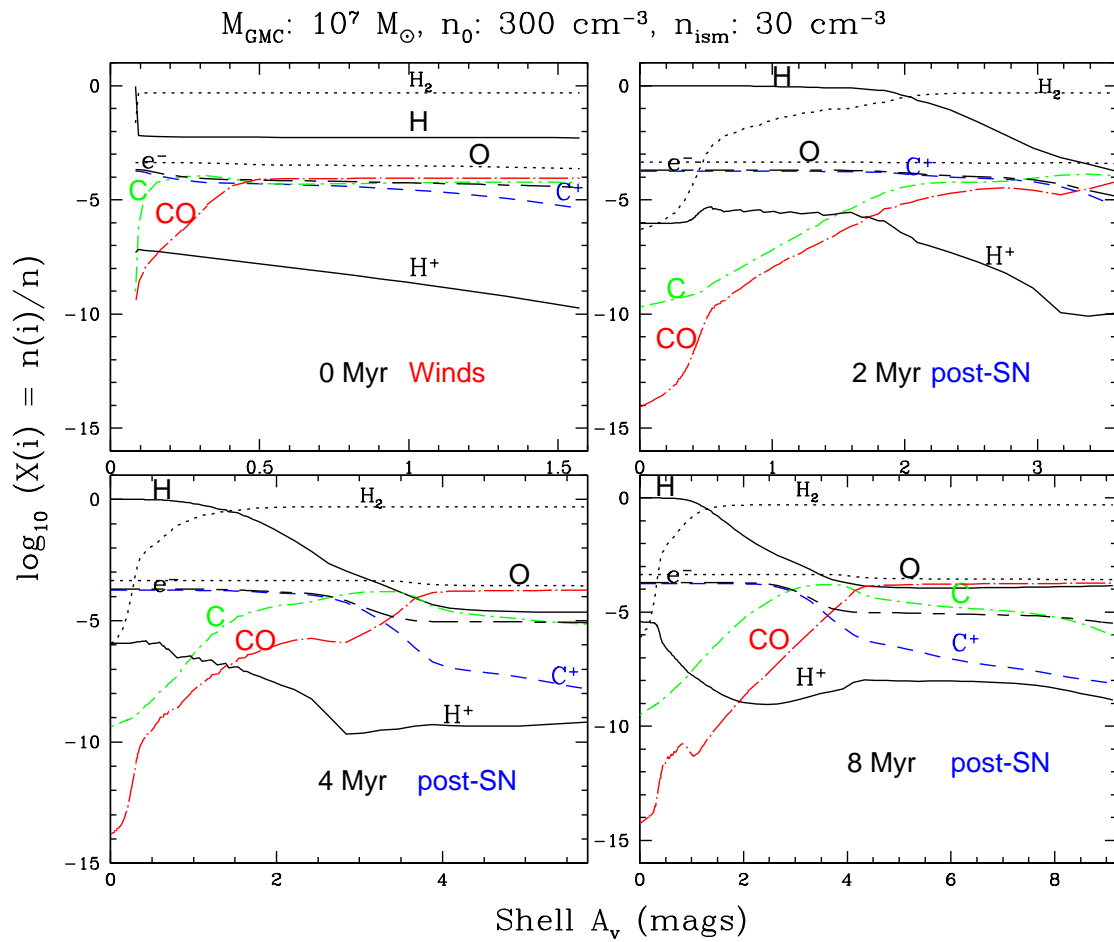


Figure 4.8 Plots of the time-dependent chemical abundances of the main species (H, H₂, H⁺, e⁻, C, C⁺, O, and CO) relative to the total hydrogen density, as a function of visual extinction A_V for an ensemble of expanding shells.

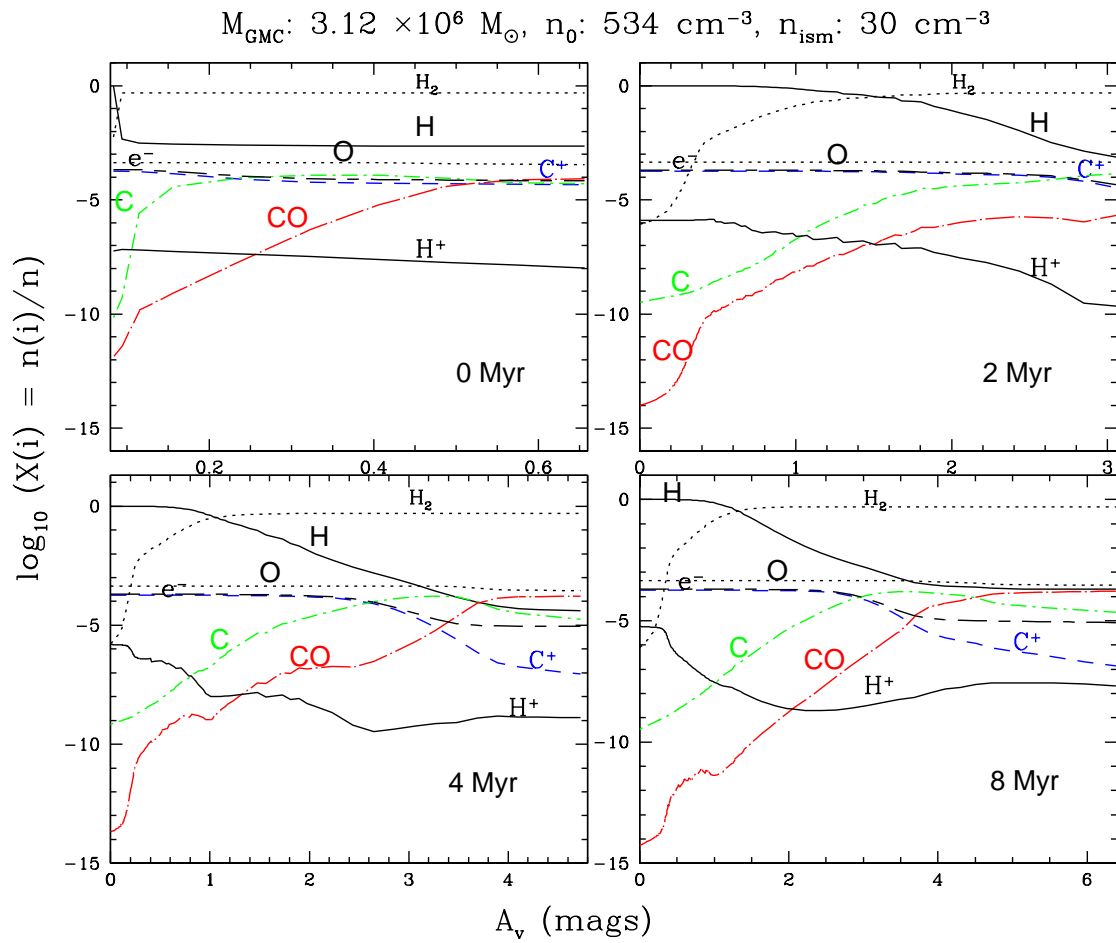


Figure 4.8 (continued)

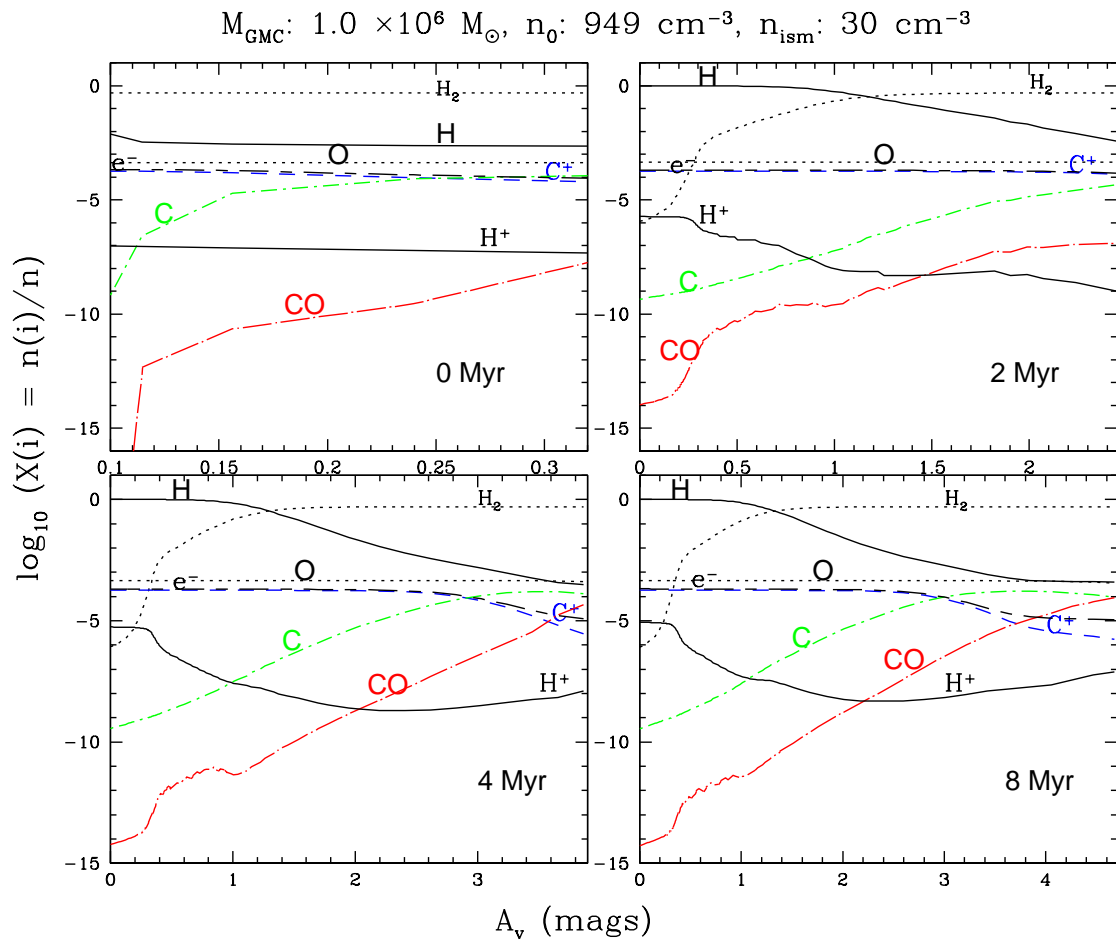


Figure 4.8 (continued)

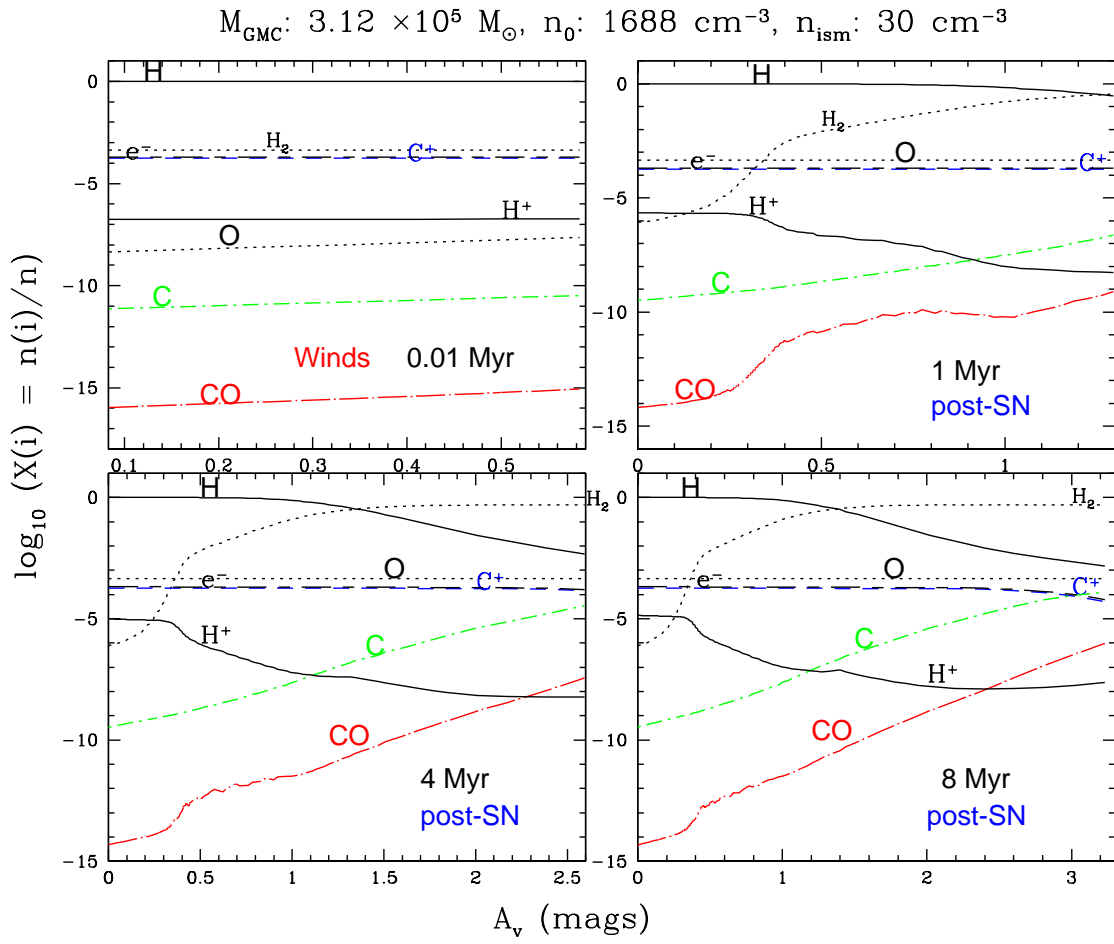


Figure 4.8 (continued)

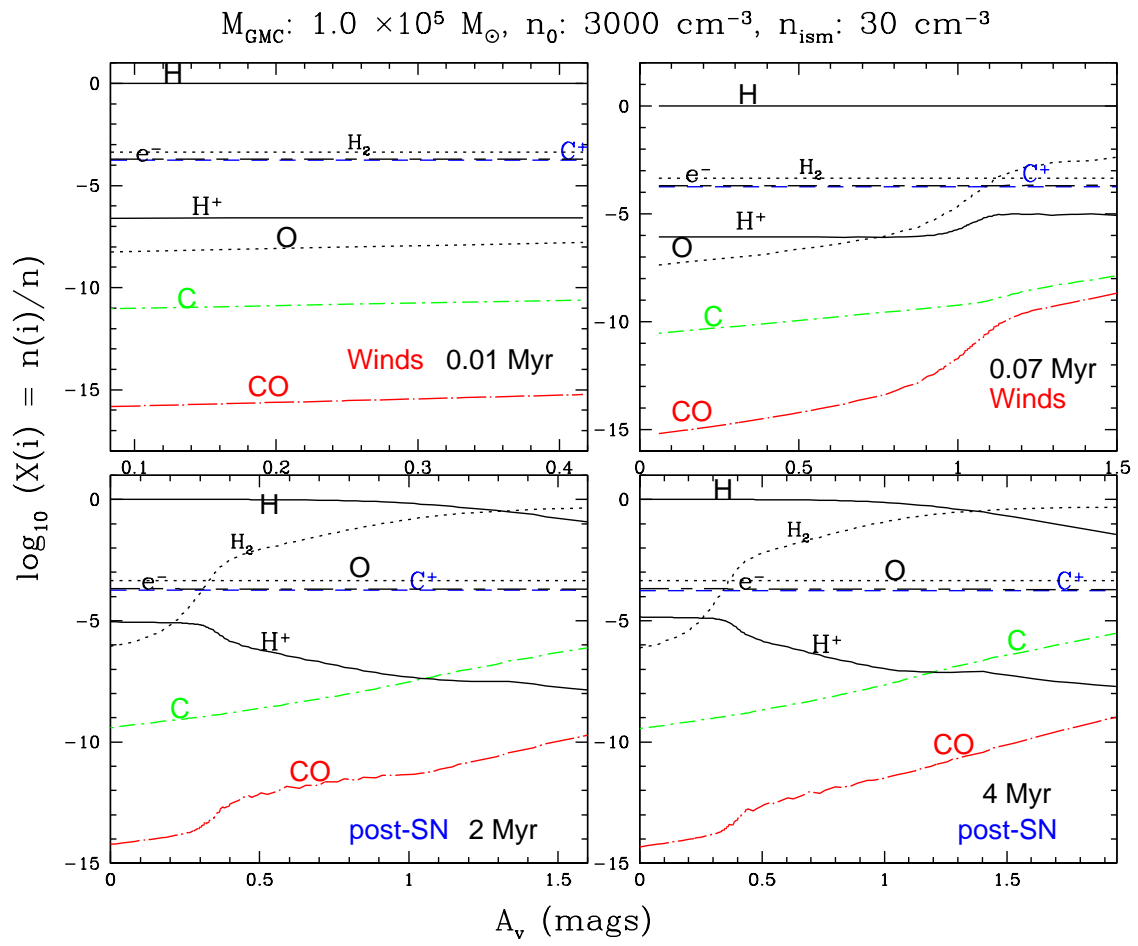


Figure 4.8 (continued)

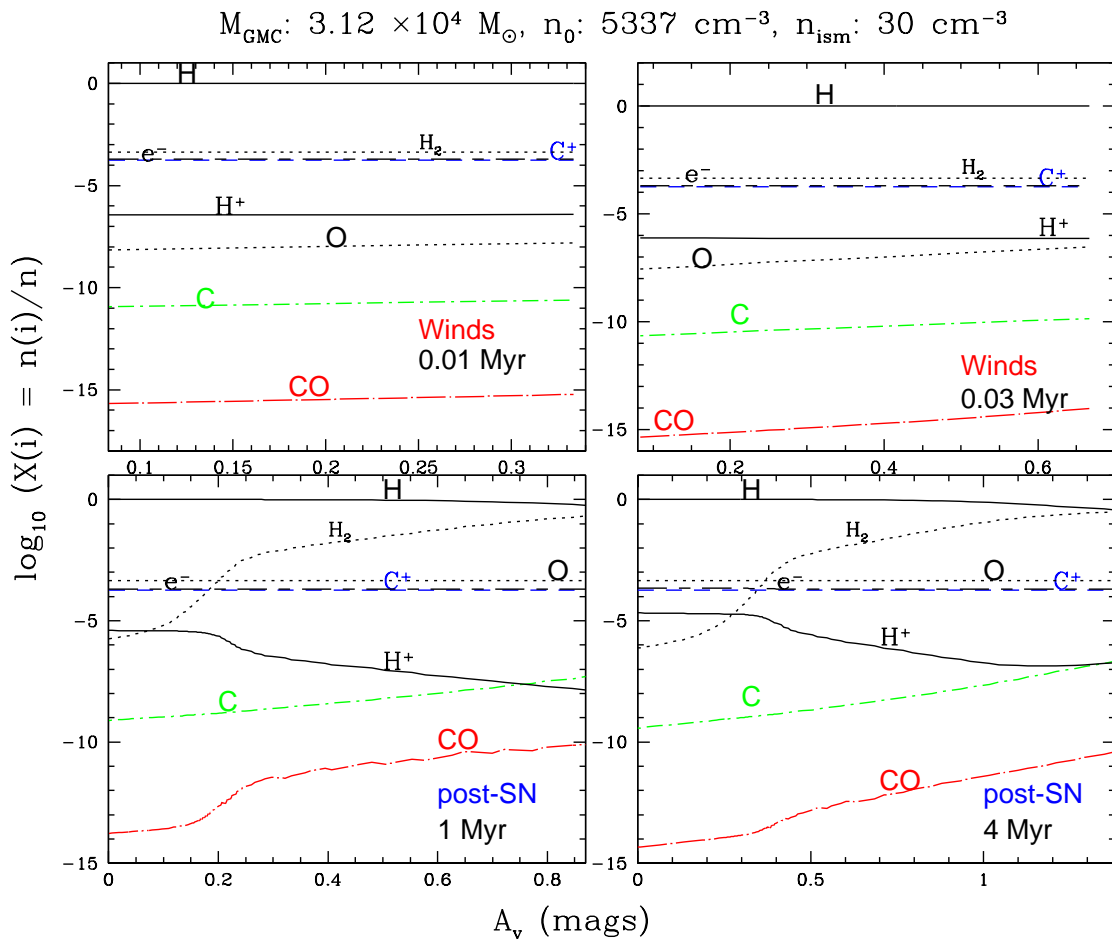


Figure 4.8 (continued)

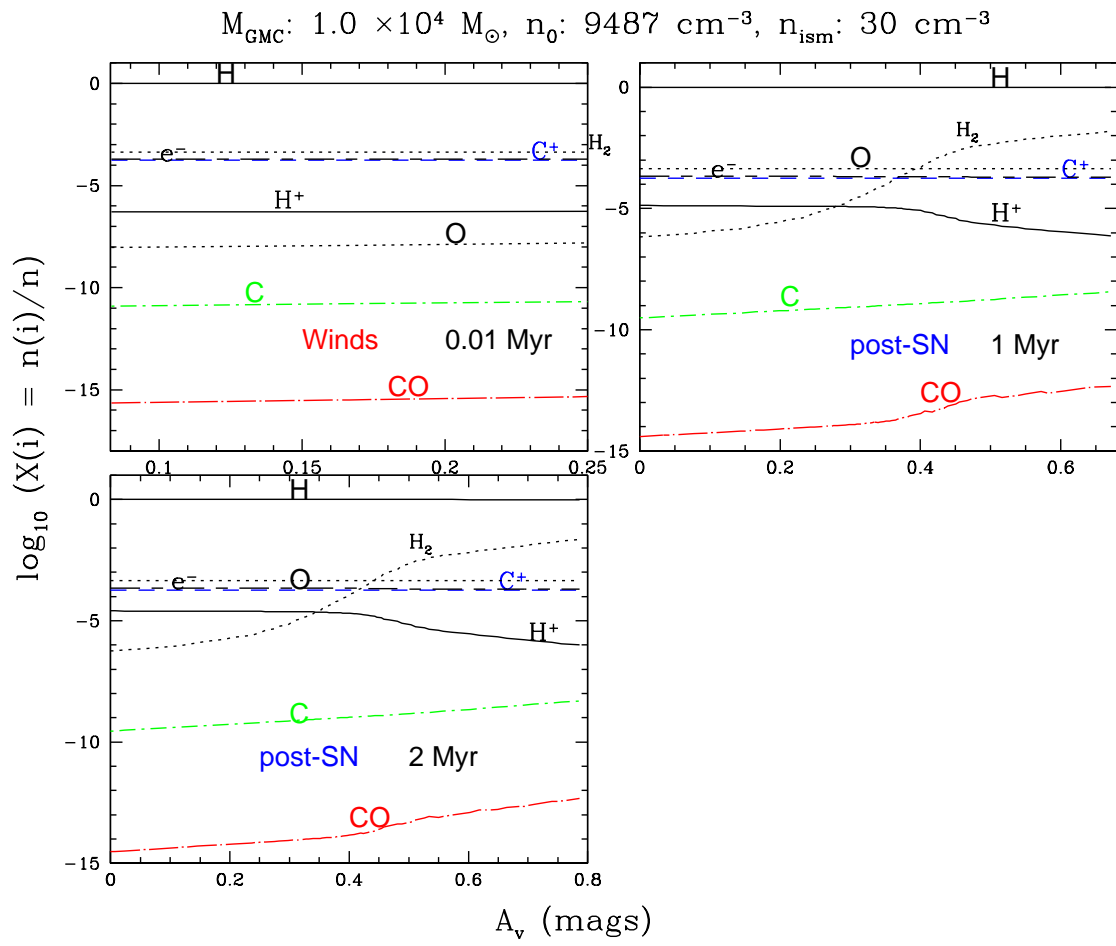


Figure 4.8 (continued)

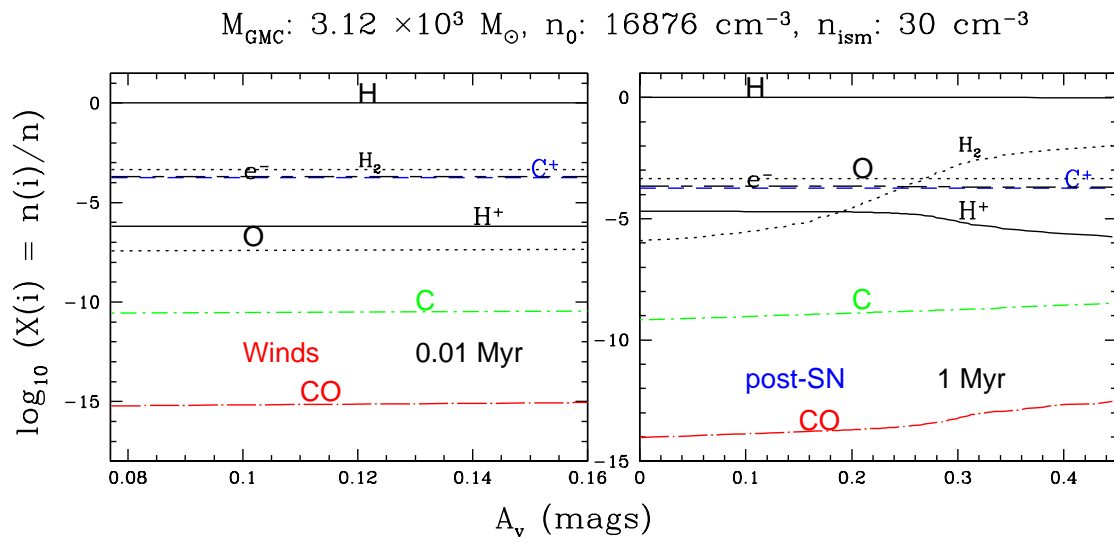


Figure 4.8 (continued)

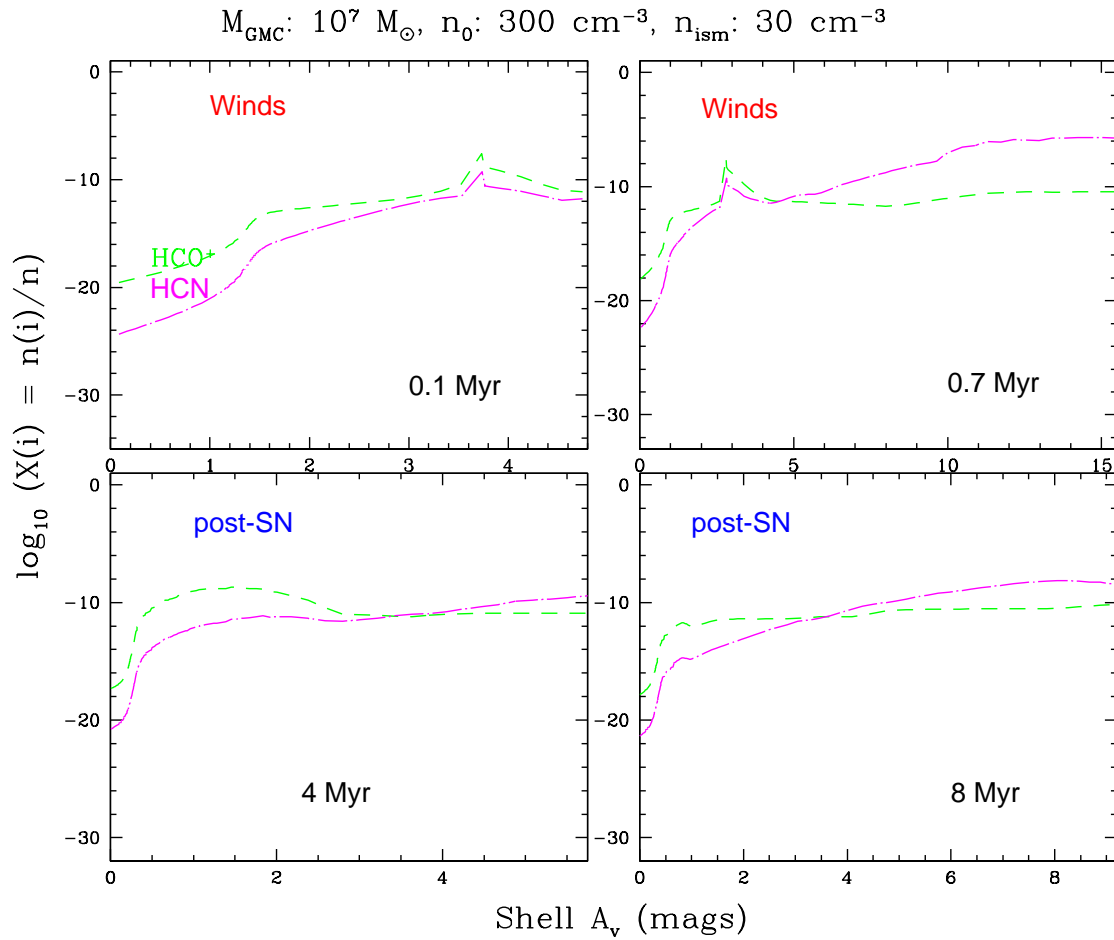


Figure 4.9 Plots of the time-dependent chemical abundances of dense gas tracers (HCN and HCO^+) relative to the total hydrogen density, as a function of visual extinction A_V for an ensemble of expanding shells.

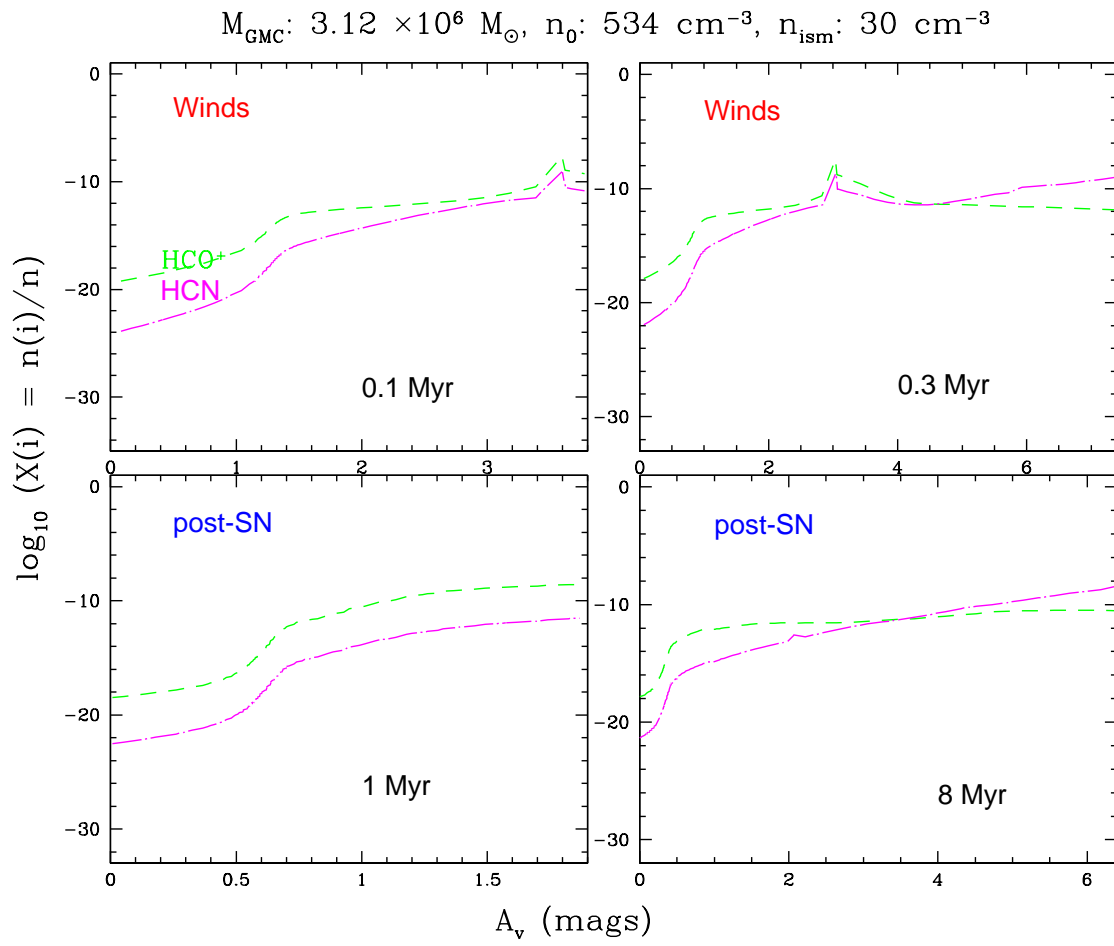


Figure 4.9 (continued)

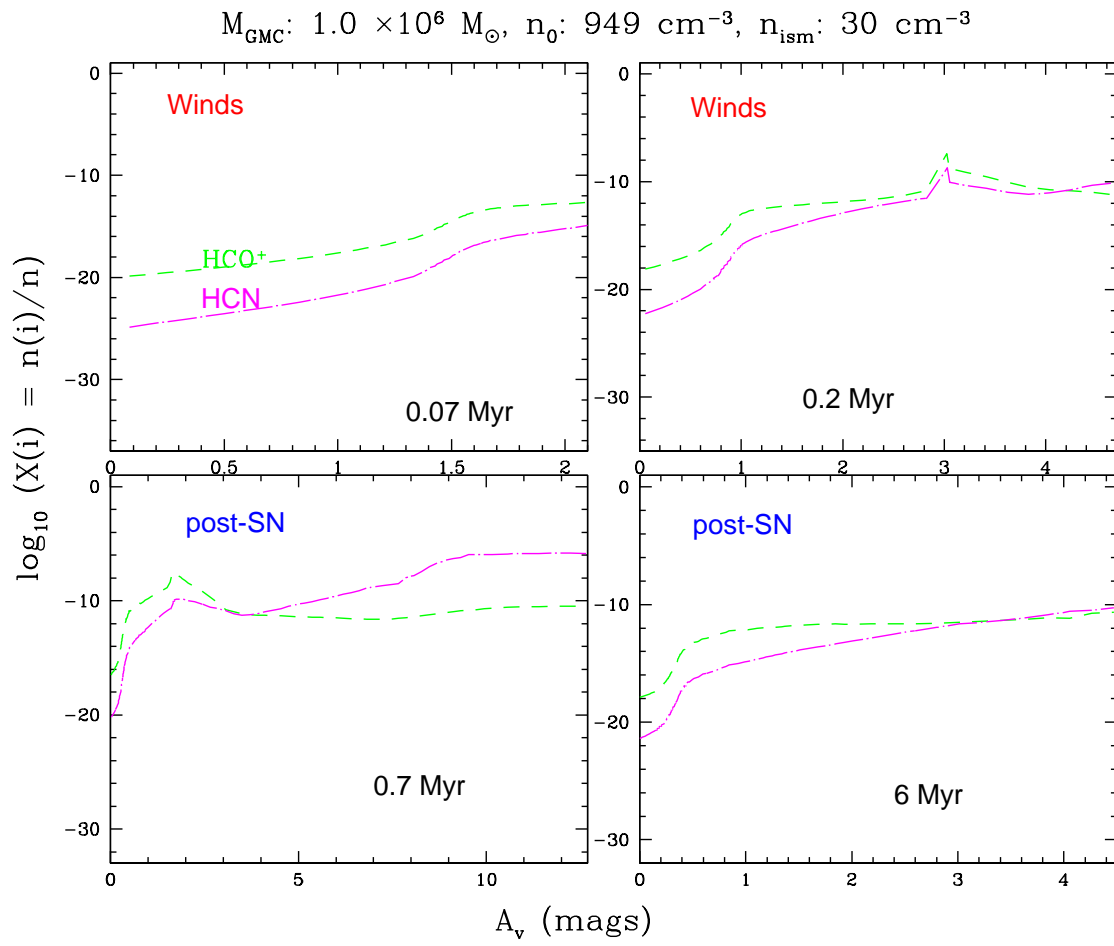


Figure 4.9 (continued)

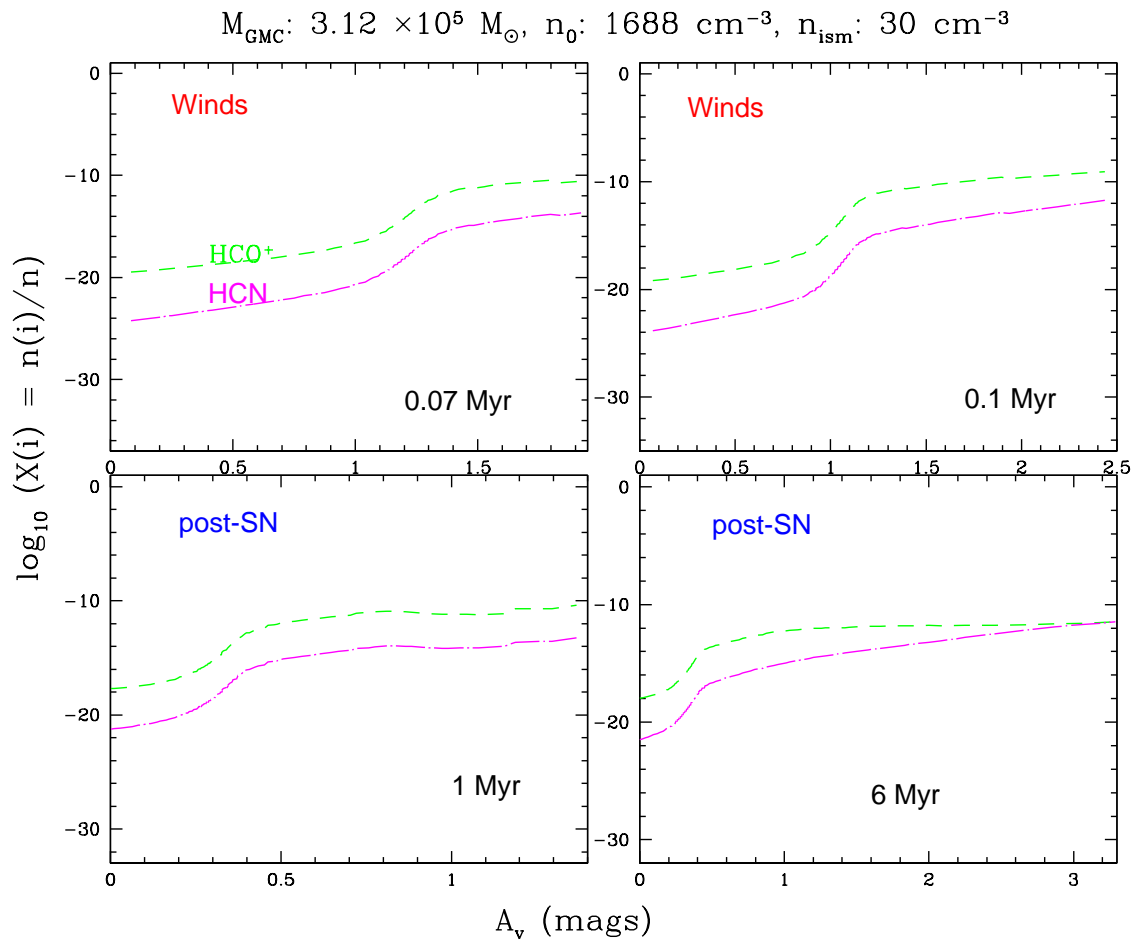


Figure 4.9 (continued)

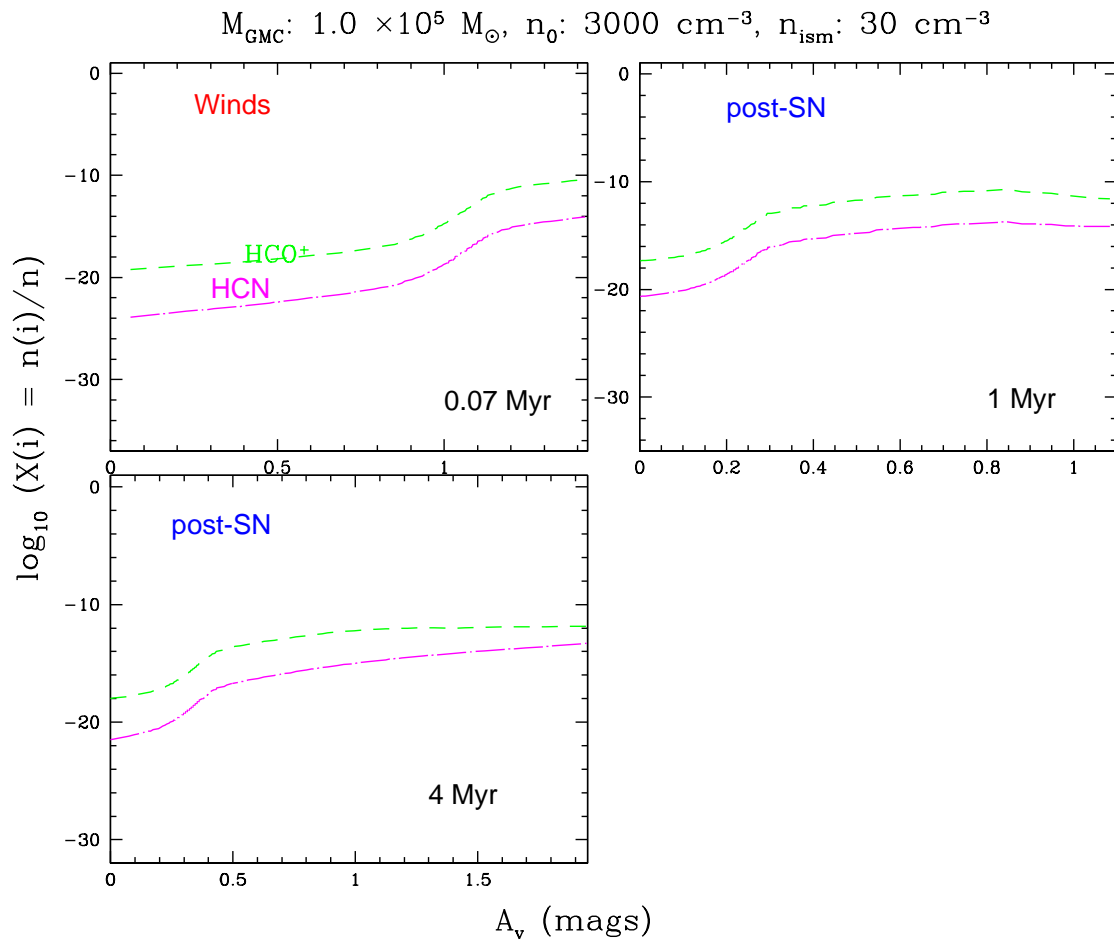


Figure 4.9 (continued)

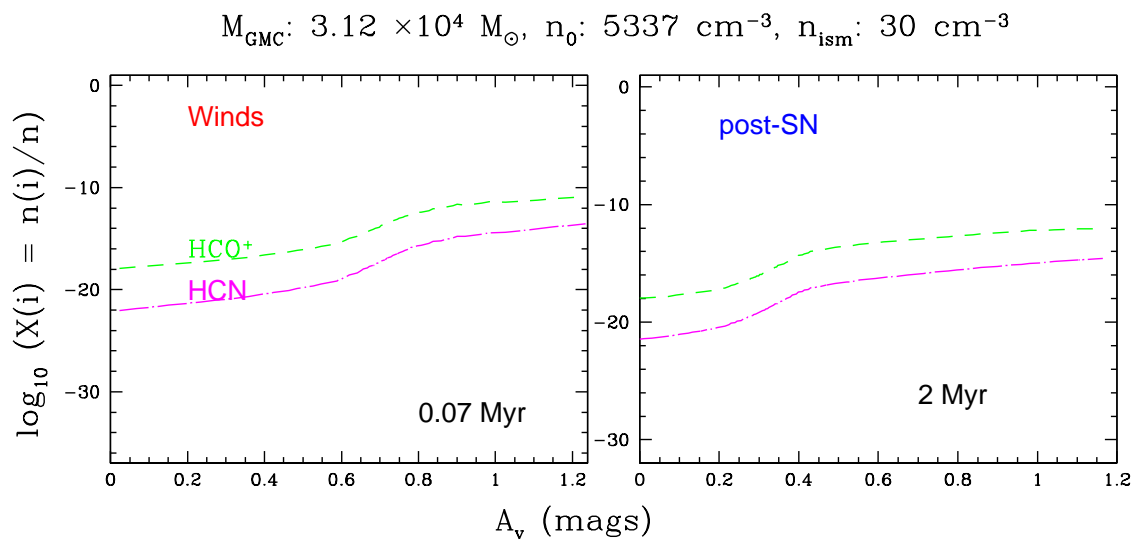


Figure 4.9 (continued)

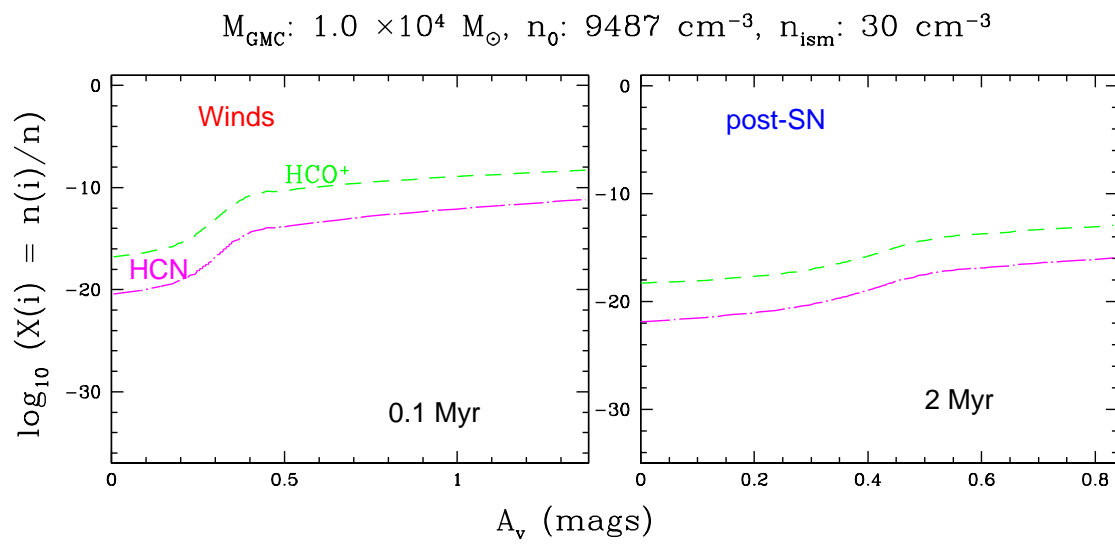


Figure 4.9 (continued)

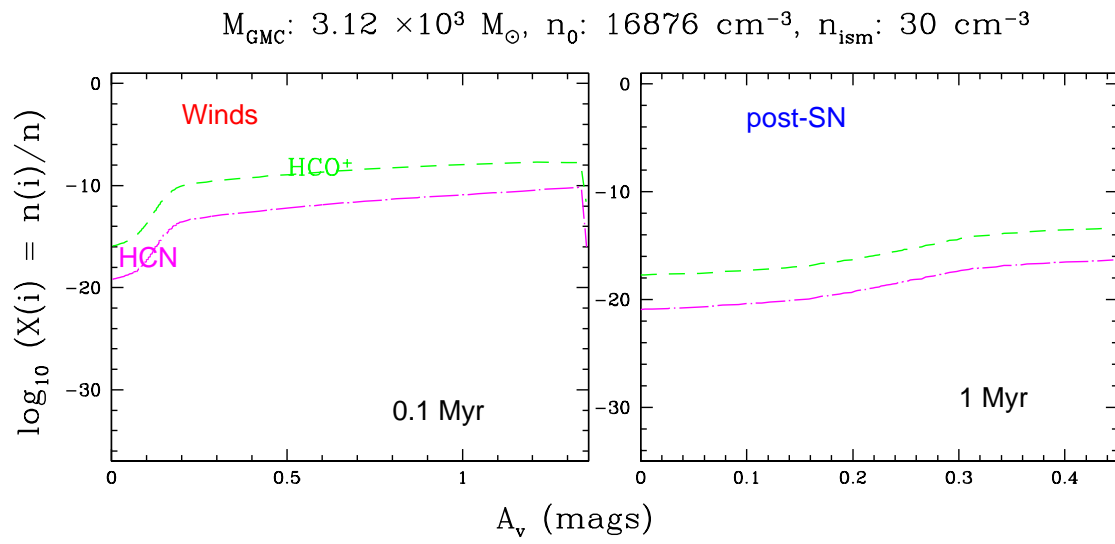


Figure 4.9 (continued)

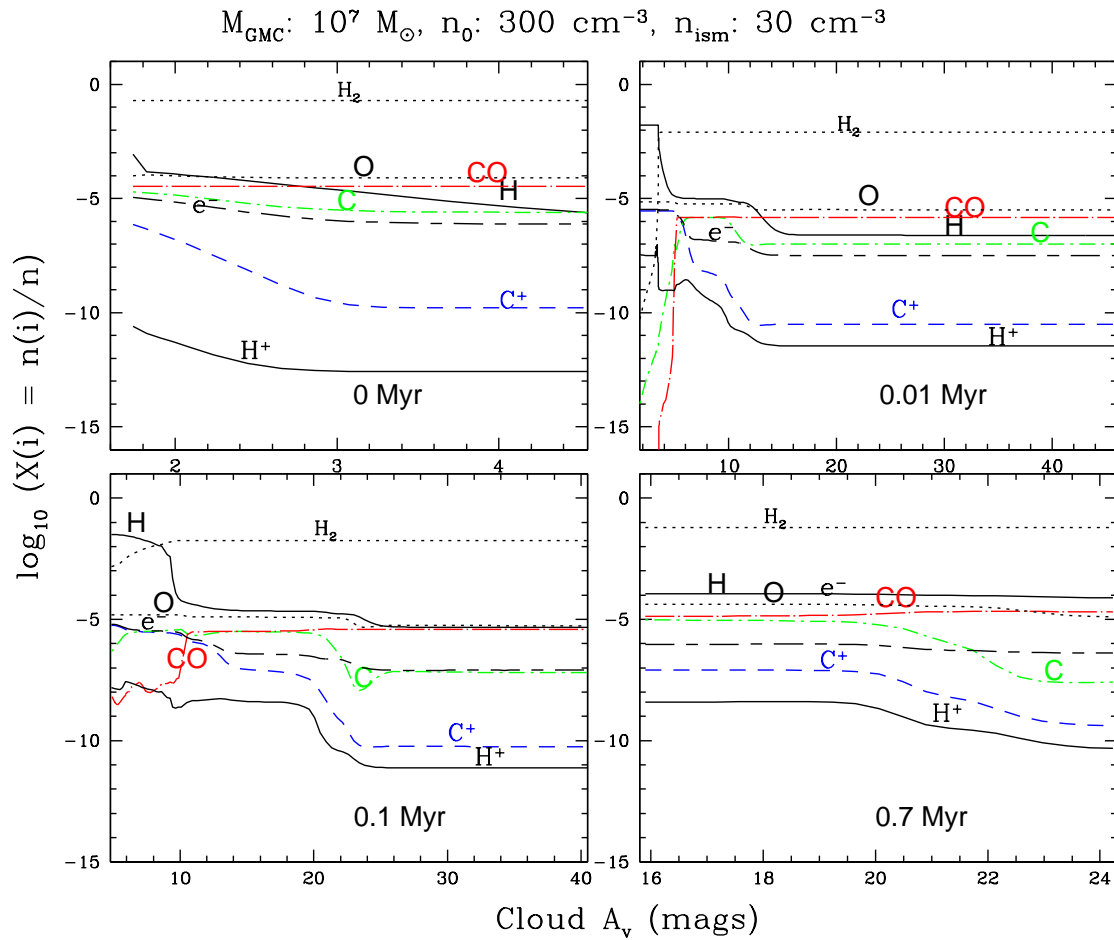


Figure 4.10 Plot of the time-dependent chemical abundances of the main species (H, H_2 , H^+ , e^- , C, C^+ , O, and CO) relative to the total hydrogen density, as a function of visual extinction A_V for the most massive GMC M7 in the ensemble.

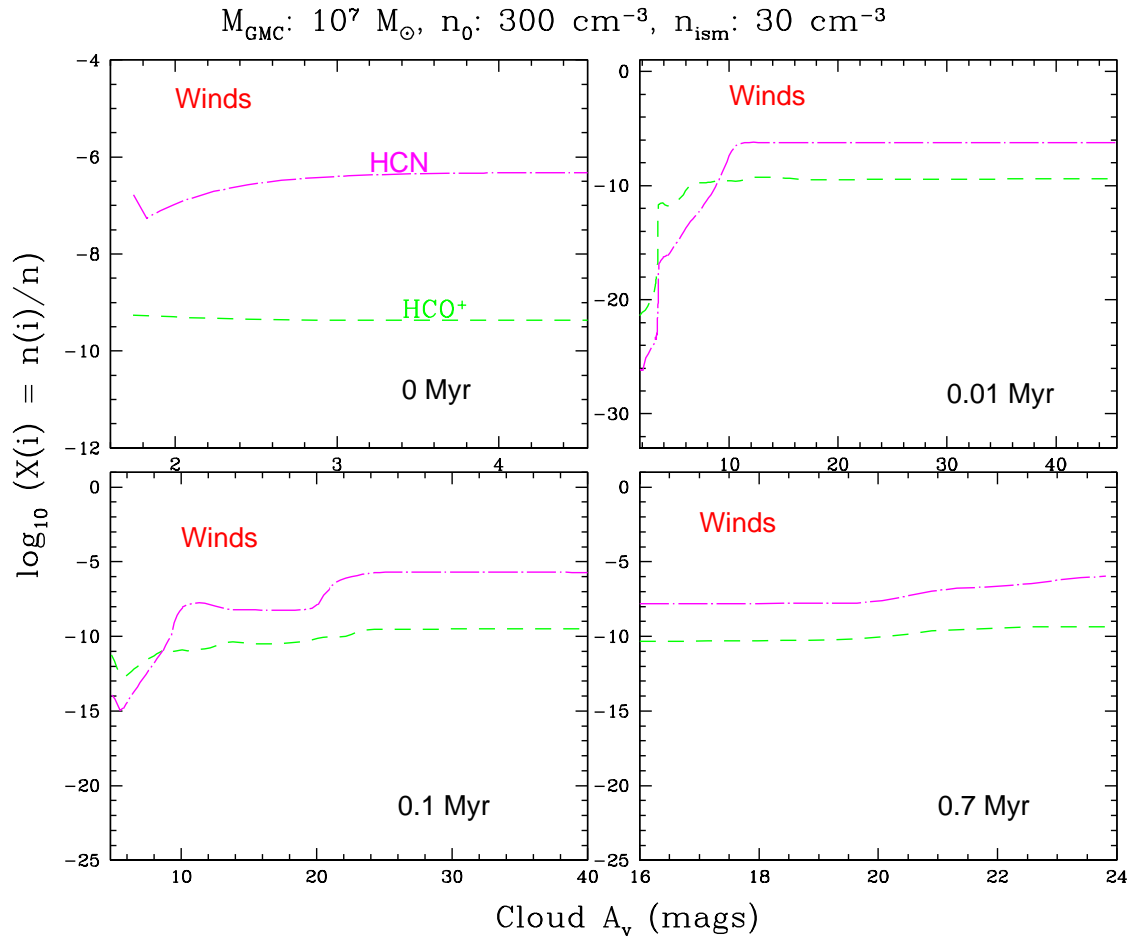


Figure 4.11 Plot of the time-dependent chemical abundances of dense gas tracers (HCN and HCO^+) relative to the total hydrogen density, as a function of visual extinction A_v for the most massive GMC (M7) in the ensemble.

4.3 FIR/sub-mm/mm Line Emission in Individual Shells and GMCs

Here we present a few examples of our model line profiles for a single expanding supershell. These model line profiles may not be directly observed, partly because one sees in reality many shells superimposed. Therefore this study does not deal extensively with structure of the line profiles. In this section, we also present our results, including the integrated line fluxes, for an expanding supershell and a shell/GMC ensemble. Comparisons of these model results with the observations of an expanding supershell and the central 1 kpc starburst region in M 82 will allow us to constrain the kinematic properties of individual shells, age, total H₂ mass, molecular and atomic gas properties in an observed region. The discussion and results of these comparisons are presented in Chapter 5.

4.3.1 Molecular Line Profiles

Our model molecular line profiles exhibit features expected for expanding geometrically thin and optically thick shells in the presence of a bright dust sub-mm continuum (e.g. double-peaks, asymmetric, and P-cygni like sine-wave absorption). For example, Figs. 4.12 and 4.13 show double-peaked line profiles of molecular CO and its isotope (symmetric at age < 8 Myr, and asymmetric at age 20 Myr). The *dip* seen in the middle of the line profiles is produced by optically thick shells with spherical symmetry and negligible thickness as may be shown by simple analytical models. This minimum disappears as the shell becomes optically thin. The asymmetry seen in profiles at higher transitions (and higher frequencies) can be ascribed to the effects of absorption of dust emission in the rear (receding) side of the shell by gas in the near (approaching) side. It occurs preferentially at higher transitions (i.e. higher frequencies), because these transitions are sub-thermally excited (and are hence associated with low excitation temperature), whereas the dust brightness temperature increases with frequency. Consequently, some

absorption features are seen in the high- J transitions for ^{12}CO (age 2 Myr) and its isotope ^{13}CO (age 5 and 20 Myr).

Again, it must be born in mind that these line profiles are calculated for individual shells only, and that there is no high-resolution observation data to validate the predictions of our model concerning the shapes of line profiles. The profiles are shown here primarily for illustrative purposes and completeness. They were used in our analysis to confirm the behavior expected by comparison with simple analytical models.

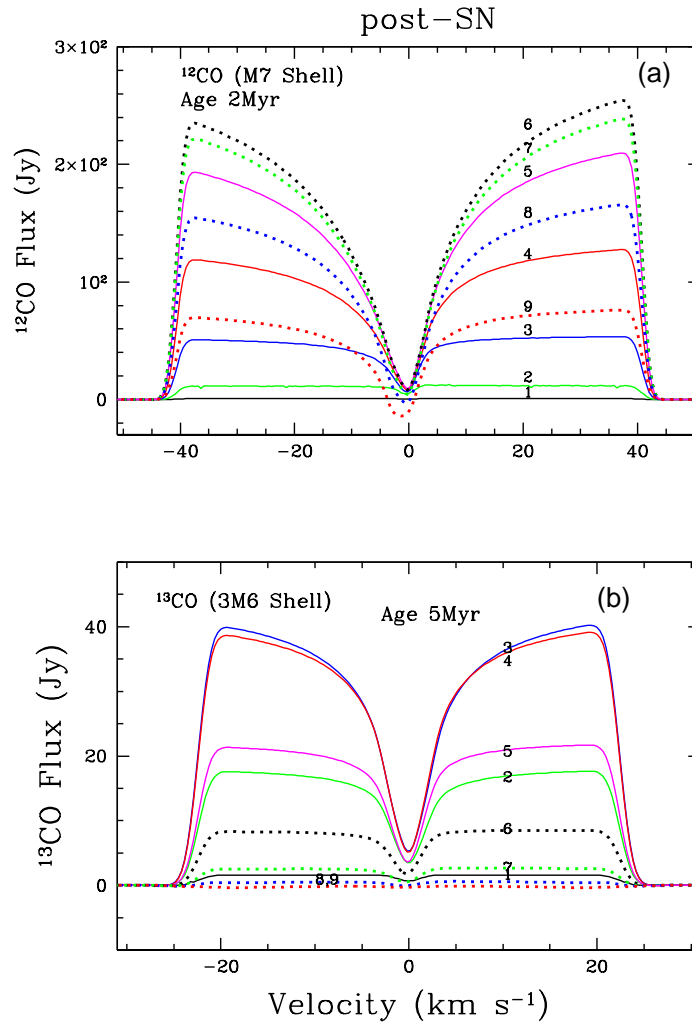


Figure 4.12 Model predicted line profiles of ^{12}CO and its isotope ^{13}CO for an M7 shell at age 5 Myr. Different CO transitions ($J \rightarrow J - 1$, $J = 1$ to 9) are labeled as 1,2,...,9 on the curves.

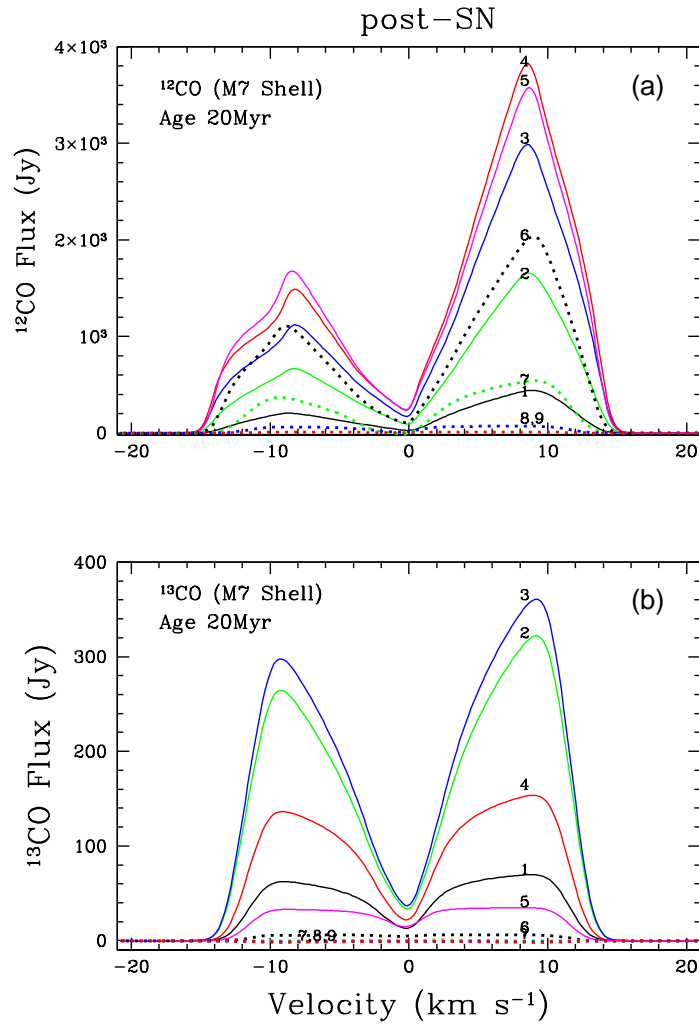


Figure 4.13 Model predicted line profiles of ¹²CO and its isotope ¹³CO for the M7 shell at age 20 Myr. Different CO transitions ($J \rightarrow J - 1$, $J = 1$ to 9) are labeled as 1, 2, ..., 9 on the curves.

4.3.2 Integrated Line Flux of An Expanding Shell

Integrated line fluxes of molecular ^{12}CO , its isotope ^{13}CO , HCN, HCO^+ , atomic C, O, and C^+ are calculated for each model shell at different evolutionary phases. For example, Table 4.2 illustrates the predictions for the CO molecule in a M7 GMC and shell in both the *Winds* and *post-SN* phases. The parent GMCs contribute significantly to the total lower- J line emission during the *Winds* phase. Table 4.3 shows that about 50% - 100% of total the $^{12}\text{CO}(1-0)$ line emission comes from the M7 cloud, but it decreases to less than 24% at the $^{12}\text{CO}(5-4)$ line, and to almost no contribution at $J > 5$. Our model M7 cloud has lower density than lower mass clouds (i.e. 3M3 - 3M6) and hence is less effective at exciting higher J transitions. At around 1 Myr, the line intensity drops by three orders of magnitude because we have not included the gas swept up in the GMCs in the subsequent model of the shells (i.e. in the *post-SN* phase). The negative line fluxes are due to the absorption effect as discussed in previous section regarding molecular line profiles (§ 4.3.1).

Tables for other molecules, and other GMCs and shells are available through the online materials³. These model line fluxes predicted for individual expanding shells can be used as a comparison with future observations, for example, the known expanding supershell centered around SNR 41.9 + 58 in M 82, in order to constrain the physical conditions of the gas and the age of individual shells.

³<http://www.astro.utoronto.ca/~yao/phdthesis/OnlineMaterials>

Table 4.2. Integrated CO line flux for a model M7 GMC and shell.

Time (t) ^a	CO(9-8) ^b	CO(8-7) ^c	CO(7-6) ^d	CO(6-5) ^e	CO(5-4) ^f	CO(4-3) ^g	CO(3-2) ^h	CO(2-1) ⁱ	CO(1-0) ^j
	1036.9 GHz	921.8 GHz	806.7 GHz	691.5 GHz	576.3 GHz	461.0 GHz	345.8 GHz	230.5 GHz	115.3 GHz
(yr)	(Jy km s ⁻¹)								
<i>Winds^k</i>									
1.0E-04	-3.13E+01 ^l	-1.06E+01	1.80E+01	8.82E+01	3.09E+02	6.60E+02	7.28E+02	4.58E+02	1.28E+02
1.0E+04	4.37E-01	1.97E+00	9.26E+00	5.72E+01	2.76E+02	6.41E+02	7.19E+02	4.57E+02	1.31E+02
1.0E+05	2.62E+03	3.06E+03	2.48E+03	1.68E+03	1.34E+03	1.74E+03	2.24E+03	1.70E+03	4.68E+02
3.0E+05	1.54E+04	1.59E+04	1.25E+04	8.83E+03	6.59E+03	4.08E+03	3.03E+03	1.60E+03	3.90E+02
5.0E+05	2.06E+04	2.18E+04	1.81E+04	1.34E+04	8.85E+03	5.64E+03	2.83E+03	1.40E+03	2.97E+02
7.0E+05	2.13E+04	2.40E+04	2.10E+04	1.62E+04	1.62E+04	4.50E+03	4.34E+03	1.74E+03	3.70E+02
<i>podr-SN</i>									
9.0E+05	-2.08E+00	7.51E-01	3.90E-01	1.15E+00	1.34E+00	9.20E-01	6.31E-01	8.80E-03	7.30E-02
1.0E+06	8.49E-01	6.92E+00	1.24E+01	1.55E+01	1.46E+01	9.38E+00	4.44E+00	6.24E-01	1.19E-02
2.0E+06	4.63E+03	9.90E+03	1.38E+04	1.46E+04	1.24E+04	8.06E+03	3.76E+03	9.20E+02	6.04E+01
3.0E+06	5.23E+03	1.47E+04	2.53E+04	3.12E+04	2.99E+04	2.28E+04	1.34E+04	5.02E+03	5.70E+02
4.0E+06	1.22E+04	3.32E+04	5.18E+04	5.78E+04	5.19E+04	3.89E+04	2.38E+04	1.01E+04	1.58E+03
5.0E+06	1.28E+04	3.78E+04	6.15E+04	6.94E+04	6.25E+04	4.72E+04	2.95E+04	1.33E+04	2.42E+03
6.0E+06	1.31E+04	4.12E+04	6.95E+04	7.93E+04	7.13E+04	5.41E+04	3.43E+04	1.59E+04	3.26E+03
7.0E+06	1.18E+04	4.06E+04	7.29E+04	8.52E+04	7.71E+04	5.89E+04	3.79E+04	1.80E+04	3.94E+03
8.0E+06	4.83E+02	3.22E+03	1.33E+04	3.09E+04	4.13E+04	3.78E+04	2.70E+04	1.41E+04	3.65E+03
9.0E+06	3.94E+02	2.72E+03	1.18E+04	2.93E+04	4.08E+04	3.80E+04	2.75E+04	1.45E+04	3.79E+03
1.0E+07	2.22E+02	1.68E+03	8.14E+03	2.37E+04	3.67E+04	3.61E+04	2.67E+04	1.43E+04	3.75E+03
2.0E+07	1.45E+02	1.26E+03	7.07E+03	2.43E+04	4.22E+04	4.33E+04	3.37E+04	1.90E+04	5.29E+03

Table 4.2—Continued

Time (t) ^a	CO(9-8) ^b	CO(8-7) ^c	CO(7-6) ^d	CO(6-5) ^e	CO(5-4) ^f	CO(4-3) ^g	CO(3-2) ^h	CO(2-1) ⁱ	CO(1-0) ^j
(yr)	(Jy km s ⁻¹)								
3.0E+07	7.89E+01	8.36E+02	5.30E+03	2.18E+04	4.44E+04	4.94E+04	4.02E+04	2.33E+04	6.68E+03
4.0E+07	4.92E+01	6.40E+02	4.46E+03	2.10E+04	4.75E+04	5.59E+04	4.68E+04	2.76E+04	8.09E+03
6.0E+07	2.13E+01	4.35E+02	3.50E+03	1.98E+04	5.31E+04	6.81E+04	5.91E+04	3.57E+04	1.06E+04
8.0E+07	9.80E+00	3.15E+02	3.00E+03	1.95E+04	5.92E+04	7.98E+04	7.09E+04	4.34E+04	1.31E+04

^aAge.

^{b-j}Transition $J \rightarrow J - 1$, $J = 9 \dots 1$.

^kEvolutionary phase.

^lThe negative line fluxes are due to the absorption effect.

Table 4.3. Fraction of emission from a M7 GMC to total integrated CO line flux.

Time (t) ^a (yr)	CO(9-8) ^b	CO(8-7) ^c	CO(7-6) ^d	CO(6-5) ^e	CO(5-4) ^f	CO(4-3) ^g	CO(3-2) ^h	CO(2-1) ⁱ	CO(1-0) ^j
				<i>Winds</i> ^k					
1.0E-04	... ¹	...	4.28E-01	8.44E-01	9.48E-01	9.74E-01	9.82E-01	9.85E-01	9.88E-01
1.0E+04	9.99E-01	9.99E-01	1.00E-00	1.00E+00	1.00E+00	1.00E+00	1.00E-00	1.00E+00	1.00E+00
1.0E+05	3.45E-04	1.04E-02	2.37E-01	7.33E-01	9.26E-01	9.78E-01	9.96E-01
3.0E+05	...	6.47E-06	1.46E-04	2.11E-03	4.00E-02	2.06E-01	4.65E-01	6.98E-01	8.71E-01
5.0E+05	3.03E-08	6.96E-07	1.59E-05	3.26E-04	6.06E-03	5.12E-02	2.14E-01	3.75E-01	5.84E-01
7.0E+05	3.38E-08	7.19E-07	1.41E-05	2.57E-04	2.96E-03	5.90E-02	1.33E-01	2.98E-01	4.76E-01

^aAge.^{b-j}Transition $J \rightarrow J - 1$, $J = 9 \dots 1$.^kEvolutionary phase.¹Negative flux from the shell or the parent cloud.

4.4 FIR/sub-mm/mm Line Emission in A Shell/GMC Ensemble

Here we present model line SEDs for several molecular and atomic species in a shell ensemble, comprising clouds which make up the chosen spectrum of cluster/cloud masses. These results will be used in subsequent chapters for our comparisons between the model line SEDs and line intensity ratios with the corresponding observations of the central 1 kpc region in M 82 and other galaxies. The relevant physics and chemistry, as well as excitation mechanisms of molecular and atomic gas are described in § 1.2 of Chapter 1 and § 2.2 to § 2.4 of Chapter 2, and § 3.4 of Chapter 3.

4.4.1 ^{12}CO and Its Isotope ^{13}CO

Fig. 4.14 shows our model line SEDs ($J = 1 \dots 9$) for CO. The same color scheme in the plots is applied to all other molecular line SED plots throughout this chapter. Four different model configurations as a function of the starburst age are used in our line SED predictions. In plot (a) the total line flux S_{CO} is summed from gas in one single expanding shell and its parent GMC with a mass of $10^7 M_{\odot}$ (M7 GMC and Shell or SS model). In plot (b) the total S_{CO} is the sum of line emission in an ensemble of shells only, whose parent cloud mass ranges from 3.1×10^3 to $10^7 M_{\odot}$ (Shell Ensemble or SE model). In plot (c) the total S_{CO} is summed from gas in high-mass shells and their parent GMCs (10^5 to $10^7 M_{\odot}$) in an ensemble (*High-mass* Shell and GMC Ensemble or TSGE model). In plot (d) total line flux S_{CO} is calculated from all shells and their parent clouds in an ensemble with $3.1 \times 10^3 \leq M_{GMC} < 10^7 M_{\odot}$ (Shell + GMC Ensemble or SGE model). If multiple transitions CO data for individual expanding shells become available in the near future, models presented in plot (a) could be useful to constrain the burst age and gas mass in the shell, such as the supershell described in previous section. Table 4.4 summarizes the total line fluxes for CO emitted from a model shell ensemble

(Configuration (d) or SGE model). Table 4.5 shows the fraction of ^{12}CO line emission from individual shells and their parent clouds. More than 80% of the ^{12}CO line emission arises from the massive shells (3M5 - M7) in the ensemble. The line SEDs have two distinct maxima with one near the $J = 6 - 5$ transition and another near the $J = 3 - 2$ transition. The first maximum is associated with burst age between 0.3 and 7 Myr, and the second maximum is mainly associated with age older than 7 Myr. At age 0.2 Myr, the two maxima (4 - 3, 8 - 7) seen in the line SEDs are due to the sum of line emission of gas in the shells and parent clouds. It is clear that the CO excitation in the line SEDs varies with shell expansion or starburst ages. At $\sim 1 (\pm 0.2)$ Myr (*Winds* and *post-SN* phase transition), the S_{CO} is a few orders of magnitude lower than those for other ages. This is an artifact of the switch from *Winds* to *post-SN* phase, where the GMC mass swept up in the *Winds* phase is not carried forward into the *post-SN* phase, and the continuity equation (or mass conservation) is applied to the less dense ISM (i.e. $n_{ism} = 30 \text{ cm}^{-3}$) instead of the GMC.

Fig. 4.15 shows the model line SED of CO isotope ^{13}CO , and Table 4.6 summarizes the total line intensities for ^{13}CO emitted from the shell ensemble (Configuration (d)). The negative line fluxes are due to the absorption effect as discussed in the previous section regarding molecular line profiles (§ 4.3.1).

Tables that summarize the integrated line flux and line intensity ratio of ^{12}CO and its isotope ^{13}CO as a function of starburst age, predicted by our evolving starburst models, are available through the online materials⁴.

⁴<http://www.astro.utoronto.ca/~yao/phdthesis/OnlineMaterials>

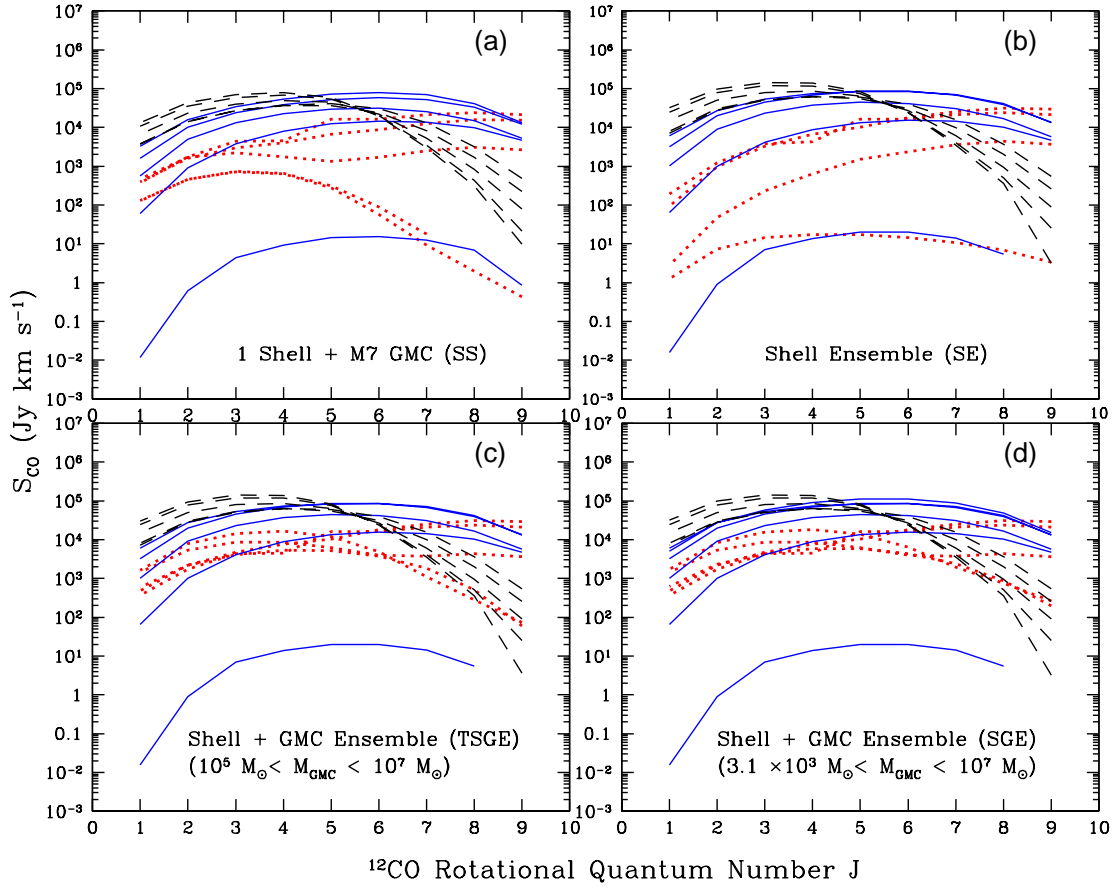


Figure 4.14 Plots of model ^{12}CO line SEDs for four different configurations. The *Winds* phase models are indicated by red dotted lines ($0 \leq t < 0.7$ Myr), while the *post-SN* phase models are indicated by blue solid lines ($1 \leq t < 8$ Myr) and black dashed lines ($8 \leq t < 100$ Myr).

Table 4.4. Integrated ^{12}CO line flux for a model shell ensemble.

Time (t) ^a	CO(9-8) ^b	CO(8-7) ^c	CO(7-6) ^d	CO(6-5) ^e	CO(5-4) ^f	CO(4-3) ^g	CO(3-2) ^h	CO(2-1) ⁱ	CO(1-0) ^j
	1036.9 GHz	921.8 GHz	806.7 GHz	691.5 GHz	576.3 GHz	461.0 GHz	345.8 GHz	230.5 GHz	115.3 GHz
(yr)	(Jy km s ⁻¹)								
A Shell Ensemble ¹									
1.0E-04	1.98E+02	8.70E+02	2.39E+03	4.36E+03	5.81E+03	5.80E+03	4.39E+03	2.34E+03	6.19E+02
1.0E+04	2.64E+02	7.46E+02	1.97E+03	6.32E+03	1.37E+04	1.79E+04	1.54E+04	8.25E+03	1.71E+03
1.0E+05	3.65E+03	4.37E+03	3.72E+03	3.95E+03	6.29E+03	8.74E+03	8.56E+03	5.35E+03	1.44E+03
3.0E+05	2.94E+04	3.14E+04	2.52E+04	1.80E+04	1.04E+04	7.62E+03	4.78E+03	2.22E+03	4.84E+02
5.0E+05	2.06E+04	2.18E+04	1.81E+04	1.34E+04	8.85E+03	5.64E+03	2.83E+03	1.40E+03	2.97E+02
7.0E+05	2.13E+04	2.40E+04	2.10E+04	1.62E+04	1.62E+04	4.50E+03	4.34E+03	1.74E+03	3.70E+02
9.0E+05	-6.15E+00 ^m	-1.99E+00	-8.97E-01	1.38E+00	1.86E+00	1.42E+00	7.15E-01	2.18E-01	2.35E+00
1.0E+06	-3.76E+00	5.43E+00	1.41E+01	2.00E+01	2.00E+01	1.37E+01	7.06E+00	9.10E-01	1.58E-02
2.0E+06	4.74E+03	1.02E+04	1.44E+04	1.54E+04	1.33E+04	8.76E+03	4.11E+03	9.99E+02	6.49E+01
3.0E+06	5.73E+03	1.66E+04	3.06E+04	4.16E+04	4.43E+04	3.70E+04	2.33E+04	9.00E+03	1.02E+03
4.0E+06	1.36E+04	3.92E+04	6.78E+04	8.56E+04	8.51E+04	6.90E+04	4.50E+04	2.00E+04	3.20E+03
5.0E+06	1.52E+04	4.83E+04	8.86E+04	1.13E+05	1.11E+05	8.93E+04	5.85E+04	2.72E+04	5.07E+03
6.0E+06	1.31E+04	4.14E+04	7.08E+04	8.42E+04	8.40E+04	7.34E+04	5.33E+04	2.73E+04	6.03E+03
7.0E+06	1.19E+04	4.10E+04	7.49E+04	9.27E+04	9.41E+04	8.12E+04	5.76E+04	2.95E+04	6.79E+03
8.0E+06	5.44E+02	3.67E+03	1.56E+04	3.94E+04	6.05E+04	6.31E+04	5.00E+04	2.79E+04	7.17E+03
9.0E+06	4.72E+02	3.27E+03	1.46E+04	3.94E+04	6.30E+04	6.75E+04	5.48E+04	3.09E+04	8.10E+03
1.0E+07	2.59E+02	2.00E+03	9.88E+03	3.09E+04	5.51E+04	6.27E+04	5.25E+04	3.02E+04	8.04E+03
2.0E+07	1.61E+02	1.41E+03	8.13E+03	3.00E+04	6.10E+04	7.48E+04	6.63E+04	4.05E+04	1.17E+04
3.0E+07	8.98E+01	9.47E+02	6.10E+03	2.67E+04	6.35E+04	8.54E+04	7.95E+04	5.03E+04	1.52E+04

Table 4.4—Continued

Time (t) ^a	CO(9-8) ^b	CO(8-7) ^c	CO(7-6) ^d	CO(6-5) ^e	CO(5-4) ^f	CO(4-3) ^g	CO(3-2) ^h	CO(2-1) ⁱ	CO(1-0) ^j
	1036.9 GHz	921.8 GHz	806.7 GHz	691.5 GHz	576.3 GHz	461.0 GHz	345.8 GHz	230.5 GHz	115.3 GHz
(yr)	(Jy km s ⁻¹)								
4.0E+07	5.72E+01	7.30E+02	5.14E+03	2.55E+04	6.71E+04	9.59E+04	9.26E+04	5.99E+04	1.85E+04
6.0E+07	2.52E+01	5.06E+02	4.08E+03	2.41E+04	7.48E+04	1.17E+05	1.18E+05	7.82E+04	2.46E+04
8.0E+07	3.22E+00	3.61E+02	3.51E+03	2.37E+04	8.25E+04	1.37E+05	1.42E+05	9.83E+04	3.20E+04

^aAge.

^{b-j}Transition $J \rightarrow J - 1$, $J = 9 \dots 1$.

^kShell/GMC type.

^lA shell/GMC ensemble using SGE model.

^mThe negative lines are due to the absorption effect.

Table 4.5. Percentage fraction of integrated ^{12}CO line rmission from different shells predicted by our ESbM models.

$J^a(\rightarrow J - 1)$	M7 ^b	3M6	M6	3M5	M5	3M4	M4	3M3
0 (Myr) ^c								
9	... ^d	2.82	9.74	26.76	6.36	11.42	29.84	28.95
8	...	2.32	13.15	39.33	4.93	10.29	17.47	13.69
7	0.75	1.77	27.24	40.54	5.69	8.12	9.51	6.30
6	2.02	2.72	35.88	38.53	5.94	6.08	5.57	3.33
5	5.32	5.64	40.14	33.35	5.35	4.47	3.61	2.03
4	11.38	9.09	39.01	28.29	4.60	3.50	2.63	1.43
3	16.58	11.09	36.93	25.13	4.08	2.94	2.13	1.13
2	19.57	12.03	35.92	23.52	3.75	2.60	1.81	0.94
1	20.68	12.38	35.89	22.98	3.47	2.27	1.44	0.68
4 (Myr)								
9	89.71	10.55	0.00
8	84.69	15.40	0.03
7	76.40	23.47	0.08	0.00
6	67.52	32.26	0.21	0.00
5	60.99	38.48	0.62	0.00
4	56.38	41.81	1.79	0.00
3	52.89	42.87	4.16	0.01
2	50.50	42.75	6.94	0.01
1	49.38	42.04	8.54	0.02	0.00	0.00	...	0.00
8 (Myr)								
9	88.79	11.06	0.23	0.01
8	87.74	11.86	0.36	0.01
7	85.26	14.18	0.40	0.01
6	78.43	21.02	0.61	0.01
5	68.26	30.43	1.32	0.02
4	59.90	36.75	3.33	0.04
3	54.00	38.94	6.89	0.11
2	50.54	39.08	9.97	0.24	0.00
1	50.91	38.76	10.05	0.29	0.00
30 (Myr)								
9	87.86	9.97	1.84	0.37	...	0.00	0.00	...
8	88.28	10.17	1.40	0.22	0.00	0.00	0.00	...

Table 4.5—Continued

$J^a(\rightarrow J - 1)$	M7 ^b	3M6	M6	3M5	M5	3M4	M4	3M3
7	86.89	11.66	1.37	0.17	0.00	0.00	0.00	...
6	81.65	16.51	1.88	0.17	0.00	0.00	0.00	...
5	69.92	25.48	4.20	0.27	0.00	0.00	0.00	...
4	57.85	31.50	9.95	0.68	0.01	0.00	0.00	...
3	50.57	31.62	16.02	1.88	0.03	0.00	0.00	...
2	46.32	30.58	19.22	3.84	0.09	0.00	0.00	...
1	43.95	30.39	20.15	5.05	0.16	0.00	0.00	...

^aMolecular rotational quantum number.

^bShell/GMC type.

^cAge.

^dNegative flux from the shell or the parent cloud.

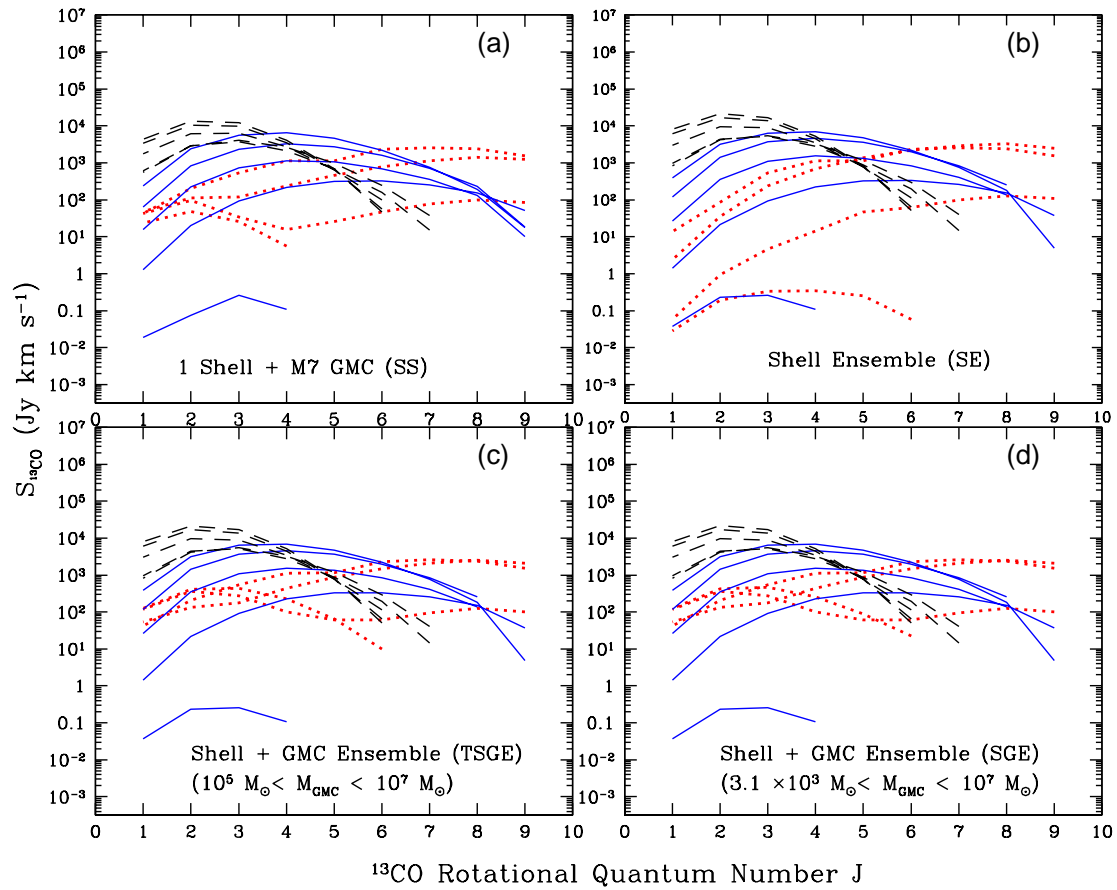


Figure 4.15 Plots of model ^{13}CO line SEDs for four different configurations. The *Winds* phase models are indicated by red dotted lines ($0 \leq t < 0.7$ Myr), while the *post-SN* phase models are indicated by blue solid lines ($1 \leq t < 8$ Myr) and black dashed lines ($8 \leq t < 100$ Myr).

Table 4.6. Integrated ^{13}CO line flux predicted by our ESbM models.

Time (t) ^a	$^{13}\text{CO}(9-8)$ ^b	$^{13}\text{CO}(8-7)$ ^c	$^{13}\text{CO}(7-6)$ ^d	$^{13}\text{CO}(6-5)$ ^e	$^{13}\text{CO}(5-4)$ ^f	$^{13}\text{CO}(4-3)$ ^g	$^{13}\text{CO}(3-2)$ ^h	$^{13}\text{CO}(2-1)$ ⁱ	$^{13}\text{CO}(1-0)$ ^j
	1036.9 GHz	921.8 GHz	806.7 GHz	691.5 GHz	576.3 GHz	461.0 GHz	345.8 GHz	230.5 GHz	115.3 GHz
(Myr)	(Jy km s ⁻¹)								
A Shell Ensemble ¹									
1.0E-04	-4.10E+01 ^m	-2.41E+01	-6.82E+00	2.26E+01	8.81E+01	2.56E+02	4.60E+02	4.21E+02	1.26E+02
1.0E+04	1.87E+00	5.36E+00	1.25E+01	3.01E+01	8.12E+01	2.22E+02	5.02E+02	5.14E+02	1.15E+02
1.0E+05	1.01E+02	1.24E+02	9.58E+01	6.18E+01	6.06E+01	9.99E+01	2.73E+02	3.62E+02	1.19E+02
3.0E+05	2.11E+03	2.55E+03	2.11E+03	1.46E+03	8.69E+02	4.34E+02	1.79E+02	1.34E+02	5.33E+01
5.0E+05	1.77E+03	2.29E+03	2.06E+03	1.58E+03	1.42E+03	6.30E+02	2.91E+02	1.20E+02	3.50E+01
7.0E+05	1.55E+03	2.39E+03	2.58E+03	2.30E+03	1.15E+03	1.13E+03	5.42E+02	2.04E+02	4.21E+01
9.0E+05	-3.95E+00	-3.14E+00	-2.38E+00	-1.69E+00	-1.10E+00	-6.31E-01	-1.00E+00	-3.04E-01	-4.07E-02
1.0E+06	-5.77E+00	-4.34E+00	-3.07E+00	-1.98E+00	-6.26E-01	-3.93E-01	-8.41E+00	-8.56E-02	9.01E-04
2.0E+06	3.70E+01	1.51E+02	2.57E+02	3.32E+02	3.27E+02	2.26E+02	9.25E+01	2.15E+01	1.43E+00
3.0E+06	-1.00E+01	1.37E+02	4.06E+02	8.38E+02	1.34E+03	1.55E+03	1.10E+03	3.54E+02	2.62E+01
4.0E+06	1.09E-01	2.56E+02	8.40E+02	1.99E+03	3.62E+03	4.63E+03	3.68E+03	1.42E+03	1.19E+02
5.0E+06	-1.75E+01	2.41E+02	9.33E+02	2.53E+03	5.20E+03	7.39E+03	6.50E+03	2.78E+03	2.64E+02
6.0E+06	4.90E+00	1.80E+02	7.62E+02	2.19E+03	4.71E+03	6.88E+03	6.39E+03	3.15E+03	3.90E+02
7.0E+06	-4.13E+01	1.49E+02	7.17E+02	2.27E+03	5.32E+03	8.40E+03	8.33E+03	4.33E+03	5.86E+02
8.0E+06	-4.53E+01	-2.61E+01	4.04E+01	2.93E+02	1.18E+03	3.28E+03	5.43E+03	4.15E+03	8.26E+02
9.0E+06	-4.28E+01	-2.60E+01	3.73E+01	2.76E+02	1.14E+03	3.30E+03	5.69E+03	4.52E+03	9.47E+02
1.0E+07	-4.00E+01	-3.00E+01	1.45E+01	1.95E+02	8.83E+02	2.77E+03	5.18E+03	4.37E+03	9.67E+02
2.0E+07	-3.49E+01	-3.49E+01	-3.45E+00	1.54E+02	8.66E+02	3.29E+03	7.36E+03	7.28E+03	2.05E+03
3.0E+07	-3.60E+01	-4.13E+01	-1.90E+01	1.14E+02	7.87E+02	3.47E+03	8.81E+03	9.59E+03	3.01E+03

Table 4.6—Continued

Time (t) ^a	¹³ CO(9-8) ^b	¹³ CO(8-7) ^c	¹³ CO(7-6) ^d	¹³ CO(6-5) ^e	¹³ CO(5-4) ^f	¹³ CO(4-3) ^g	¹³ CO(3-2) ^h	¹³ CO(2-1) ⁱ	¹³ CO(1-0) ^j
	1036.9 GHz	921.8 GHz	806.7 GHz	691.5 GHz	576.3 GHz	461.0 GHz	345.8 GHz	230.5 GHz	115.3 GHz
(Myr)	(Jy km s ⁻¹)								
4.0E+07	-3.60E+01	-4.66E+01	-3.08E+01	9.18E+01	7.73E+02	3.81E+03	1.05E+04	1.21E+04	4.06E+03
6.0E+07	-4.09E+01	-5.85E+01	-5.01E+01	6.41E+01	7.81E+02	4.47E+03	1.37E+04	1.68E+04	6.09E+03
8.0E+07	-2.81E+01	-5.07E+01	-5.39E+01	5.14E+01	8.25E+02	5.22E+03	1.69E+04	2.15E+04	8.11E+03

^aAge.

^{b-j}Transition $J \rightarrow J - 1$, $J = 9 \dots 1$.

^kShell/GMC type.

^lA shell/GMC ensemble using SGE model.

^mThe negative lines are due to the absorption effect.

4.4.2 HCN and HCO⁺

Figs. 4.16 and 4.17 show the model line SEDs of HCN and HCO⁺ ($J = 1 \dots 9$). The model configuration and color scheme are the same as those described in the CO line SED plots. Tables 4.7 and 4.8 summarize the total line fluxes for HCN and HCO⁺ emitted from the shell ensemble (Configuration (d)). Again, the negative line fluxes are due to the absorption effect as discussed in previous (§ 4.3.1). Tables 4.9 and 4.10 show the fraction of HCN and HCO⁺ line emission in individual shells and parent clouds. Before the shells sweep up the materials in their parent clouds, the clouds are the dominant source for the line emission of CO and HCN at all J . For the HCO⁺, the shells dominate the line emission throughout the entire evolution. Almost all of the high- J ($J \geq 5$) HCO⁺ line emission originates from the *Winds* phase, i.e. size < 50 pc, related to a burst age less than 0.7 Myr. These compact regions are strongly influenced by intense FUV radiation field with gas temperature $T_{gas} > 200$ K and H₂ density $n(\text{H}_2) = 10^4 - 10^6 \text{ cm}^{-3}$. Similar to CO molecular gas, about 85 - 90% of the HCN line emission arises from warm PDRs of massive shells (3M5 - M7) in the ensemble. However, this is not the case for HCO⁺ lines. For example, Table 4.10 shows that at age 0.1 Myr about 50% of the HCO⁺ lines are emitted from 3M5 - M7 shells, another 40% from 3M3 - M4 shells, but only 10% arises in 3M4 - M5 shells. At age 0.5 Myr, about 85% of the HCO⁺ lines come from M4 - 3M5 shells; between 1 and 8 Myr, greater than 90% of the HCO⁺ line emission originates in 3M6 and M7 shells. This implies that the excitation and chemical abundance of HCO⁺ are more sensitive to the physical states of molecular gas than CO and HCN during the first eight million years of the starburst evolution.

Tables that summarize the integrated line flux and the intensity ratio of HCN, and HCO⁺ as a function of starburst age, predicted by our evolving starburst models, are available through the online materials⁵.

⁵<http://www.astro.utoronto.ca/~yao/phdthesis/OnlineMaterials>

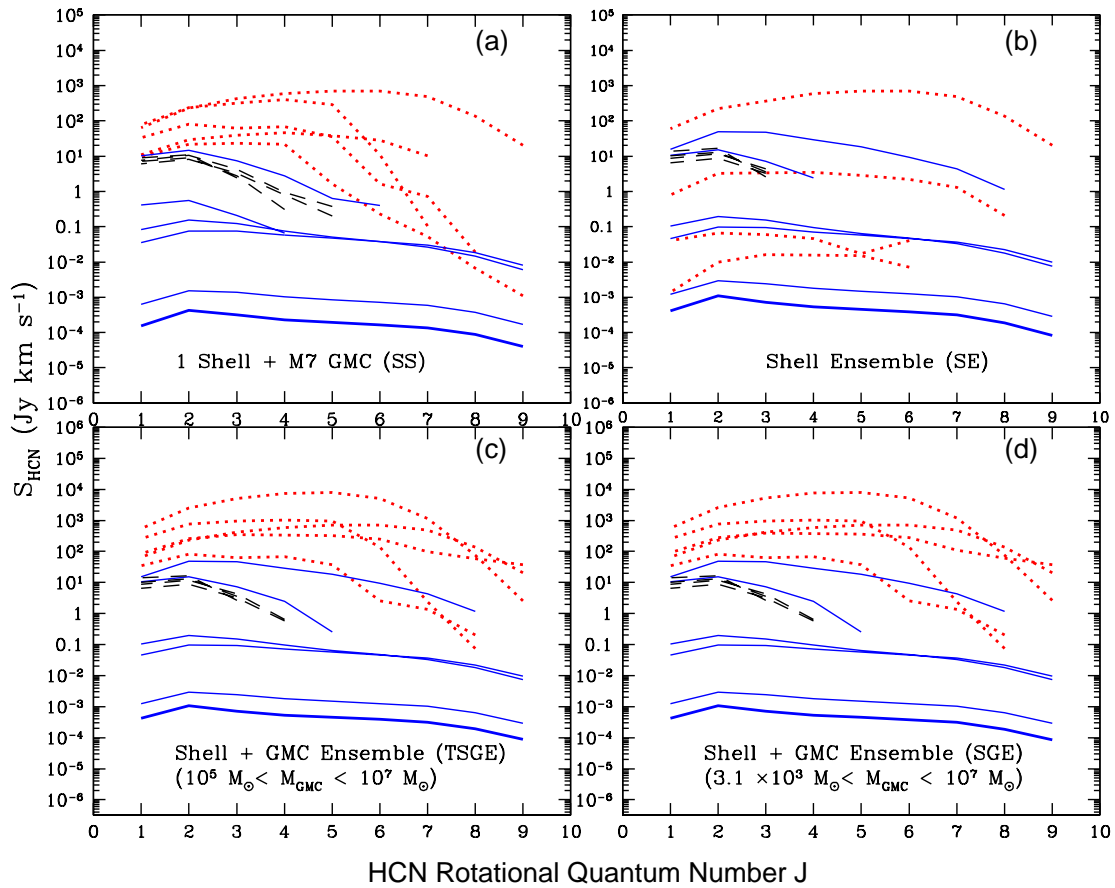


Figure 4.16 Plots of model HCN line SEDs for four different configurations. The *Winds* phase models are indicated by red dotted lines ($0 \leq t < 0.7$ Myr), while the *post-SN* phase models are indicated by blue solid lines ($1 \leq t < 8$ Myr) and black dashed lines ($8 \leq t < 100$ Myr).

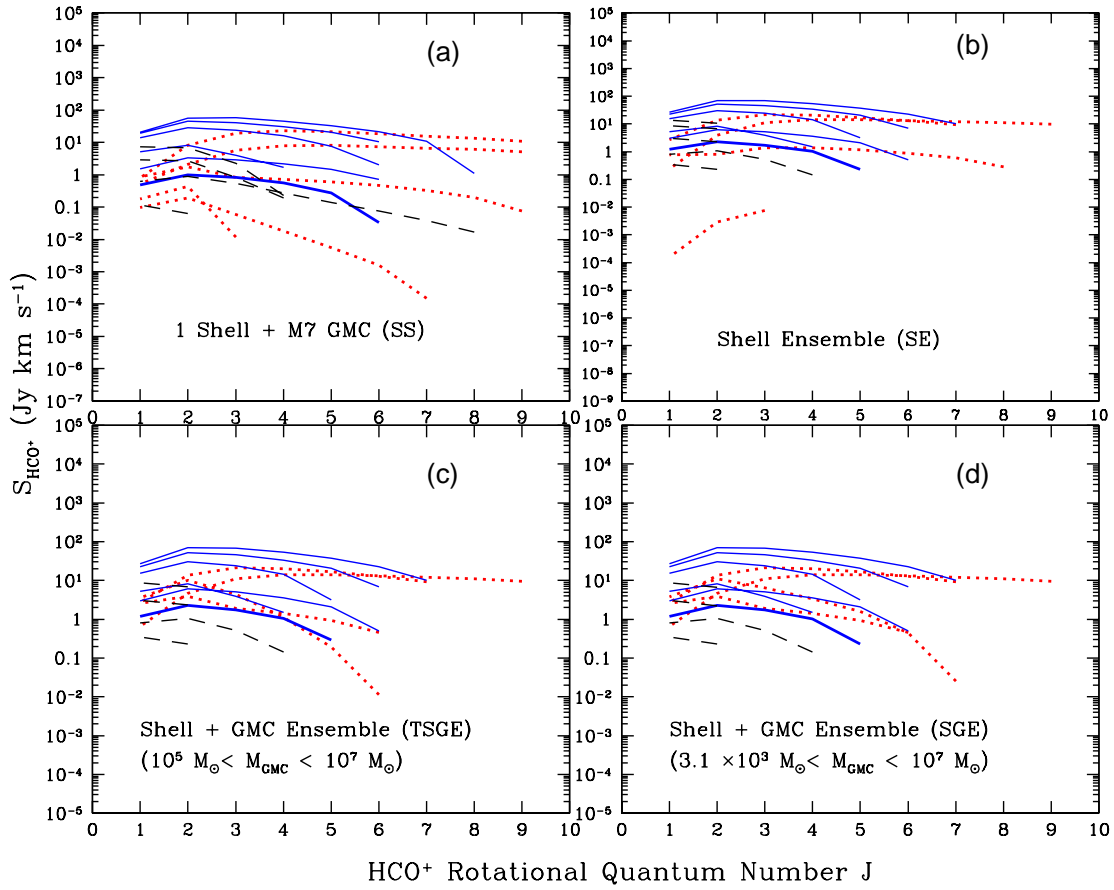


Figure 4.17 Plots of model HCO^+ line SEDs for four different configurations. The *Winds* phase models are indicated by red dotted lines ($0 \leq t < 0.7$ Myr), while the *post-SN* phase models are indicated by blue solid lines ($1 \leq t < 8$ Myr) and black dashed lines ($8 \leq t < 100$ Myr).

Table 4.7—Continued

Time (t) ^a	HCN(9-8) ^b	HCN(8-7) ^c	HCN(7-6) ^d	HCN(6-5) ^e	HCN(5-4) ^f	HCN(4-3) ^g	HCN(3-2) ^h	HCN(2-1) ⁱ	HCN(1-0) ^j
(yr)	(Jy km s ⁻¹)								
4.0E+07	-5.17E-01	-2.34E+00	-3.80E+00	-4.11E+00	-3.91E+00	-9.92E-01	3.12E+00	1.38E+01	1.14E+01
6.0E+07	-6.00E-01	-2.90E+00	-5.27E+00	-6.13E+00	-6.30E+00	-4.96E+00	2.62E+00	1.64E+01	1.39E+01

^aAge.^{b-j}Transition $J \rightarrow J - 1$, $J = 9 \dots 1$.^kShell/GMC type.^lA shell/GMC ensemble using SGE model.^mThe negative lines are due to the absorption effect.

Table 4.8. Integrated HCO⁺ line flux predicted by our ESbM models.

Time (<i>t</i>) ^a	HCO ⁺ (9-8) ^b	HCO ⁺ (8-7) ^c	HCO ⁺ (7-6) ^d	HCO ⁺ (6-5) ^e	HCO ⁺ (5-4) ^f	HCO ⁺ (4-3) ^g	HCO ⁺ (3-2) ^h	HCO ⁺ (2-1) ⁱ	HCO ⁺ (1-0) ^j
	802.5 GHz	713.3 GHz	624.2 GHz	535.1 GHz	445.9 GHz	356.7 GHz	267.6 GHz	178.4 GHz	89.2 GHz
(Myr)	(Jy km s ⁻¹)								
A Shell Ensemble ¹									
1.0E-04	-9.06E+00 ^m	-6.59E+00	-4.28E+00	-2.38E+00	-9.61E-01	2.99E-01	2.11E+00	6.51E+00	2.40E+00
1.0E+04	-1.37E-01	-7.73E-02	2.51E-02	4.48E-01	1.60E+00	3.32E+00	6.37E+00	1.12E+01	3.75E+00
1.0E+05	-1.19E+00	-6.24E-01	-6.59E-02	4.54E-01	9.41E-01	1.40E+00	1.90E+00	3.88E+00	2.53E+00
3.0E+05	9.57E+00	1.12E+01	1.21E+01	1.31E+01	1.41E+01	1.42E+01	1.11E+01	4.62E+00	6.61E-01
5.0E+05	1.10E+01	1.34E+01	1.57E+01	1.87E+01	2.17E+01	2.31E+01	1.90E+01	8.00E+00	7.95E-01
7.0E+05	1.06E-06	1.09E-05	9.30E+00	1.29E+01	1.66E+01	2.02E+01	2.12E+01	1.36E+01	2.71E+00
9.0E+05	-3.27E+00	-2.33E+00	-1.46E+00	-4.97E-01	2.32E-01	1.01E+00	1.72E+00	2.29E+00	1.18E+00
1.0E+06	-4.15E+00	-2.60E+00	-8.19E-01	4.97E-01	2.07E+00	3.61E+00	5.12E+00	6.12E+00	2.98E+00
2.0E+06	-1.69E+01	-4.37E+00	1.02E+01	2.27E+01	3.77E+01	5.33E+01	6.85E+01	6.92E+01	2.69E+01
3.0E+06	-3.77E+01	-2.19E+01	-6.91E+00	6.83E+00	2.08E+01	3.33E+01	4.58E+01	5.12E+01	2.28E+01
4.0E+06	-6.27E+01	-4.24E+01	-2.51E+01	-5.87E+00	3.20E+00	1.44E+01	2.40E+01	3.01E+01	1.51E+01
5.0E+06	-8.69E+01	-6.14E+01	-4.05E+01	-2.32E+01	-5.19E+00	1.88E+00	1.05E+01	1.66E+01	9.58E+00
6.0E+06	-6.67E+01	-4.77E+01	-3.24E+01	-1.97E+01	-9.53E+00	1.51E+00	3.88E+00	8.15E+00	5.25E+00
7.0E+06	-8.51E+01	-6.15E+01	-4.26E+01	-2.72E+01	-1.53E+01	-6.42E+00	4.46E-02	4.37E+00	3.56E+00
8.0E+06	-2.91E-02	-3.96E-02	-5.37E-02	-4.97E-02	-1.06E-04	1.42E-01	5.20E-01	1.05E+00	8.02E-01
9.0E+06	-9.81E-02	-1.49E-01	-2.21E-01	-2.75E-01	-2.60E-01	-1.77E-01	2.49E-01	9.41E-01	8.28E-01
1.0E+07	-1.46E-01	-2.63E-01	-4.00E-01	-5.24E-01	-5.84E-01	-5.57E-01	-2.62E-01	2.32E-01	3.50E-01
2.0E+07	-2.24E-01	-4.49E-01	-7.72E-01	-1.10E+00	-1.34E+00	-1.24E+00	-7.85E-01	9.37E-01	1.49E+00
3.0E+07	-2.50E-01	-5.16E-01	-9.59E-01	-1.42E+00	-1.80E+00	-1.77E+00	-6.47E-01	2.22E+00	3.07E+00

Table 4.8—Continued

Time (t) ^a	HCO ⁺ (9-8) ^b	HCO ⁺ (8-7) ^c	HCO ⁺ (7-6) ^d	HCO ⁺ (6-5) ^e	HCO ⁺ (5-4) ^f	HCO ⁺ (4-3) ^g	HCO ⁺ (3-2) ^h	HCO ⁺ (2-1) ⁱ	HCO ⁺ (1-0) ^j
	802.5 GHz	713.3 GHz	624.2 GHz	535.1 GHz	445.9 GHz	356.7 GHz	267.6 GHz	178.4 GHz	89.2 GHz
(Myr)	(Jy km s ⁻¹)								
4.0E+07	-3.03E-01	-6.07E-01	-1.18E+00	-1.81E+00	-2.33E+00	-2.43E+00	-7.39E-01	3.82E+00	4.99E+00
6.0E+07	-3.25E-01	-6.51E-01	-1.39E+00	-2.32E+00	-3.22E+00	-3.65E+00	-8.39E-01	6.66E+00	8.74E+00

^aAge.

^{b-j}Transition $J \rightarrow J - 1$, $J = 9 \dots 1$.

^kShell/GMC type.

^lA shell/GMC ensemble using SGE model.

^mThe negative lines are due to the absorption effect.

Table 4.9. Percentage fraction of integrated HCN line emission from different shells predicted by our ESbM models.

$J^a(\rightarrow J - 1)$	M7 ^b	3M6	M6	3M5	M5	3M4	M4	3M3
0 (Myr) ^c								
9	... ^d	76.06	52.64	2.96	0.21	0.15	0.29	0.40
8	...	62.35	39.30	3.46	0.49	0.43	1.01	2.05
7	9.36	38.81	24.99	14.90	0.71	1.48	4.81	4.98
6	10.22	15.09	30.35	33.04	1.60	2.86	3.82	3.03
5	10.27	10.57	37.57	28.38	2.96	3.34	3.80	2.94
4	12.08	10.18	33.68	29.26	3.75	4.04	4.22	3.01
3	10.26	8.06	36.40	30.93	4.27	4.03	3.64	2.38
2	10.39	8.22	38.82	30.00	4.29	3.59	2.93	1.80
1	12.21	9.04	39.28	28.47	4.07	3.14	2.39	1.38
4 (Myr)								
9	64.15
8
7
6	100.00
5	100.00	0.00	0.00	0.00	0.00	0.00
4	0.23	...	100.00	0.00	0.00	0.00	0.00	0.00
3	0.44	0.24	99.30	0.00	0.00	0.00	0.00	0.00
2	1.15	0.05	98.83	0.00	0.00	0.00	0.00	0.00
1	2.64	0.08	97.04	0.00	0.00	0.00	0.00	0.00
8 (Myr)								
9
8
7
6
5
4	100.0	19.26	0.00	0.00	...	0.00
3	100.0	6.43	0.00	0.00	...	0.00
2	92.80	8.74	0.00	0.00	0.00	0.00
1	91.45	9.03	0.00	0.00	0.00	0.00

^aMolecular rotational quantum number.

^bShell/GMC type.

^cAge.

^dNegative flux from the shell or the parent cloud.

Table 4.10. Percentage fraction of integrated HCO^+ line emission from different shells predicted by our ESbM models.

$J^a(\rightarrow J - 1)$	M7 ^b	3M6	M6	3M5	M5	3M4	M4	3M3
0.1 (Myr) ^c								
9	... ^d
8	27.13	11.51	0.65	0.00	30.21	...
7	12.05	5.81	0.31	4.83	21.34	76.33
6	9.69	4.90	0.27	5.34	19.95	65.33
5	8.57	4.41	0.81	...	0.25	5.31	19.44	62.08
4	7.72	4.38	1.95	0.92	0.22	5.13	18.97	60.84
3	7.31	3.65	3.81	2.34	0.18	4.78	18.45	59.24
2	15.45	2.94	11.40	4.79	0.12	3.54	14.81	47.07
1	19.45	16.64	15.84	6.40	0.17	1.64	8.54	31.28
3 (Myr)								
9
8
7	0.01	0.00	0.00	0.00
6	100.0	...	1.73	...	0.00	0.00	0.00	0.00
5	99.52	1.17	0.86	...	0.00	0.00	0.00	0.00
4	92.79	6.96	0.89	...	0.00	0.00	0.00	0.00
3	89.74	9.93	0.92	...	0.00	0.00	0.00	0.00
2	87.30	12.13	0.79	...	0.00	0.00	0.00	0.00
1	83.77	15.45	1.03	...	0.00	0.00	0.00	0.00
8 (Myr)								
9
8
7
6
5
4	100.0	61.70	11.35	...	0.38	0.13	0.02	0.01
3	100.0	29.55	5.15	...	0.20	0.07	0.02	0.00
2	83.05	21.91	3.64	...	0.18	0.08	0.02	0.01
1	78.18	21.50	3.05	...	0.09	0.04	0.01	0.00

^aMolecular rotational quantum number.

^bShell/GMC type.

^cAge.

^dNegative flux from the shell or the parent cloud.

4.4.3 Atomic C, O, and C⁺

The atomic forbidden transitions are the most important cooling lines arising in PDRs. The ratios of these lines and CO cooling lines (see Table 2.1) can be used to derive the physical conditions in PDRs: for example, the incident FUV flux G_0 , gas density n and temperature T_{gas} , as well as the ratio of G_0/n , discussed in § 2.2 of Chapter 2. By comparing these model line ratios with observations, we can constrain the physical properties of atomic gas within a detected region, which will be presented in the subsequent chapter.

Fig. 4.18 shows the model line flux (in Jy km s⁻¹) for shell/GMC ensemble as a function of time for the C(2-1) line at 809.3 GHz ([C I] 370 μ m) and C(1-0) line at 492.1 GHz ([C I] 612 μ m) for four different model configurations. The atomic line fluxes along with the molecular line fluxes that we presented here are for the template model of the star clusters and molecular H₂ clouds. The values for the actual masses for M 82 will be derived from a fit of the fluxes of this template model to the observed fluxes. The same color scheme in the plots is applied to all other atomic line SED plots throughout this chapter. The C(2-1) line flux emitted in the shells is generally higher than that in the C(1-0) line, whereas in the cooler less dense parent clouds seen during the *Winds* phase the C(2-1) to (1-0) ratio is close to one (as seen in plots (a), (c), and (d)). The massive shells are the dominant source for the neutral carbon line emission in the *post-SN* phase. The discontinuity seen in the plots (near 1 Myr) is a result of switching phase from *Winds* to *post-SN* as explained previously in connection with molecular emission.

Fig. 4.19 shows the model line fluxes as a function of time for O(1-0) line at 4744.8 GHz ([O I] 63 μ m) and O(2-1) line at 2060.1 GHz ([O I] 145 μ m). The intensity increases with time for both lines, and then levels off after 8 Myr. The O(1-0) line flux is clearly stronger than the O(2-1) line throughout the entire starburst evolution.

Fig. 4.20 show the model line flux of C⁺(1-0) line at 1900 GHz (i.e. [C II] 158 μ m) as a function of time. Tables 4.11 to 4.13 summarize the simulations of the total line fluxes for C, O and C⁺ emitted from the shell ensemble (Configuration (d)).

Tables that summarize the integrated line flux of C, O, and C⁺ as a function of starburst age, predicted by our evolving starburst models, are available through the online materials⁶.

⁶<http://www.astro.utoronto.ca/~yao/phdthesis/OnlineMaterials>

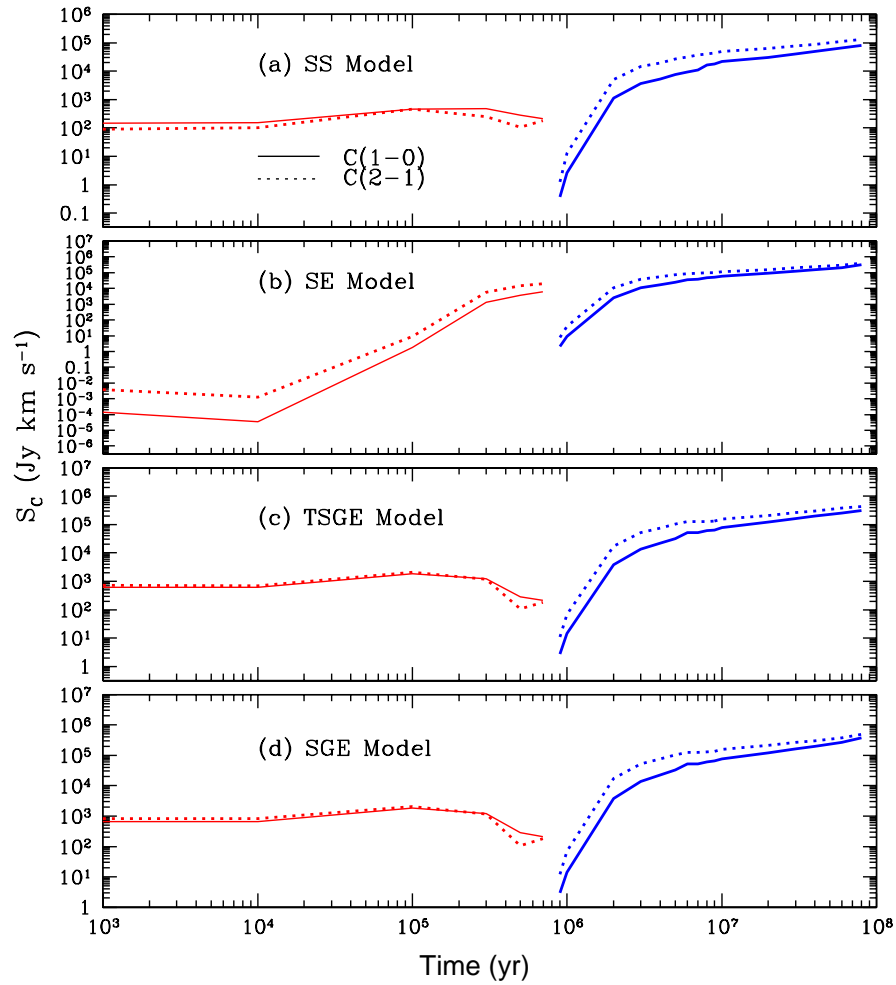


Figure 4.18 Plots of model neutral atomic carbon line flux as a function of time. The solid curves are the C(1-0) lines, and the dashed curves are the C(2-1) lines. The red color indicates *Winds* model, and the blue color indicated *post-SN* model.

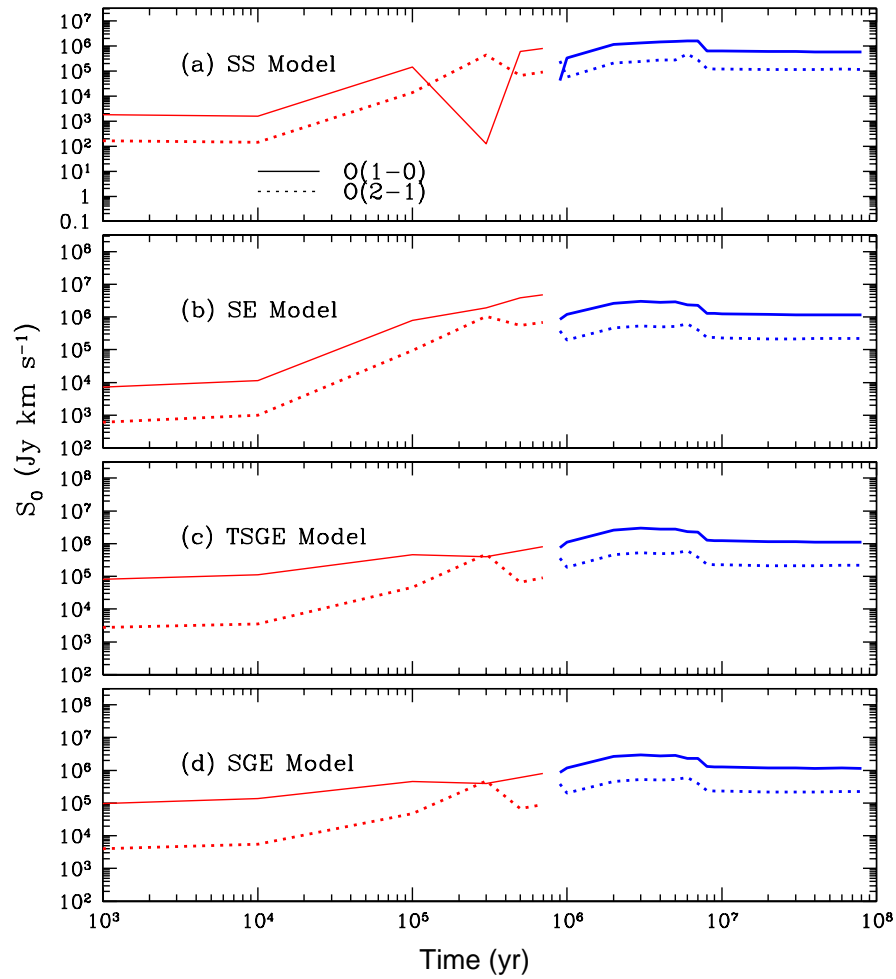


Figure 4.19 Plots of model neutral atomic oxygen line flux as a function of time. The solid curves are the $\text{O}(1-0)$ lines, and the dashed curves are the $\text{O}(2-1)$ lines. The red color indicates *Winds* model, and the blue color indicated *post-SN* model.

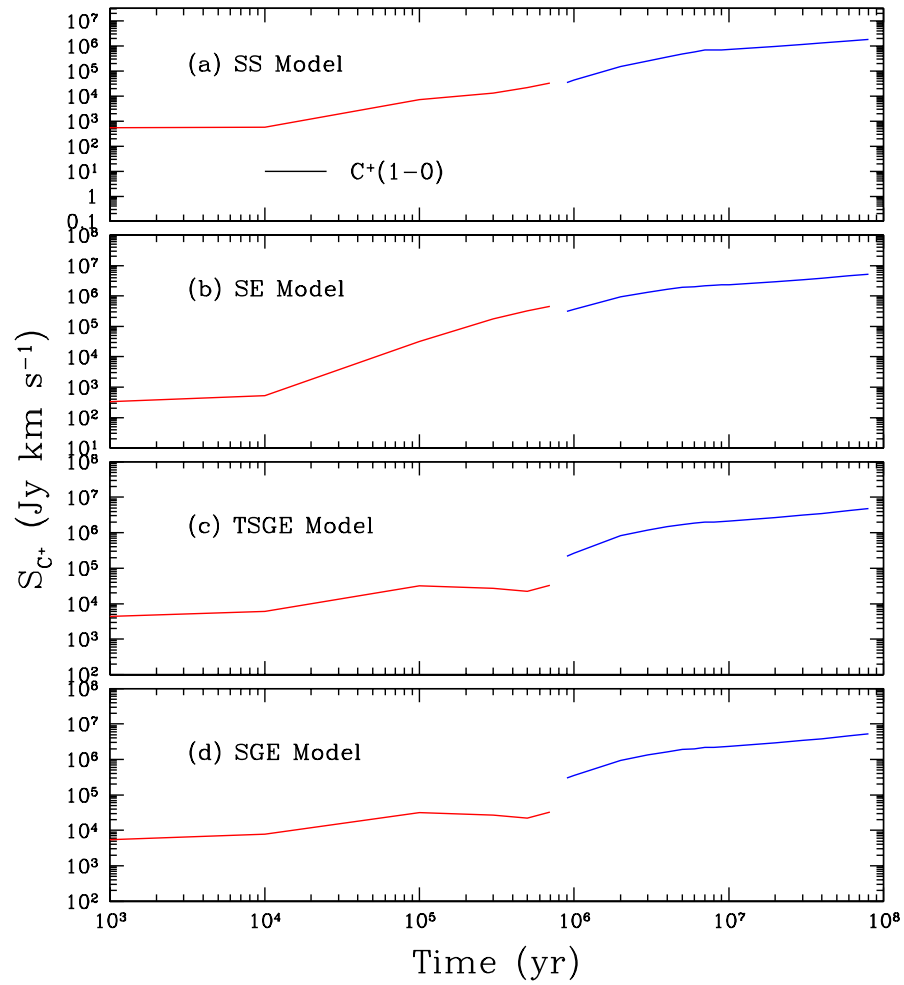


Figure 4.20 Plots of model $C^+(1-0)$ line flux as a function of time. The red color indicates *Winds* model, and the blue color indicated *post-SN* model.

Table 4.11. Integrated C line flux predicted by our ESbM models.

Time (t) ^a	C(2-0) ^b	C(2-1) ^c	C(1-0) ^d
	1301.5 GHz	809.3 GHz	492.1 GHz
(yr)	(Jy km s ⁻¹)	(Jy km s ⁻¹)	(Jy km s ⁻¹)
A SGE Ensemble ^f			
1.0E-04	1.46E+00	9.01E+02	7.37E+02
1.0E+04	4.65E-05	8.21E+02	6.58E+02
1.0E+05	5.45E-03	2.08E+03	1.85E+03
3.0E+05	5.03E-02	1.18E+03	1.21E+03
5.0E+05	9.55E-04	1.07E+02	2.88E+02
7.0E+05	2.20E-04	1.84E+02	2.12E+02
9.0E+05	2.78E-06	1.21E+01	2.94E+00
1.0E+06	7.64E-06	6.98E+01	1.44E+01
2.0E+06	1.17E-03	1.72E+04	3.81E+03
3.0E+06	3.71E-03	5.14E+04	1.37E+04
4.0E+06	5.60E-03	7.64E+04	2.23E+04
5.0E+06	7.76E-03	1.03E+05	3.25E+04
6.0E+06	1.07E-02	1.26E+05	5.22E+04
7.0E+06	1.04E-02	1.25E+05	5.29E+04
8.0E+06	1.11E-02	1.30E+05	6.07E+04
9.0E+06	1.13E-02	1.33E+05	6.43E+04
1.0E+07	1.38E-02	1.55E+05	7.68E+04
2.0E+07	1.96E-02	2.10E+05	1.21E+05
3.0E+07	2.48E-02	2.62E+05	1.62E+05
4.0E+07	2.85E-02	3.02E+05	1.96E+05
6.0E+07	3.56E-02	3.78E+05	2.62E+05
8.0E+07	5.12E-02	4.94E+05	3.77E+05

^aAge.^{b-d}Transition $J \rightarrow J - 2$ or $J - 1$, $J = 2 \dots 1$.^eShell/GMC type.^fA shell/GMC ensemble using SGE model.

Table 4.12. Integrated O line flux predicted by our ESbM models.

Time (t) ^a	O(2-0) ^b	O(1-0) ^c	O(2-1) ^d
	6804.8 GHz	4744.8 GHz	2060.1 GHz
(yr)	(Jy km s ⁻¹)	(Jy km s ⁻¹)	(Jy km s ⁻¹)
A SGE Ensemble ^f			
1.0E-04	2.42E+03	7.44E+03	5.42E+02
1.0E+04	3.96E+02	1.38E+05	5.45E+03
1.0E+05	2.58E+03	4.61E+05	4.69E+04
3.0E+05	2.47E+03	4.02E+05	4.78E+05
5.0E+05	6.13E+03	6.11E+05	6.71E+04
7.0E+05	1.25E+04	8.11E+05	9.06E+04
9.0E+05	5.19E+03	8.47E+05	3.80E+05
1.0E+06	6.10E+03	1.19E+06	1.99E+05
2.0E+06	1.99E+04	2.62E+06	4.62E+05
3.0E+06	3.27E+04	2.97E+06	5.33E+05
4.0E+06	4.67E+04	2.80E+06	5.06E+05
5.0E+06	5.92E+04	2.86E+06	5.16E+05
6.0E+06	6.64E+04	2.33E+06	6.08E+05
7.0E+06	7.99E+04	2.30E+06	3.97E+05
8.0E+06	7.95E+04	1.30E+06	2.41E+05
9.0E+06	8.67E+04	1.27E+06	2.35E+05
1.0E+07	9.20E+04	1.26E+06	2.32E+05
2.0E+07	1.39E+05	1.20E+06	2.16E+05
3.0E+07	1.82E+05	1.18E+06	2.17E+05
4.0E+07	2.29E+05	1.15E+06	2.18E+05
6.0E+07	2.99E+05	1.17E+06	2.24E+05
8.0E+07	3.73E+05	1.14E+06	2.22E+05

^aAge.^{b-d}Transition $J \rightarrow J - 2$ or $J - 1$, $J = 2 \dots 1$.^eShell/GMC type.^fA shell/GMC ensemble using SGE model.

Table 4.13. Integrated C⁺(1-0) line flux predicted by our ESbM models.

Time (t) ^a (yr)	A SGE Ensemble ^b (Jy km s ⁻¹)
1.0E-04	4.58e+02
1.0E+04	7.89e+03
1.0E+05	3.21e+04
3.0E+05	2.68e+04
5.0E+05	2.21e+04
7.0E+05	3.31e+04
9.0E+05	3.04E+05
1.0E+06	3.57E+05
2.0E+06	9.46E+05
3.0E+06	1.34E+06
4.0E+06	1.63E+06
5.0E+06	1.89E+06
6.0E+06	2.01E+06
7.0E+06	2.19E+06
8.0E+06	2.21E+06
9.0E+06	2.29E+06
1.0E+07	2.36E+06
2.0E+07	2.94E+06
3.0E+07	3.43E+06
4.0E+07	3.86E+06
6.0E+07	4.58E+06
8.0E+07	5.26E+06

^aAge.^bA shell/GMC ensemble using SGE model.

Chapter 5

Understanding of Molecular Gas and Starburst Ages in M 82

In this chapter, we apply our evolving starburst models by comparisons to an expanding molecular supershell centered around the supernova remnant SNR 41.9 + 58 in the starburst galaxy M 82, and to the multiwavelength data of the central 1 kpc regions of M 82. The basic goals are to investigate if we can model FIR/sub-mm/mm line emission in a massive star-forming region, and if we can relate the molecular gas properties in a starburst region to its recent star formation history.

5.1 The Supershell Surrounding SNR 41.9 + 58

Observations have detected an expanding supershell centered around the bright SNR 41.9 + 58 in both molecular line and radio continuum (e.g. Weiss et al., 1999; Wills et al., 1999). This supershell has a diameter of ~ 130 pc, an expansion velocity of ~ 45 km s $^{-1}$, and a mass of $\sim 8 \times 10^6 M_{\odot}$. The kinetic energy of the observed supershell is estimated to be about 1.6×10^{53} ergs (Weiss et al., 1999). The kinematic evidence for the supershell appears most readily in the $^{13}\text{CO}(1 - 0)$ position-velocity (PV) plot (Neininger et al., 1998) as a depression on the west side of M 82, bounded by a feature emerging toward

lower velocities and possibly blended with emission associated with gas following orbits in the bar potential. Neininger et al. (1998) conclude that the depression seen in the $^{13}\text{CO}(1-0)$ PV plot coincides with peaks in emission of [Ne II] and radio recombination lines, providing evidence that the void is populated by ionized gas inside the supershell. Seaquist et al. (2006) show that their PV plot reveals no depression in $^{12}\text{CO } J = 6 - 5$ but instead find a region filled with $^{12}\text{CO } J = 6 - 5$ emission that is not evident in the underlying $^{12}\text{CO } J = 1 - 0$ map. Their line ratio PV map is consistent with the appearance of the channel maps, which show emission in the shell region extending over a very broad range in velocity. Seaquist et al. (2006) conclude that the location of this supershell contains CO with higher than average excitation, together with the ionized gas. The cavity created by the supershell is not associated with prominent emission in higher density tracer such as HCN and HCO^+ in their low-excitation lines (Brouillet & Schilke, 1993; Seaquist et al., 1998). This implies that the higher state of excitation may be due to higher kinetic temperature. Besides the known expanding supershell centered around SNR $41.9 + 58$, there is evidence for other shells having sizes from several tens of parsecs to more than 1 kiloparsec, and kinetic energies between $\sim 10^{50}$ and 10^{55} ergs (e.g. Lo et al., 1987; García-Burillo et al., 2001; Wills et al., 2002; Bartel & Bietenholz, 2005; Bayet et al., 2008).

Using a set of initial cloud conditions selected for our expanding shell simulations (presented in Chapter 4), i.e. a cloud mass $M_{GMC} = 10^7 M_{\odot}$, a star cluster mass $M_{SC} = 2.5 \times 10^6 M_{\odot}$, cloud density $n_0 = 300 \text{ cm}^{-3}$, ambient ISM density $n_{ism} = 30 \text{ cm}^{-3}$, we derive a swept-up shell that has very similar characteristics to the observed one. At the observed radius of $\sim 65 \text{ pc}$, our model indicates an age of 0.8 Myr, an expansion velocity of $\sim 47 \text{ km s}^{-1}$, and a swept-up H_2 mass of $\sim 7.5 \times 10^6 M_{\odot}$. The requirements of the kinetic energy measured for the supershell (1.6×10^{53} ergs) are too large for a single SN according to the model developed in this study. Our model predicts a kinetic energy of $\sim 1.5 \times 10^{53}$ ergs for the expanding shell centrally illuminated by a younger

Table 5.1. Characteristics of the expanding supershell in M 82.

Parameter	Observation	Model
Radius (pc)	65.0	64.0
Age (Myr)	1.0	0.8
Expansion velocity (km s ⁻¹)	45	47
Total H ₂ molecular gas mass ($\times 10^6 M_{\odot}$)	8.0	7.5
Kinetic Energy ($\times 10^{53}$ ergs)	1.6	1.5
Total stellar mass in the center cluster ($\times 10^6 M_{\odot}$)	...	2.5
Total number of O stars ($\geq 40 M_{\odot}$)	...	1700
Total Mechanical Energy ($\times 10^{54}$ ergs)	...	1.5

star cluster at the age of ~ 0.8 Myr. The total mechanical energy needed for the creation of this supershell is $\sim 1.5 \times 10^{54}$ ergs, which is contributed mostly by mechanical winds associated with ~ 1700 O stars with individual star mass $m_* \geq 40 M_{\odot}$ in an unidentified cluster coinciding approximately with the luminous SNR candidate 41.9 + 58. Hence, our model predicts that about 10% of the total energy is present in the form of kinetic energy of the expanding shell.

The comparison of the kinetics of our single shell model with the observed supershell in M 82 is summarized in Table 5.1. Our model results and the observations agree remarkably well.

Finally, we investigate the state of excitation of the molecular gas in the supershell relative to that of the surrounding CO emitting gas in M 82, by comparing the predicted line ratios in the shell to those in the surrounding gas. For the surrounding gas we use line ratios computed for the bulk of the disk molecular gas based on our forthcoming analysis

of fitting our model for a shell ensemble to the observed line ratios for the central 1 kpc (see § 5.2.2). Fig. 5.1 shows this for the line ratios of ^{12}CO high J transitions to the (1-0) transition (i.e. $I_{CO}/I_{CO(1-0)}$, I_{CO} in units of Jy km s^{-1}) for the model supershell shown in Table 5.1. The jump in the ratios seen at $J = 3$ to 5 results from the addition of line emission of M7 shell to that of its parent cloud, where the GMC contributes 5 - 45% to the total line emission for $J \leq 4$, but less than 0.2% for $J > 4$. The plot shows clearly that our model for the supershell (red dashed curve) predicts that its line SED exhibits a higher level of excitation than the surrounding emission within M 82 (represented by the adjacent curve). Thus, one can expect some excess emission at high excitation transitions in the supershell after the underlying low excitation is subtracted out. Our model results are in qualitative agreement with the observational evidence for higher than average excitation emission in the supershell (e.g. Neininger et al., 1998; Seaquist et al., 2006). When higher quality and more extensive data on the excitation become available, our model predictions can be useful in interpreting the observations.

5.2 FIR/Sub-mm/mm Line Emission in The Central Region

Here we use the model components described in Chapter 4 to produce a fit of our model line spectral energy distribution to the observations of molecular gas in the central 1 kpc region. The purpose is to determine whether it is possible to model the FIR/sub-mm/mm line emission in a massive star-forming galaxy, and whether there is a relation between the molecular gas properties and the age of the starburst (i.e. finding the *age indicator*), and to assess the overall impact of the starburst on the fine scale structure and physical conditions of the ISM in M 82.

We treat the entire central 1 kpc as an evolving starburst region, which can be modeled by following the evolution of an ensemble of expanding shells and clouds at different stages

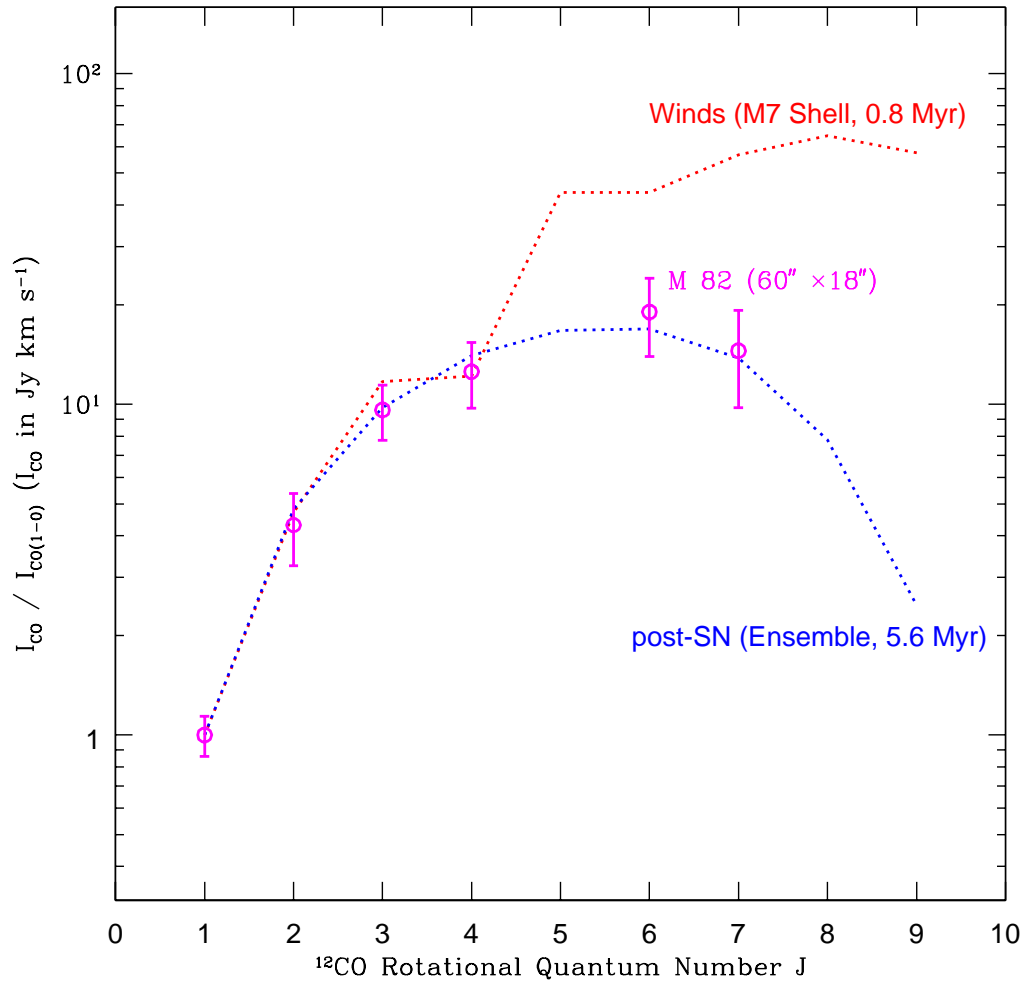


Figure 5.1 Plot of model line ratios of ^{12}CO high J transitions to the (1-0) transition (i.e. $I_{CO}/I_{CO(1-0)}$, I_{CO} in units of Jy km s^{-1}) as a function of rotational quantum number J for an expanding supershell (M7) at age 0.8 Myr (*Winds* phase, red dashed curve). For comparison, a similar plot is shown of the observed and modeled SED of the central $60'' \times 18''$ region of the disk of M 82 to represent the background disk emission with lower excitation. For details of the latter model fit, see section 5.2.2.

of the shell expansion. Hence, different gas chemistry scenarios can be simultaneously at play in the center of this galaxy. However, our model does not attempt to reproduce or model the geometrical distribution of shells in an actual starburst system. In any event this distribution is unknown since the individual shells are not observed. The total line emission is assumed to be represented by the sum of the emission from all the shells in the model ensemble, which will then be used to compare with the observed data to estimate the stellar mass, the total H_2 mass swept up, and the age of the associated starburst in the measured region.

5.2.1 Observational Data

The central concentration (~ 1 kpc) of molecular gas in M 82, which feeds the strong star formation activity, has been studied by many authors since the 1980s (e.g. Young & Scoville, 1984; Wild et al., 1992; Gusten et al., 1993; Weiss et al., 1999; Mao et al., 2000; Petitpas & Wilson, 2000; Weiss et al., 2001; Ward et al., 2003). Interesting results arise from these studies. For example, the observed CO line SED and line ratios can be reproduced by emission from low ($n(\text{H}_2) \approx 10^3 \text{ cm}^{-3}$) and high ($n(\text{H}_2) \approx 10^{3.5-4.5} \text{ cm}^{-3}$, $T_{kin} \geq 40 \text{ K}$) excitation gas components using a LVG method (Weiss et al., 2005, and references therein). The high excitation component, responsible for the excitation of levels beyond $J = 4$, arise from dense and warm gas, while the low excitation component is emitted by diffuse low density gas. The LVG method is commonly used to model the excitation conditions of molecular gas, in order to interpret the origin of the observed line emission and its relationship to the physical state of the measured gas. It assumes a uniform abundance and velocity gradient across the modeling region, and no star formation history is considered as a cause for these conditions. It is this singular distinction which is the focus of this thesis.

The excitation conditions of multiple transitions of dense gas tracers HCN and HCO^+ in M 82 have also been investigated, for example, by Seaquist & Frayer (2000). It was

found from an LVG model, that both species are excited under a common set of conditions in star-forming regions where the $n(\text{H}_2)$ is near 10^5 cm^{-3} , $T_{kin} = 50 \text{ K}$, and the abundances of HCN and HCO^+ are 2×10^{-8} and 1×10^{-8} , respectively (Seaquist & Frayer, 2000). Molecular lines are commonly observed at $22''$ beam size, which covers about 680 pc of the center with a total H_2 mass of a few times $10^8 M_\odot$ in M 82.

The atomic coolant, far-infrared lines in M 82, e.g. [C I] $370 \mu\text{m}$, $612 \mu\text{m}$, [O I] $63 \mu\text{m}$, $146 \mu\text{m}$, and [C II] $158 \mu\text{m}$, have been studied by several groups (e.g. Stutzki et al., 1997; Colbert et al., 1999; Petitpas & Wilson, 2001; Negishi et al., 2001, and references therein). As is the case for the molecular lines, the ratios of these cooling lines may be used to constrain physical parameters and possibly the age of the starburst. These ratios are sensitive to the physical and chemical conditions (density, temperature, and abundance), hence provide an opportunity to model the physical state of the neutral gas. In addition, unlike optical atomic line tracers, these FIR lines are relatively insensitive to extinction. A close examination of these lines emitted in M 82 may provide a template for future comparisons to infrared-bright, dust obscured starburst galaxies like M 82, including those at high- z .

In order to provide a useful indication on the starburst age(s), it is desirable to make comparisons with multiple transitions for various molecules and atoms. However, meaningful comparisons can be made only for regions where observations refer to the same beam size. The diagnostic tracers used in this study are molecular ^{12}CO , its isotope ^{13}CO , HCN, HCO^+ , and atomic C, O, and C^+ . The low- J ^{12}CO lines are easily excited at relatively low densities and temperature, and are found essentially in every molecular gas cloud, and so they are good diagnostic tools for total molecular H_2 content, diffuse gas conditions, and star formation history. The less abundant ^{13}CO isotope has a much lower optical depth, and the line ratios between optically thin transitions in ^{13}CO are more reliable probes of the total gas content than ^{12}CO . The CO molecule is not considered a good tracer of dense and highly excited gas that is directly involved in starburst (i.e.

earlier phase of star formation). However, molecular HCN and HCO⁺ lines are more sensitive to dense gas (i.e. pre- or post-birth of stars) owing to their higher critical densities than CO. The atomic C, O, and C⁺ fine structure lines are excellent probes of the PDRs in starburst regions, and their line ratios can be used for diagnosing the conditions of the associated FUV flux and gas density, as well as for indicating the ages of the later stages of starbursts.

In this work, we use the observations of molecular and atomic gas in the central 1 kpc of M 82 described above. Tables 5.2- 5.4 summarize the molecular data to be used in comparisons with our models. The data in Table 5.2 is from Weiss et al. (2005) and covers the central 1 kpc region of the disk with dimensions approximately 60'' × 18'', whereas the data in Table 5.3 and 5.4 are for a 22'' diameter region (Seaquist & Frayer, 2000; Mao et al., 2000). Table 5.5 summarizes the atomic data (Negishi et al., 2001) to be used in our ratio-ratio diagram analysis, which are obtained from a larger beam area (60'' - 80'') than for the molecular data. Note that the atomic C data are not included in our table and later ratio-ratio analysis, because the two [C I] line data correspond to different beam sizes (Stutzki et al., 1997).

There are good data on HI 21 cm in the disk of M 82 (e.g. Cottrell, 1977), the HI 21 cm emission is ideal for estimating HI column densities, but this parameter does not trace the gas excitation, which is the primary focus of our model analysis as described in Chapter 1.

Table 5.2. Observations of molecular ^{12}CO in the center 1 kpc of M 82.

Transition	Observation [Jy km s $^{-1}$]
CO(1-0)	$5.1\text{E}3 \pm 5.0\text{E}2$
CO(2-1)	$2.2\text{E}4 \pm 5.0\text{E}3$
CO(3-2)	$4.9\text{E}4 \pm 8.0\text{E}3$
CO(4-3)	$6.4\text{E}4 \pm 1.3\text{E}4$
CO(5-4)	...
CO(6-5)	$9.7\text{E}4 \pm 2.4\text{E}4$
CO(7-6)	$7.4\text{E}4 \pm 2.3\text{E}4$
CO(8-7)	...
CO(9-8)	...

Note. — Data are taken from Weiss et al. (2005). The center mask defined in Weiss et al. (2005) is ~ 1000 arcsec 2 . The region is a roughly rectangular region about $60'' \times 18''$ with the principal axis along the major axis of the disk.

Table 5.3. Observations of molecular HCN, and HCO⁺ in the center 22'' of M 82.

Transition	Observation [Jy km s ⁻¹]
HCN(1-0)	63.0 ± 8.0
HCN(2-1)	...
HCN(3-2)	276.0 ± 42.0
HCN(4-3)	222.0 ± 43.0
HCN(5-4)	...
HCN(6-5)	...
HCO ⁺ (1-0)	130.0 ± 14.0
HCO ⁺ (2-1)	...
HCO ⁺ (3-2)	832.0 ± 90.0
HCO ⁺ (4-3)	795.0 ± 80.0
HCO ⁺ (5-4)	...
HCO ⁺ (6-5)	...

Note. — Data are taken from Seaquist & Frayer (2000).

Table 5.4. Observations of molecular ^{12}CO and ^{13}CO in the center $22''$ of M 82.

Transition	Observation ^a [Jy km s ⁻¹]
$^{12}\text{CO}(1-0)$	$3.4\text{E}3 \pm 3.1\text{E}0$
$^{12}\text{CO}(2-1)$	$1.7\text{E}4 \pm 2.5\text{E}1$
$^{12}\text{CO}(4-3)$	$3.9\text{E}4 \pm 1.1\text{E}3$
$^{12}\text{CO}(7-6)$	$4.6\text{E}4 \pm 1.4\text{E}3$
$^{13}\text{CO}(1-0)$	$2.1\text{E}2 \pm 2.6\text{E}0$
$^{13}\text{CO}(2-1)$	$1.2\text{E}3 \pm 2.3\text{E}1$
$^{13}\text{CO}(3-2)$	$2.2\text{E}3 \pm 2.1\text{E}2$

Note. — Data are taken from Mao et al. (2000).

^aThe 1σ errors in the line fluxes were determined from Gaussian fits. No systematic uncertainties are included.

Table 5.5. Observations of atomic O and C⁺ in the center 80'' of M 82.

Transition	Observation
	[10 ⁻¹⁵ W m ²]
[O I]63 μm	169 \pm 34
[O I]145 μm	15 \pm 3
[C II]158 μm	128 \pm 26

Note. — Data are taken from Negishi et al. (2001).

5.2.2 Model Fit to the Line Spectral Energy Distribution

The SED of ^{12}CO Lines

This section outlines the procedure for fitting our model to the data. The model constitutes the family of expanding shells outlined in previous chapters. The data are contained in Table 5.2, comprising the flux densities of ^{12}CO in the central ~ 1 kpc of the M 82 disk (Weiss et al., 2005). We consider first a model involving a single instantaneous starburst, and later consider whether extended starbursts could also provide an adequate fit.

Part I: Instantaneous Starburst Model

Our initial starburst model involves a single event in which all of the stars are formed simultaneously and instantaneously, associated with a unique age t and a star cluster mass M_* (corresponding to a GMC mass $M_{\text{GMC}} = 4M_*$ at the birth time). An instantaneous model, though physically unrealistic, is an acceptable representation of the SED if the duration of the star forming event is short compared to the age of the starburst. The intent is to derive these two parameters by fitting to the data. By extension, the total mass of H_2 swept-up in the ISM at any age is also determined. A comparison of the latter with the total observed mass of H_2 in the region will also provide an estimate of the degree of disruption and porosity of the ISM caused by this starburst.

The method used for fitting is a numerical chi-squared (χ^2) procedure, where the reduced chi-squared is,

$$\chi^2_{\nu} = \frac{1}{N-p} \sum_N \left[\frac{S_{obs}^J - S_{model}^J(f, t)}{\sigma^J} \right]^2 \quad (5.1)$$

where N is the number of data points ($N = 6$ for CO data), p is the number of free parameters (in this case $p = 2$), $N - p$ (> 0) is the degrees of freedom, σ^J is the standard error in flux measurement S_{obs}^J in rotational level J . The quantity S_{model}^J represents the corresponding model to be fitted, expressed as,

$$S_{model}^J(f, t) = f S_{temp}^J(t) \quad (5.2)$$

where $S_{temp}^J(t)$ is the model template line SED at age t , as given in Fig. 4.14 and Table 4.4 (see Chapter 4), corresponding to a model template GMC mass M_{temp}^{GMC} , a model template cluster mass M_{temp}^* , and a model template swept-up mass by the shells M_{temp}^{sh} . The values for these parameters are $M_{temp}^{GMC} = 1.69 \times 10^7 M_{\odot}$, and $M_{temp}^* = 4.2 \times 10^6 M_{\odot}$. These initial masses correspond to the 127 clusters included in Table 3.1 (see Chapter 3). The ratio of stellar cluster to GMC mass is 0.25 according to the assumed SFE. The adjustable dimensionless parameter f is introduced to control the amplitude of the model line SED (and hence the total cluster mass), and the age parameter t controls its shape and slope. These are simultaneously adjusted to provide the best fit corresponding to the minimum χ_{ν}^2 . By assumption, the line fluxes $S_{temp}^J(t)$ are summed over the contributions of all clusters and GMCs, so that the best fit GMC mass M_{GMC} , cluster mass M_* , and the shell swept-up mass M_{sh} are determined from the corresponding best fit value of the parameter f by the relations,

$$M_{GMC} = f M_{temp}^{GMC}, \quad (5.3)$$

$$M_* = f M_{temp}^*, \quad (5.4)$$

$$M_{sh} = f M_{temp}^{sh} \quad (5.5)$$

Using Equation (5.1) we calculate χ_{ν}^2 for a range of t and f . A minimum χ_{ν}^2 value is obtained with a standard error estimation (i.e. the traditional likelihood method from using an inverse Hessian matrix or covariance matrix). In the results there were found to be two minima with acceptable values of $\chi_{\nu}^2(\min)$, one for the *Winds* phase and the other for the *post-SN* phase. The two solutions are given in Table 5.6 with the corresponding values of $\chi_{\nu}^2(\min)$.

The chi-squared contours surrounding each minimum are shown in Fig. 5.2, where the

Table 5.6. The chi-squared fitting results to the observed ^{12}CO line SED.

Phase	t (Myr)	f	$M_*(t=0)$ ($10^6 M_\odot$)	$M_{GMC}(t=0)$ ($10^7 M_\odot$)	M_{sh} ($10^8 M_\odot$)	$\chi_\nu^2(\text{min})$
Winds	0.07 ± 0.03	9.23 ± 0.8	40 ± 3.4	16 ± 1.4	1.6 ± 0.1	0.54
post-SN	5.6 ± 0.5	0.87 ± 0.07	3.7 ± 0.3	1.5 ± 0.1	2.0 ± 0.1	0.20

contours are $\chi_\nu^2 = \chi_\nu^2(\text{min}) + i / (N - p)$, and $i = 1, 2, 3, \dots$, corresponding to contour intervals of 1σ . The existence of a numerically acceptable solution for each phase signifies that there exist conditions in the molecular clouds of the *Winds* phase which are similar to those found in the compressed shells associated with the *post-SN* phase. However, only the *post-SN* phase solution is acceptable physically, since an age of 0.07 Myr is implausibly small for a variety of reasons. For example, it is impossibly short compared to the dynamical time for the region (a few Myr) which would control the duration of the starburst. Such a small age might be barely plausible for an individual shell, but not for the molecular gas occupying this entire region.

The best fit line SEDs and ^{12}CO line SEDs at 4 and 7 Myr are shown superposed on the data in Fig. 5.3. The initial stellar mass and GMC mass are relatively small, but the impact on the surrounding ISM is significant. The total H_2 mass swept up by the shells is $\sim 2.0 \pm 0.1 \times 10^8 M_\odot$ at the best fit age of 5.6 Myr. This predicted value is in good agreement with the total gas mass within the central 1 kpc region obtained by other studies (a few $10^8 M_\odot$) (e.g. Rieke et al., 1980; Mao et al., 2000). The model total stellar luminosity at this best fit is $\sim 1.4 \times 10^9 L_\odot$ using information from *Starburst99* based on our instantaneous starburst model.

To examine the impact on the ISM, we can compare the swept-up mass with the

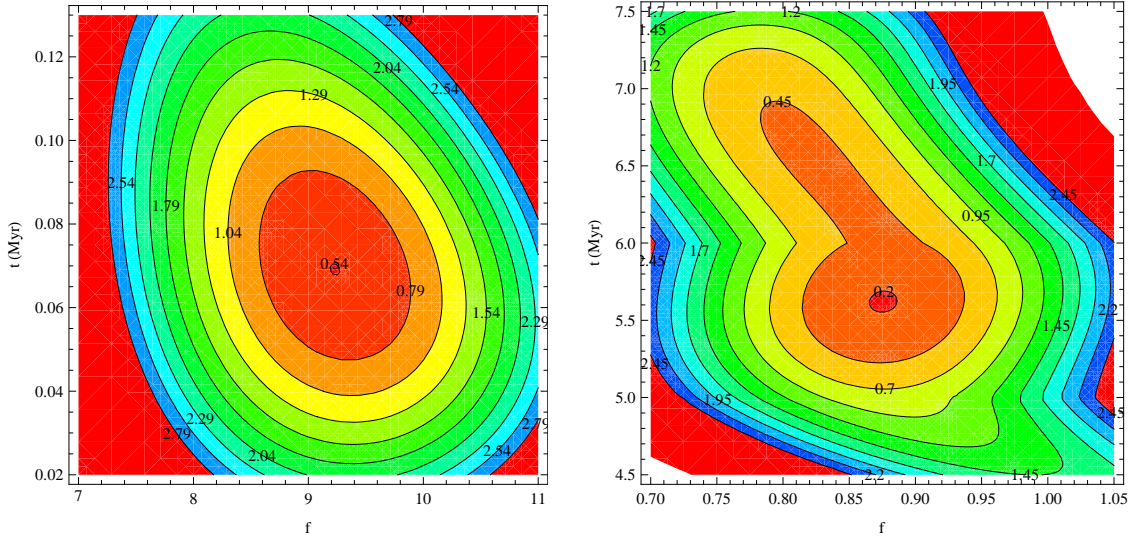


Figure 5.2 A contour plot of χ^2 values as a function of mass coefficient f and burst age t at *Winds* phase (left panel) and *post-SN* phase (right panel).

total ISM mass in our model, assuming our uniform model ISM density of 30 cm^{-3} (in H_2 form). Within the central region associated with this study ($\sim 1 \text{ kpc}$) the total mass of H_2 gas at this density would be $\sim 7.0 \times 10^8 M_\odot$. Thus, the fraction of the total mass swept up by the expanding shells at $t = 5.6 \text{ Myr}$ is about 29%, which also represents the volume fraction in shells, i.e. the porosity of the medium. We conclude that the effect of a starburst of this magnitude on the ISM is to *puncture* about 30% of the ISM with holes, leaving shells and shell fragments, the latter which (according to our model) represent the entire observed CO emission.

In order to investigate how sensitive the results are to the assumed initial upper mass limit of the cluster spectrum (and corresponding GMC mass spectrum), we repeated the above analysis with revised upper mass limits of both $7.5 \times 10^5 M_\odot$ and $2.5 \times 10^5 M_\odot$ for the stellar spectrum, and corresponding GMC upper mass limits of $3 \times 10^6 M_\odot$ and $10^6 M_\odot$ respectively. For the first case, we find $t = 5.0 \pm 0.4 \text{ Myr}$, $f = 1.8 \pm 0.2$ with $\chi_\nu^2 = 0.9$, and for the second case an unacceptable fit with a $\chi_\nu^2 = 33$. Thus, a comparable solution may be found with a choice of a slightly lower upper mass cutoff,

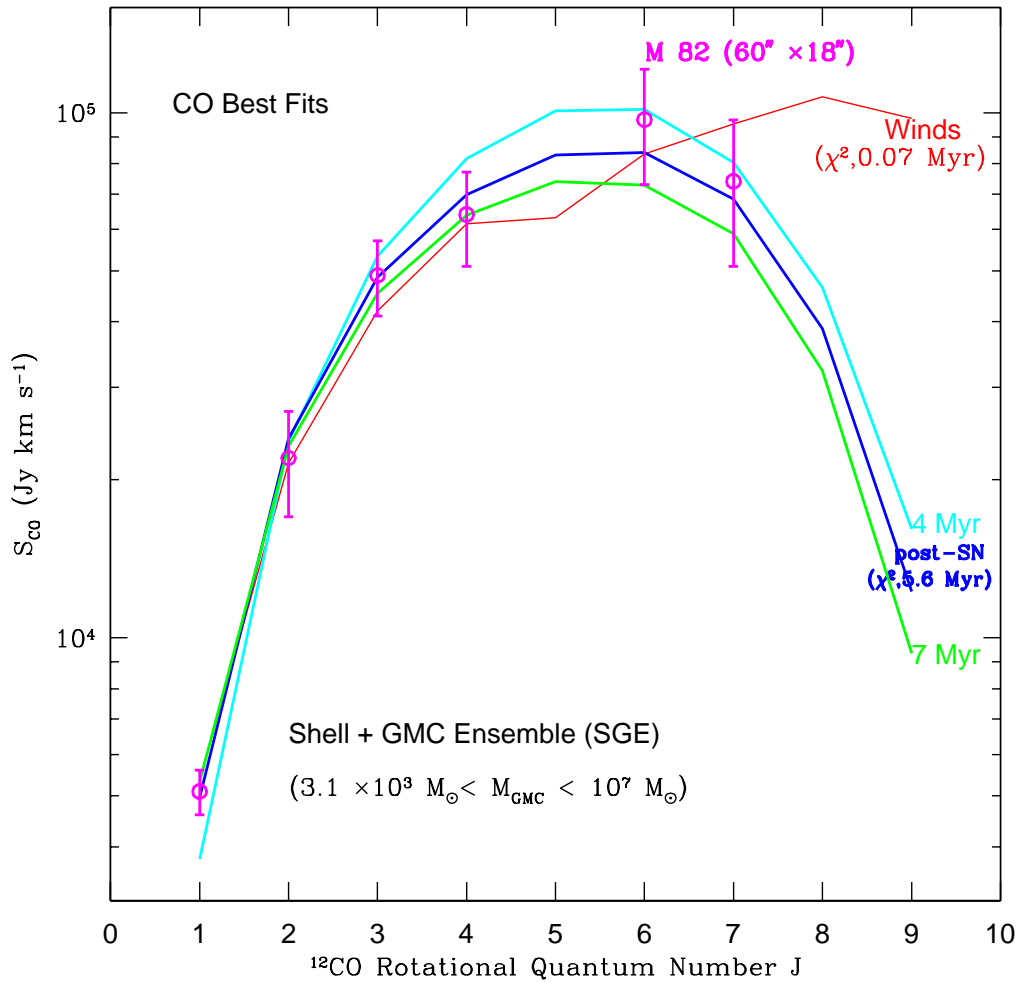


Figure 5.3 A χ^2 fit of an instantaneous starburst model to the ^{12}CO line SED for the central 1 kpc disk region of M 82. The red curve indicates the best fit age at 0.07 Myr for the *Winds* phase, the blue curve is the best age at 5.6 Myr for the *post-SN* phase, the cyan curve is the line SED at 4 Myr, the green curve is the line SED at 7 Myr, and the observed data are indicated by magenta open circles with error bars (Weiss et al., 2005).

but no acceptable solutions are found with values reduced by a factor of 10 or more in the upper cutoff of the cluster mass spectrum. We conclude that the model can provide acceptable fits to the data only if the dominant initiating starburst clusters are massive, at least $5 \times 10^5 M_{\odot}$.

Our models show that the H_2 density of the shells at the best fitted age 5.6 Myr is between 10^3 and 10^4 cm^{-3} , and the gas temperature is $\sim 50 - 100 \text{ K}$. These values are comparable with the two-component LVG predictions (Weiss et al., 2005). The evolution of CO abundance as a function of A_V is illustrated in Fig. 4.8. The CO abundances in massive clouds (M6 - M7) are above 10^{-5} with respect to the total H density, providing most of the CO emission.

Part II: Extended Starburst Model

The foregoing discussion and results assume an instantaneous starburst with the result that our CO best fit model has an age of 5.6 Myr. The question naturally arises whether a model with a period of more continuous star formation would also provide a satisfactory solution. One can anticipate that the answer might be yes, if the best fit line SED were to be roughly equally represented by the SED of an outburst at one epoch, or an average SED over some time period roughly centered on, and symmetrically distributed about this epoch. Fortunately, it is straight forward to test this hypothesis since the SED for a smoothly varying star formation model may be constructed from a superposition of instantaneous bursts at different times.

We are thus led to consider the extreme case of a uniform star formation rate (or SFR) occurring between an epoch 10 Myr ago and the present time. This starting point of the event may be considered appropriate because the most massive shells from even earlier epochs would now be large enough to exceed the thickness of the nuclear disk and thus their emission would begin to fall outside the region modeled. Fortuitously, this period is also almost symmetrically distributed about the epoch for the best fit instantaneous model.

We do not discuss the procedure in detail here, since the analysis proceeds as before, but with only one parameter, namely the star formation rate over the past 10 Myr. The SED employed is then an integral of the CO line SED profiles over a time period of 10 Myr. The result is that an acceptable fit (minimum $\chi^2_{\nu} = 0.78$) can be found for a continuous $SFR = 0.5 \pm 0.05 M_{\odot} \text{ yr}^{-1}$. The total stellar mass produced during this period is $(5.0 \pm 0.5) \times 10^6 M_{\odot}$, which is, not surprisingly, close to the total mass (i.e. $4.3 \times 10^6 M_{\odot}$) required for the single epoch model. The conclusion is that a uniform SFR over the past 10 Myr also produces a satisfactory fit to the ^{12}CO data. In addition, it may be plausibly inferred that a variety of star formation histories would work, provided the SFR rate profile is more or less symmetrically distributed about the epoch of 5.6 Myr.

The implication of this result is that in terms of the agreement between the model and the data, the star formation need not be instantaneous, or even sharply peaked at 5.6 Myr. However this epoch nevertheless represents a unique point of time associated with the history of star formation in M 82 since it would emerge from various representations of the star formation profile. If the star formation is viewed as instantaneous, then it would have occurred 5 - 6 Myr ago. If the star formation is not instantaneous, then this epoch would represent a characteristic time about which the recent star formation history is centered.

The SEDs of HCN and HCO⁺ Lines

We conducted various χ^2 tests for HCN and HCO⁺ using a two parameter model as before, but we were unable to find a satisfactory fit when including both HCN and HCO⁺ (reduced χ^2 values are $> \sim 30$). We then performed a two parameter fit ($N = 3, p = 2$) to HCN and HCO⁺ independently. Good fits are found only in the *Winds* phase. The fitting results are given in Table 5.7 with the corresponding values of $\chi^2_{\nu}(\text{min})$.

Figs. 5.4 and 5.5 show the best fitted line SEDs of HCN and HCO⁺ (fitted independently of one another) superposed on the observed $22''$ data (Seaquist & Frayer, 2000),

Table 5.7. The chi-squared fitting results to the observed HCN and HCO⁺ line SEDs (22'').

Molecule (Winds)	t (Myr)	f	$M_*(t=0)$ ($10^6 M_\odot$)	$M_{GMC}(t=0)$ ($10^7 M_\odot$)	M_{sh} ($10^8 M_\odot$)	$\chi^2_\nu(\text{min})$
HCN	0.04 ± 0.05	0.81 ± 0.2	3.5 ± 0.8	1.4 ± 0.3	0.14 ± 0.03	0.64
HCO ⁺	0.75 ± 0.02	38.8 ± 2.2	165.5 ± 9.0	65.8 ± 3.7	7.4 ± 0.4	0.22

respectively. For the best fit HCN model, the corresponding HCO⁺ line fluxes are several order of magnitudes lower than the data. Neither *Winds* solution is acceptable for reasons similar to that for the CO *Winds* phase solution. The burst age is too young compared to the dynamical time for the region (a few Myr). In addition, since there is no solution in the *post-SN* regime, there can be no agreement with the age determined from the CO data. Hence, our fitting results show that our model does not produce significant emission from the shell ensemble except at very early stages (the *Winds* phase). The fluxes in the *post-SN* stage (required by the CO model fitting results) are far too low to account for the data, since the gas densities fall below the critical densities for all transitions. HCN may be associated with the dense shells and their parent GMCs at the earlier phase of starburst evolution, but another principal source is required, most probably dense gas associated with the cores of potential star forming regions, not included in our model. The low HCO⁺ line fluxes predicted by our models may be a result of the low chemical abundance of HCO⁺ due to a low cosmic-ray rate included in our model simulations.

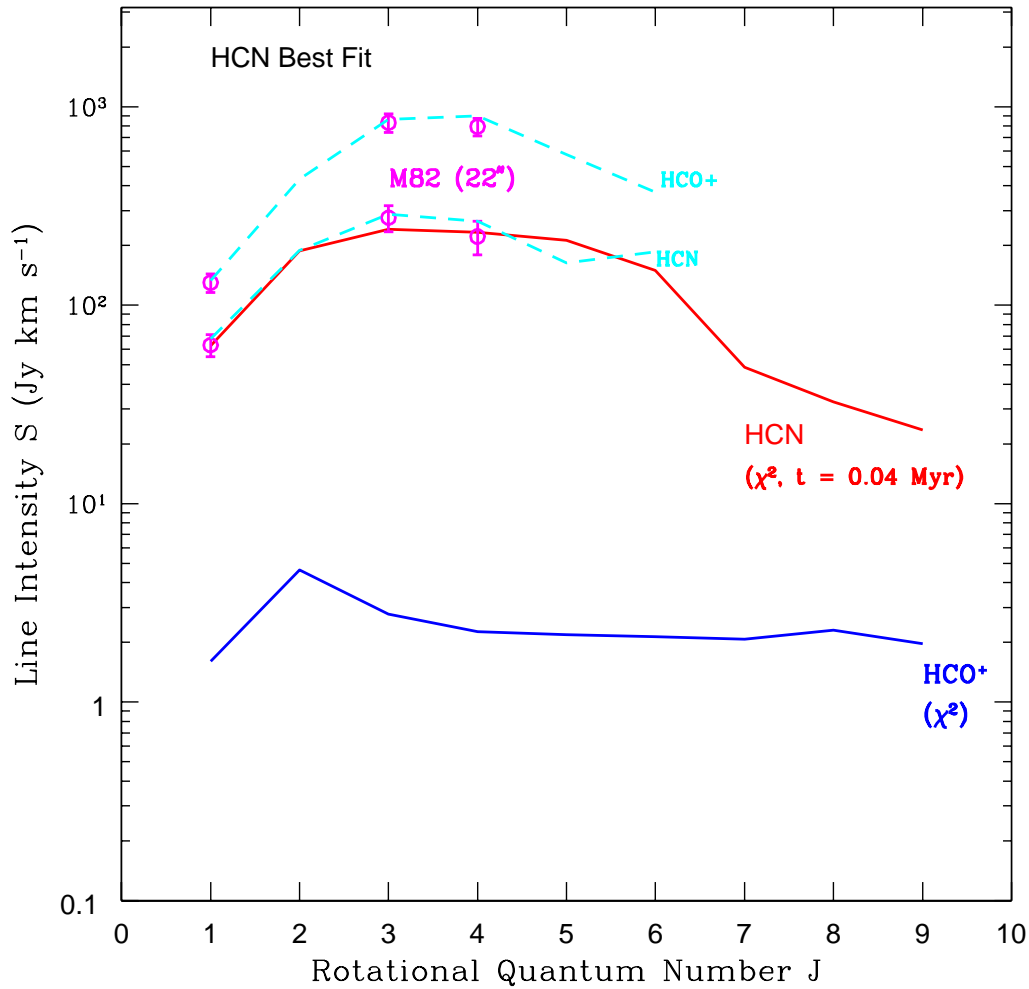


Figure 5.4 A χ^2 fit of an instantaneous starburst model to the HCN line SED for the central $22''$ region of M 82. The magenta circles with error bars connected with cyan dashed lines are the observed HCN and HCO⁺ data for the central $22''$ region in M 82 (Seaquist & Frayer, 2000), and the curves (cyan color) correspond to their model based on LVG methods. The red solid curve is the best fit HCN line SED to the data. The blue solid curve is the model HCO⁺ line SED at the HCN best fit.

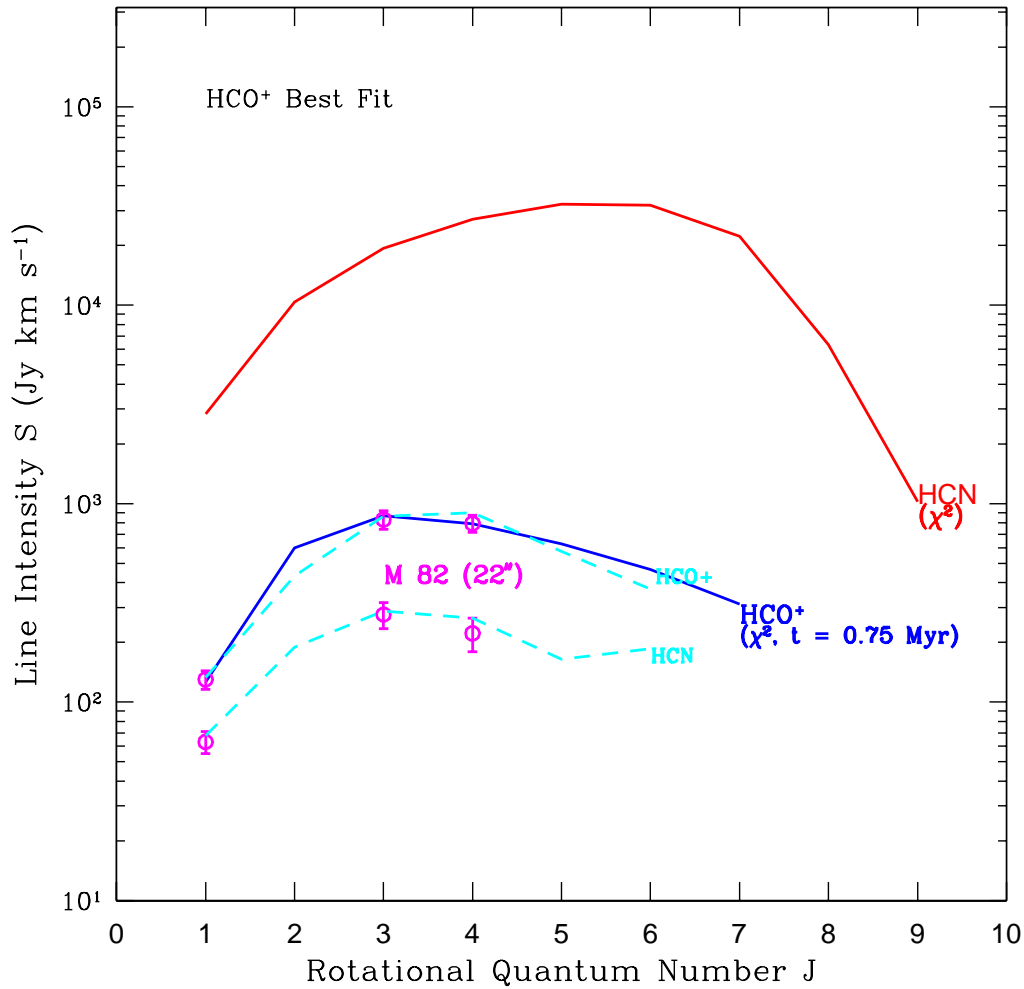


Figure 5.5 A χ^2 fit of an instantaneous starburst model to the HCO^+ line SED for the central $22''$ region of M 82. The magenta circles with error bars connected with cyan dashed lines are the observed HCN and HCO^+ data for the central $22''$ region in M 82 (Seaquist & Frayer, 2000), and the curves (cyan color) correspond to their model based on LVG methods. The blue solid curve is the best fit HCO^+ line SED to the data. The red solid curve is the model HCN line SED at the HCO^+ best fit.

5.2.3 Molecular and Atomic Line Ratio Diagrams

The line intensity/flux ratio-ratio diagram can be another diagnostic tool for studying the gas excitation conditions and properties, as well as their relations to starburst evolution, especially when there are not enough data points available for the type of model fitting discussed in the previous section. Since the line ratio is independent of the total gas mass in the measured region, the ratio-ratio diagram cannot be used to provide an estimate of the total gas mass directly. However, once the age t is obtained, we can scale the template line flux spectrum to the flux observed, and calculate the model value for the swept-up H_2 mass.

^{12}CO and Its Isotope ^{13}CO

Fig. 5.6 shows our model line intensity ratio of ^{12}CO high J transitions to the (1-0) transition ($I_{\text{CO}} / I_{\text{CO}(1-0)}$, I_{CO} in units of Jy km s^{-1}) as a function of time. The high ratios (> 1.0) seen in the *Winds* phase and earlier stages of the *post-SN* phase imply highly excited gas arising from warm and dense gas components in the model ensemble. A good match between our models and the observed data is found at 5 - 6 Myr, which is consistent with our reduced χ^2 fitting to the ^{12}CO line SEDs.

Fig. 5.7 illustrates the ratio-ratio diagrams for different transitions involving ^{12}CO and ^{13}CO predicted by our model (*post-SN*), and a comparison with the observations. The observed data refer to the center of M 82 with a beam-width of $22''$ (see Table 1 in Mao et al. 2000). All line brightnesses are compared in units of Jy km s^{-1} . The isotope abundance ratio $[\text{CO}]/[\text{CO}]$ of 55 is adopted for the ensemble modeling. In the plots, we include the systematic uncertainties (31% for $^{12}\text{CO}(7-6)$, 20% for $^{12}\text{CO}(4-3)$, 16% for $^{12}\text{CO}(3-2)$, 23% for $^{12}\text{CO}(2-1)$, 10% for $^{12}\text{CO}(1-0)$) into the line ratio error estimations (i.e. sizes of error bars). In plot (a) the model ratios of $^{12}\text{CO}(7-6)/(4-3)$ versus $(2-1)/(1-0)$ match nicely (as expected) with the observations at age 5 - 6 Myr for the central $22''$. It is similar to the age derived from the chi-squared fit to the ^{12}CO line SED in the center

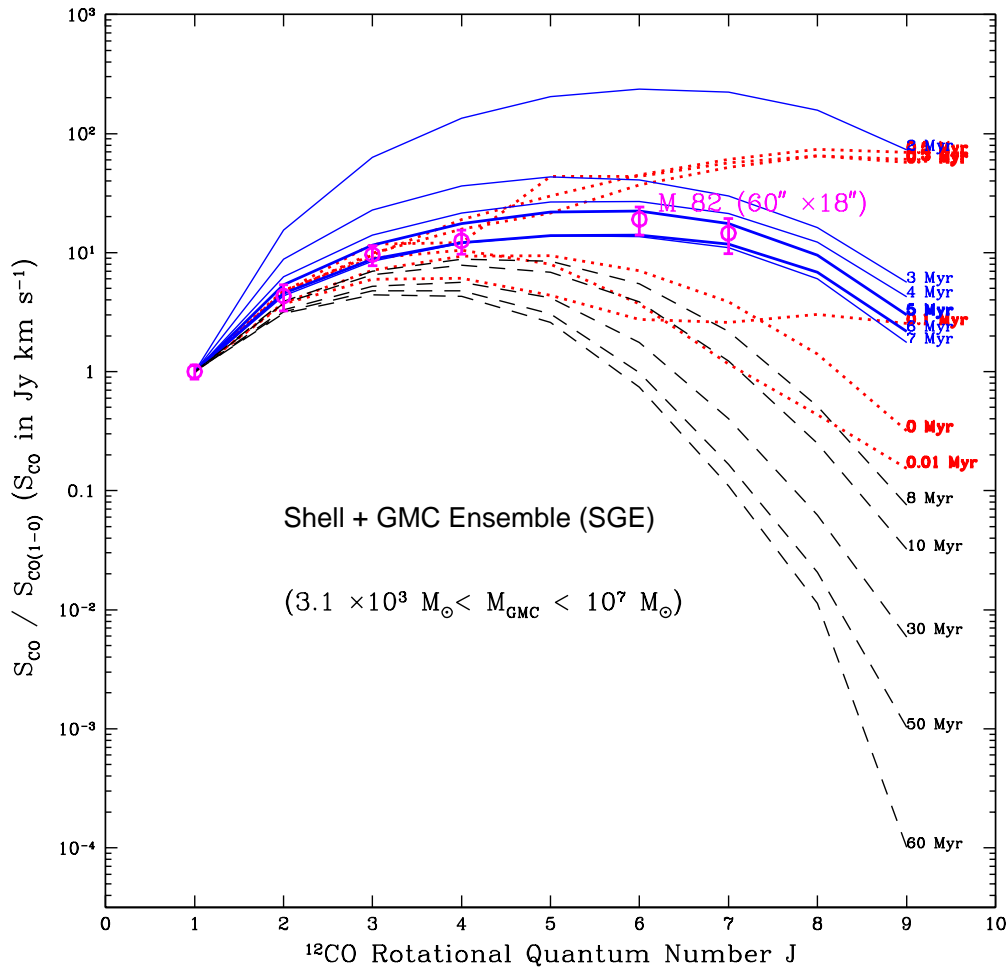


Figure 5.6 Plot of the ^{12}CO line intensity ratios as a function of rotational quantum number J for a sequence of burst ages. The red dotted curves indicate *Winds* phase ($t \leq 0.7$ Myr), the blue solid ($0.7 < t \leq 8$ Myr) and black dashed ($t > 8$ Myr) curves indicate *post-SN* phase. The observed CO data of the central 1 kpc region are indicated by magenta open circles with error bars (Weiss et al., 2005).

$60'' \times 18''$ (Weiss et al., 2005) even though the angular size of the region is different. This is expected, since $\sim 65 - 80\%$ of the ^{12}CO emission from the inner 1 kpc disk originates from the central $22''$ starburst regions. Plots (b) and (c) show a poor match between our model line ratios of $^{13}\text{CO}(3-2)/(2-1)$ versus $(2-1)/(1-0)$ and $^{12}\text{CO}(2-1)/^{13}\text{CO}(2-1)$ versus $^{12}\text{CO}(1-0)/^{13}\text{CO}(1-0)$ (blue-dashed curves) and the observed data. The closest match within the observed uncertainties is 7 - 8 Myr for plot (b), 5 - 6 Myr for plot (c), where the latter is in a fair agreement with ^{12}CO best fitted age.

Our model fails to produce the right ratios for lines involving ^{13}CO . If the choice of the isotope abundance ratio is to be considered as the reason for such poor fit, adopting a different isotope abundance ratio (55 is used in this study) can affect the result in plot (c) but not that in plot (b). Mao et al. (2000) indicated that their $^{13}\text{CO}(2-1)$ values should be considered with caution, due to uncertainty of convolving a smaller beam ($13''$) to a larger beam size ($22''$). If we assume that the best match age for plot (b) and (c) should be between 5 and 6 Myr, and if we assume that an erroneous value for the $^{13}\text{CO}(2-1)$ model flux is the reason for lower ratios seen in plot (b) and (c), we estimate that this value is underestimated by a factor of 1.5. Another factor that contributes to the poor match between our model results and the data is that the line ratios involving ^{13}CO may be particularly sensitive to optical depth if the intensities are not optically thick.

We also investigated the effect of reducing the upper mass limit to the GMC mass spectrum as was done for the ^{12}CO model, and found that changing the upper mass limit to the GMC mass spectrum has no effect in resolving this problem.

Atomic O and C⁺

Fig. 5.8 shows the model ratio-ratio diagram for $[\text{O I}]63\mu\text{m}/[\text{C II}]158\mu\text{m}$ versus $[\text{O I}]63\mu\text{m}/[\text{O I}]145\mu\text{m}$, and a comparison with the observations of these atomic lines from the central 1.2 kpc region in M 82 (Negishi et al., 2001). All line fluxes are compared in units of W m^{-2} . The model $[\text{C II}]158\mu\text{m}$ line flux may be underestimated, since we

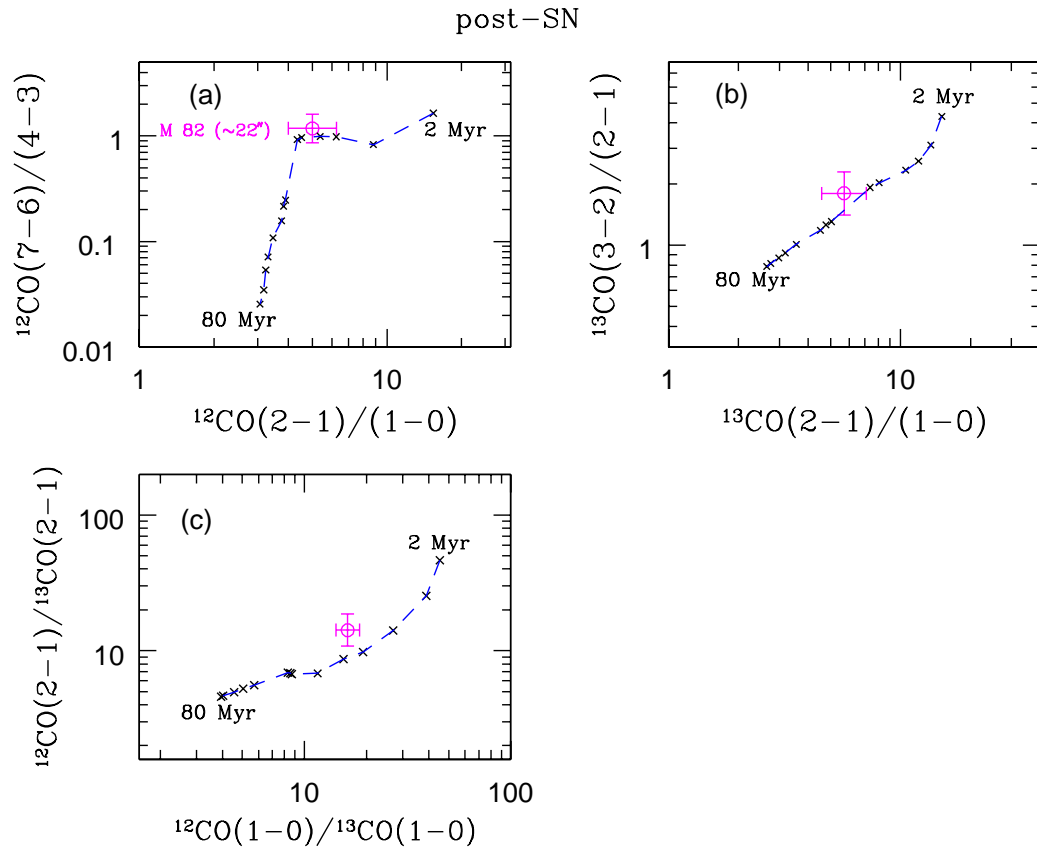


Figure 5.7 The ratio-ratio diagrams of molecular ^{12}CO and ^{13}CO line intensities (in units of Jy km s^{-1}). Model results for a shell ensemble are indicated by the crosses connected with blue dashed lines. The age sequence is 2, 3, 4, 5, 6, 7, 8, 9, 10, 20, 30, 40, 60, and 80 Myr. The magenta filled circles with error bars are the observed data ($22''$ resolution data from Table 1 of Mao et al. 2000; the errors include systematic uncertainties).

ignore the line emission that arises from the H II region. A good match between our model and the observation is obtained with age $t \sim 10$ Myr. The age predicted from atomic data is older than the age ($\sim 5 - 6$ Myr) derived from our ^{12}CO line SED analysis. This may be because the atomic line data are based on a $80'' \times 80''$ beam area whereas the ^{12}CO line data pertain only to the $60'' \times 18''$ beam area. We suggest that these two ages may be a result of sampling different regions. More discussion of this possibility will be given in § 5.3.2.

The ranges of gas conditions for the model shells at 10 Myr are $G_0 \sim 350 - 1.4 \times 10^4$, $n(\text{H}_2) \sim 10^2 - 2.4 \times 10^3 \text{ cm}^{-3}$, and $T_{gas} > 20$ K. The gas conditions derived from our atomic models for this sampling region are comparable with the study by Colbert et al. (1999) ($G_0 = 630$, $n = 2.0 \times 10^3 \text{ cm}^{-3}$), but the age is greater than that (3 - 5 Myr) derived by Colbert et al..

The total molecular gas swept up into shells cannot be obtained directly from the ratio-ratio diagram. However we can obtain this from the ratio of observed [O I]63 μm line flux to the model template [O I]63 μm flux at age 10 Myr, i.e. $f = S_{obs} / S_{model}^{temp} = 0.84$, where $S_{obs} = 169 \times 10^{-15} \text{ W m}^{-2}$ and $S_{model}^{temp} = 202 \times 10^{-15} \text{ W m}^{-2}$. We compute the total H_2 gas in the measured $80''$ region by multiplying $f = 0.84$ by the model template H_2 mass M_{model}^{temp} . Hence, the result is $M(\text{H}_2)$ at age 10 Myr is $\sim 3.4 \times 10^8 M_{\odot}$.

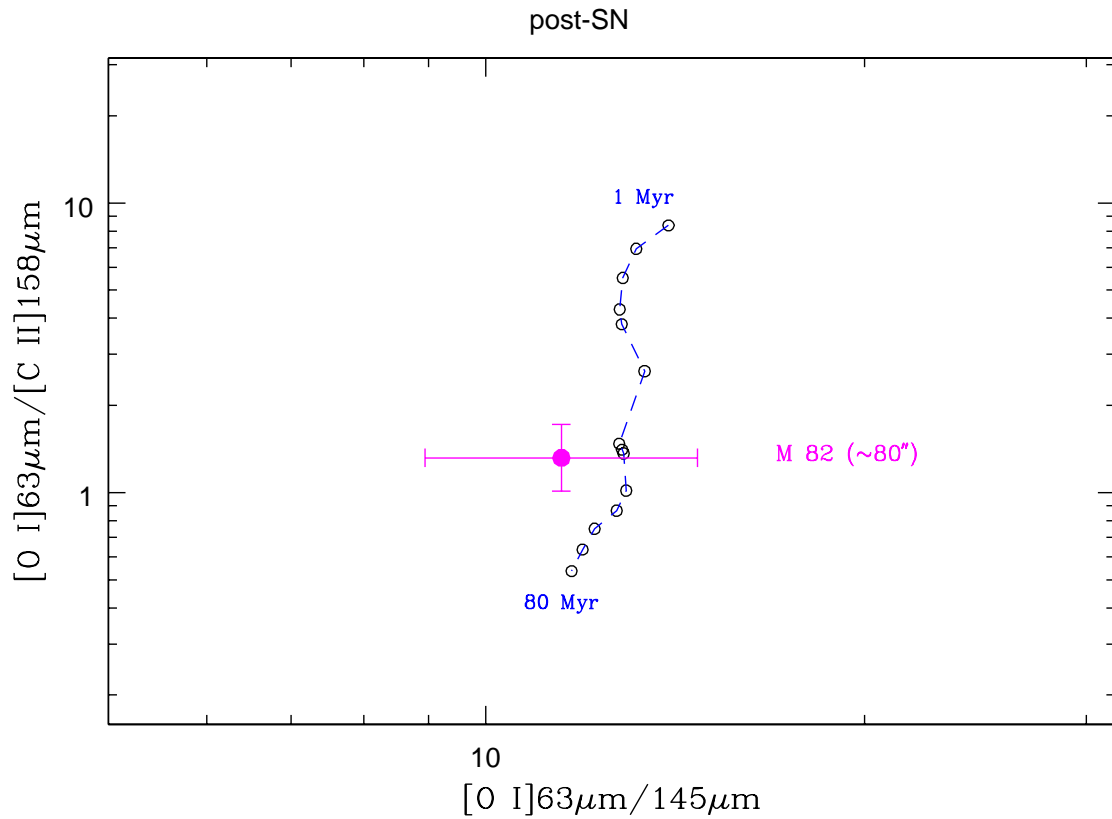


Figure 5.8 The ratio-ratio diagram of atomic fine structure line fluxes (in units of W m^{-2}). The models are indicated by open circles connected with a blue-dashed curve for *post-SN* phase. The age sequence is 1, 2, 3, 4, 5, 7, 8, 9, 10, 20, 30, 40, 60, and 80 Myr for the *post-SN* phase. The filled circle with error bars show the observed data for the center 1.2 kpc of M 82 (Negishi et al., 2001).

5.3 Discussion and Summary

We have presented a set of starburst models that allow us to relate the observed FIR/sub-mm/mm properties of molecular and atomic gas in a starburst galaxy to its recent star formation history. We have also applied our models to the observations of the expanding supershell centered around the M 82 SNR 41.9 + 58 and the central 1 kpc starburst region in M 82, in order to arrive at some conclusions about the nature of these two regions.

5.3.1 An Expanding Supershell Associated with SNR 41.9+58

The very good agreement between our supershell kinematic model and the observations is consistent with the hypothesis that this expanding supershell is created by strong mechanical winds from a young star cluster with a total mass of about $2.5 \times 10^6 M_{\odot}$ which formed at its center about 0.8 Myr ago. This agreement also suggests that the set of models we have put forward in this study may be used to interpret other shells in M 82 or shells in other starburst galaxies. Although like any other model, the result depends to some degree on the set of initial conditions and assumptions that we selected for our models. The reliability of the age and mass for this supershell derived from our kinematic study needs to be further examined in near future when high resolution maps of multiple transitions of CO emission in this shell are available to compare with our model.

Meanwhile we relate our model CO line ratio SED (i.e. $I_{CO}/I_{CO(1-0)}$) as a function of J) for the SNR 41.9 + 58 (i.e. M7) supershell at age 0.8 Myr to the corresponding line SED for the surrounding gas in the inner $60'' \times 18''$ starburst region of M 82. The comparison shows clearly that the emission in the M7 supershell exhibits a higher degree of excitation than the surrounding emission. This implies the existence of an excess emission at high excitation transitions in the supershell after the underlying low

excitation is subtracted out. This is consistent with the provisional detection of such excess emission at CO $J = 6 - 5$ in the region of the supershell (Seaquist & Frayer, 2000).

There are a number of issues arising from the supershell study. They are as follows: (1) it is interesting to ask whether our results are consistent with a possible physical association between the supershell and the bright SNR 41.9 + 58 near its center. If the bright SNR were within or near the SSC, there may not be sufficient gas remaining to form an SNR after the action of the winds from the cluster; and (2) the SSC responsible for the formation of the supershell might also have provided the stellar mass for the several hundred solar mass black hole detected by Chandra X-ray observations near its center (e.g. Dewangan et al., 2006). Theories for the formation of this black hole include the collapse of a *hyperstar* formed by the coalescence of many normal stars, or the direct merger of stellar mass black holes (e.g. Kawakatu & Umemura, 2005). The SSC is adequately endowed with sufficient mass since there would have been 1,700 O stars, each with mass greater than or equal to about $40 M_{\odot}$ (Yao et al., 2006).

5.3.2 Central Starburst Region

Age of Recent Starburst and Star Formation History

In order to place the work of this thesis in the context of previous work, we briefly review the methods of investigating the star formation history in galaxies, with particular emphasis on M82. Previously, the age and evolution of the starburst in the central 1 kpc region of M 82 has been studied using optical and/or (near- and mid-) infrared spectra (e.g. Förster-Schreiber et al., 2001, 2003; Smith et al., 2006; Barker et al., 2008). These data have permitted studies of the young stellar population and bright SCs using high-resolution photometry and spectroscopic imaging observations. Age and reddening for clusters can be determined using synthetic spectra from evolutionary synthesis models. For example, Rieke et al. (1993) and Förster-Schreiber et al. (2003) found two bursts (ages 10 and 5 Myr) that are needed to reproduce the observational properties. The first

burst happened in the center ~ 10 Myr ago, and the second one occurred predominantly in a circumnuclear ring and along the stellar bar ~ 5 Myr ago. The detailed modeling on small scales (25 pc) throughout the entire 3D field of view by Förster-Schreiber et al. reduced the bias toward ages preferentially in the regions with brightest continuum or line emission, and with deepest or shallowest CO bandheads.

The ages derived from near- and mid-IR observations are supported by optical spectroscopic studies, e.g., see Smith et al. (2006) and Melo et al. (2005). The latter author used H_α emission and four optical broadband filters and comparisons with images in [Fe II] 1.644 μm emission by Alonso-Herrero et al. (2003) that are not as affected by extinction as in the optical. They found 197 SSCs in the central 500 pc nuclear region of M 82. The stellar masses of these SSCs lie between 10^4 to $10^6 M_\odot$ with ages ranging from 1 to 25 Myr. Studies of SSCs also revealed that the star formation episodes outside the central 500 pc region are older (10 Myr and 25 - 60 Myr between 0.5 - 1 kpc region) (e.g. de Grijs et al., 2001). Ages derived from other optical studies are $\sim 30 - 100$ Myr by Rieke et al. (1993) and Barker et al. (2008).

The importance of optical and near-IR spectroscopy in studies of dusty star-forming galaxies has long been recognized. But studies of young stellar populations at these wavelengths remain difficult. The age determinations are affected by residual effects due to the age-metallicity degeneracy, and age-IMF degeneracy. In addition, the completeness of the sampled stellar population is affected by the unavoidable effects of extinction in the optical and near-IR.

The star formation history of M 82 has also been studied using mid-infrared and far-infrared spectroscopy (Colbert et al., 1999; Efstathiou et al., 2000). At these wavelengths, the fine structure line emissions are relatively insensitive to extinction, and hence can provide a unique probe of age and star formation history in an infrared-bright, dust-obscured galaxy like M 82. Colbert et al. (1999) obtained a burst age of 3 - 5 Myr for the central 1 kpc (65 - 85'') region using an instantaneous starburst model and a

steady-state PDR model (A CLOUDY PDR model, Version 90¹). However, their single burst model is dominated by the brightest and most recently formed stars (the hot spots seen in mid-IR). Efstathiou et al. (2000) presented an evolving starburst model for dusty media using state of the art codes for calculating the radiative transfer in dust shells, and incorporating a model for the composition and size distribution of grains in the ISM. Their study concluded that it is possible to relate the observed infrared spectrum of dust associated with a starburst to its age and its star formation history by following the evolution of an ensemble of GMCs of identical mass induced by massive star formation in their centers. They show that the burst age for the central 500 pc region of M 82 is between 10 and 30 Myr using a model with two instantaneous bursts. Their derived ages are supported by near-IR spectroscopy and high-resolution imaging of stellar clusters (Satyapal et al., 1997). Efstathiou et al. (2000) also suggested that far-IR surveys may preferentially detect older starbursts than mid-IR studies, based on an argument concerning the evolution of the luminosity of starbursts observed at different wavelengths.

Given the complexity of M 82, a full understanding of star formation epochs requires various diagnostic tools to trace different ISM components in starburst regions. Especially since both optical and near- to mid-infrared emissions are subject to higher extinction in dusty media, the selection of SSCs may be biased toward either younger or older age as mentioned before. Since the ISM is nearly transparent to FIR/sub-mm/mm emission, the analysis in this thesis, employing atoms and molecules emitting in this range, forms a useful complementary investigation to those already mentioned. Using our evolving starburst model for neutral gas media, we have been able to probe the recent star formation history of M 82 throughout the entire volume of the central starburst region.

The starburst ages derived from optical and infrared spectra are 5 - 6 Myr, 10 - 25 Myr, and 30 - 100 Myr. On large scales the burst for the outer 500 pc region is

¹<http://www.nublado.org>

younger than the inner 500 pc region (i.e. the outwardly propagating star formation) (e.g. Satyapal et al., 1997). But on the smaller scale of individual clouds (≤ 50 pc), the star formation appears to propagate inwardly (e.g. Keto et al., 2005). The age derived from our analysis of CO line SEDs and ratio-ratio diagrams is 5 - 6 Myr for the central $1 \text{ kpc} \times 280 \text{ pc}$ rectangular regions; although the region used is 1 kpc, about 70% is concentrated toward more central regions (~ 350 pc). The age derived from our atomic data is slightly older, i.e. 10 Myr for a larger area (~ 1.2 kpc). We suggest that these two ages may be a result of sampling different regions as mentioned earlier. It is unclear from our analysis whether these two ages refer to the same period of star forming activity or to two spatially separated independent bursts. A more sophisticated model and more data are needed to clarify the picture.

The burst ages derived from our model are similar to the results found in the aforementioned studies by Förster-Schreiber et al. (2003) and Efstathiou et al. (2000). However, for the atomic data there is a discrepancy between our result (10 Myr) and the study by Colbert et al. (1999) (3 - 5 Myr) using a similar set of data (by Negishi et al. 2001). Nevertheless, our derived gas conditions for the shells at 10 Myr ($G_0 \sim 350 - 1.4 \times 10^4$, $n(\text{H}_2) \sim 10^2 - 2.4 \times 10^3 \text{ cm}^{-3}$, and $T_{gas} > 20 \text{ K}$) are similar to those derived by Colbert et al.. The age discrepancy may be caused by differences in the choice of models. Colbert et al. used the steady-state PDR model (CLOUDY) to compute the line flux, while our line flux is computed using a time-dependent PDR chemistry model and a non-LTE radiative transfer model.

Molecular Gas Properties

Our evolving shell models yield familiar values for the gas density, temperature, and structure scales compared to those measured in the center of M 82 (e.g. Lynds & Sandage, 1963; Rieu et al., 1989; Stutzki et al., 1997; Seaquist & Frayer, 2000; Mao et al., 2000; Negishi et al., 2001; Ward et al., 2003). The shell densities are in the range $10^2 - 10^6$

cm^{-3} , and the gas temperatures are in the range 20 K to 1000 K across the shell for various shells. The total H_2 mass swept up by the shells within the inner $60'' \times 18''$ ($\sim 2.0 \pm 0.1 \times 10^8 M_\odot$) and $80''$ (circular region; $\sim 3.4 \pm 0.3 \times 10^8 M_\odot$) detection regions are compatible with those derived from the CO luminosity using the CO-to- H_2 conversion factor (Wild et al., 1992; Mao et al., 2000; Walter et al., 2002). It is also comparable with the total ambient gas mass in our model. Hence, the picture suggested is that of a *porous* neutral ISM in the central star-forming region of M 82, a product of evolving shells. In reality, many or most shells are probably in the form of fragments, small cloud clumps, sheets, or partial and full circular arcs (e.g. Lo et al., 1987; Yao et al., 2006, and references therein).

Molecular Ring Formation Mechanism

Although different stages of starburst evolution are applicable to different central regions of M 82, the shell sizes and the physical conditions of the gas within the rings (diameter $\sim 300 - 600$ pc) predicted by our model are similar to what is expected from models involving expanding shells from a central starburst such as those proposed by Carlstrom & Kronberg (1991). Their hypothesis is that molecular rings in M 82 are a result of compressed gas in a starburst region. This hypothesis is supported by the observations of the geometrical structure of the CO line emission and continuum emission, as well as the discovery of supershells that have not yet had time to break out of the galactic plane. However, the conclusion drawn from the shell size and average gas conditions in the inner 1 kpc region is only suggestive, since our model does not handle the physical distribution of molecular gas in the center of M 82. It is also important to realize that the foregoing interpretation of the lobes as a ring is not unique. A number of authors have argued that the molecular rings are a product of Linblad resonance instabilities associated with the gravitational effects of the bar (e.g. Shen & Lo, 1996; Wills et al., 2000).

5.3.3 Limitations of Our Model and Their Impacts

We have demonstrated that the kinematic and FIR/sub-mm/mm emission properties of individual expanding shells and star-forming regions in a starburst galaxy like M 82 can be understood by following the evolution of individual massive super star clusters or an ensemble of such clusters surrounded by compressed shells and GMCs. It is an important piece of complementary work to the existing optical and infrared studies, and it helps us to obtain a more complete and or accurate picture of star formation episodes in the center of M 82.

However, our model also has a number of caveats, limitations, and potential sources of systematic error. Here is the important list:

(1) We have neglected throughout the effects of the ambient pressure in slowing down and perhaps stalling the shells. This applies to both *Winds* and *post-SN* phases. We recall that the shells will stall when their expansion velocities decrease sufficiently that they are approximately equivalent to the sound speed $(P/\rho)^{\frac{1}{2}}$ of the external medium. To estimate the effects of this pressure, we can thus compute the sound speed associated with estimates of the pressure and compare this with the shell speeds. We compute the total pressure P_{cloud} inside the cloud, assuming it is in virial equilibrium from the following equations (McCray & Kafatos, 1987),

$$P_{cloud} = P_{external} + P_{internal}, \quad (5.6)$$

$$P_{external} = 2n_0kT, \quad (5.7)$$

$$P_{internal} = 0.5G\Sigma^2 \quad (5.8)$$

where $P_{external}$ is the external pressure, $P_{internal}$ is the internal pressure, n_0 is the cloud H_2 density, k is the Boltzmann constant (1.38×10^{-16} erg K^{-1}), G is the gravitational constant (6.67×10^{-8} cm³ g⁻¹ s⁻²), and $\Sigma = M_{GMC} / (\pi R_{GMC}^2)$. The sound speed in a GMC can be calculated from the equation,

$$c_{cloud} = \left(\frac{P_{cloud}}{\rho_{cloud}} \right)^{\frac{1}{2}} \quad (5.9)$$

We obtain a sound speed of $c_{cloud} = 19 \text{ km s}^{-1}$ in a M7 cloud ($n(\text{H}_2) = 300 \text{ cm}^{-3}$, $M_{GMC} = 10^7 M_{\odot}$, and $R_{GMC} = 47 \text{ pc}$), assuming $P_{external}/k = 10^7 \text{ K cm}^{-3}$ in starburst regions of M 82 (Silich et al., 2007), where k is the Boltzmann constant. We can further combine Equations (5.6) through (5.9) with the cloud relations Equations (3.1) and (3.2) to furthermore yield the sound speed in any given GMC,

$$c_{cloud} = 19 \text{ km s}^{-1} \left(\frac{M_{GMC}}{10^7 M_{\odot}} \right)^{\frac{1}{4}} \quad (5.10)$$

For the external ambient medium, we use the aforementioned external pressure to obtain the sound speed for the ISM ($n_{ism} = 30 \text{ cm}^{-3}$),

$$c_{ism} = 40 \text{ km s}^{-1} \quad (5.11)$$

The comparison between sound speeds inside the clouds (Equation 5.10) and shell expansion velocities for the *Winds* phase indicates that shells from cloud masses above $10^5 M_{\odot}$ would not be trapped, and those equal or below this mass would be stalled if the effects of cloud pressure were included.

We also compare the sound speeds in the ISM (40 km s^{-1}) with shell expansion velocities for the *post-SN* phase. For example, for the shells associated with the three most massive GMCs, namely M7, 3M6, and M6 in our model ensemble, the shells have radii of 220, 180, and 130 pc at the best fit age 5.6 Myr without ambient ISM pressure, respectively. But the stall radii and ages for these three shells are 112 pc at 2 Myr, 70 pc at 1.2 Myr, and 42 pc at 0.8 Myr, respectively. Thus, without the inclusion of the effects of pressure it may be said that the shell radii at the time of observation are probably overestimated by more than a factor of two compared to the stall values when pressure is included. Since the swept-up mass by the shell is proportional to the R_s^3 , an overestimate

by a factor of two in shell radius would yield a factor of eight in the total swept-up mass for a given GMC/SC mass. This may help to understand the shortfall in IR luminosity predicted by our starburst model (see point (3) for detailed discussion).

Another issue worth mentioning is that the confining pressure will vary greatly with location in the galaxy, especially between the center and the edges of the disk where some of the observed supershells are located. For example, as we mentioned earlier in this chapter, observations have detected an expanding supershell centered around the bright SNR 41.9 + 58 in both molecular line and radio continuum (e.g. Weiss et al., 1999; Wills et al., 1999). This supershell has a diameter of ~ 130 pc, an expansion velocity of ~ 45 km s $^{-1}$, and a mass of $\sim 8 \times 10^6 M_{\odot}$. If $P_{external}/k = 10^7$ K cm $^{-3}$ were the relevant external pressure in this case, then this shell will stall soon. However, the pressure may well be lower than the above value in this region, since part of the shell is seen outside the disk. Other expanding shells (incomplete arclike shapes) with velocities possibly as low as 10 to 15 km s $^{-1}$ with radii ~ 200 pc are also observed in the central region (Lo et al., 1987), suggesting a sound speed less than the 40 km s $^{-1}$ figure used above.

(2) Observations of nearby bubbles in our own Galaxy and in the Magellanic Clouds indicate that the simple adiabatic bubble/shell theory (Weaver et al., 1977; McCray & Kafatos, 1987) coupled with the mechanical luminosities calculated by *Starburst99* for this study leads to significant overestimates of the bubble pressure and hence the shell radius (e.g. Oey & García-Segura, 2004, and references therein). Either the wind power is lower or some hot bubble gas escapes from the bubble interior. In addition, Dopita et al. (2005) argued that the conventional bubble/shell dynamical model may overestimate the winds and supernova mechanical power. Another argument is that gravitational instability may induce new star formation inside the shells. If such effects were present, they would have an impact on the estimate of the total stellar mass and luminosity in our model, as described in more detail in point (3).

(3) The bolometric luminosity for the best fit cluster mass of $3.7 \times 10^6 M_{\odot}$ and best fit age of 5.6 Myr is $1.5 \times 10^9 L_{\odot}$ (based on *Starburst99* model). The observed IR luminosity of M 82 disk is about $3.0 \times 10^{10} L_{\odot}$. Since the bolometric luminosity should be an upper bound to the IR luminosity from the same stars, the shortfall in the model luminosity is about a factor of 20. This shortfall is similar to that (also about a factor of 20) between the star formation rate derived from our continuous star formation model ($\sim 0.5 M_{\odot} \text{ yr}^{-1}$), and the measured star formation rate $\sim 5 - 10 M_{\odot} \text{ yr}^{-1}$ for the center of M 82 (e.g. de Grijs et al., 2001; Lipsy & Plavchan, 2004). Hence, the stellar cluster mass needed according to the model to produce the observed CO luminosity is not sufficient to account for all of the stellar luminosity or young stellar mass in M 82.

There are several reasons that our shell ensemble model may have overestimated the swept-up gas mass and the line emission for a given cluster mass, or equivalently underestimated the stellar mass and luminosity required for a given swept-up gas mass. Points (1) and (2) above show that our model itself may be fundamentally optimistic in its impact on the ISM, i.e. the model shells may be too big for the stellar mass which generates them, thus leading to an overestimate in the swept-up shell masses and CO luminosity per unit stellar mass. The radii of the shells are larger than they would be in a more realistic model where the pressure of the ISM is included and where the effects of lower mechanical luminosity and leakage of bubble gas are included. These might be major effects and they both act in the same direction. If the shells at the best fit age are smaller, then we simply need more of them to build up the H_2 mass sufficient to explain the observed CO flux. In particular, if the shells were to stall early at radii about half that in our model, then a model which includes this effect would require about eight times the cluster mass for the shell ensemble. This factor already accounts for much of the missing stellar luminosity/mass. Thus the stellar mass required is very sensitive to the adopted model.

There are several other possible factors contributing to the shortfall in stellar lumi-

osity represented by our model. Some SCs blow their shells out of the disk and are not detected, some or perhaps even most OB stars do not form in SSCs, and perhaps earlier generations of stars will augment the FIR luminosity to some degree.

(4) Our model neglects the emission from the low density ambient ISM ($n_{ism} = 30 \text{ cm}^{-3}$), due to the lack of knowledge of the structure of this component in a starburst galaxy, and to the lack of direct observational data of this gas component that could be used to distinguish this gas and its physical state from the shell emitting gas in our models. If the ambient medium were uniform, as assumed in the model, it would produce no observable emission, since the density is too low to excite even the first excited rotational level. Furthermore, a straight forward calculation shows that such a gas would be so optically thick in $^{12}\text{CO } J = 1 - 0$, that no shells would be detectable in this transition. If, however, the ambient gas is assumed to be highly non-uniform, as is more likely the case, we can use the total mass adopted for the sampled volume to estimate its CO emission by simply using the X -factor for the CO emitting gas in our own Galaxy. We find that, before the shells form, the $^{12}\text{CO}(1-0)$ emission from this ambient gas component would be about 54% of the total current emission within the central $60'' \times 18''$ region. Note however that at high- J , there may be only very weak emission from this ISM component. Hence, the consequence of adding the emission of this lower density ambient gas component to the model would be to reduce the apparent excitation of the combined emission, especially the lower- J transitions.

(5) The cosmic-ray ionization rate ζ adopted in this study (the standard Galactic value, i.e. $1.3 - 2.0 \times 10^{-17} \text{ s}^{-1}$) is up to two orders of magnitude lower than that measured in M 82 (e.g. Farquhar et al., 1994), and thus the influence of cosmic-rays in the shell heating is underestimated. Bell (2006) found that by increasing the ζ value, the corresponding increase in the cosmic-ray heating rate causes a rise in gas temperature, becoming the dominant heating mechanism at larger depths ($A_V > 1 \text{ mag}$) for an increase in ζ by a factor of 100, and at all depths for an increase in ζ by a factor of 1000. This

increase will promote CO formation and emission, and counters, in part, the increased destruction rate. It will also lead to an increase in the CO excitation.

(6) A fixed turbulent Doppler velocity ($\delta v_D = 1.5 \text{ km s}^{-1}$) is used in our model. However, the choice of turbulent velocity directly affects the computed CO line flux densities. In the optically thick case, the flux is directly proportional to the turbulent velocity, whereas in the optically thin case there is no dependence. Since the lower- J transitions are optically thick, more so than the higher level transitions, we anticipate that the use of a higher turbulent velocity would reduce the slope of the line SED (see Fig. 4.14).

(7) The assumption of the semi-infinite plane-parallel geometry in our PDR code is certainly a limitation, as the FUV intensity may be underestimated due to leakage of radiation from the region exterior to the cloud/shell, resulting in an increase in the local mean intensity at the edge of the slab. More advanced models of the shell geometry are simply beyond the scope of the PDR code at the time, and solving for the radiation field from both sides of the slab dramatically increases the computation time and would make the code too slow to run.

(8) Other effects will invalidate our model for later stages of shell evolution. For example, after 30 Myr the largest radius of the shells in our model ensemble is about 678 pc. Thus, it will be merged with other shells, an effect which is not included in the model. It will also have extended beyond the scale height of the disk (300 pc along the minor axis), and be subjected to shear due to differential galactic rotation. However, these problems occur at ages older than our CO best fit model, and they should not significantly affect our best fit result.

Overall, our analysis shows that the sub-mm/mm line emission reflects the recent star formation history in a starburst galaxy. The foregoing list of caveats and limitations ultimately limit the precision with which one can obtain a realistic age for the starburst by the method described in this thesis. Some of the effects described lead to an under-

estimate and some to an overestimate. Thus, to some extent, the effects are liable to cancellation. However, the one factor upon which the ages depend most strongly is stellar evolution, since the evolutionary state of the cluster governs the flux of FUV emission incident upon the shell, and this in turn has an important influence on the SED of the molecular line emission. A consequence is that the age is unlikely to be profoundly affected by the effects listed. This also means that there should be little surprise with the agreement with other methods. However, the total cluster mass responsible is exceptionally sensitive to the model for the expansion of the shell, and consequently this quantity is less well determined than the age. In our model, it appears likely that this stellar mass in our cluster ensemble is severely underestimated.

Chapter 6

Applications to Luminous Infrared Galaxies Beyond M 82

In this chapter, we present the application of our models to starburst galaxies at distances beyond M 82. We examine one issue in particular - whether the relation between the degree of molecular gas excitation and the star formation properties can be understood in terms of our models. This issue is a follow-up to an earlier observational paper by Yao et al. (2003) in which a clear connection between these two properties was identified. In particular, we investigate whether the variations in these properties from galaxy to galaxy may derive simply from seeing galaxies in different stages of their post starburst evolution, as seen in our models. Previous interpretation of these effects require that they reflect the diversity in the intrinsic properties of galaxies, with no necessary connection to starburst evolutionary phases. As a separate issue, we explore the time dependence in our model of the well known CO-to-H₂ conversion factor X in a starburst region.

Using the shell ensemble that we developed for M 82 as a template, we first compute the relevant star formation related characteristics as a function of time for a model shell ensemble, then we compare these predicted characteristics with those observed in a modest but nearly complete sample of nearby luminous IR galaxies. Each galaxy in the

sample is presumed to represent a different evolutionary stage of our model starburst. Ratios of quantities, specifically, line intensity ratio r_{31} , and FIR luminosity to molecular gas mass ratio $L_{FIR} / M(\text{H}_2)$, are used in our analysis. These ratios describe intrinsic properties independent of galaxy size and assumed distance. In the standard literature, the L_{FIR} is used as an indicator of star formation rate, and the quantity L_{FIR} / L_{CO} or $L_{FIR} / M(\text{H}_2)$ is taken to be a measure of the star formation efficiency, i.e. star formation rate per unit available gas mass. However, in our model this ratio does not measure star formation efficiency, but is a parameter which undergoes a dramatic evolution during the tens of millions of years following a starburst event. The far-infrared luminosity L_{FIR} can be readily derived from a dusty starburst model, but not by our gas model. In this study, we use the stellar cluster luminosity L_{SC} to represent the L_{FIR} , by crudely assuming that all of the stellar light is processed into far-infrared by dust enshrouding the star clusters and distributed in the galaxies. An instantaneous starburst model is also assumed here, the same as our previous study of nearby starburst galaxy M 82.

6.1 Degree of CO Excitation and Star Formation Properties

Low-lying CO rotational line transitions at mm and sub-mm wavelengths are often used as tracers of total molecular hydrogen content in a galaxy. It is also known that the ratio of $^{12}\text{CO}(3-2)$ to $(1-0)$ line emission r_{31} provides a more sensitive measure of the gas temperature and density than the ratio of $^{12}\text{CO}(2-1)$ to $(1-0)$ lines (e.g. Jansen, 1995). Most observations of the $^{12}\text{CO}(3-2)$ line cover the central region of nearby objects (e.g. Mauersberger et al., 1999; Dumke et al., 2001), where the physical conditions of molecular gas may be different from those prevailing in molecular clouds in the disk of the galaxy.

In 2003 Yao et al. presented the first statistical survey of the properties of the $^{12}\text{CO}(1-0)$ and $^{12}\text{CO}(3-2)$ line emission from the nuclei of a nearly complete subsample

of 45 luminous infrared galaxies selected from SLUGS objects (Dunne et al. 2000). This subsample is flux limited at $S_{60\mu m} \geq 5.24$ Jy with FIR luminosities mostly at $L_{FIR} > 10^{10} L_{\odot}$ and distance limited between 20 and 300 Mpc. The angular resolution for both CO lines in Yao et al. (2003) is nearly identical ($\sim 15''$), which is also nearly identical to that of the SLUGS survey. The projected beam size on SLUGS sources ranges from 1.8 - 20 kpc.

An important feature observed in luminous IR galaxies is that the degree of ^{12}CO excitation measured by the $^{12}\text{CO}(3-2)/(1-0)$ line intensity ratio or r_{31} ratio has a trend of increasing with increasing concentration and efficiency of star-forming activity (Yao et al., 2003). Here we examine the effects of starburst phase in our model on the excitation ratio r_{31} by comparing a theoretical plot based on our results of Chapter 4 with this observed relationship found in Yao et al. (2003). We begin with the explanation of the effect outlined by Yao et al. (2003), and follow this with a different possible origin based on our starburst evolution scenario.

Plot (a) of Fig. 6.1 (see also Fig. 10 of Yao et al. (2003)) shows that there is a significant observed correlation between r_{31} and $L_{FIR}/M(\text{H}_2)$ within the $15''$ aperture. The SLUGS sample shown is divided into two ranges by gas mass centered at $M(\text{H}_2) = 10^8 M_{\odot}$, and also by dust FIR luminosity centered at $L_{FIR} = 10^{10} L_{\odot}$ which are indicated by three different symbols in the plot. The segmentation according to gas mass-range and dust IR luminosity-range shows the relationship between L_{FIR} and $M(\text{H}_2)$ and position in the plot. The line represents a linear regression fit to the data with $L_{FIR}/M(\text{H}_2) \leq 200 L_{\odot}/M_{\odot}$. The correlation is diminished at $L_{FIR}/M(\text{H}_2) > 200 L_{\odot}/M_{\odot}$, where r_{31} ranges between 0.5 and 1.72. The molecular gas mass in the SLUGS sample is derived from CO luminosities by applying the conversion factor $X = 2.7 \times 10^{19} \text{ cm}^{-2} [\text{K km s}^{-1}]^{-1}$ obtained for SLUGS objects (Yao et al., 2003). The result is $M(\text{H}_2) = 1.1 \times 10^3 D_L^2/(1+z) S_{CO} M_{\odot}$ obtained by scaling the result of Kenney & Young (1989) to the different X -factor used here, where D_L is the luminosity distance of a galaxy in Mpc,

and S_{CO} is the $^{12}\text{CO}(1-0)$ flux in Jy km s^{-1} measured within a $15''$ beam. According to Yao et al. (2003), both r_{31} and $L_{FIR}/M(\text{H}_2)$ ratios are found to be independent of the galaxy distance (or the projected beam size on galaxy), and in turn the H_2 gas mass. There are also no significant correlations found between r_{31} and star formation rate (or L_{FIR}), dust temperature and mass, the color indices, or the luminosity of the IR or radio continuum. Yao et al. suggested that the observed correlation between r_{31} and $L_{FIR}/M(\text{H}_2)$ and the lack of correlation of r_{31} with properties related to total star formation implies a dependence only on localized conditions within the molecular clouds. According to this picture, the dependence of r_{31} on the $L_{FIR}/M(\text{H}_2)$ ratio reflects a higher degree of CO excitation that is associated with a higher spatial concentration and efficiency of star forming activity. Such conditions would arise in an intense starburst where the surface density of such activity is high. The saturation effect (approaching unity) of r_{31} seen at $L_{FIR}/M(\text{H}_2) > 200 L_{\odot}/M_{\odot}$ reflects a limit imposed on this ratio at the highest excitation where the excitation temperatures for $^{12}\text{CO}(3-2)$ and $(1-0)$ (both assumed optically thick) are equivalent.

As mentioned earlier the $L_{FIR}/M(\text{H}_2)$ ratio is traditionally used as an indicator of star formation efficiency. In our model, this ratio and its variation with time are simple and direct consequences of the evolution in stellar luminosity (represented by L_{SC}) and swept-up gas mass within a single starburst. Plot (b) of Fig. 6.1 shows the model r_{31} ratio versus the $L_{SC}/M(\text{H}_2)$ ratio, where the total cluster luminosity L_{SC} has been used in place of the observed FIR luminosity L_{FIR} . This assumes that the FIR luminosity produced in a recent starburst is the dominant component of the FIR luminosity. The $M(\text{H}_2)$ for the model is derived from S_{CO} , thus using the same method as employed for the SLUGS sample except with a fixed $D_L = 3.25$ Mpc used in our model computations. Thus, S_{CO} and $M(\text{H}_2)$ are both functions of time and size of the shells. The model curve clearly shows a trend similar to that in the observational plot in Fig. 6.1 (a), i.e. the r_{31} ratio increases with increasing $L_{SC}/M(\text{H}_2)$ ratio, and then saturates at high $L_{SC}/M(\text{H}_2)$

($> 200 L_{\odot}/M_{\odot}$). The model r_{31} ratios vary between 0.7 and 1.3 for the *Winds* phase, and between 0.4 and > 2.0 for the *post-SN* phase. The key point associated with Fig. 6.1 (b) is that the relationship between r_{31} and L_{SC} is governed by the age or phase of the starburst. At earlier stages the cluster luminosity is high and the mass of swept-up gas is small. Since the shells are comparatively small and expanding rapidly, they are also more effectively heated and compressed than at later stages. Thus, at earlier phases, both r_{31} and $L_{SC}/M(\text{H}_2)$ are higher than in the later phases of the expansion. Since the parent GMCs contribute more to the $^{12}\text{CO}(1-0)$ line than the (3-2) line, the r_{31} ratio is lower for the *Winds* phase, although the L_{SC} is higher than that from the *post-SN* phase. An important point associated with this interpretation is that the degree of molecular gas excitation is a consequence of star-forming activity, rather than a reflection of initial conditions prior to the starburst, as often assumed.

As described above, our model yields a result similar to the observations, and suggests that the observed behavior results from recent starbursts in these galaxies. This result furthermore implies that the relationship between the degree of CO excitation (r_{31}) and the $L_{FIR}/M(\text{H}_2)$ ratio associated with star formation properties may be determined by the phase of the starburst rather than by the more traditional view of variation in the efficiency of star formation.

One of the interesting properties of Fig. 6.1 plot (a) is that the data points tend to concentrate toward the origin. A similar effect is discernible in the theoretical plot if points are plotted at equal intervals in age. The concentration in the latter case occurs because the rate of change of the variables on both axes decreases with time as the age becomes large. This suggests a further test of the hypothesis that the behavior in Fig. 6.1 (a) is the consequence of seeing starbursts in different stages of their evolution. Accordingly, we compare the frequency distribution (or histogram) of the 45 SLUGS galaxies with respect to the observed $L_{FIR}/M(\text{H}_2)$ and r_{31} ratios to the frequency distribution of 45 pseudo galaxies with respect to the model $L_{SC}/M(\text{H}_2)$ and r_{31} ratios, as shown

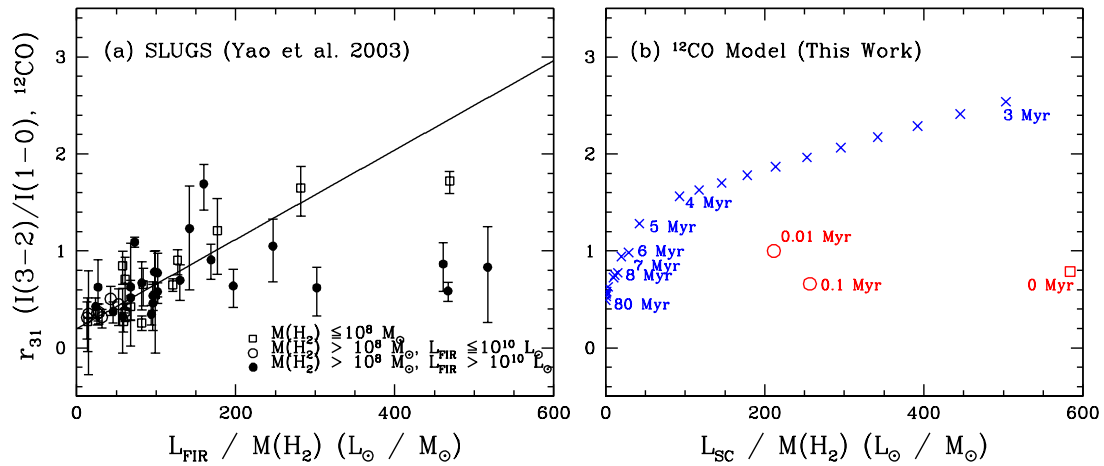


Figure 6.1 Plots of the line intensity ratio r_{31} (expressed as brightness temperatures integrated over velocity) versus the $L_{\text{FIR}}/M(\text{H}_2)$ ratio. Plot (a) is the observed r_{31} versus the $L_{\text{FIR}}/M(\text{H}_2)$ measured within a $15''$ aperture for the SLUGS sample. Plot (b) is our model result. Red open symbols (square: $t < 0.01$ Myr, circle: $0.01 \leq t \leq 0.1$ Myr, triangle: $0.1 - 0.7$ Myr) are for the *Winds* phase, and blue crosses are for the *post-SN* phase. The age sequence for the *post-SN* from right to left is 3, 4, 5, . . . , 80 Myr.

in Figs. 6.2 and 6.3. The pseudo galaxies were assigned ages drawn randomly from a uniform probability distribution between 3 Myr and 20 Myr, and the parameters r_{31} and $L_{SC}/M(\text{H}_2)$ then computed for these ages using our model. The model age range (3 - 20 Myr) reflects the range of validity of the model for the *post-SN* phase. The lower boundary corresponds to a plausible lower limit on the dynamical timescale for the starburst region and the upper boundary corresponds to the epoch beyond which the bubble shells escape the disk of the galaxy. The comparison reveals a similarity in the distributions between model and observation for both $\log_{10}(L_{FIR}/M(\text{H}_2))$ and r_{31} , though the peak in the former distribution occurs at a lower value in the model (see later for further discussion of this point). The qualitative similarity between the two histograms thus supports the hypothesis that the quantities $L_{FIR}/M(\text{H}_2)$ and r_{31} are related to starburst age. However, the evidence presented is not conclusive, merely suggestive.

We also tested our model result with different starburst age ranges (1 to 10 Myr and 1 to 80 Myr) for the 45 pseudo galaxies. These tests produced numerically different but qualitatively similar results.

As noted, the foregoing analysis supports the hypothesis that the plots in Fig. 6.1 signify that the excitation of the gas following a starburst is closely related to the age of the starburst. However, there are a number of considerations which need to be examined which may affect the credibility of this result, for example, the selection effect on the observed frequency distributions. Fortunately, the SLUGS subsample investigated here is nearly complete with a limiting FIR flux density and a limiting distance, so that the selection effects are well understood. Essentially all members of the sample are detected at both CO transitions, but the flux limit imposes a minimum detectable luminosity which increases with D_L^2 . The dramatic decline in galaxy number density with distance confirms this selection and indicates that the sample comprises the high luminosity tail of the underlying galaxy population. The question then is: could the luminosity selection affect the distribution of $L_{FIR}/M(\text{H}_2)$, particularly in producing a deficiency of ratios

below the peak of the observed distribution? There are two approaches to investigate this effect. First, we can examine the direct relations between $L_{FIR}/M(H_2)$ and galaxy distance, as well as r_{31} and galaxy distance. We find no significant correlation between these two quantities and distance. Second, we divide the sample of 45 SLUGS galaxies into two parts, each with 23 objects, divided according to $D_L < 45$ Mpc and $D_L \geq 45$ Mpc. We find no significant difference between the frequency distributions of $L_{FIR}/M(H_2)$ in these two subgroups. Thus, there is no evidence that the selection effect in luminosity produces a corresponding selection in the ratio $L_{FIR}/M(H_2)$. We also conducted a similar analysis for the ratio r_{31} , and there is also no evidence of selection effect on this ratio.

Other observational effects, for example, the random and systematic errors in the observed data, would contribute to the disagreement between the model and the observed histograms, assuming that the theory were the correct explanation for the observation. It must also be recalled here that there is a deficiency of about an order of magnitude between model and observation in the total stellar luminosity for M 82. This deficiency in the model luminosity will contribute to, and possibly even account for, the systematic difference in location of the peak of the two distributions of $L_{FIR}/M(H_2)$ shown in Fig. 6.2.

The hypothesis presented here that the ratios r_{31} and $L_{FIR}/M(H_2)$ are related to the starburst age can be further tested by direct measurements of the ages of the young stellar populations in the SLUGS subsample. Probably the best approach would be the fitting of population synthesis models to optical and IR spectroscopy of SLUGS objects, as discussed in Chapter 5.

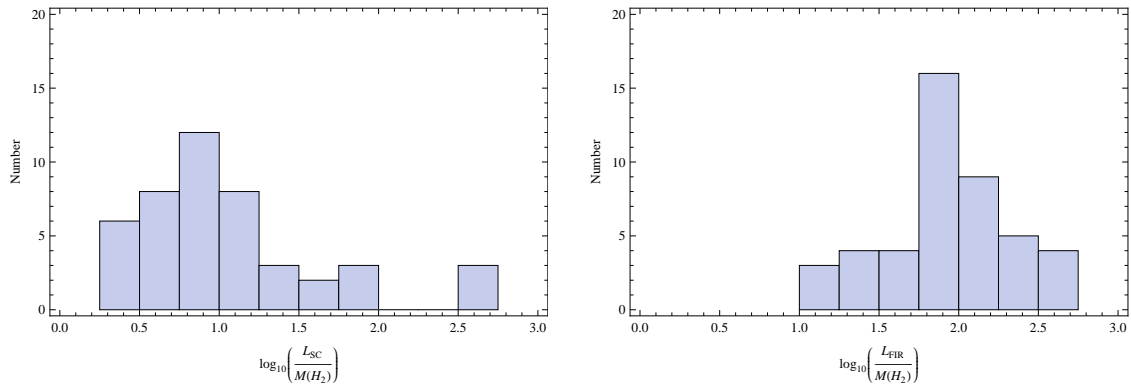


Figure 6.2 Histograms of the $L_{SC}/M(H_2)$ ratio derived from our starburst model and the $L_{FIR}/M(H_2)$ ratio measured for 45 SLUGS galaxies by Yao et al. (2003).

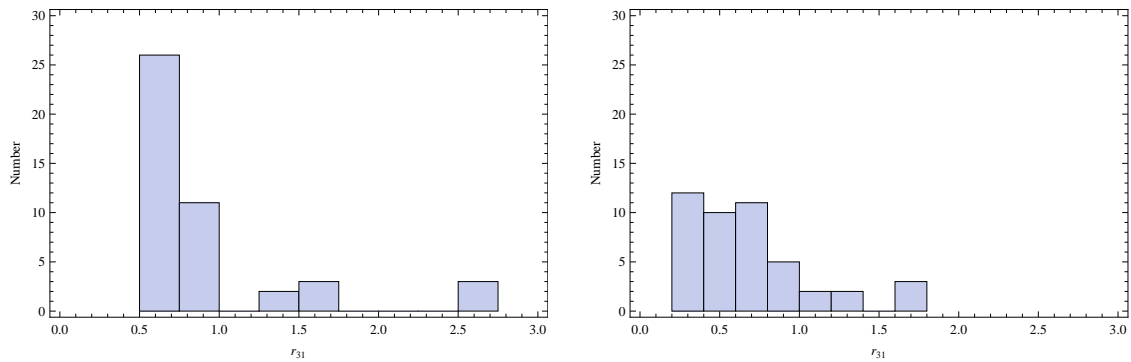


Figure 6.3 Histograms of the $^{12}\text{CO}(3-2)/(1-0)$ line ratio (r_{31}) derived from our starburst model and the r_{31} ratio measured for 45 SLUGS galaxies by Yao et al. (2003).

6.2 The CO-to-H₂ Conversion Factor X

The most common method of deriving H₂ masses from CO luminosities relies on a reliable estimate of the controversial parameter X , which converts CO line intensity or luminosity to the H₂ column density or mass. Studies have shown that this parameter varies from galaxy to galaxy (Booth & Aalto, 1998; Boselli et al., 2002), and it is thought to be higher in metal-poor galaxies and lower in starburst galaxies than in Galactic molecular clouds, where X is about $2.8 \times 10^{20} \text{ cm}^{-2} [\text{K km s}^{-1}]^{-1}$ (Bloemen et al., 1986; Strong et al., 1988). Hereafter we refer to this as the standard value. Thus in starburst galaxies, application of the standard factor can produce a significant overestimate (4 - 10 times) of molecular hydrogen mass (Solomon et al., 1997; Downes & Solomon, 1998; Yao et al., 2003).

Our evolving starburst model allows us to investigate, purely from a theoretical standpoint, the relationship between the X -factor and starburst phase, because the physical properties of molecular gas in an evolving starburst region changes with time. The X -factor may be determined from the following equation,

$$X(t) = \frac{M(H_2)}{4.1 \times 10^2 D_L^2 S_{CO}} \quad (6.1)$$

where $M(H_2)$ is the total H₂ gas mass swept up by the shells at time t in units of M_\odot , D_L is the luminosity distance, in this case to M 82 (used in our model computations) in unit of Mpc, S_{CO} is the ¹²CO(1-0) line flux in units of Jy km s⁻¹, and X value is in units of $10^{19} \text{ cm}^{-2} [\text{K km s}^{-1}]^{-1}$.

In the *Winds* phase, the value of X mainly increases with time. Because the parent GMCs are the dominant sources of ¹²CO(1-0) line emission during the earlier *Winds* phase, and because the gas inside the parent clouds is highly excited due to high FUV radiation, this results in a progressive decrease in ¹²CO(1-0) line emission from the GMCs with decreasing GMC mass. On the other hand, the compressed dense gas inside the

shells is also highly excited, but the $^{12}\text{CO}(1-0)$ line emission increases with increasing swept-up mass of the shells. Overall the $^{12}\text{CO}(1-0)$ line emission from the shell and GMC ensemble increases with time, and slightly decreases from 0.5 to 0.7 Myr, while the system H_2 mass is fixed at $1.9 \times 10^7 M_\odot$. In the *post-SN* phase, the X -factor mainly increases with time, because the ^{12}CO gas is highly excited at early stages of this phase. Although both the $^{12}\text{CO}(1-0)$ line emission and swept-up shell mass $M(\text{H}_2)$ increase with time, the increasing rate in $M(\text{H}_2)$ is higher than that in the $^{12}\text{CO}(1-0)$ luminosity between 5 and 80 Myr. However, the increasing rate in $M(\text{H}_2)$ is lower than that in the $^{12}\text{CO}(1-0)$ luminosity in a brief interval between 2 and 5 Myr, producing a brief decline in the value of X shown in Fig. 6.4. The discontinuity between 0.8 and 1 Myr corresponds to the transition between *Winds* and *post-SN* phases.

The values for the X -factor derived from our models for the two best fit ages (5.6 and 10 Myr) for the central 1 kpc starburst regions of M 82 are 9.5×10^{19} and $1.1 \times 10^{20} \text{ cm}^{-2} [\text{K km s}^{-1}]^{-1}$, respectively. These values are comparable to the empirical values found from the studies of starburst galaxies (Weiss et al. 2001, Downes & Solomon 1998). They also lie between those derived for the Galaxy and nearby LIRGs (Yao et al., 2003). Our model X -factor shows a trend of increasing with time in the *post-SN* phase, i.e. lower values are associated with more highly excited gas. This is consistent with the observed results indicated in the above references, since starburst galaxies have lower values than those of the non-starburst (or normal) galaxies like our own Galaxy.

We also investigated the effect of reducing the upper mass limit on the GMC mass spectrum (i.e. from $10^7 M_\odot$ to $3 \times 10^6 M_\odot$ and $10^6 M_\odot$) on our model X -factor as was done for the ^{12}CO model in Chapter 5. Recall that in Chapter 5 we conclude that the model can provide acceptable fits to the data only if the dominant initiating starburst clusters are massive, at least $5 \times 10^5 M_\odot$. Here we find that the X value is also very sensitive to the assumed initial upper mass limit of the cluster spectrum (and corresponding GMC mass spectrum). For the first case with a slightly lower upper limit

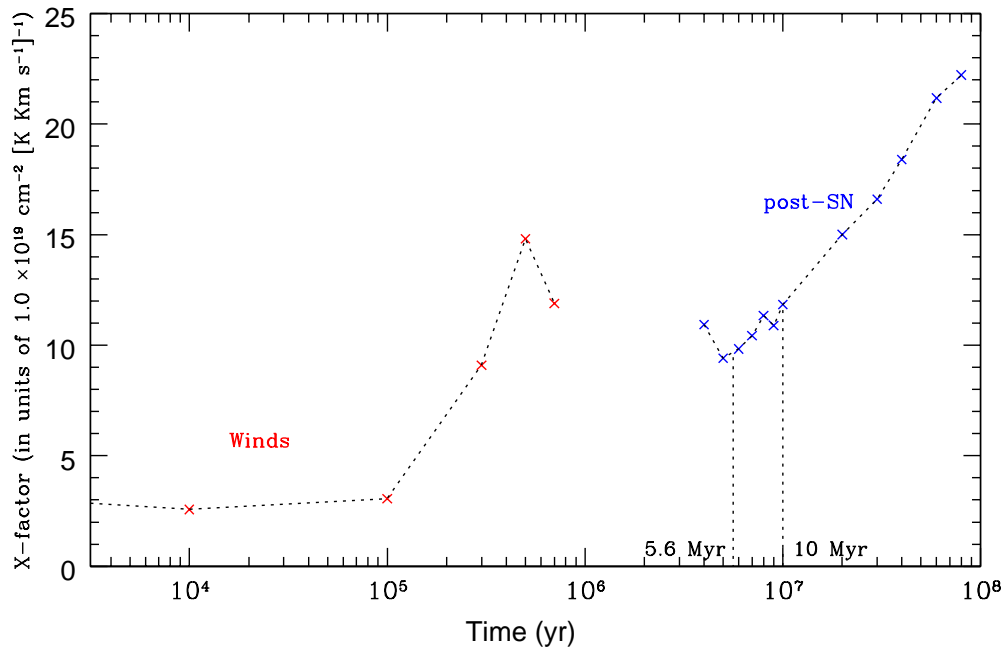


Figure 6.4 Plot of our model CO-to-H₂ conversion factor X as a function of time. Red cross symbols connect with black dashed curve are for the *Winds* phase, and blue crosses connected with black dashed curve are for the *post-SN* phase. The two best fitted ages (5.6 and 10 Myr) are also indicated in the plot.

of GMC mass $3 \times 10^6 M_{\odot}$ (corresponding to stellar mass of $7.5 \times 10^5 M_{\odot}$), we found a solution similar to the result presented in Fig. 6.4. The value of X is about 15% and less for the *Winds* phase, but it is about a factor of 1.4 higher at 5.6 Myr and 1.2 higher at 10 Myr for the *post-SN* phase. But for the second case with a ten times or more reduction in the upper cutoff of the GMC (and cluster) mass spectrum, the value of X starts showing an opposite trend of decreasing with time, because in this case the increasing rate in $^{12}\text{CO}(1-0)$ luminosity is faster than the increasing rate in $M(\text{H}_2)$ mass swept up by the shells. The value of X is about 45% less for the *Winds* phase, but it is about a factor of 5 higher at 5.6 Myr and 2.3 higher at 10 Myr for the *post-SN* phase. Hence, acceptable solutions for modeling the X -factor in starburst galaxies are obtained only when our model system is dominated by initiating starburst clusters that are massive, at least $5 \times 10^5 M_{\odot}$.

The accuracy of the X -factor predicted by our model is limited by several conditions. The CO flux for a given H_2 mass depends upon a variety of factors which were discussed in § 5.3.3 of Chapter 5 (e.g. the dependence on the assumed turbulent velocity, the neglect of the CO emission from the ambient ISM). Equally important however is that the X -factor will depend to some degree on the assumed mass spectrum for the star clusters (as shown above), and on the assumed relation governing the expansion of the bubble driven shells. The latter relation governs the amount of H_2 mass swept up in a given period of time and the hence also the number of star clusters required to produce the total observable H_2 mass, as discussed also in Chapter 5.

It is important to understand that a precise value for the X -factor ultimately relies exclusively on the empirical determinations involving careful measurements of CO luminosity and H_2 mass. What our results do show, however, is that these empirical values may be reasonably replicated by a starburst model of the type investigated in this thesis, and that considerable insight regarding the causes of the variation from galaxy to galaxy may be obtained from the temporal behavior in our model exhibited during the

expansion of the starburst bubbles/shells.

Chapter 7

Summary and Future Directions

7.1 Summary

Knowledge of the physical properties and evolution of the *gas* and *dust* content in the interstellar medium of starburst galaxies is essential for understanding the *cause* and *temporal evolution* of star-forming activity. The bursts of massive star formation can dramatically alter the structure and evolution of their host galaxies by injecting large amounts of energy and mass into the ISM via strong stellar winds and repeated supernova explosions. Observations of *FIR/sub-mm/mm line emission* from nearby starburst galaxies provide us with detailed information on the connection between the gas properties and the active star formation, and provide an essential basis for modeling the effect of a starburst on the surrounding interstellar medium.

This study presents a *first attempt* at addressing the question of whether there is a *signal* in the FIR/sub-mm/mm molecular and atomic line data of the phase of a starburst. We treat an evolving star formation region in a starburst galaxy as *an ensemble of non-interacting spherical GMCs/shells* expanding into a uniform gas medium. These shells are driven by winds from star clusters during *an instantaneous burst*. The underlying stellar radiation from the clusters has a pronounced effect on the properties and structure

(density, temperature, size, and chemical abundances) of PDR regions in the shells. These properties are affected by the size and rate of expansion of the shells and the evolutionary stage of the clusters. Thus, the SEDs of the molecular and atomic line emission from these swept-up shells and the associated parent GMCs should indeed contain a *signature* of the stage of evolution of the starburst.

By comparing our evolving starburst models with available data of nearby starburst galaxies, notably M 82, we show that it is possible to (1) successfully model the *time-dependent* FIR/sub-mm/mm line emission of molecular and atomic gas; (2) relate the observed molecular line properties of a starburst galaxy to its *age*, and hence to constrain the global *star formation history*; (3) examine the possible relevance to the *formation of the molecular rings* in M 82; and (4) interpret the *observed correlation* between the degree of CO excitation (r_{31}) and the $L_{FIR}/M(\text{H}_2)$ ratio, observed among nearby luminous infrared galaxies, as also *consequences of starburst evolution*.

In essence, we have provided a *complementary study* to the previous work on estimating the age(s) of starburst in M 82 using quite different methods. In particular, the method is analogous to that of Efstathiou et al. (2000), which considered the observable effects of an evolving cluster on the IR emission from the surrounding expanding dust shell. We have also provided support for the *hypothesis* of molecular ring formation in the center of M 82, and a *new interpretation* of the underlying reason for a localized starburst phenomena observed in nearby LIRG galaxies.

In *Chapter 2*, we described our model assumptions, physics of shell/bubble expansion around a young star cluster (i.e. standard dynamical theory for the bubble/shell structure), the physical conditions of the gas swept up inside the shell, the chemical evolution of the surrounding gas in massive star-forming regions, and the non-LTE radiative transfer theory for molecular and atomic line emission. Our simulation methods, described in *Chapter 3*, focus on modeling the FIR/sub-mm/mm emission from several important molecular and atomic gas tracers (^{12}CO , ^{13}CO , HCN, HCO^+ , C, O, and C^+)

in the expanding shells. We divided the set of the models into two phases, i.e. *Winds* and *post-SN*, which are treated independently. The *Winds* phase begins at the onset of the stars, and ends when the shells sweep up all of the materials in its parent clouds. The *post-SN* phase starts when the most massive star in the clusters terminates as a supernova.

In *Chapter 4*, we presented simulation results for individual expanding shells and these shells as an ensemble. By around 0.8 Myr , all shells have swept up the gas in their parent GMCs, and the *Winds* phase ends. The shells enter the *post-SN* phase, and begin to expand into the less dense, uniform ambient ISM. Over the 100 Myr of evolutionary timescale considered, the radius of our model shells changes from less than 1 pc to several hundred parsec. The velocities of the shells vary with time and from shell to shell, and is between a few and several hundred kilometer per second. The FUV radiation field of our model shell ensemble also spans 4 - 5 orders of magnitude across the 100 Myr time span. It is these variations which allow us to simulate a *large range of molecular gas excitation conditions* for comparisons with *multiple transitions* of molecular and atomic data. Values of integrated line flux as a function of time for the molecular and atomic tracers mentioned earlier are also presented, forming a *template model* of the behavior, to be fitted later to the data. Different excitation conditions of the gas are shown in the shells and in their parent clouds, and at different evolutionary phases.

In *Chapters 5* and *6*, we presented applications to the nearby starburst galaxy M 82 and luminous IR galaxies. The burst age and total H_2 mass are derived from a *chi-squared* model fit of the aforementioned template model to the observed SED of molecular emission and from an analysis of the line ratios involving some atomic FIR transitions for the central 1 kpc region of M 82. The main conclusions drawn from comparisons of our model with the observation are:

1. There is good agreement between our *supershell kinematic* model and the observations of the expanding supershell centered around the presumed supernova remnant

SNR $41.9 + 58$ in M 82. The agreement supports the *hypothesis* that this supershell is created by strong winds from a young star cluster with a total mass of $2.2 \times 10^6 M_{\odot}$ which formed at its center about 0.8 Myr ago, and the total mechanical energy needed for the creation of this supershell is about 1.5×10^{54} ergs. This is the energy equivalent of the winds associated with ~ 1700 O stars (each with $m_* \geq 40 M_{\odot}$). Our model also shows that there should be *excess CO emission* at high excitation transitions in this supershell. This is consistent with the provisional detection of such excess emission at $^{12}\text{CO}(6-5)$ in the region of this supershell seen after the surrounding disk emission is removed. Both agreements suggest that the set of *evolving starburst models* we have put forward in this study can be used to interpret other shells in M 82 or shells in other starburst galaxies.

2. The *age* derived from our analysis of CO line SEDs and line ratio diagrams using an instantaneous burst model is $5 - 6 \text{ Myr}$ for the central $60'' \times 18''$ region, with most of the CO emission arising from the central $22''$ region. The age derived from our atomic data is slightly older (10 Myr) for a larger area $80'' \times 80''$. We suggest that these two ages may be a result of sampling different regions. It is unclear from our analysis whether they refer to the same period of star forming activity or to two spatially separated independent bursts. A more sophisticated model and more data are needed to clarify the picture. We do note however that our extended starburst model result also shows that a *uniform star formation rate* over the past 10 Myr can also produce a satisfactory model fit to the ^{12}CO data. Hence, the star formation in M 82 can be either viewed as instantaneous burst occurred 5 - 6 Myr ago, or this epoch could represent a *characteristic time* about which recent star formation history is *centered*. These burst ages derived from our models are similar to the results found in optical and infrared studies. These results lead us to conclude that *the observed FIR/sub-mm/mm line spectra of a starburst galaxy can be successfully modeled in terms of the evolutionary scheme of an GMC/shell ensemble, and such studies can usefully constrain the age(s) or star formation history of a starburst galaxy.*

The starburst ages derived from our model are dependent on a great variety of assumptions, e.g. the initial upper mass limit of the cluster spectrum. We find that the model can provide acceptable fits to the data only if the dominant initiating starburst clusters are massive, at least $5 \times 10^5 M_{\odot}$, corresponding to a GMC mass of $2 \times 10^6 M_{\odot}$. The uncertainty of the derived age is also affected by many other model assumptions, and the effects of varying these assumptions have not been examined. These include, for example, the effect of including the CO emission (especially low- J transitions) from the lower density ambient ISM, the effect of including a higher cosmic-ray ionization rate, and the effect of increasing the shell microturbulent velocity. Some of these effects would lead to an underestimate and some to an overestimate of the age, and hence to some extent, these effects would be expected to cancel each other out. However, since the evolutionary state of the cluster governs the flux of FUV radiation incident upon the shell, and this in turn has a pronounced effect on the SED of the molecular line emission, the stellar evolution is a crucial factor in constraining the derived age. The starburst stellar mass and luminosity predicted by our models are significantly underestimated, based on a comparison with the observed FIR luminosity which is a factor of about twenty larger than our model value for the total luminosities of the clusters. Probable causes for this underestimate include (1) the neglect of the effects of the pressure exerted by the ambient gas, resulting in an overestimate of the shell radii; and (2) an overestimate of the supernova mechanical power which would also lead to an overestimate of the shell radii. Including these effects would allow more stellar luminosity in the starburst for the mass of gas swept up in the shells required to match the CO data. Hence, the shortfall in our predicted stellar luminosity tends to support the widely held idea that bubbles/shells grow more slowly than the simple bubble theory predicts (Weaver et al., 1977; McCray & Kafatos, 1987). Our model also cannot provide a basis for incorporating higher density tracers (e.g. HCN and HCO⁺), because for example, HCN in the model is associated with the dense shells and their parent GMCs seen only at the earliest phase of the

starburst evolution. The low HCO^+ line fluxes predicted by our models may be a result of the low chemical abundance of HCO^+ due to a low cosmic-ray ionization rate adopted by our model.

3. The results of the model analysis described above (item 2), also yield insights into the *total gas content* and its *structure*. For example, the total H_2 gas mass $\sim 2 - 3.4 \times 10^8 M_\odot$, is consistent with that measured independently in the center of M 82, and the porosity of the ISM in M 82 must be very high. The inference is that the neutral ISM and possibly the molecular ring in the center of M 82 are largely the *products of evolving shells*. However, our interpretation concerning the ring formation is not unique, and the rings may also be created by Linblad resonance instabilities associated with the gravitational effects of the bar.

4. Our model is compared to a limited extent with our published ^{12}CO observations of 45 nearby luminous IR galaxies, yielding some insight into the relevance of starburst evolution in a larger context. Both the model and the data show that the degree of CO excitation r_{31} increases with the increasing ratio $L_{\text{FIR}}/M(\text{H}_2)$, and that the frequency distributions of these two parameters in both the model prediction and the data are similar. This suggests that the observed behavior results from recent starbursts in these galaxies observed at different stages of their evolution rather than from a wide range of their intrinsic properties (e.g. greatly varying degrees of star forming efficiency). This result also implies that the degree of molecular gas excitation is a *consequence* of star-forming activity, rather than a *reflection of initial conditions* prior to the starburst, as often assumed. The test of the above hypothesis ultimately lies in determining the ages of starbursts in many other luminous infrared galaxies, most probably by the method of stellar population synthesis.

5. Our evolving starburst model shows that the CO-to- H_2 conversion factor X is *strongly related* to the starburst phase, because the physical properties of molecular gas in an evolving starburst region changes with time as summarized before. The model X -

factor shows a trend of increasing with time in the *post-SN* phase, i.e. lower values of X are associated with more highly excited gas. This is consistent with the observed results that starburst galaxies have lower values of X -factor than those of the non-starburst galaxies. The absolute numerical value for X -factor derived from our model is sensitive to the assumed initial upper mass limit of star clusters spectrum and corresponding GMC mass spectrum. In addition, the value will be affected to some degree by those factors that affect the age prediction described above (item 2).

7.2 Future Directions

From the preceding section, it is clear that more work is needed. As it stands, a major weakness is that there is a very sophisticated treatment of PDR and molecular line radiative transfer models, somewhat out of proportion to the model for the shell behavior which is exceedingly crude by comparison. More balance is needed, and probably the most important modification is to permit exploration of a wider degree of behavior in the models (e.g. a proper integration of the equations of shell motion permitting a treatment of non-uniform cloud media with ISM pressure, a cosmic ray ionization rate that better reflects a starburst environment, incorporation of magnetic field compression in shell, reduced bubble pressure, and inclusion of emission from the ISM). The computational challenge here is to allow a wide variation in the assumed fixed parameters of the model so that their effects can be fully explored. Although other dynamical models, for example, magneto-hydrodynamic (MHD) model, would include such effects, in order to make progress in the directions presented by this work, they must be fully integrated with the stellar population and evolution synthesis model, the time-dependent PDR, and molecular line radiative transfer model. This is a big challenge and will not likely be accomplished in the near future. An alternative approach is to numerically model the expanding shells without the PDR and molecular line radiative transfer codes and

permit comparisons with optical data to help decide the choice of the some of the fixed parameters, and thus to permit more extensive modeling along the lines outlined in this thesis.

Appendix A

List of Acronyms

- AGB - asymptotic giant branch
- AGN - active galactic nuclei
- ALI - Approximated/Accelerated Lambda Iteration
- ALMA - Atacama Large Millimeter Array
- ESA - European Space Agency
- ESbM - Evolving Starburst Model
- FIR - far-infrared
- FUV - far-ultra violet
- GMC - giant molecular cloud
- HST - Hubble Space Telescope
- IMF - initial mass function
- IR - infrared
- IRAS - Infrared Astronomical Satellite

- ISM - interstellar medium
- LIRG - luminous infrared galaxy
- LMC - Large Magellanic Cloud
- LTE - local thermal equilibrium
- LVG - Large Velocity Gradient
- M82 - Messier 82
- MHD - magneto-hydrodynamic
- mm - millimeter
- NASA - National Aeronautics and Space Administration
- non-LTE - non-local thermal equilibrium
- PAH - polycyclic aromatic hydrocarbons
- PDR - photodissociation region
- PV - position-velocity
- R-T - Rayleigh-Taylor
- SC - star cluster
- SE - shell ensemble
- SED - spectral energy distribution
- SFE - star formation efficiency
- SFR - star formation rate
- SLUGS - SCUBA Local Universe Galaxy Survey

- SN - supernova
- SNR - supernova remnant
- SSC - super star cluster
- sub-mm - sub-millimeter
- ULIRG - ultra luminous infrared galaxy
- UV - ultra violet
- WR - Wolf-Rayet

Appendix B

List of Math Symbols

- L_{FIR} - far-infrared luminosity
- L_{IR} - infrared luminosity
- L_{\odot} - solar luminosity
- z - redshift
- B_0 - molecular rotational constant
- J - rotational quantum number
- $n(\text{H}_2)$ - molecular hydrogen density
- T_{kin} - kinetic temperature
- X - CO-to- H_2 conversion factor
- M_{GMC} - giant molecular cloud mass
- M_* - star cluster mass
- τ_{H_2} - formation timescale of molecular hydrogen
- R_{HII} - radius of H II region

- V_{HII} - expansion velocity of H II region
- R_S - initial Strömgren radius
- c_i - sound speed in the ionized gas
- F_* - number of Lyman continuum photons
- n_c - cloud core H₂ density
- η - star formation efficiency
- R_w - shell radius at *Winds* phase
- V_w - shell expansion velocity at *Winds* phase
- L_w - wind mechanical luminosity
- n - ambient gas density
- m_* - star mass
- R_{SN} - shell radius at *post-SN* phase
- V_{SN} - shell expansion velocity at *post-SN* phase
- N_* - number of stars with masses $\geq 8 M_\odot$ in a SC
- M_\odot - solar mass
- E_{SN} - energy produced by each supernova explosion
- t_c - radiative cooling time of hot bubble
- \mathcal{Z} - metallicity with respect to the solar
- R_{SP} - shell radius at *snow-plow* phase
- V_{SP} - shell expansion velocity at *snow-plow* phase

- c_{ism} - thermal sound speed in the ISM
- $P_{external}$ - external pressure
- ρ_{ism} - ambient ISM volume density
- G_0 - FUV radiation intensity
- A_V - visual extinction
- λ - wavelength
- ξ_λ - extinction at λ to that in the visual ($\sim 5550 \text{ \AA}$)
- ω - albedo of the dust grains
- ϕ_c - Coulomb potential
- W - work function of the grain
- n_{cr} - critical density
- T_{gas} - gas temperature
- E_{upper} - upper energy level
- R_f - molecular H_2 formation rate
- ν - frequency
- I - radiative intensity
- j - emission coefficient
- α - absorption coefficient
- τ - optical depth between the point where I is evaluated and spatial infinity along the line of sight

- L_* - stellar luminosity
- R_s - shell radius
- V_s - shell velocity
- T_{dust} - dust temperature
- T_s - shell temperature (has T_{gas} and T_{dust})
- n_s - shell density
- d_s - shell thickness
- χ^2 - chi-squared
- χ^2_ν - reduced chi-squared
- $M7$ - GMC with $M_{GMC} = 10^7 M_\odot$
- $3M6$ - GMC with $M_{GMC} = 3.16 \times 10^6$
- $M6$ - GMC with $M_{GMC} = 10^6 M_\odot$
- $3M5$ - GMC with $M_{GMC} = 3.16 \times 10^5$
- $M5$ - GMC with $M_{GMC} = 10^5 M_\odot$
- $3M4$ - GMC with $M_{GMC} = 3.16 \times 10^4$
- $M4$ - GMC with $M_{GMC} = 10^4 M_\odot$
- $3M3$ - GMC with $M_{GMC} = 3.16 \times 10^3$
- μ - effective molecular weight per hydrogen molecule
- R_{GMC} - GMC radius
- n_0 - average GMC H_2 density

- L_{SC}^* - stellar luminosity of a SC
- L_{SC}^{mech} - wind mechanical luminosity of a SC
- n_H - number density of atomic hydrogen
- n - number density of hydrogen nuclei, $n = n_H + 2n(\text{H}_2)$
- n_a - ambient number density of molecular hydrogen
- k - Boltzmann constant
- m_H - mass of the hydrogen atom
- σ - Stephan-Boltzmann constant
- ζ - molecular H_2 ionization rate by cosmic-ray
- δv_D - microturbulent Doppler velocity
- $n(i)$ - number density of species i
- $X(i)$ - gas-phase elemental abundance, $X(i) = n(i) / n$
- T_{GMC} - GMC gas temperature
- n_{ism} - number density of ISM gas
- $M(\text{H}_2)$ - molecular H_2 mass
- M_{sh} - molecular gas mass swept-up by the shells
- E_{kin} - shell kinetic energy
- E_{mech} - wind mechanical energy
- I - molecular or atomic line intensity
- S - molecular or atomic line flux

- M_{SC} - star cluster mass
- χ_ν - reduced chi-squared
- p - number of free parameters used in reduced chi-squared fitting
- N - number of data points used in reduced chi-squared fitting
- $N - p$ - degrees of freedom used in reduced chi-squared fitting
- S_{obs}^J - observed line flux in rotational level J
- S_{model}^J - model line flux in rotational level J
- S_{temp}^J - model template line flux in rotational level J
- M_{temp}^{GMC} - model template GMC mass used in reduced chi-squared fitting
- M_{temp}^* - model template SC mass used in reduced chi-squared fitting
- M_{temp}^{sh} - model template swept-up molecular gas mass by the shells used in reduced chi-squared fitting
- P_{cloud} - pressure inside the cloud
- $P_{internal}$ - internal pressure
- G - gravitational constant
- c_{cloud} - sound speed in a cloud
- r_{31} - $^{12}\text{CO}(3-2)$ to $(1-0)$ line intensity ratio
- R_{10} - $I_{12\text{CO}(1-0)} / I_{13\text{CO}(1-0)}$ ratio

Bibliography

Abbott, D. C. 1982, *ApJ*, 263, 723

Adelberger, K. L., & Steidel, C. C. 2000, *ApJ*, 544, 218

Alonso-Herrero, A., Rieke, G., Rieke, M., & Kelly, D. M. 2003, *AJ*, 125, 1210

Bakes, E. L. O., & Tielens, A. G. G. M. 1994, *ApJ*, 427, 822

Bally, J., Stark, A. A., Wilson, R. W., & Henkel, C. 1988, *ApJ*, 324, 223

Barker, S., de Grija, R., & Cerviñs, M. 2008, *A&A*, 484, 711

Bartel, N., & Bietenholz, M. F. 2005, *AdSpR*, 35, 1057

Bastian, N., Gieles, M., Efremov, Yu. N., & Lamers, H. J. G. L. M. 2005, *A&A*, 443, 79

Bayet, E., et al. 2008, *ApJ*, accepted.

Beck, S. C., Lacy, J. H., Baas, F., & Townes, C. H. 1978, *ApJ*, 226, 545

Bell, T. A. 2006, *Ph.D. Thesis*, University College London, UK

Bell, T. A., Viti, S., Williams, D. A., Crawford, I. A., & Price, R. J. 2005, *MNRAS*, 357, 961

Black, J. H. 1994, *ASPC*, 58, 355

Bloemen, J. B. G. M., et al. 1986, *A&A*, 154, 25

- Booth, R. S. & Aalto, S. 1998, in *The Molecular Astrophysics of Stars and Galaxies*, T. W. Hartquist & D. A. Williams (eds.), Oxford Science Publications, 437
- Boselli, A., Lequeux, J., & Gavazzi, G. 2002, *A&A*, 384, 33
- Brouillet, N., & Schilke, P. 1993, *A&A*, 277, 381
- Carlstrom, J. E., & Kronberg, P. P. 1991, *ApJ*, 366, 422
- Castor, J., McCray, R., & Weaver, R. 1975, *ApJ*, 200, L107
- Colbert, J. W. et al., 1999, *ApJ*, 511, 721
- Cottrell, G. A. 1977, *RASMN*, 178, 577
- Dame, T. M., Elmegreen, B. G., Cohen, R. S., & Thaddeus, P. 1986, *ApJ*, 305, 892
- de Grijs, R., O'Connell, R. W., & Gallagher, J. S., III 2001, *AJ*, 121, 768
- de Jong, T. 1977, *A&A*, 55, 137
- Dewangan, G. C., Titarchuk, L., & Griffiths, R. E. 2006, *ApJ*, 637, 21
- Dopita, M. A., Mathewson, D. S., & Ford, V. L. 1985, *ApJ*, 297, 599
- Dopita, M. A. et al., 2005, *ApJ*, 619, 755
- Downes, D. & Solomon, P. M. 1998, *ApJ*, 507, 615
- Draine, B. T., & Bertoldi F. 1996, *ApJ*, 468, 269
- Dumke, M., Nieten, Ch., Thuma, G., Wielebinski, R., & Walsh, W. 2001, *A&A*, 373, 853
- Dunne, L., Eales, S., et al. 2000, *MNRAS*, 315, 115D
- Efstathiou, A., Rowan-Robinson, M., & Siebenmorgen, R. 2000, *MNRAS*, 313, 734
- Elmegreen, G. G., Lada, C. J., & Dickinson, D. F. 1979, *ApJ*, 230, 415

- Fagotto, F., Bressan, A., Bertelli, G., & Chiosi, C. 1994, *A&AS*, 105, 29
- Farquhar, P. R. A., Millar, T. J., & Herbst, E. 1994, *MNRAS*, 269, 641
- Förster-Schreiber, N. M., Genzel, R., Lutz, D., Kunze, D., & Sternberg, A. 2001, *ApJ*, 552, 544
- Förster-Schreiber, N. M., Genzel, R., Lutz, D., & Sternberg, A. 2003, *ApJ*, 599, 193
- Franco, J., Tenorio-Tagle, G., & Bodenheimer, P. 1990, *ApJ*, 349, 126
- Galliano, F., et al. 2003, *A&A*, 407, 159
- Gao, Y., Lo, K. Y., Lee, S.-W., & Lee, T.-H. 2001, *ApJ*, 548, 172
- Gao, Y., & Solomon, P. M. 2004, *ApJS*, 152, 63
- Gao, Y., & Solomon, P. M. 2004, *ApJ*, 606, 271
- García-Burillo, S., Martín-Pintado, J., Fuente, A., & Neri, R. 2001, *ApJ*, 563, 27
- Glover, S. C. O., & Mac Low, M. 2007, *ApJ*, 659, 131
- Goldreich, P. & Kwan, J. 1974, *ApJ*, 189, 441
- Grebel, E. K.; & Chu, Y-H. 2000, *ApJ*, 119, 787
- Gusten, R., et al. 1993, *ApJ*, 402, 537
- Hartquist, T. W., Falle, S. A. E. G., Williams, D. A. 2003, *Ap&SS*, 288, 369
- Harwit, M., & Pacini, F. 1975, *ApJ*, 200, 127
- Heckman, T. M., et al. 1998, *ApJ*, 503, 646
- Hollenbach, D. J., Takahashi, T., Tielens, A. G. G. M. 1991, *ApJ*, 377, 192
- Hollenbach, D. J. & Tielens, A. G. G. M. 1997, *ARA&A*, 35, 179

Hollenbach, D. J. & Tielens, A. G. G. M. 1999, *RvMP*, 71, 173

Hosokawa, T. & Inutsuka, S. 2005, *ApJ*, 623, 917

Jansen, D. 1995, PhD Thesis, Leiden Observatory, Netherlands

Jog, C. J., & Solomon, P. M. 1992, *ApJ*, 387, 152

Jura, M. 1974, *ApJ*, 190, 33

Kaufman, M. J., Wolfire, M. G., Hollenbach, D. J., & Luhman, M. L. 1999, *ApJ*, 527, 795

Kawakatu, N., & Umemura, M. 2005, *ApJ*, 628, 721

Kenney, J. D. P. & Young, J. S. 1989, *ApJ*, 344, 171

Kennicutt, R. C., Jr. 1983, *ApJ*, 272, 54

Kennicutt, R. C., Jr. 1998, *ApJ*, 498, 541

Keto, E., Ho, L. C., Lo, K.-Y. 2005, *ApJ*, 635, 1062

Koo, B. & McKee, C. F. 1992, *ApJ*, 388, 93

Leitherer, C. et al., 1999, *ApJS*, 123, 3

Leitherer, C., 2005, *AIPC*, 783, 280

Lerate, M. R., et al. 2006, *MNRAS*, 370, 597

Le Teuff, Y. H., Millar, T. J., & Markwick, A. J. 2000, *A&AS*, 146, 157

Lipsy, S. J., & Plavchan, P. 2004, *ApJ*, 603, 82

Lo, K. Y., et al. 1987, *ApJ*, 312, 574

- Lonsdale, C. J.; Farrah, D.; & Smith, H. E. 2006, *Astrophysics Updated 2*, edited by J. W. Mason. Springer-Verlag, Heidelberg, Germany, page 285.
- Lynds, C. R., & Sandage, A. R. 1963, *ApJ*, 137, 1005
- Mac Low, M. M., & McCray, R. 1988, *ApJ*, 324, 776
- Madau, P. et al., 1998, *ApJ*, 498, 106M
- Martin, P. G., & Mandy, M. E. 1995, *ApJ*, 455, 89
- Mao, R. Q., et al. 2000, *A&A*, 358, 433
- Mathis, J. S., Mezger, P. G., & Panagia, N. 1983, *A&A*, 128, 212
- Mathis, J. S., 1990, *ARA&A*, 28, 37
- Mauersberger, R., Henkel, C., Walsh, W., & Schulz, A. 1999, *A&A*, 341, 256
- McCray, R. & Kafatos, M. 1987, *ApJ*, 317, 190
- Melo, V. P., Muñoz-Tuñón, C., Maíz-Apellániz, J., & Tenorio-Tagle, G. 2005, *ApJ*, 619, 270
- Meurer, G. R., Heckman, T. M., Leitherer, C., Kinney, A., Robert, C., & Garnett, D. R. 1995, *AJ*, 110, 2665
- Muxlow, T. W. B., Pedlar, A., Wilkinson, P. N., Axon, D. J., Sanders, E. M., & de Bruyn, A. G. 1994, *MNRAS*, 266, 455 %
- Negishi, T., Onaka, T., Chan, K.-W., & Roellig, T. L. 2001, *A&A*, 375, 566
- Neininger, N., t al. 1998, *A&A*, 339, 737
- Oey, M. S., & García-Segura, G. 2004, *ApJ*, 613, 302
- Olofsson, H., & Rydbeck, G. 1984, *A&A*, 136, 17

- Pedlar, A., Muxlow, T., & Wills, K. A. 2003, *RMxAC*, 15, 303
- Petitpas, G. R., & Wilson, C. D. 2000, *ApJ*, 538, 117
- Petitpas, G. R., & Wilson, C. D. 2001, *ESASP*, 460, 483
- Rieke, G. H., & Low, F. J. 1975, *ApJ*, 199, 17
- Rieke, G. H., Lebofsky, M. J., Thompson, R. I., Low, F. J., & Tokunaga, A. T. 1980, *ApJ*, 238, 24
- Rieke, G. H., Loken, K., Thompson, M. J., & Tamblyn, P. 1993, *ApJ*, 412, 99
- Rawlings, J. M. C., & Yates, J. A. 2001, *MNRAS*, 326, 1423
- Rieu, N. Q., Nakai, N., Jackson, J. M. 1989, *A&A*, 220, 57
- Röllig, M., et al. 2007, *A&A*, 467, 187
- Rybicki, G. B., & Lightman, A. P. 1979, *Radiative Processes in Astrophysics* (New York: Wiley)
- Salpeter, E. E. 1955, *ApJ*, 121, 161
- Sanders, D. B., Scoville, N. Z., & Solomon, P. M. 1985, *ApJ*, 289, 373
- Sanders, D. B., et al. 1988, *ApJ*, 325, 74
- Satyapal, S., et al. 1999, *ApJ*, 483, 148
- Schöier, F. L., et al. 2005, *A&A*, 432, 369
- Shen, Jianjun, & Lo, K. Y. 1996, *IAUS*, 170, 101
- Seaquist, E. R., Frayer, D. T., & Bell, M. B. 1998, *ApJ*, 507, 745
- Seaquist, E. R., & Frayer, D. T. 2000, *ApJ*, 540, 765

- Seaquist, E. R., Lee, S. W., & Moriarty-Schieven, G. H. 2006, *ApJ*, 638, 148
- Siebenmorgen, R., & Krügel, E. 2007, *A&A*, 461, 445
- Silich, S., Tenorio-Tagle, G., & Muñoz-Tuñón, C. 2007, *ApJ*, 669, 952
- Smith, L. J., et al. 2006, *MNRAS*, 370, 513
- Solomon, P. M., Rivolo, A. R., Barrett, J., & Yahil, A. 1987, *ApJ*, 319, 730
- Solomon, P. M., Downes, D., Radford, S. J. E., & Barrett, J. W. 1997, *ApJ*, 478, 144
- Spitzer, L. 1978, *Physical Processes in the Interstellar Medium*, Wiley Interscience, New York
- Stacey, G. J. et al. 1993, *ApJ*, 404, 219
- Stoerzer, H., Stutzki, J., & Sternberg, A. 1997, *A&A*, 323, 13
- Strong, A. W. et al. 1988, *A&A*, 207, 1
- Stutzki, J. et al. 1997, *ApJ*, 477, 33
- Tielens, A. G. G. M., & Hollenbach, D. 1985, *ApJ*, 291, 722
- van Dishoeck, E. F., Blake, G. A. 1988, *ApJ*, 334, 771
- van Dishoeck, E. F., Blake, G. A. 1998, *ARA&A*, 36, 317
- van Zadelhoff, G. J. et al., 2002, *A&A*, 395, 373
- Vazquez, G. A., & Leitherer, C. 2005, *ApJ*, 621, 695
- Visvanathan, N. 1974, *ApJ*, 192, 319
- Walter, F., Weiss, A., & Scoville, N. 2002, *ApJ*, 580, 21
- Ward, J. S., Zmuidzinas, J., Harris, A. I., & Isaak, K. G. 2003, *ApJ*, 587, 171

- Weaver, R., McCray, R., Castor, J., Shapiro, P., & Morre, R. 1977, *ApJ*, 218, 377
- Weiss, A., Walter, F., Neininger, N., & Klein, U. 1999, *A&A*, 345, 23
- Weiss, A., Neininger, N., Hhttemeister, S., & Klein, U. 2001, *A&A*, 365, 571
- Weiss, A., Walter, F., & Scoville, N. Z. 2005, *A&A*, 438, 533
- Weliachew, L., Fomalont, E. B., & Greisen, E. W. 1984, *A&A*, 137, 335
- Wild, W. et al., 1992, *ApJ*, 265, 447
- Wills, K. A., Redman, M. P., Muxlow, T. W. B., & Pedlar, A. 1999, *MNRAS*, 309, 395
- Wills, K. A., Das, M., Pedlar, A., Muxlow, T. W. B., & Robinson, T. G. 2000, *MNRAS*, 316, 33
- Wills, K. A., Pedlar, A., & Muxlow, T. W. B. 2002, *MNRAS*, 331, 313
- Wilson, C., et al. 2008, *ApJS*, 178, 189
- Yao, Lihong, Seaquist, E. R., Kuno, N., & Dunne, L. 2003, *ApJ*, 597, 1271
- Yao, Lihong, Bell, T., Viti, S., Yates, J. A., & Seaquist, E. R. 2006, *ApJ*, 636, 881
- Young, J. S., & Scoville, N. Z. 1984, *ApJ*, 287, 153
- Yun, M. S., Ho, P. T. P., & Lo, K. Y. 1993, *ApJ*, 411, 17